David Dritschel
Editor

IUTAM Bookseries

IUTAM Symposium on Turbulence in the Atmosphere and Oceans

Proceedings of the IUTAM Symposium on Turbulence in the Atmosphere and Oceans, Cambridge, UK, December 8–12, 2008

Springer

IUTAM Symposium on Turbulence
in the Atmosphere and Oceans

IUTAM BOOKSERIES

Volume 28

Aims and Scope of the Series

The IUTAM Bookseries publishes the proceedings of IUTAM symposia under the auspices of the IUTAM Board.

For other titles published in this series, go to
www.springer.com/series/7695

David Dritschel
Editor

IUTAM Symposium on Turbulence in the Atmosphere and Oceans

Proceedings of the IUTAM Symposium on Turbulence in the Atmosphere and Oceans, Cambridge, UK, December 8–12, 2008

Springer

Editor
David Dritschel
University of St Andrews
Mathematical Institute
St Andrews, Fife KY16 9SS
UK
dgd@mcs.st-and.ac.uk

ISSN 1875-3507 e-ISSN 1875-3493
ISBN 978-94-007-0359-9 e-ISBN 978-94-007-0360-5
DOI 10.1007/978-94-007-0360-5
Springer Dordrecht Heidelberg London New York

Cover design: VTEX, Vilnius

Printed on acid-free paper

Springer is part of Springer Science+Business Media (www.springer.com)

پیل اندر خانه‌ی تاریک بود
عرضه را آورده بودندش هنود

دیدنش با چشم چون ممکن نبود
اندر آن تاریکی‌اش کف می‌بسود

آن یکی را کف به خرطوم اوفتاد
گفت همچون ناودان است این نهاد

آن یکی را دست بر گوشش رسید
آن بر او چون بادبیزن شد پدید

در کف هرکس اگر شمعی بدی
اختلاف از گفتشان بیرون شدی

The elephant was in a dark house
As it was impossible to see it by eye
The palm of one fell on the trunk
The hand of one reached the ear
Had they had a candle in their palms

Some Hindus had brought it for exhibition
In the dark people felt it with their palms
'This is like a water-spout' he said
To him it was evidently like a fan
They would have said the same

Extract taken from "Tales from Masnavi", "The Elephant", by
Jalāl ad-Dīn Muhammad Rūmī (1207 – 1273)

Preface

The text of the Persian poet Rūmī, written some eight centuries ago, and reproduced at the beginning of this book is still relevant to many of our pursuits of knowledge, not least of turbulence. The text illustrates the inability people have in seeing the whole thing, the 'big picture'. Everybody looks into the problem from his/her viewpoint, and that leads to disagreement and controversy. If we could see the whole thing, our understanding would become complete and there would be no controversy.

The turbulent motion of the atmosphere and oceans, at the heart of the observed general circulation, is undoubtedly very complex and difficult to understand in its entirety. Even 'bare' turbulence, without rotation and stratification whose effects are paramount in the atmosphere and oceans, still poses great fundamental challenges for understanding after a century of research. Rotating stratified turbulence is a relatively new research topic. It is also far richer, exhibiting a host of distinct wave types interacting in a complicated and often subtle way with long-lived coherent structures such as jets or currents and vortices. All of this is tied together by basic fluid-dynamical nonlinearity, and this gives rise to a multitude of phenomena: spontaneous wave emission, wave-induced transport, both direct and inverse energy scale cascades, lateral and vertical anisotropy, fronts and transport barriers, anomalous transport in coherent vortices, and a very wide range of dynamical and thermodynamical instabilities.

This book stems from the IUTAM symposium "Rotating Stratified Turbulence and Turbulence in the Atmosphere and Oceans" which took place at the Isaac Newton Institute for Mathematical Sciences in Cambridge from 8 to 12 December 2008, and came at the end of a four-month Programme on "High Reynolds Number Turbulence". This symposium, widely attended by researchers from around the world, aimed to better understand the complex nature of fluid flows found in Nature, particularly in the Earth's atmosphere and oceans, but also in other planetary atmospheres and in the Sun's interior. Talks covered a broad range of subjects, from theoretical studies of fundamental vortex interactions, to laboratory experiments and observations, and to state-of-the-art computational studies. The full programme and videos

of many of the talks can be found at www.newton.ac.uk/programmes/HRT/hrtw04p.html.

The present volume presents a cross-section of the research presented at the symposium, or in some cases, of the research inspired by it. Herein, 23 peer-reviewed papers are collected (39 talks were presented). The research is loosely divided into four main topics: (1) Waves and Imbalance, (2) Turbulence and Convection, (3) Instability and Vortex Dynamics, and (4) Jets: Formation and Structure. In (1), the impact of waves, principally inertia–gravity waves, on the circulation of the atmosphere and oceans is examined. In (2), the distinguishing anisotropic features of atmospheric and oceanic turbulence, and of solar convection, that arise from rotation and stratification are discussed. In (3), vortex dynamical instabilities as well as the interactions between coherent vortices in rotating, stratified flows are examined. And in (4), various models and theories are put forward to explain the formation and persistence of "jets", nearly zonal currents in the atmosphere and oceans, in the giant gas planets, and probably also in the solar interior.

Research on these topics is rapidly developing, yet we still have much to learn, and there is no shortage of controversy! This volume brings together in a concise way current research by eminent mathematicians, scientists and engineers. As such, this makes an excellent resource for future studies exploring fundamental aspects of atmospheric and oceanic turbulence.

St Andrews,

July 2010 *David Dritschel*

Acknowledgements Generous support of the Isaac Newton Institute in Cambridge and the International Union of Theoretical and Applied Mechanics made this work possible, and moreover provided the opportunity for researchers to meet in a stimulating environment to discuss common research ideas and future directions. This was greatly appreciated by all involved. I would like to thank the staff of the Isaac Newton Institute for their highly professional conduct and for their help in all aspects of the organisation of the symposium. I would also like to thank the Scientific Organising Committee — Peter Bartello, Peter Davidson, Ross Griffiths, Keith Moffatt, Joël Sommeria, Kraig Winters, and Shigeo Yoden — for their extensive help along the way, from conceiving and developing the original idea to creating and running the final programme.

The Persian text and its translation (adapted from www.khamush.com/tales_from_masnavi.htm#The%20Elephant) were generously provided by Ali Mohebalhojeh. This story of the elephant, we feel, reflects beautifully the struggle we face in understanding many things, and the importance of seeing the whole.

Contents

List of Contributors

Jonathan Apsden
School of Mathematics and Maxwell Institute, University of Edinburgh, Edinburgh EH9 3JZ, UK, e-mail: j.m.aspden@sms.ed.ac.uk

Peter Bartello
Department of Atmospheric and Oceanic Sciences, McGill University, Montréal H3A 2K6, Quebec, Canada, e-mail: bartello@math.mcgill.ca

Paul Billant
Hydrodynamics Laboratory (LadHyX), Ecole Polytechnique, 91128 Palaiseau Cedex, France, e-mail: billant@ladhyx.polytechnique.fr

Nicolas Boulanger
Technologies Avancées pour le Génome et la Clinique, INSERM, 163 Avenue de Luminy, 13288 Marseille, France, e-mail: boulanger@tagc.univ-mrs.fr

Friedrich Busse
Institute of Physics, University of Bayreuth, D-95440 Bayreuth, Germany, e-mail: busse@uni-bayreuth.de

George Carnevale
Scripps Institution of Oceanography, University California San Diego, La Jolla, CA 92093, USA, e-mail: gcarnevale@ucsd.edu

Xavier Carton
LPO/UBO, 29200 Brest, France, e-mail: xcarton@univ-brest.fr

Jean-Marc Chomaz
Hydrodynamics Laboratory (LadHyX), Ecole Polytechnique, 91128 Palaiseau Cedex, France, e-mail: chomaz@ladhyx.polytechnique.fr

Stuart Dalziel
DAMTP, Centre for Mathematical Sciences, Wilberforce Road, Cambridge, CB3 0WA, e-mail: S.Dalziel@damtp.cam.ac.uk

Peter Davidson
University of Cambridge, Department of Engineering, Trumpington Street, Cambridge, CB2 1PZ, UK, e-mail: pad3@eng.cam.ac.uk

Axel Deloncle
Hydrodynamics Laboratory (LadHyX), Ecole Polytechnique, 91128 Palaiseau Cedex, France, e-mail: axel.deloncle@ladhyx.polytechnique.fr

David Dritschel
Mathematical Institute, University of St Andrews, St Andrews KY16 9SS, UK, e-mail: dgd@mcs.st-and.ac.uk

Jérôme Fontane
ISAE – DAEP, 1 place Emile Blouin, BP 75064, 31033 Toulouse, France, e-mail: j.fontane@isae.fr

Alan Guillou
IFREMER, 29280 Plouzane, France, e-mail: alain.guillou@ifremer.fr

Yoshi-Yuki Hayashi
Graduate School of Science, Kobe University, Kobe, 657-8501, Japan, e-mail: shosuke@gfd-dennou.org

Jackson Herring
NCAR, Boulder CO 80307, USA, e-mail: herring@ucar.edu

Shintaro Hoshi
Department of Mechanical Engineering and Intelligent Systems, University of Electro-Communications, Chofu, Tokyo, 182-8585, Japan, e-mail: s.hoshi@miyazaki.mce.uec.ac.jp

Keiichi Ishioka
Division of Earth and Planetary Sciences, Graduate School of Science, Kyoto University, Kyoto, 606-8502, Japan, e-mail: ishioka@gfd-dennou.org

Hidefumi Kimura
Department of Mechanical Engineering and Intelligent Systems, University of Electro-Communications, Chofu, Tokyo, 182-8585, Japan, e-mail: hidefumi@miyazaki.mce.uec.ac.jp

Yoshifumi Kimura
Graduate School of Mathematics, Nagoya University, Furo-cho, Chikusa-ku, Nagoya 464-8602, Japan, e-mail: kimura@math.nagoya-u.ac.jp

Yuji Kitamura
Meteorological Research Institute, Japan Meteorological Agency, Tsukuba, 305-0052, Japan, e-mail: kitamura@mri-jma.go.jp

Rudolf Kloosterziel
School of Ocean and Earth Science and Technology, University of Hawaii, Honolulu, HI 96822, USA, e-mail: rudolf@soest.hawaii.edu

Eric Kunze
School of Earth and Ocean Sciences, University of Victoria, Victoria, BC V8P 5C2, Canada, e-mail: kunze@uvic.ca

Stéphane Le Dizès
Institut de Recherche sur les Phenomenes Hors Equilibre, CNRS, Aix-Marseille Universites, 49 rue Joliot-Curie, 13384 Marseille, France, e-mail: ledizes@irphe.univ-mrs.fr

M.-Pascale Lelong
NorthWest Research Associates, P.O. Box 3027 Bellevue WA 98009-3027, USA, e-mail: pascale@nwra.com

Mahdi Mahdizadeh
Hormozgan University, Bandar Abbas, Iran, e-mail: mehdizadeh@hormozgan.ac.ir

Michael McIntyre
DAMTP, Centre for Mathematical Sciences, Wilberforce Road, Cambridge, CB3 0WA, e-mail: M.E.McIntyre@damtp.cam.ac.uk

James McWilliams
Institute of Geophysics and Planetary Physics, University of California, Los Angeles, CA 90095-1567, USA, e-mail: jcm@atmos.ucla.edu

Sergey Medvedev
Institute of Computational Technologies, Novosibirsk, Russia, e-mail: medvedev@ict.nsc.ru

Patrice Meunier
Institut de Recherche sur les Phenomenes Hors Equilibre, CNRS, Aix-Marseille Universites, 49 rue Joliot-Curie, 13384 Marseille, France, e-mail: meunier@irphe.univ-mrs.fr

Takeshi Miyazaki
Department of Mechanical Engineering and Intelligent Systems, University of Electro-Communications, Chofu, Tokyo, 182-8585, Japan, e-mail: miyazaki@mce.uec.ac.jp

Sergey Nazarenko
Mathematics Institute, University of Warwick, Gibbet Hill Road, Coventry CV4 7AL, UK, e-mail: S.V.Nazarenko@.warwick.ac.uk

Seiya Nishizawa
Graduate School of Science, Kobe University, Kobe, 657-8501, Japan, e-mail: seiya@gfd-dennou.org

Paolo Orlandi
Dipartimento di Meccanica e Aeronautica, Università di Roma, “La Sapienza,” via Eudossiana 18, 00184 Rome, Italy, e-mail: orlandi@kolmogorov.ing.uniroma1.it

Ivane Pairaud
IFREMER, La Seyne sur Mer, France, e-mail: Ivane.Pairaud@ifremer.fr

Xavier Perrot
LPO/UBO, 29200 Brest, France, e-mail: xperrot@univ-brest.fr

Brenda Quinn
Mathematics Institute, University of Warwick, Gibbet Hill Road, Coventry CV4 7AL, UK, e-mail: B.E.Quinn@warwick.ac.uk

Peter Rhines
School of Oceanography, University of Washington, Box 355351, Seattle, WA 98195, e-mail: rhines@ocean.washington.edu

Xavier Riedinger
Institut de Recherche sur les Phenomenes Hors Equilibre, CNRS, Aix-Marseille Universites, 49 rue Joliot-Curie, 13384 Marseille, France, e-mail: riedinger@irphe.univ-mrs.fr

Richard Scott
Mathematical Institute, University of St Andrews, St Andrews KY16 9SS, UK, e-mail: rks@mcs.st-and.ac.uk

Victor Shrira
Department of Mathematics, EPSAM, Keele University, Keele, Staffordshire ST5 5BG, UK, e-mail: v.i.shrira@maths.keele.ac.uk

Radostin Simitev
Department of Mathematics, University of Glasgow, Glasgow G12 8QW, UK, e-mail: r.simitev@maths.gla.ac.uk

Daan van Sommeren
Technische Universiteit Eindhoven, 5600 MB Eindhoven, The Netherlands, e-mail: d.d.j.a.v.sommeren@student.tue.nl

Joël Sommeria
LEGI UMR 5519, CNRS & Université de Grenoble, BP 53, 38041 Grenoble, France, e-mail: joel.sommeria@legi.grenoble-inp.fr

Chantal Staquet
LEGI, CNRS & Université de Grenoble, France, e-mail: Chantal.Staquet@hmg.inpg.fr

Philip Staplehurst
BP Exploration – Sunbury, Chertsey Road, Sunbury-on-Thames, Middlesex TW16 7LN, UK

Sin-ichi Takehiro
Research Institute for Mathematical Sciences, Kyoto University, Kyoto, 606-8502, Japan, e-mail: takepiro@gfd-dennou.org

Steven Tobias
Department of Applied Mathematics, University of Leeds, Leeds LS2 9JT, UK, e-mail: smt@maths.leeds.ac.uk

William Townsend
Department of Mathematics, EPSAM, Keele University, Keele, Staffordshire ST5 5BG, UK, e-mail: w.a.townsend@epsam.keele.ac.uk

Jacques Vanneste
School of Mathematics and Maxwell Institute, University of Edinburgh, Edinburgh EH9 3JZ, UK, e-mail: j.vanneste@ed.ac.uk

Antoine Venaille
GFDL-AOS Princeton University, Princeton NJ, 08540, USA, e-mail: venaille@princeton.edu

Michio Yamada
Research Institute for Mathematical Sciences, Kyoto University, Kyoto, 606-8502, Japan, e-mail: yamada@kurims.kyoto-u.ac.jp

Shigeo Yoden
Division of Earth and Planetary Sciences, Graduate School of Science, Kyoto University, Kyoto, 606-8502, Japan, e-mail: yoden@kugi.kyoto-u.ac.jp

Vladimir Zeitlin
LMD, Univercity Paris VI and Ecole Normale Supérieure, Paris, France, e-mail: zeitlin@lmd.ens.fr

Part I
Waves and Imbalance

On spontaneous imbalance and ocean turbulence: generalizations of the Paparella–Young epsilon theorem

Michael E. McIntyre

Abstract Recent progress in understanding the balance–imbalance problem is highlighted, with emphasis on spontaneous-imbalance phenomena associated with the exponentially fast "wave capture" of inertia–gravity waves. These phenomena are excluded from shallow-water models and are outside the scope of the classical Lighthill theory. Also discussed is progress on a different topic, an effort to extend the Paparella–Young *epsilon theorem* to realistic ocean models. The theorem constrains turbulent dissipation rates ε in horizontal-convection thought-experiments, in which mechanically-driven stirring is switched off. The theorem bears on the so-called "ocean heat engine" and "ocean desert" controversies. The original theorem (2002) applied only to very idealized ocean models. Several restrictions on the original proof can now be lifted including the restriction to a linear, thermal-only equation of state. The theorem can now be proved for fairly realistic equations of state that include thermobaric effects, and nonlinearity in both temperature and salinity. The restriction to Boussinesq flow can also be lifted. The increased realism comes at some cost in terms of weakening the constraint on ε. The constraint is further weakened if one allows for the finite depth of penetration of solar radiation. This is collaborative work with Francesco Paparella and William Young.

1 Introduction

Following the organizers' aims, I had originally undertaken to talk only about the first topic in this paper, spontaneous imbalance and accurate PV (potential vorticity) inversion. Recent progress in that field has been remarkable, throwing a clear light on where the Lighthill paradigm is relevant and where it is not, as well as finding the first accurate and completely self-consistent PV inversion operators. However,

Michael E. McIntyre, Department of Applied Mathematics and Theoretical Physics, Wilberforce Rd, Cambridge CB3 0WA, United Kingdom. http://www.atm.damtp.cam.ac.uk/people/mem/

D. Dritschel (ed.), *IUTAM Symposium on Turbulence in the Atmosphere and Oceans*, IUTAM Bookseries 28, DOI 10.1007/978-94-007-0360-5_1,

most of what I had to say about this is already in print elsewhere [12; 13]. Here I give only a quick summary, in Section 2, then move on to the second topic.

The second topic concerns the oceanic MOC, the meridional overturning circulation. It is sometimes called the thermohaline "conveyor belt" despite having nothing like the inextensibility of a real mechanical conveyor belt. The aspect crucial to questions such as the desertification, or not, of the upper ocean under global warming is the rising branch relative to the stratification surfaces in the main thermocline and elsewhere. It is upward material transport across stratification surfaces that is germane to questions about the supply of nutrients to the upper ocean [21], and hence about desertification or not.

It has sometimes been thought that buoyancy forcing alone can "drive the conveyor belt", a scenario much discussed under the heading "horizontal convection". The idea seems to be that the cooling of the sea surface in high latitudes is the main control, not only driving the deep-convective plumes and gravity currents of which the downward branch is composed but also supplying sufficient stirring, hence diapycnal mixing, to sustain the upward branch against the stable stratification N^2. Clearly the plumes and gravity currents must cause a certain amount of stirring and mixing.

Such a picture might tempt one to suppose that the "conveyor belt" circulation is something that can be shut off entirely by reducing the buoyancy forcing – by either warming or freshening the high-latitude sea surface, or both. A contrary view is that the *upward* branch depends, rather, on mechanical stirring by winds, tides, and possibly biota [2; 15; 25; 28]. In that case the upward branch would hardly be affected by shutting off the few tens of sverdrups [5] of flow in the downward branch. The sole effect would be to make the stratification surfaces drift downward, very gradually, without much affecting the upward material transport across them.[1]

The theorem of Paparella and Young published in 2002 [19], hereafter PY02, puts important and mathematically rigorous constraints on our thinking about these questions. It does so by placing a severe upper bound on the average turbulent dissipation rates ε attainable in a horizontal-convection scenario for small molecular diffusivities. If one accepts the usual empirical (Ellison–Britter–Osborn) relation between ε values and diapycnal mixing rates

$$K_z \sim \gamma\varepsilon/N^2 \tag{1}$$

where K_z is the vertical eddy diffusivity describing the mixing, and $\gamma \lesssim 0.2$, see e.g. [17], also [11], then one can strengthen the arguments for the importance of me-

[1] For instance "very gradually" would mean a downward drift of just under a kilometre per millennium for every ten sverdrups of downward flow that remained shut off. This downward drift of the stratification surfaces would not, however, detach the main thermocline from its Southern Ocean outcrop and therefore would not shut off the wind-driven mechanical stirring and Ekman transport across the outcropping stratification surfaces, contributing to the "upward" branch [25, & refs.]. This is because of the way in which the speed of the Antarctic Circumpolar Current is regulated internally, almost independently of wind stress but very much favouring the outcropping, e.g. [22] & refs. – a very different circumstance from that in the hothouse climate of the early Eocene 50 million years ago, when the Sun was about half a percent cooler but the Drake Passage still closed.

chanical stirring to the upward branch [14; 15; 28], including the superficial stirring and Ekman transport across the Southern Ocean outcrop [25, & refs.], and hence to the transports of nutrients across the ocean's stratification surfaces into the upper ocean, along with other questions about the oceanic general circulation.

However, PY02's epsilon theorem applies only to a highly idealized Boussinesq ocean model, in a rectangular domain, with a linear equation of state that neglects salinity altogether. In my talk at the international Workshop on 10 December 2008 I described a generalization in which all these restrictions were lifted except the Boussinesq approximation. (A video of the talk, "Beyond Lighthill...", was made publicly available via `http://sms.cam.ac.uk/media/518985/formats` later that month.) In particular, the new epsilon theorem allowed for arbitrary bottom topography, curved geopotentials and an equation of state that included not only salinity, but also the two main nonlinearities of real seawater, the thermal and thermobaric nonlinearities. This was work in collaboration with Francesco Paparella and William R. Young. Young had earlier reported our first breakthrough, the first result for a nonlinear equation of state, to the Stockholm Sandström Centennial Meeting on 3 November 2008.

As shown in Sects. 3 and 4 below, the key to proving these generalized epsilon theorems, and further generalizations arrived at after the Workshop, was to exploit Young's formulation of Boussinesq energetics. The formulation is a simple way of handling thermobaricity and is essentially that given, with due acknowledgement, on p. 73 of the textbook by Vallis [26]. Young (personal communication and ref. [30]) beautifully clarifies the way in which a vestige of the thermodynamic energies survives in the Boussinesq limit, adding to the gravitational potential energy.

Armed with Young's formulation, we were able to go on to prove epsilon theorems for still more realistic equations of state, including those being standardized by the international SCOR/IAPSO Working Group 127 on the *Thermodynamics and Equation of State of Seawater*. The accuracies are state of the art, comparable to those in recent publications such as [3; 7]. In addition, we were able to lift the Boussinesq restriction and thereby shed a fundamentally new light on the subject. A full report is in preparation, whose first part is to be submitted to the *Journal of Fluid Mechanics*, hereafter "JFM".

A few days before submission of the present paper, we learned that Jonas Nycander [16] had independently arrived at a generalized epsilon theorem based on Young's Boussinesq energy equation, (13) below, and a nonlinear equation of state almost the same as (20) below. Nycander's Boussinesq result almost exactly parallels the result to be described in Sect. 4 below, and reported in my December Workshop talk.

2 Spontaneous imbalance

The recent progress in this area concerns spontaneous imbalance of the kind discovered in the 1990s by O'Sullivan and Dunkerton [18], in continuously stratified

flows. In particular, it is now clear why these continuously stratified scenarios – let us call them OSD-type scenarios – are at an opposite extreme to what would be expected from the Lighthill theory [9], which applies not only to Lighthill's original case of acoustic imbalance but also to typical shallow-water scenarios [4]. The Lighthill theory is the classic milestone in the field. When it was published in 1952 it offered profound new insights. These were the first generic insights into the nature of spontaneous imbalance, even though not all-embracing, as it now turns out. A review and historical perspective may be found in [12].[2]

In brief, the continuously stratified, OSD-type scenarios differ drastically from Lighthill-type scenarios in three respects. First, the radiation reaction on the wave generation region is substantial. In a Lighthill scenario, by contrast, the radiation reaction is weak, permitting non-iterative computation of the spontaneous imbalance and the resulting wave emission after first computing the vortical motion using PV inversion, i.e. altogether neglecting the wave emission. This was Lighthill's most fundamental point. The vortical motion can be regarded as known before computing the wave emission.

Such non-iterative computation is impossible in an OSD-type scenario. The vortical motion and wave emission are intimately part of each other throughout the wave source region. As pointed out in [12], the wave emission process is fundamentally similar to mountain-wave generation except in one crucial respect. In order for the analogy to be accurate, recognizing the substantial radiation reaction, one must consider the notional mountain to be made of an elastic substance so pliable that the wave emission process substantially changes the shape of the mountain, hence substantially changes the vertical velocity field.

The second and related respect is the lack of scale separation in the wave source region, in an OSD-type scenario. The reason why the spontaneous wave emission is weak in a Lighthill scenario is the destructive interference arising from scale separation. The emitted waves have typical scales, or reciprocal wavenumbers, that greatly exceed typical vortex scales. In an OSD scenario, by contrast, the waves arise in the source region with reciprocal wavenumbers indistinguishable from typical scales of the vortex motion. As they propagate away from the source region the waves undergo "wave capture", or strain-enhanced critical-layer absorption, with wavenumbers increasing exponentially fast [20, & refs.]. This ensures that back-reflection and resonance phenomena are negligible and that the radiation reaction on the source is similar to that of waves satisfying a radiation condition.

The third respect is unsteadiness versus quasi-steadiness of the wave emission process. In a Lighthill scenario, unsteadiness of the vortical motion is a crucial part of the spontaneous-imbalance mechanism. In an OSD scenario, with its mountain-wave-like character, it is now clear that one can have inertia–gravity wave emission from a steady vortical flow. Perhaps the first work to point clearly to that fact was the study reported in [24], in which a surface temperature front was prevented from collapsing by applying an artificial diffusivity, holding the front approximately steady. Recently, examples have come to light for which perfectly steady flow is a natural

[2] Also available from `www.atm.damtp.cam.ac.uk/people/mem/#imbalance`

idealization. These are the propagating vortex dipoles described in several recent papers including [23] and [27]. They were discovered through high-resolution numerical experiments. The review in [12] gives a careful description and comparison between the two best-resolved cases, including the evidence for a substantial radiation reaction.

3 Epsilon theorems for realistic ocean models

PY02's epsilon theorem [19] constrains the turbulent dissipation rates ε attainable in an idealized horizontal-convection scenario. A Boussinesq liquid in a rigid, thermally insulating, box-shaped container of depth H, with gravity uniform and the top surface exactly horizontal, is set in motion purely by maintaining a nonuniform temperature ϑ at the top surface. The buoyancy acceleration b is a linear function of ϑ alone. No mechanical stirring is allowed. A statistically steady state is assumed. For this scenario PY02 rigorously established a bound proportional to the range Δb of buoyancy-acceleration values at the top surface,

$$\langle\langle \varepsilon \rangle\rangle \leqslant \kappa \Delta b / H \tag{2}$$

where the double angle brackets denote the domain and time average and where κ is the thermal molecular diffusivity. Therefore, in particular, $\langle\langle \varepsilon \rangle\rangle$ goes to zero as the first power of κ in the limit of small molecular diffusivities, for instance holding the Prandtl number ν/κ constant where ν is the molecular diffusivity of momentum. The vanishing of $\langle\langle \varepsilon \rangle\rangle$ in that limit was at first called an "anti-turbulence theorem". However, we now prefer to call it an "epsilon theorem" for two reasons, first because the theorem does not rule out locally finite ε values in the limit, in shrinking subvolumes of the domain, and second because, even if ε were to go to zero at the same rate as $\langle\langle \varepsilon \rangle\rangle$ in all locations, it would still be possible to have weak yet fully-developed turbulence in the sense of having a Richardson cascade and a vanishingly small Kolmogorov scale $(\nu^3/\varepsilon)^{1/4} \propto \kappa^{1/2}$.

Now the key to proving epsilon theorems is to avoid considering the complete energetics. Indeed, one must dissect the complete energetics in a certain way. This happens automatically for the Boussinesq equations and is one of the facts implicitly exploited in PY02's proof, along with the linearity of the equation of state, $b \propto \vartheta$. In the Boussinesq equations the internal and chemical energies of seawater are relegated to an almost passive role. For the full equations the proof is harder to spot because the complete energetics must, of course, take account of the full thermodynamics including the internal and chemical energies.

Even within the Boussinesq equations there are nontrivial technical obstacles to be overcome, beyond making the geometry and the centrifugal–gravitational field more realistic. They concern the nonlinearities in realistic equations of state for seawater. The first steps toward overcoming these obstacles were taken by Francesco Paparella, William R. Young and myself, working together last year. The key was

to recognize first that a mathematical device used in PY02, consisting of two successive integrations with respect to altitude z – the steps leading from (2.1b,c) to (2.3) and then to (3.3), in ref. [19] – could be replaced by a single integration after multiplication by z. The second step was to recognize that this integration was a pointer toward using the Boussinesq energy formulation discovered by Young (personal communication and ref. [30]), working on a different problem after PY02 was published. For a general, nonlinear equation of state the crucial step is to introduce a quantity most aptly called the *dynamic enthalpy*, which in this context takes on the superficial appearance of a buoyancy-associated potential energy, the quantity denoted by Π in Eq. (2.116) of Vallis [26] but here denoted by $h^{\ddagger}$ in order to flag the connection with enthalpy. That connection is carefully explained in [30]. It clarifies the "almost passive" role of the internal and chemical energies.

Consider a domain like that in Fig. 1 with arbitrary topography and curved geopotentials. It is now easiest to take the Boussinesq equations in coordinate-independent form

$$\mathrm{D}\mathbf{u}/\mathrm{D}t + 2\boldsymbol{\Omega}\times\mathbf{u} + \boldsymbol{\nabla}p - b\boldsymbol{\nabla}\mathcal{Z} \;=\; \boldsymbol{\nabla}\cdot\boldsymbol{\sigma}\,, \tag{3}$$

$$\mathrm{D}\vartheta/\mathrm{D}t \;=\; -\boldsymbol{\nabla}\cdot\mathbf{J}_\vartheta\,, \tag{4}$$

$$\mathrm{D}S/\mathrm{D}t \;=\; -\boldsymbol{\nabla}\cdot\mathbf{J}_S\,, \tag{5}$$

$$\boldsymbol{\nabla}\cdot\mathbf{u} \;=\; 0\,, \tag{6}$$

where $\boldsymbol{\Omega}$ is the Earth's angular velocity, $\mathrm{D}/\mathrm{D}t$ the material derivative $\partial/\partial t + \mathbf{u}\cdot\boldsymbol{\nabla}$, $\mathbf{u}(\mathbf{x},t)$ the relative velocity, $p(\mathbf{x},t)$ the pressure anomaly with the reference density $\rho = \rho_0 = 1$ in suitable units, $\mathcal{Z} = \mathcal{Z}(\mathbf{x})$ a scaled geopotential height to be defined below, with its zero level at the top surface, $\boldsymbol{\sigma}$ the viscous stress tensor with components $\sigma_{ij} = \sigma_{ji}$ while S and ϑ are salinity and conservative temperature [10], and $\mathbf{J}_S$

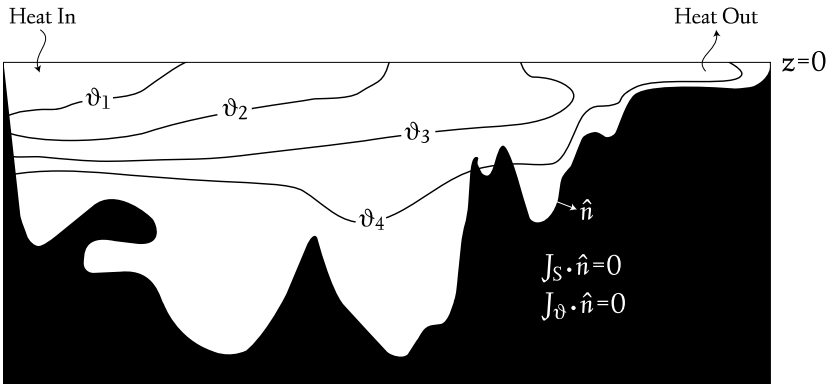

Fig. 1 Schematic of a model ocean. Instead of PY02's idealized rectangular domain, arbitrary topography is allowed, across which there are no salt or heat fluxes. The geothermal heat flux is assumed negligible. Salinity as well as temperature variations are allowed, as is a fully nonlinear equation of state. The effective geopotentials (gravitational plus centrifugal) are allowed to curve realistically, with gravity plus centrifugal force nonuniform, and $\mathcal{Z}$ the geopotential altitude.

and $\mathbf{J}_\vartheta$ their molecular-diffusive fluxes in suitable units. These may include cross-diffusivities arising from the Soret and Dufour effects and other thermodynamic dependences. The nonlinear equation of state has the generic form

$$b = b(\vartheta, \mathcal{Z}, S)\,. \tag{7}$$

To help formalize the Boussinesq limit, it is convenient to define $\mathcal{Z}$ as the actual geopotential relative to the top surface divided by a constant reference value g_0 of the gravity acceleration g, so that $\mathcal{Z}$ is approximately the geometric altitude and $\boldsymbol{\nabla}\mathcal{Z}$ approximately a unit vertical vector. Then b is $-g_0$ times the fractional density anomaly. Thermobaric nonlinearities are represented within the Boussinesq framework by the dependence of b on $\mathcal{Z}$, since the background reference pressure $= -\rho_0 g_0 \mathcal{Z} +$ (surface pressure). Defining $\mathcal{W} := \mathrm{D}\mathcal{Z}/\mathrm{D}t$ and $\varepsilon := \boldsymbol{\nabla}\mathbf{u}{:}\boldsymbol{\sigma} = u_{i,j}\sigma_{ij}$, the local per-unit-mass viscous rate of conversion of mechanical energy into thermal energy, and taking the scalar product of (3) with $\mathbf{u}$ we have, using incompressibility (6),

$$\frac{\partial}{\partial t}\left(\tfrac{1}{2}|\mathbf{u}|^2\right) \,-\, \mathcal{W}b \,+\, \boldsymbol{\nabla}\cdot\left\{\mathbf{u}\left(\tfrac{1}{2}|\mathbf{u}|^2 + p\right) - \mathbf{u}\cdot\boldsymbol{\sigma}\right\} \,=\, -\varepsilon \tag{8}$$

where $\boldsymbol{\nabla}\cdot(\mathbf{u}\cdot\boldsymbol{\sigma}) = (u_i\sigma_{ij})_{,j}$. The problem now is what to do with the buoyancy term $\mathcal{W}b$. Standard ways to turn it into a rate of change of potential energy fail because of thermobaricity. The difficulty can be overcome by introducing Young's dynamic enthalpy $h^\ddagger$ (personal communication and ref. [30]), whose definition is

$$h^\ddagger(\vartheta, \mathcal{Z}, S) \,:=\, \int_{\mathcal{Z}}^{0} b(\vartheta, \mathcal{Z}', S)\mathrm{d}\mathcal{Z}'\,. \tag{9}$$

Then, by the chain rule,

$$\frac{\mathrm{D}h^\ddagger}{\mathrm{D}t} \,=\, -\mathcal{W}b + \mathscr{D}(\vartheta, \mathcal{Z}, S) \tag{10}$$

where the dissipative contribution

$$\mathscr{D}(\vartheta, \mathcal{Z}, S) \,:=\, \frac{\partial h^\ddagger}{\partial \vartheta}\frac{\mathrm{D}\vartheta}{\mathrm{D}t} \,+\, \frac{\partial h^\ddagger}{\partial S}\frac{\mathrm{D}S}{\mathrm{D}t} \tag{11}$$

$$= \,-\frac{\partial h^\ddagger}{\partial \vartheta}\,\boldsymbol{\nabla}\cdot\mathbf{J}_\vartheta - \frac{\partial h^\ddagger}{\partial S}\,\boldsymbol{\nabla}\cdot\mathbf{J}_S\,. \tag{12}$$

Then from (6), (8) and (10) we have an equation whose left-hand side is in conservation form,

$$\frac{\partial}{\partial t}\left(\tfrac{1}{2}|\mathbf{u}|^2 + h^\ddagger\right) \,+\, \boldsymbol{\nabla}\cdot\left\{\mathbf{u}\left(\tfrac{1}{2}|\mathbf{u}|^2 + p + h^\ddagger\right) - \mathbf{u}\cdot\boldsymbol{\sigma}\right\} \,=\, -\varepsilon + \mathscr{D}(\vartheta, \mathcal{Z}, S)\,, \tag{13}$$

and whose domain and time average is, for the statistically steady state,

$$\langle\!\langle \varepsilon \rangle\!\rangle \, - \, \langle\!\langle \mathscr{D}(\vartheta, \mathcal{Z}, S) \rangle\!\rangle \, = \, 0 \, , \tag{14}$$

there being no mass flow across the boundary, $\mathbf{u} \cdot \hat{\mathbf{n}} = 0$ where $\hat{\mathbf{n}}$ is the outward normal, and no work done by surface viscous stresses since there is no mechanical stirring e.g. by wind stress at the top surface. Using (12) we now have

$$\langle\!\langle \varepsilon \rangle\!\rangle \, - \, \langle\!\langle \mathbf{J}_\vartheta \cdot \boldsymbol{\nabla} (\partial h^\ddagger / \partial \vartheta) \, + \, \mathbf{J}_S \cdot \boldsymbol{\nabla} (\partial h^\ddagger / \partial S) \rangle\!\rangle \, = \, 0 \tag{15}$$

after integrating by parts. This last step produces no boundary terms – the most crucial step in proving an epsilon theorem – because of (a) the vanishing of $\mathbf{J}_\vartheta \cdot \hat{\mathbf{n}}$ and $\mathbf{J}_S \cdot \hat{\mathbf{n}}$ on the topography and (b) the vanishing of $\partial h^\ddagger / \partial \vartheta$ and $\partial h^\ddagger / \partial S$, thanks to (9), on the top surface where $\mathcal{Z} = 0$. On the top surface $\mathbf{J}_\vartheta \cdot \hat{\mathbf{n}}$ and $\mathbf{J}_S \cdot \hat{\mathbf{n}}$ need not vanish, indeed cannot both vanish if the system is to be forced into motion without mechanical stirring.

Now the most accurate models of seawater all assume, with strong justification, that conditions are everywhere close to local thermodynamic equilibrium. Thus the temperature T is well defined, and $\mathbf{J}_\vartheta$ and $\mathbf{J}_S$ can be expressed as linear combinations of $\boldsymbol{\nabla} T$ and $\boldsymbol{\nabla} \mu$ where μ is the chemical potential of salt relative to water [8]. The expressions for $\mathbf{J}_\vartheta$ and $\mathbf{J}_S$ include the Dufour and Soret cross-diffusive terms. Respectively, those terms represent a contribution to $\mathbf{J}_\vartheta$ from $\boldsymbol{\nabla} \mu$ and to $\mathbf{J}_S$ from $\boldsymbol{\nabla} T$. Since T and μ are functions of state we may write

$$T \, = \, T(\vartheta, \mathcal{Z}, S) \qquad \text{and} \qquad \mu \, = \, \mu(\vartheta, \mathcal{Z}, S) \tag{16}$$

where the functional dependence, expressing local thermodynamic equilibrium, may reasonably be assumed smooth. Then $\mathbf{J}_\vartheta$ and $\mathbf{J}_S$ become linear combinations of $\boldsymbol{\nabla} \vartheta$, $\boldsymbol{\nabla} \mathcal{Z}$ and $\boldsymbol{\nabla} S$, and the second term in (15) a quadratic form in the components of $\boldsymbol{\nabla} \vartheta$, $\boldsymbol{\nabla} \mathcal{Z}$ and $\boldsymbol{\nabla} S$. That is, (15) has the form

$$\begin{aligned} \langle\!\langle \varepsilon \rangle\!\rangle \, + \, \kappa_0 \big\langle\!\big\langle A \, |\boldsymbol{\nabla} \vartheta|^2 + B \boldsymbol{\nabla} \vartheta \cdot \boldsymbol{\nabla} S \, + \, C \, |\boldsymbol{\nabla} S|^2 \, + \\ + \, D \boldsymbol{\nabla} \vartheta \cdot \boldsymbol{\nabla} \mathcal{Z} \, + \, E \, \boldsymbol{\nabla} S \cdot \boldsymbol{\nabla} \mathcal{Z} \, + \, F \, |\boldsymbol{\nabla} \mathcal{Z}|^2 \big\rangle\!\big\rangle \, = \, 0 \, , \end{aligned} \tag{17}$$

where the coefficients A, B, .. are smooth functions of ϑ, $\mathcal{Z}$, and S. The coefficient κ_0 is a reference diffusivity, whose ratio to each actual molecular diffusivity and cross-diffusivity (including ν, the molecular diffusivity of momentum) will be held constant in the small-diffusivities limit $\kappa_0 \to 0$. This is the natural generalization of PY02's constant Prandtl number. The coefficients $A, B, \ldots F$ are bounded as $\kappa_0 \to 0$.

As illustrated in the next section, the terms on the second line of (17) can be bounded as $\kappa_0 \to 0$, under reasonable assumptions, using the fact that $\mathcal{Z}$ is a smoothly-varying field independent of κ_0. An epsilon theorem $\langle\!\langle \varepsilon \rangle\!\rangle = O(\kappa_0)$ can then be proved whenever the first line of (17) is non-negative definite, which is true if

$$A \, \geqslant \, 0 \, , \quad C \, \geqslant \, 0 \, , \quad \text{and} \quad B^2 - 4AC \, \leqslant \, 0 \tag{18}$$

for all oceanographically relevant values of ϑ, $\mathcal{Z}$, and S. For if κ_0 times the second line of (17) goes to zero in the limit then both $\langle\!\langle \varepsilon \rangle\!\rangle$ and the rest of the first

line, when non-negative, must go to zero together in the limit. If (18) holds with A, B, and $B^2 - 4AC$ bounded away from zero for fixed, nonzero $\mathcal{Z}$, then (17) also puts significant constraints on the mean square gradients of ϑ and S, supplementing comparison-function constraints of the kind found by Balmforth and Young [1] and Winters and Young [29]. By themselves, the latter constraints would be insufficient to control the mean square gradients tightly enough to produce an epsilon theorem.

As will be noted in the next section, (18) is satisfied by the usual nonlinear models of seawater properties as described, for instance, in [26]. We are currently investigating whether (18) is satisfied by the still more accurate, state-of-the-art model currently being standardized by SCOR/IAPSO Working Group 127. The calculations are laborious but it seems clear that (18) is satisfied by this model as well, albeit by a slender margin at abyssal depths. The slender margin is mainly due to a contribution to the coefficient B not from the Dufour and Soret effects but from the interdependence of T, ϑ and S expressed by (16).

If (18) were violated, as appears thermodynamically possible, and realizable for conceivable fluid microstructures, then our proof would fail. Rather than signalling any dramatically different fluid behaviour, I suspect that this would merely widen the gap between what is true and what is provable, or what has so far been provable.

4 Specific examples

For illustrative purposes we simplify the expressions for $\mathbf{J}_\vartheta$ and $\mathbf{J}_S$ [8] to

$$\mathbf{J}_\vartheta \;=\; -\kappa\,(\boldsymbol{\nabla}\vartheta - \Gamma_\vartheta \boldsymbol{\nabla}\mathcal{Z}) \quad \text{and} \quad \mathbf{J}_S \;=\; -\kappa_S\,(\boldsymbol{\nabla}S + \Gamma_S \boldsymbol{\nabla}\mathcal{Z})\;, \tag{19}$$

in units compatible with (4) and (5), where κ_S is the molecular salt diffusivity. The correction terms in Γ_ϑ and Γ_S are necessary in order that $\mathbf{J}_\vartheta$ and $\mathbf{J}_S$ vanish when $\boldsymbol{\nabla}T = 0$ and $\boldsymbol{\nabla}\mu = 0$. Both Γ_ϑ and Γ_S are positive. In the case of Γ_S this allows the salinity S to find its natural scale height, with S diminishing upward under gravity at $\sim 3\,‰\,\mathrm{km}^{-1}$ in a stagnant ocean with $\mathbf{J}_S = 0$ [6, & refs.]. Conservative temperature ϑ, being numerically close to the ordinary potential temperature [10], increases upward at $\sim 0.15\,\mathrm{K\,km}^{-1}$ in an isothermal stagnant ocean. Other small contributions to the fluxes arising from (16) and from the Dufour and Soret effects are neglected. They will be re-introduced and carefully discussed in our JFM paper.

For the equation of state we take a model similar to that in [26] except for the inclusion of a nonlinear term in salinity S,

$$b(\vartheta,\mathcal{Z},S) = g_0\left\{\beta_\vartheta(1-\gamma^*\rho_0 g_0\mathcal{Z})\vartheta + \tfrac{1}{2}\beta^*_\vartheta\vartheta^2 - \beta_S S + \tfrac{1}{2}\beta^*_S S^2 + \frac{g_0\mathcal{Z}}{c_0^2}\right\}, \tag{20}$$

$$\Rightarrow\; h^\ddagger \;=\; -g_0\mathcal{Z}\left\{\beta_\vartheta\left(1-\tfrac{1}{2}\gamma^*\rho_0 g_0\mathcal{Z}\right)\vartheta + \tfrac{1}{2}\beta^*_\vartheta\vartheta^2 - \beta_S S + \tfrac{1}{2}\beta^*_S S^2 + \frac{g_0\mathcal{Z}}{2c_0^2}\right\}. \tag{21}$$

Here ϑ and S are defined as increments relative to reference values such as $T_0 = 273\text{K}$, $S_0 = 35‰$, while β_ϑ, γ^*, ρ_0, β^*_ϑ, β_S, β^*_S, and c_0 are positive constants. To a first approximation, (20) represents the the two principal nonlinearities of seawater, the thermobaricity γ^* and the temperature nonlinearity β^*_ϑ, along with the weaker salinity nonlinearity β^*_S, as well as compressibility.[3] Then

$$\frac{\partial h^\ddagger}{\partial \vartheta} \;=\; -g_0 z\big(\beta_\vartheta - \tfrac{1}{2}\gamma^*\beta_\vartheta\rho_0 g_0 z + \beta^*_\vartheta\vartheta\big) \quad \text{and} \quad \frac{\partial h^\ddagger}{\partial S} \;=\; g_0 z(\beta_S - \beta^*_S S)\,, \tag{22}$$

so that

$$\begin{aligned} \boldsymbol{\nabla}\frac{\partial h^\ddagger}{\partial \vartheta} \;&=\; -g_0 z\beta^*_\vartheta\boldsymbol{\nabla}\vartheta - g_0\big(\beta_\vartheta - \gamma^*\beta_\vartheta\rho_0 g_0 z + \beta^*_\vartheta\vartheta\big)\boldsymbol{\nabla}z \\ \text{and}\quad \boldsymbol{\nabla}\frac{\partial h^\ddagger}{\partial S} \;&=\; -g_0 z\beta^*_S\boldsymbol{\nabla}S + g_0\,(\beta_S - \beta^*_S S)\boldsymbol{\nabla}z\,. \end{aligned} \tag{23}$$

The expression $g_0\big(\beta_\vartheta - \gamma^*\beta_\vartheta\rho_0 g_0 z + \beta^*_\vartheta\vartheta\big)$ multiplying $\boldsymbol{\nabla}z$ is always positive-valued for seawater (even well below freezing temperatures), because at realistic salinities the ratio $\beta_\vartheta/\beta^*_\vartheta$ is typically well above 10 K, for instance 16.7 K with the values in footnote 3. Substituting (19) and (23) into (15) we recover (17) with

$$A \;=\; \hat\kappa_\vartheta\beta^*_\vartheta g_0|z|\,, \tag{24a}$$

$$B \;=\; 0\,, \tag{24b}$$

$$C \;=\; \hat\kappa_S\beta^*_S g_0|z|\,, \tag{24c}$$

$$D \;=\; -\hat\kappa_\vartheta g_0\big(\beta_\vartheta + \gamma^*\beta_\vartheta\rho_0 g_0|z| + \beta^*_\vartheta\vartheta\big) - \hat\kappa_\vartheta\Gamma_\vartheta\beta^*_\vartheta g_0|z|\,, \tag{24d}$$

$$E \;=\; \hat\kappa_S g_0\,(\beta_S - \beta^*_S S) + \hat\kappa_S\Gamma_S\beta^*_S g_0|z|\,, \tag{24e}$$

$$F \;=\; \hat\kappa_\vartheta g_0\Gamma_\vartheta\big(\beta_\vartheta + \gamma^*\beta_\vartheta\rho_0 g_0|z| + \beta^*_\vartheta\vartheta\big) + \hat\kappa_S g_0\Gamma_S\big(\beta_S - \beta^*_S S\big)\,, \tag{24f}$$

where $\hat\kappa_\vartheta := \kappa/\kappa_0$ and $\hat\kappa_S := \kappa_S/\kappa_0$, both order-unity quantities. Thus all the coefficients $A, B, \ldots, F$ are order-unity quantities in the limit $\kappa_0 \to 0$.

We can now see PY02's result in perspective. It is the case $A = B = C = E = F = 0$; the bound (2) comes from the D term in the second line of (17) with $D =$ con-

[3] The positive constant c_0 is a nominal sound speed, notwithstanding that the actual Boussinesq sound speed is infinite because of the incompressibility condition (6); in any case the γ^* term makes the actual sound speed differ from the nominal c_0, typically by a few percent, unless $\vartheta = 0$. Table 1.2 of Vallis [26] gives a sufficient idea of the orders of magnitude: $c_0 = 1490\ \text{m}\,\text{s}^{-1}$, $\beta_\vartheta = 1.67\times10^{-4}\text{K}^{-1}$, $\gamma^* = 1.2\times10^{-8}\text{Pa}^{-1}$ (this is Vallis's γ'^*, his γ^* increased by a small increment $+0.07\times10^{-8}\text{Pa}^{-1}$), $\rho_0 = 1.027\times10^3\text{kg}\,\text{m}^{-3}$, $\beta^*_\vartheta = 1.0\times10^{-5}\text{K}^{-2}$, and $\beta_S = 0.78\times10^{-3}\,‰^{-1}$. Over the full range of oceanic conditions β^*_S is always positive, with order of magnitude $\beta^*_S \gtrsim 0.5\times10^{-6}\,‰^{-2}$ and reaching just over twice this value in some conditions, according to the accurate equation of state defined by Table B2 of [7]. Values of the molecular diffusivities κ and κ_S are respectively of the order of $10^{-7}\,\text{m}^2\text{s}^{-1}$ and $10^{-9}\,\text{m}^2\text{s}^{-1}$.

stant, allowing a trivial integration by parts, leaving only a term bounded by a geometric factor $\sim H^{-1}$ times $\kappa g_0 \beta_\vartheta \Delta\vartheta = \kappa \Delta b$, with Δ as in (2). The term $-\kappa\langle\langle b\nabla^2 \mathcal{Z}\rangle\rangle$ vanishes in PY02's case of uniform gravity.

In the more general case defined by (20)–(24), the crucial definiteness condition (18) is satisfied thanks to the lucky accident that β^*_ϑ and β^*_S are both positive for seawater (typical values in footnote 3). This enables us to prove a strong epsilon theorem. The bound is still $O(\kappa_0)$ in the limit, as in PY02. The independent work of Nycander [16] produced a similarly strong bound, $O(\kappa_0)$, albeit for the slightly less general case $A \geqslant 0$ with $B = C = F = 0$. There, the adiabatic gradients Γ_ϑ and Γ_S in (19) were taken to be zero along with β^*_S.

However, these epsilon theorems with $\langle\langle\varepsilon\rangle\rangle = O(\kappa_0)$ all rely on assuming constancy of the coefficients β_ϑ etc. in (20). For then we can still bound the D and E terms in the second line of (17) since the potentially dangerous factors $\vartheta\boldsymbol{\nabla}\vartheta$ and $S\boldsymbol{\nabla}S$ take the form of gradients, $\frac{1}{2}\boldsymbol{\nabla}(\vartheta^2)$ and $\frac{1}{2}\boldsymbol{\nabla}(S^2)$, so that we can again integrate by parts and use the boundedness of $|\nabla^2\mathcal{Z}|$. This eliminates the gradients of ϑ and S from the second line of (17), again giving a bound as the first power of κ_0.

When the coefficients are fully variable, however, such integrations by parts in the second line of (17) do not eliminate the gradients of ϑ and S, which if not integrated away can be dangerous because of the small scales in the ϑ and S fields. We then have to resort to a blunter tool, the Cauchy–Schwartz inequality. Despite this, it turns out to be possible to obtain bounds that are asymptotically nearly as good as in PY02, under reasonable assumptions. They are "nearly as good" in the sense that the bounds are proportional to the first power of κ_0 times only a logarithmic factor, $\langle\langle\varepsilon\rangle\rangle = O(\kappa_0 \ln \kappa_0)$. This comes from exploiting the constraints mentioned below (18).

5 Concluding remarks

Apart from lifting the Boussinesq restriction, the JFM paper will prove the $\langle\langle\varepsilon\rangle\rangle = O(\kappa_0 \ln \kappa_0)$ result and will push further toward the most realistic possible thermodynamics and equation of state. In a subsequent paper to the *Journal of Physical Oceanography* it is hoped to discuss the extent to which these epsilon theorems constrain our understanding of the real oceans' upper and lower meridional overturning circulations, taking account of the extent to which the bounds on $\langle\langle\varepsilon\rangle\rangle$ are further degraded by allowing a finite depth of radiative penetration of surface heating from the visible solar spectrum. The emphasis will then shift away from the asymptotic behaviour and will focus, rather, on the best numerical bounds on $\langle\langle\varepsilon\rangle\rangle$ obtainable for realistically small but finite values of κ_0.

Acknowledgements I thank the organizers, the participants, and the staff at the Isaac Newton Institute at Cambridge, for a wide-ranging and stimulating Workshop in congenial surroundings. Rainer Feistel, David Jackett and Trevor McDougall generously shared with me their prepublication work on the new international standards on the thermodynamics and equation of state

of seawater, soon to appear as the report of SCOR/IAPSO Working Group 127; and Colm Caulfield, Jim Riley, Peter Rhines, Emily Shuckburgh, Luke Skinner, Rémi Tailleux, and Kraig Winters kindly helped with important background information on mixing efficiencies and ocean circulations. Timothy Lenton kindly brought me up to date on James Lovelock's "ocean desertification" hypothesis. But above all I am grateful to Francesco Paparella and William Young for extensive discussions and detailed work on the mathematical, fluid-dynamical, and thermodynamical issues involved in extending PY02 to realistic ocean models, and for their permission to incorporate this progress report into the present conference paper in advance of our joint JFM paper in preparation.

References

[1] Balmforth, N.J., Young, W.R.: Diffusion-limited scalar cascades. J. Fluid Mech. **482**, 91–100 (2003)
[2] Dewar, W.K., Bingham, R.J., Iverson, R.L., Nowacek, D.P., Laurent, L.C.S., Wiebe, P.H.: Does the marine biosphere mix the ocean?. J. Marine Res. **64**, 541–561 (2006)
[3] Feistel, R.: A Gibbs function for seawater thermodynamics for -6 to 80°C and salinity up to 120 g kg^{-1}. Deep Sea Res. I **55**, 1639–1671 (2008)
[4] Ford, R., McIntyre, M.E., Norton, W.A.: Balance and the slow quasimanifold: some explicit results. J. Atmos. Sci. **57**, 1236–1254 (2000)
[5] Ganachaud, A., Wunsch, C.: Improved estimates of global ocean circulation, heat transport and mixing from hydrographic data. Nature **408**, 453–457 (2000; correction **410**, 240, 2001)
[6] Gregg, M.C.: Entropy generation in the ocean by small-scale mixing. J. Phys. Oceanog. **14**, 688–711 (1984)
[7] Jackett, D.R., McDougall, T.J., Feistel, R., Wright, D.G., Griffies, S.M.: Algorithms for density, potential temperature, conservative temperature, and the freezing temperature of seawater. J. Atmos. Ocean. Techn. **23**, 1709–1728 (2006)
[8] Landau, L.D., Lifshitz, E.M.: Fluid Mechanics. Pergamon Press (1959)
[9] Lighthill, M.J.: On sound generated aerodynamically. I. General theory. Proc. Roy. Soc. Lond. A **211**, 564–587 (1952)
[10] McDougall, T.J.: Potential enthalpy: a conservative oceanic variable for evaluating heat content and heat fluxes. J. Phys. Oceanog. **33**, 945–963 (2003)
[11] McIntyre, M.E.: On dynamics and transport near the polar mesopause in summer. J. Geophys. Res. **94**, 14,617–14,628 (1989)
[12] McIntyre, M.E.: Spontaneous imbalance and hybrid vortex–gravity structures. J. Atmos. Sci. **66**, 1315–1326 (2009)
[13] Mohebalhojeh, A.R., McIntyre, M.E.: Local mass conservation and velocity splitting in PV-based balanced models. I: The hyperbalance equations. J. Atmos. Sci. **64**, 1782–1793 (2007)
[14] Munk, W.H.: Abyssal recipes. Deep Sea Res. **13**, 707–730 (1966)
[15] Munk, W.H., Wunsch, C.: Abyssal recipes II: energetics of tidal and wind mixing. Deep Sea Res. **45**, 1977–2010 (1998)

[16] Nycander, J.: Horizontal convection with a non-linear equation of state: generalization of a theorem of Paparella and Young. Tellus **62A**, 134–137 (2010)
[17] Osborn, T.R.: Estimates of the local rate of vertical diffusion from dissipation measurements. J. Phys. Oceanog. **10**, 83–89 (1980)
[18] O'Sullivan, D., Dunkerton, T.J.: Generation of inertia-gravity waves in a simulated life cycle of baroclinic instability. J. Atmos. Sci. **52**, 3695–3716 (1995)
[19] Paparella, F., Young, W.R.: Horizontal convection is non-turbulent. J. Fluid Mech. **466**, 205–214 (2002)
[20] Plougonven, R., Snyder, C.: Gravity waves excited by jets: propagation versus generation. Geophys. Res. Lett. **32**, L18802 (2005). DOI 10.1029/2005GL023730
[21] Sarmiento, J.L., Gruber, N., Brzezinski, M.A., Dunne, J.P.: High-latitude controls of thermocline nutrients and low latitude biological productivity. Nature **427**, 56–60 (2004)
[22] Smith, K.S., Marshall, J.C.: Evidence for enhanced eddy mixing at middepth in the southern ocean. J. Phys. Oceanog. **39**, 50–69 (2009)
[23] Snyder, C., Muraki, D.J., Plougonven, R., Zhang, F.: Inertia–gravity waves generated within a dipole vortex. J. Atmos. Sci. **64**, 4417–4431 (2007)
[24] Snyder, C., Skamarock, W.C., Rotunno, R.: Frontal dynamics near and following frontal collapse. J. Atmos. Sci. **50**, 3194–3211 (1993)
[25] Toggweiler, J.R., Samuels, B.: New radiocarbon constraints on the upwelling of abyssal water to the ocean's surface. In: M. Heimann (ed.) The Global Carbon Cycle, pp. 334–366. Springer-Verlag, Heidelberg (1993)
[26] Vallis, G.K.: Atmospheric and Oceanic Fluid Dynamics. Cambridge University Press (2006)
[27] Viúdez, A.: The origin of the stationary frontal wave packet spontaneously generated in rotating stratified vortex dipoles. J. Fluid. Mech. **593**, 359–383 (2007)
[28] Whitehead, J.A., Wang, W.: A laboratory model of vertical ocean circulation driven by mixing. J. Phys. Oceanog. **38**, 1091–1106 (2008)
[29] Winters, K.B., Young, W.R.: Available potential energy and buoyancy variance in horizontal convection. J. Fluid Mech. **629**, 221–230 (2009)
[30] Young, W.R.: Dynamic enthalpy, conservative temperature, and the seawater Boussinesq approximation. J. Phys. Oceanog. **40**, 394–400 (2010)

Inertia-gravity-wave generation: a geometric-optics approach

J. M. Aspden and J. Vanneste

Abstract The generation of inertia-gravity waves in the atmosphere and oceans is examined using a geometric-optics approach. This approach considers the dynamics of a small-scale wavepacket in prescribed time-dependent, balanced flows. The wavepacket is assumed to be in the so-called wave-capture regime, where the wave intrinsic frequency is negligible compared to the Doppler shift. The dynamics is reduced to a number of ordinary differential equations describing the evolution of the wavepacket position, of its wavevector, and of three scalar fields describing the wavepacket amplitude and polarisation. The approach clearly identifies two classes of wave-generation processes: unbalanced instabilities, associated with linear interactions between inertia-gravity waves, and spontaneous generation, associated with a conversion between vortical and inertia-gravity modes. Applications to simple steady flows and to random-strain models are discussed.

1 Introduction

The dynamics of the atmosphere and ocean is dominated by large-scale, slow motion in nearly geostrophic and hydrostatic balance. Small-scale, fast motion, in the form of inertia-gravity waves can play an important role, however, for instance by transporting momentum or by enhancing mixing. There is, therefore, considerable interest in identifying and quantifying sources of wave activity. Among the source mechanisms, one has proved particularly elusive: the dynamical generation of waves by the evolving balanced flow, often termed spontaneous generation. The difficulty

J. M. Aspden
School of Mathematics and Maxwell Institute, University of Edinburgh, Edinburgh EH9 3JZ, UK,
e-mail: j.m.aspden@sms.ed.ac.uk

J. Vanneste
School of Mathematics and Maxwell Institute, University of Edinburgh, Edinburgh EH9 3JZ, UK,
e-mail: j.vanneste@ed.ac.uk

D. Dritschel (ed.), *IUTAM Symposium on Turbulence in the Atmosphere and Oceans*,
IUTAM Bookseries 28, DOI 10.1007/978-94-007-0360-5_2,

in capturing this mechanism stems from the smallness of the waves and from the ambiguity that exists in the separation between balanced flow and waves. Nonetheless, several recent results, both numerical and analytical, have clearly demonstrated that spontaneous generation occurs in the small-Rossby-number regime relevant to most of the atmosphere and oceans [22; 17; 23; 24; 18; 16, and references therein]. Asymptotic results, in particular, show that the waves generated in this regime are exponentially small in the Rossby number [22; 20; 21].

The asymptotic work carried so far, relying on the smallness of the Rossby number, has been limited to very simple flows. Here, we propose an alternative approach, based on a spatial-scale separation between waves and balanced flows. This approach can in principle be applied to complex flows, e.g. derived from numerical simulations. It is motivated by the observation that, in many realistic circumstances, the inertia-gravity waves that are generated have a much smaller scale than the balanced flow. A key advantage is that there is no restriction to a large frequency separation between waves and flow, so that the wave generation can be captured when it is at it largest, that is, when relatively short time scales appear. The exponential smallness is of course recovered in the limit of small Rossby number.

2 Geometric-optics approach

The approach we propose is closely related to the geometric-optics approach to stability reviewed in Ref. [7]. This has recently been applied to rotating-stratified flows in [8], where equations equivalent to the ones we now derive have been obtained. The approach considers the evolution of a wavepacket with small wavelength superimposed to a spatially-varying, time-independent basic flow, with velocity $\mathbf{U} = (U, V, 0)$ satisfying $\nabla \cdot \mathbf{U} = 0$. The perturbation fields, in particular the x-component of the velocity, are written in the form

$$u(\mathbf{x}, t) = \hat{u}(\mathbf{x}, t) \mathrm{e}^{\mathrm{i}\theta(\mathbf{x},t)/\mu} + \text{c.c.}, \tag{1}$$

where $\mu \ll 1$ characterises the spatial scale separation. Introduction into the three-dimensional Boussinesq equations gives

$$\frac{D\theta}{Dt} = \frac{\partial \theta}{\partial t} + \mathbf{U} \cdot \nabla \theta = 0 \tag{2}$$

at leading order in μ. This equation governs the change in the phase $\theta(\mathbf{x}, t)/\mu$ of wavepackets whose trajectories obey

$$\frac{D\mathbf{x}}{Dt} = \mathbf{U}, \tag{3}$$

that is, they are simply advected by the basic flow. Taking the gradient of (2) leads to

$$\frac{D\mathbf{k}}{Dt} = -(\nabla\mathbf{U})^{\mathrm{T}}\,\mathbf{k}, \tag{4}$$

where $\mathbf{k} = (k,l,m) = \nabla\theta$ is the wavevector (scaled by μ). This is the standard WKB result for waves whose frequency

$$\omega_0 = \mathbf{U}\cdot\mathbf{k} \tag{5}$$

is entirely associated with the Doppler shift. This is a natural outcome for small-scale inertia-gravity waves, since their intrinsic frequencies

$$\omega_1 = \pm\left(f^2m^2 + N^2(k^2+l^2)\right)^{1/2}/\kappa, \tag{6}$$

where $\kappa = |\mathbf{k}|$, are formally smaller by a factor μ than the Doppler shift frequency. (Here f and N are the Coriolis and Brunt–Väisälä frequencies, respectively.) The regime considered here, where wavepackets are simply advected by the flow, can be recognised as the wave-capture regime examined in Refs. [3; 4]. Note that this regime is a feature of three-dimensional stratified fluids without analogue in the shallow-water model.

Carrying out the expansion to the next order in μ leads to a system of equations governing the evolution of the complex amplitudes $\hat{u}(\mathbf{x},t)$, $\hat{v}(\mathbf{x},t)$, etc. along the wavepacket trajectory. This system can be reduced to a set of three equations for the amplitudes of divergence $\hat{\delta}(\mathbf{x},t)$, vertical vorticity $\hat{\zeta}(\mathbf{x},t)$, and potential vorticity $\hat{q}(\mathbf{x},t)$. Ignoring the effects of the basic-flow buoyancy, these equations reduce to

$$\begin{aligned}\frac{D\hat{\delta}}{Dt} &= \left(\frac{m^2 f}{\kappa^2} + \frac{k^2+l^2}{\alpha\kappa^2}N^2 + \frac{2m^2}{\kappa^2(k^2+l^2)}\left(kl(\partial_x U - \partial_y V) + l^2\partial_x V - k^2\partial_y U\right)\right)\hat{\zeta} \\ &\quad + \left(\frac{m^2-k^2-l^2}{m\kappa^2}\left(k\partial_z U + l\partial_z V\right)\right. \\ &\quad \left. - \frac{2m^2}{\kappa^2(k^2+l^2)}\left(kl(\partial_x V + \partial_y U) + l^2\partial_y V + k^2\partial_x U\right)\right)\hat{\delta} - \frac{k^2+l^2}{\alpha\kappa^2}\hat{q},\end{aligned} \tag{7}$$

$$\frac{D\hat{\zeta}}{Dt} = -\alpha\hat{\delta}, \tag{8}$$

$$\frac{D\hat{q}}{Dt} = 0, \tag{9}$$

where $\alpha = f + \Omega + l\partial_z U/m - k\partial_z V/m$ and $\Omega = \partial_x V - \partial_y U$. The perturbation velocity field $\hat{\mathbf{u}}$ is reconstructed from $\hat{\delta}$ and $\hat{\zeta}$ according to

$$\hat{\mathbf{u}} = \frac{1}{k^2+l^2}\left(\mathrm{i}l\hat{\zeta} - \mathrm{i}k\hat{\delta}, -\mathrm{i}k\hat{\zeta} - \mathrm{i}l\hat{\delta}\right).$$

Equations (3)–(4) and (7)–(9) form a closed system of nine ordinary differential equations governing the position, wavevector and amplitude of the wavepacket. They can be solved for a given, possibly time-dependent, flow to assess whether perturbations to this flow grow; when the Rossby number is small, the perturbation

can further be approximately decomposed into a balanced (or vortical) part and an inertia-gravity-wave part, and the growth of latter implies a mechanism of inertia-gravity-wave generation.

When $\mathbf{U}$ is zero or uniform, the wavevector $\mathbf{k}$ is constant, and the system (7)–(9) is readily solved by letting

$$(\hat{\delta}, \hat{\zeta}, \hat{q}) = \exp(-\mathrm{i}\omega_1 t)\mathbf{e}, \tag{10}$$

where $\mathbf{e}$ is a constant three-dimensional vector. The corresponding eigenvalue problem for ω_1 has the three solutions $\omega_1 = 0$ and the two values given in (6) corresponding to the vortical mode and the two inertia-gravity modes, respectively. A non-uniform $\mathbf{U}$ has two consequences for (7)–(9): first, it leads to a time-dependent wavevector $\mathbf{k}$, and second it directly introduces terms proportional to $\nabla\mathbf{U}$. In general, the ordinary differential equations (3)–(4) and (7)–(9) need to be solved numerically. Some general comments about the behaviour of their solutions can nonetheless be made. To the order of accuracy considered, the perturbation potential vorticity has a constant amplitude: $\hat{q}(t) = \hat{q}(0)$. The equations (7)–(8) for $\hat{\delta}$ and $\hat{\zeta}$ are then equivalent to the equations governing a linear oscillator with time-dependent frequency and time-dependent forcing. Note that the wavevector enters these equations only through its direction $\mathbf{k}/\kappa$

For small Rossby number, the frequency of this oscillator is approximately given by (6); it depends on time on a scale fixed by the Lagrangian time-scale of the strain $\nabla\mathbf{U}$. This gives a good local definition of a Rossby number as the inverse of the product of this time scale by ω_1. When this number is small, the growth of free-oscillations in $(\hat{\delta}, \hat{\zeta})$ – the mark of inertia-gravity-wave generation – is very weak; in fact, it can be expected to be exponentially small in the Rossby number if the (Lagrangian) time dependence of $\nabla\mathbf{U}$ is smooth (real analytic). Two mechanisms of wave generation can be distinguished. First, for $\hat{q}(0) \neq 0$, the response of $(\hat{\delta}, \hat{\zeta})$ is balanced to all orders in the Rossby numbers; any transient behaviour of $\nabla\mathbf{U}$ does however lead to exponentially small free oscillations. Since these cannot be eliminated by initialisation, the mechanism is one of genuine spontaneous generation [22; 21]; it may be interpreted as a conversion from the vortical mode into the two gravity-wave modes. Note that this conversion is not a conservative one since the background flow provides a source of energy. The second mechanism is active with $\hat{q} = 0$. In this case, the equations for $(\hat{\delta}, \hat{\zeta})$ describe a slowly varying (unforced) oscillator, and the adiabatic invariance of the action, which holds to all orders in the Rossby number, applies; thus, in a transient scenario where $\mathbf{U}$ is uniform as $t \to \pm\infty$, $(\hat{\delta}, \hat{\zeta})$ can only change by an exponentially small amount. However, if $\mathbf{U}$ remains time dependent, e.g. if the wavepacket trajectories are periodic or chaotic, the changes can accumulate, leading to the growth of $(\hat{\delta}, \hat{\zeta})$. This mechanism of inertia-gravity-wave generation can be interpreted as a form of parametric instability. In the next section, we discuss solutions of (3)–(4) and (7)–(9) in simple flows which illustrate the mechanisms just described.

3 Applications to simple flows

We consider three time-independent flows: a vertically sheared, horizontally strained flow, an elliptical flow, and a dipolar flow. We then briefly discuss the behaviour that can be expected in more complex flows with chaotic wavepacket trajectories on the basis of random-strain models.

3.1 Horizontal strain and vertical shear

Perhaps the simplest flow leading to a non-trivial time dependence of $\mathbf{k}$ is a pure strain flow. Here we consider the added effect of a vertical strain and take $\mathbf{U} = (\beta x, -\beta y + \Sigma z, 0)$ for some constants $\beta > 0$ and Σ. We focus on the case $\hat{q} = 0$ and on the long time behaviour, when the wavevector is approximately

$$(k, l, m) \sim (0, \mathrm{e}^{\beta t}, \Sigma \mathrm{e}^{\beta t}/\beta),$$

up to an irrelevant constant factor. This leads to constant coefficients in (7)–(8) and to a solution $(\hat{\delta}, \hat{\zeta}) \propto \exp(\sigma t)$, where the growth rate σ satisfies

$$2\sigma = \beta \pm \left(\beta^2 - 4 \frac{\Sigma^2 + N^2 \beta^2 / f^2}{\beta^2 + \Sigma^2} \right)^{1/2}.$$

Thus the divergence and vertical vorticity $(\hat{\delta}, \hat{\zeta})$ of the wavepacket increases exponentially. Their growth rate is however less than the growth rate β of the wavevector magnitude κ. Still, the unbounded growth of $(\hat{\delta}, \hat{\zeta})$ is significant: in particular it implies the growth of the vertical gradient of the density and the ultimate breaking of the wavepacket (cf. [4]).

3.2 Elliptical flow

The parametric instability associated with periodic fluctuations of $\mathbf{k}$ is illustrated by the uniform-vorticity elliptical flow $\mathbf{U} = (ay, -by, 0)$, where a and b are constants satisfying $ab > 0$. The instability of this flow is an example of elliptical instability [10], here of a rotating stratified fluid. Equations (7)–(8) have periodic coefficents, and their stability can be analysed using Floquet theory. Numerical and explicit results in the limit of small eccentricity $|a/b - 1| \ll 1$ have been obtained by several authors [10; 13; 12]. They indicate that perturbations whose wavenumber satisfy some resonance conditions grow. In the presence of rotation and stratification, the growth rates decrease rapidly, however. More specifically, for $N > f$, the growth rates can be shown to be exponentially small in the Rossby number $\sqrt{ab}/f$. They never vanish, so that elliptical flows, both anticyclonic ($ab > 0$) and cyclonic

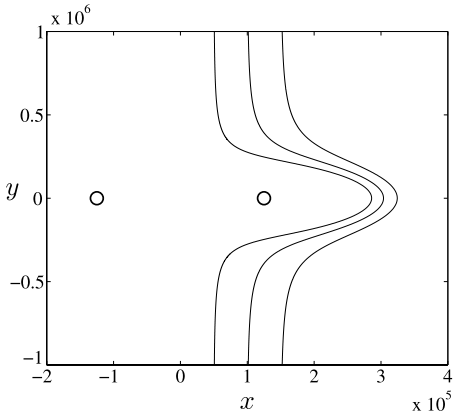

Fig. 1 Trajectories of three wavepackets in the flow generated by a quasi-geostrophic dipole. The location of the two point vortices is indicated by circles. The wavepackets, which travel in the plane $z = 0$ of the dipole, are characterised by their distance $d = 50$, 100 and 150 km from the axis of the dipole as $t \pm \infty$.

($ab < 0$) are unstable, albeit in exponentially narrow bands of wavenumbers (see [2] for asymptotic estimates of the growth rates). Qualitatively, the same conclusions are expected to hold for all time-independent flows with closed particle trajectories and hence closed wavepacket trajectories.

3.3 Dipole

To illustrate the spontaneous generation of inertia-gravity waves by wavepackets with $\hat{q} \neq 0$, we consider the evolution of a wavepacket in the simple flow corresponding, in the three-dimensional quasi-geostrophic approximation, to a dipole. (This flow is only a solution of the fluid equations in the limit of large f and N, but we use it as a crude model since we expect the qualitative properties of the wavepacket evolution to be insensitive to the details of the flow.) The potential vorticity of the dipole is $Q = \kappa(\delta(x-L) - \delta(x+L))\delta(y)\delta(z)$, with the separation of the point vortices chosen to be $2L = 250$ km. The strength κ was taken such that the propagation speed of the dipole is 10 m s^{-1}. It is convenient to think of this dipole as arrested by a uniform flow; wavepackets located at large distances from the dipole in the y-direction are then swept past the dipole and experience a transient change of wavevector. Figure 1 shows the corresponding trajectories in the (x,y)-plane for three wavepackets located at distances $d = 50$, 100 and 150 km from the dipole axis as $|t| \to \pm\infty$. Since the flow is uniform for $t \to \pm\infty$, we can use the exact solution (10) to decompose the perturbation into a vortical mode and two inertia-gravity waves for $|t|$ large. For $t \to -\infty$, we assume that only the vortical mode is excited. As a result of the transient activity, the inertia-gravity-wave modes are excited and their amplitude $A(t)$ becomes simply $A(t) \sim A_\infty \exp(\pm i\omega_1 t)$ as $t \to \infty$. The constant A_∞ is therefore an appropriate measure of the spontaneous generation that occurs.

We report results obtained for a wavepacket with $m/\sqrt{k^2+l^2} \approx 10$ located in the plane $z = 0$ of the dipole. The other relevant parameters are $f = 10^{-4}$ s^{-1} and

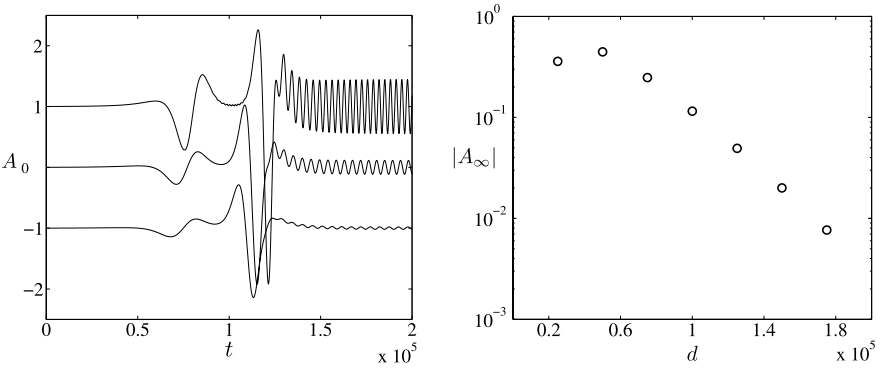

Fig. 2 Inertia-gravity waves generated spontaneously as vortical-mode wavepackets are swept past a dipole. The left panel shows the amplitude of one of the two inertia-gravity-wave mode as a function of time for wavepackets located at distances $d = 25, 50$ and 100 km (from top to bottom curves) of the dipole axis as $t \to \pm\infty$. The top and bottom curves are offset by ± 1 unit in the A-direction. The right panel shows the ampltitude of the inertia-gravity-wave mode as $t \to \infty$ as a function of the distance d of the wavepacket to the dipole axis.

$N = 10^{-2}$ s^{-1}. Figure 2 shows results obtained for the different values of the distance d of the wavepacket to the dipole axis. The left panel shows the amplitude of the inertia-gravity-wave component of the flow (obtained by projecting $(\hat{\delta}, \hat{\zeta}, \hat{q})$ on one of the inertia-gravity-wave mode) for $d = 25, 50$ and 100 km. It demonstrates clearly the appearance of fast oscillations that follows the transient behaviour associated with the encounter with the dipole. It also illustrates the strong dependence of the inertia-gravity-wave ampliude on d which can be thought of as a proxy for an inverse Rossby number. The right panel of Figure 2 shows the magnitude of the amplitude A_∞ that characterises the inertia-gravity waves for $t \to \infty$. It uses linear–logarithmic coordinates to demonstrate the exponential dependence of A_∞ on d and hence on the inverse Rossby number. Note that an exponential-asymptotics analysis similar to that of Ref. [22] could be carried out to obtain an explicit approximation for A_∞.

3.4 Random-strain models

As is well known from the study of particle advection, the trajectories of particles and hence wavepackets are typically chaotic when the velocity field is time dependent. The Lagrangian time dependence of the strain $\nabla\mathbf{U}$ that appears on the right-hand side of (4) is therefore very complicated; it is natural to model it by a stationary random process. This is the key idea of the random-strain models proposed by Kraichan [11] in the context of passive-scalar avection (the scalar-concentration gradient obeys (4)). Haynes and Anglade [9] considered random-strain models adapted to the layerwise two-dimensional nature of geophysical flows and concluded that

while, typically, $\kappa \to \infty$, the aspect ratio $m/\sqrt{k^2+l^2}$ reaches a stationary distribution. Since this ratio together with $\nabla\mathbf{U}$ determine the coefficients of (7)–(8) for $\hat{q} = 0$ for random-strain models, these equations are essentially those of a linear oscillator with stationary random coefficients. This observation makes it possible to draw some conclusion about the behaviour of $(\hat{\delta}, \hat{\zeta})$. First, these quantities typically grow exponentially, with a deterministic growth rate defined by $\lim_{t\to\infty} t^{-1} \log|\zeta|$, say, that can be recognised as the Lyapunov exponent of the system. Second, in the limit of small Rossby number, naturally defined using the correlation time of the random process determining the oscillator frequency, the growth rate can be expected to depend crucially on the smoothness of this process. Specifically, the explicit results available for closely related problems [1; 6] suggest that the growth rate is proportional to the power spectrum of the random process evaluated at twice the average oscillator frequency. In the small-Rossby-number limit this average frequency is in the tail of the spectrum and hence entirely controlled by the smoothness of the process. In particular, if the process is real-analytic, the growth rate will be exponentially small in the Rossby number. Thus spontaneous inertia-gravity-wave generation is predicted by random-strain models to have a similar Rossby-number dependence in complex flows as in simple steady flows. The key assumption, which may not always be satisfied, is that the Lagrangian time series of $\nabla\mathbf{U}$ is real-analytic. Note that a simple model for which analytic progress is possible would take $\nabla\mathbf{U}$ to be a white noise so as to apply the techniques developed for the Kazantsev–Kraichnan models of kinematic dynamo and passive-scalar advection (see, e.g., [5; 14] and references therein). This would however be appropriate only for flows with correlation times short compared to f^{-1} and to the inverse strain.

4 Discussion

This paper applies the geometric-optics approach to fluid stability (e.g. [7]) in order to study the spontaneous generation of inertia-gravity waves in a variety of flows. This application, which requires introducing the effect of rotation and stratification, is straightforward because of the particular dispersion relation of inertia-gravity waves: since their intrinsic frequency remains $O(1)$ as $|\mathbf{k}| \to \infty$, the kinematics of short waves is dominated by the Doppler shift, and wavepackets are simply advected by flows like fluid particles. Nine coupled ordinary differential equations govern the dynamics of the wavepackets, with three controlling their amplitude. This implies that the three types of modes that can be identified when $\mathbf{U}$ is uniform – the vortical mode and the two inertia-gravity modes – are strongly coupled. Only when the Lagrangian evolution is slow compared to the inertia-gravity-wave frequency, that is, in the limit of small (Lagrangian) Rossby number, are they asymptotically decoupled. It is interesting to note that the three amplitude equations then form a two-time-scale system with the same structure as the complete (partial differential) fluid equations [25]. The general conclusions that can be drawn for these system apply, and the generation of inertia-gravity waves, either through spontaneous con-

version of the vortical modes or through unbalanced instabilities, is exponentially weak in the Rossby number. The simple models discussed in this paper make this explicit.

The key interest of the geometric-optics approach is that it makes it possible to examine the growth of perturbations to solutions of partial-differential equations by solving ordinary differential equations. (See Refs. [19; 15] for an alternative approach, namely the pressureless approximation, which also leads to ordinary differential equations.) Here we have considered highly idealised flows for which the velocity field can be written in closed form. This is not necessary, and our future work will implement the solutions of the amplitude equations (7)–(9) for more complex flows obtained from numerical simulations. It will also consider the scaling $f, N = O(\mu^{-1})$ for which the intrinsic frequency is of the same order as the Doppler shift; in this case interactions between the vortical and inertia-gravity modes remain possible, but they are exponentially small in μ.

Acknowledgements The authors are supported by the UK Natural Environment Research Council through a studentship (JMA) and a research grant (JV), and by the EPSRC Network 'Wave–Flow Interactions'. JV thanks the organisers of the IUTAM workshop 'Rotating Stratified Turbulence in the Atmosphere and Oceans' for a stimulating meeting.

References

[1] Arnold, L., Papanicolaou, G., Wihstutz, V.: Asymptotic analysis of the Lyapunov exponent and rotation number of the random oscillator and applications. SIAM J. Appl. Math. **46**, 427–450 (1986)

[2] Aspden, J.M., Vanneste, J.: Elliptical instability of a rapidly rotating, strongly stratified fluid. Phys. Fluids (2009). Submitted

[3] Badudin, S.I., Shrira, V.I.: On the irreversibility of internal waves dynamics due to wave trapping by mean flow inhomogeneities. part 1. local analysis. J. Fluid Mech. **251**, 221–253 (1993)

[4] Bühler, O., McIntyre, M.E.: Wave capture and wave–vortex duality. J. Fluid Mech. **534**, 67–95 (2005)

[5] Falkovich, G., Gawędzki, K., Vergassola, M.: Particles and fields in fluid turbulence. Rev. Modern Phys. **73**(4), 913–975 (2001)

[6] Figotin, A., Pastur, L.: Spectra of Random and Almost-Periodic Operators. Springer (1992)

[7] Friedlander, S.J., Lipton-Lifschitz, A.: Localized instabilities in fluids. In: S. Friedlander, D. Serre (eds.) Handbook of Mathematical Fluid Dynamics, vol. II, pp. 289–353. Elsevier Science (2003)

[8] Guimbard, D., Leblanc, S.: Local stability of the Abrashkin–Yakubovich family of vortices. J. Fluid Mech. **567**, 91–110 (2006)

[9] Haynes, P.H., Anglade, J.: The vertical-scale cascade in atmospheric tracers due to large-scale differential advection. J. Atmos. Sci. **54**, 1121–1136 (1997)

[10] Kerswell, R.R.: Elliptical instability. Ann. Rev. Fluid Mech. **34**, 83–113 (2002)
[11] Kraichnan, R.H.: Convection of a passive scalar by a quasi-uniform random straining field. J. Fluid Mech. **64**, 737–762 (1974)
[12] McWilliams, J.C., Yavneh, I.: Fluctuation growth and instability associated with a singularity of the balance equations. Phys. Fluids **10**, 2587–2596 (1998)
[13] Miyazaki, T.: Elliptical instability in a stably stratified rotating fluid. Phys. Fluids A **5**, 2702–2709 (1993)
[14] Nazarenko, S., West, R.J., Zaboronski, O.: Fourier space intermittency of the small-scale turbulent dynamo. Phys. Rev. E **68**, 026311 (2003)
[15] Ngan, K., Straub, D.N., Bartello, P.: Three-dimensionalization of freely-decaying two-dimensional turbulence. Phys. Fluids **16**, 2918–2932 (2004)
[16] Ólafsdóttir, E.I., Olde Daalhuis, A.B., Vanneste, J.: Inertia-gravity-wave radiation by a sheared vortex. J. Fluid Mech. **596**, 169–189 (2008)
[17] Plougonven, R., Snyder, C.: Gravity waves excited by jets: propagation versus generation. Geophys. Res. Lett. **32**, L18802 (2005)
[18] Snyder, C., Muraki, D., Plougonven, R., Zhang, F.: Inertia-gravity waves generated within a dipole vortex. J. Atmos. Sci. **64**, 4417–4431 (2007)
[19] Straub, D.N.: Instability of 2D flows to hydrostatic 3D perturbations. J. Atmos. Sci. **60**, 79–87 (2003)
[20] Vanneste, J.: Inertia-gravity-wave generation by balanced motion: revisiting the Lorenz-Krishnamurthy model. J. Atmos. Sci. **61**, 224–234 (2004)
[21] Vanneste, J.: Exponential smallness of inertia-gravity-wave generation at small Rossby number. J. Atmos. Sci. **65**, 1622–1637 (2008)
[22] Vanneste, J., Yavneh, I.: Exponentially small inertia-gravity waves and the breakdown of quasi-geostrophic balance. J. Atmos. Sci. **61**, 211–223 (2004)
[23] Viúdez, A.: Spiral patterns of inertia-gravity waves in geophysical flows. J. Fluid Mech. **562**, 73–82 (2006)
[24] Viúdez, A.: The origin of the stationary frontal wave packet spontaneously generated in rotating stratified vortex dipoles. J. Fluid Mech. **593**, 359–383 (2007)
[25] Warn, T., Bokhove, O., Shepherd, T.G., Vallis, G.K.: Rossby number expansions, slaving principles, and balance dynamics. Quart. J. R. Met. Soc. **121**, 723–739 (1995)

Parallels between stratification and rotation in hydrodynamics, and between both of them and external magnetic field in magnetohydrodynamics, with applications to nonlinear waves

S. Medvedev and V. Zeitlin

Abstract We revisit the well-known analogy between the effects of stratification and rotation in hydrodynamics, and between both and the external magnetic field in magnetohydrodynamics. After sketching the similarities among models in what concerns linear and nonlinear stationary waves, we show that the Hamiltonian structure of the 2D versions of the models is the same, and use this fact to 1) find a canonical (skew-diagonal) form of the Hamiltonian equations, and 2) to treat in a unified manner the problem of weak turbulence of, respectively, internal gravity, gyroscopic, and Alfvèn waves in scale-invariant limits. We thus find stationary energy spectra in the long- and short-wave limits for all three types of waves.

1 Introduction

The analogy between the effects of rotation and stratification in hydrodynamics, and between both and magnetic field in magnetohydrodynamics (MHD below) is well-known and is, in fact, part of folklore. In what follows, we will remind this analogy and its precise mathematical meaning using the simplest 2D models, and then exploit it in the context of weak turbulence of waves engendered by each effect, i.e. respectively, internal gravity waves, gyroscopic waves, and Alfvén waves. We will thus show how some recent results on gyroscopic waves may be obtained without calculations from the earlier ones for internal gravity waves, and also get new results on wave turbulence in 2D MHD.

S. Medvedev
Institute of Computational Technologies, Novosibirsk, Russia, e-mail: sbm@lmd.ens.fr

V. Zeitlin
LMD, Univercity Paris VI and Ecole Normale Supérieure, Paris, France, e-mail: zeitlin@lmd.ens.fr

D. Dritschel (ed.), *IUTAM Symposium on Turbulence in the Atmosphere and Oceans*,
IUTAM Bookseries 28, DOI 10.1007/978-94-007-0360-5_3,

2 Models

We use the 2D, or 2.5D equations, corresponding to full non-dissipative 3D models with imposed symmetry with respect to translations in one spatial direction, and present them one by one below, describing in short the basic properties.

2.1 2D stratified Boussinesq equations

The stratified Boussinesq equations in the vertical (i.e. parallel to gravity acceleration) plane with no rotation (2D SB) are written as

$$\begin{aligned} u_t + uu_x + ww_z + \phi_x = 0, \\ w_t + uw_x + ww_z + \Xi + \phi_z = 0, \\ u_x + w_z = 0, \quad \Xi_t + u\Xi_x + w\Xi_z = 0. \end{aligned} \tag{1}$$

Here $\Xi = \frac{g(\rho(z)+\sigma)}{\rho_0}$ - full buoyancy, including effects of background stratification $\rho(z)$, $\phi = \frac{P}{\rho_0}$ - geopotential, ρ_0 - constant normalization density, σ - density perturbation.

In *streamfunction/buoyancy variables* they are rewritten as

$$\begin{aligned} \Delta\psi_t + \mathscr{J}(\psi, \Delta\psi) + \Xi_x = 0, \\ \Xi_t + \mathscr{J}(\psi, \Xi) = 0. \end{aligned} \tag{2}$$

where ψ - streamfunction, $\mathscr{J}$ is Jacobian in $x-z$ plane, and Δ is Laplacian.

The conserved energy is

$$E = \frac{1}{2}\int dxdz \left(\zeta\psi + \frac{\Xi^2}{N^2}\right), \tag{3}$$

where $\zeta = -\Delta\psi$ - horizontal vorticity, $N = \text{const}$ - Brunt Väisälä frequency, and we suppose for simplicity from now on that $\rho(z) = -N^2 z$.

An important *hydrostatic (long-wave) limit* of (2) is:

$$\begin{aligned} \psi_{zzt} + \mathscr{J}(\psi, \psi_{zz}) + \Xi_x = 0, \\ \Xi_t + \mathscr{J}(\psi, \Xi) = 0. \end{aligned} \tag{4}$$

2.2 2.5D rotating Euler equations

Rotating Euler equations in the vertical (i.e. parallel to the rotation axis) plane (2.5D RE) are written as

$$\begin{aligned} v_t + uv_x + wv_z + fu &= 0, \\ u_t + uu_x + ww_z - fv + \phi_x &= 0, \\ u_x + w_z = 0, \;\; w_t + uw_x + ww_z + \phi_z &= 0. \end{aligned} \tag{5}$$

Here $f = 2\Omega$ - Coriolis parameter, Ω - overall angular velocity. In *streamfunction/-geostrophic momentum variables* they are rewritten as:

$$\begin{aligned} \Delta\psi_t + \mathscr{J}(\psi, \Delta\psi) + M_z &= 0, \\ M_t + \mathscr{J}(\psi, M) &= 0. \end{aligned} \tag{6}$$

ψ - streamfunction, $\zeta = -\Delta\psi$ - (horizontal) vorticity, $M = f(v + fx)$ - geostrophic momentum.

The analogy between stratification and rotation becomes obvious as these equations are identical to 2D SD up to the changes $M \to \Xi$, $z \to x$ and sign changes. The conserved energy is also similar to SD:

$$E = \frac{1}{2}\int dxdz \left(\zeta\psi + \frac{M^2}{f^2}\right). \tag{7}$$

An important *geostrophic (long-wave) limit* of (6) is:

$$\begin{aligned} \psi_{xxt} + \mathscr{J}(\psi, \psi_{xx}) + M_z &= 0, \\ M_t + \mathscr{J}(\psi, M) &= 0. \end{aligned} \tag{8}$$

The parallel with hydrostatic limit in SB is obvious.

2.3 2D magnetohydrodynamics

For 2D motions in the $x - z$ plane, the equations of 2D MHD read:

$$\begin{aligned} \nabla\cdot\mathbf{v} = 0, \quad \nabla\cdot\mathbf{h} &= 0 \\ \mathbf{v}_t + \mathbf{v}\cdot\nabla\mathbf{v} - \mathbf{h}\cdot\nabla\mathbf{h} + P^*_x &= 0, \\ \mathbf{h}_t - \nabla\wedge(\mathbf{v}\wedge\mathbf{h}) &= 0. \end{aligned} \tag{9}$$

Here $\mathbf{v}$, $\mathbf{h}$ - velocity and magnetic fiel *in the plane*, $P^* = P + \frac{\mathbf{h}^2}{2}$ - magnetic pressure.

In *streamfunction/magnetic potential variables* they are rewritten as:

$$\begin{aligned} \Delta\psi_t + \mathscr{J}(\psi, \Delta\psi) - \mathscr{J}(a, \Delta a) &= 0, \\ a_t + \mathscr{J}(\psi, a) &= 0. \end{aligned} \tag{10}$$

Here ψ - streamfunction, a - magnetic potential, $j = -\Delta a$ - electric current *perpendicular to the plane*.

The conserved energy is:

$$E = \frac{1}{2}\int dxdz\,(\zeta\psi + aj)\,. \tag{11}$$

In the presence of constant *external (mean) magnetic field*:

$$\mathbf{h} = \mathbf{H} + \eta, \quad \mathbf{H} = \text{const} \tag{12}$$

Without loss of generality $\mathbf{H} = H\hat{\mathbf{x}}$, and we replace $a \to -Hz + a$. An analog of hydrostatic and geostrophic balances is *"magnetic balance"*:

$$Ha_{xx} = -P_z^* \;\Rightarrow -P_z = -H\Delta a = Hj. \tag{13}$$

3 Similarity between models I: waves and structures

3.1 Linear waves

Each of the effects: stratification, rotation, external magnetic field engenders its proper type of linear waves which are obtained by straightforward linearization in SB and RE, and linearization about constant H in MHD. All these waves are *anisotropic*.

- SB: internal gravity waves with dispersion relation:

$$\omega^2 = N^2\frac{k^2}{k^2+m^2}, \tag{14}$$

- RE: inertial (gyroscopic) waves with dispersion relation:

$$\omega^2 = f^2\frac{m^2}{k^2+m^2}; \tag{15}$$

- MHD: Alfvèn waves with dispersion relation:

$$\omega^2 = H^2k^2; \tag{16}$$

Above ω - wavefrequency, $\mathbf{k} = k\hat{\mathbf{x}} + m\hat{\mathbf{z}}$ - wavevector. The important limits corresponding to quasi -vertical and quasi-horizontal propagation in SB and RE, respectively, are (only positive branches of dispersion relation displayed):

1. $k^2 \ll m^2$:
   - SB
   $$\omega = N\frac{k}{m}, \tag{17}$$
   - RE
   $$\omega = f\left(1 - \frac{k^2}{2m^2}\right); \tag{18}$$

2. $m^2 \ll k^2$

- SB

$$\omega = N\left(1 - \frac{m^2}{2k^2}\right), \tag{19}$$

- RE

$$\omega = f\frac{m}{k}. \tag{20}$$

Remarks: In these limits frequencies are either *homogeneous functions of* k, m, or constants plus homogeneous functions. Frequency of Alfvèn waves is always homogeneous. The limit $k^2 \ll m^2$ in SB ($m^2 \ll k^2$ in RE) corresponds to hydrostatic (geostrophic) limit. In MHD it corresponds to magnetic balance. The similarity between SB and RE is again seen in the identical (up to replacement $k \leftrightarrow m$) dispersion relations.

3.2 Structures: nonlinear waves/vortices

The analogy between the models is also clearly seen if one considers their *fully nonlinear stationary solutions*

3.2.1 Stationary solutions in SB and RE

- SB

$$\begin{aligned} \mathscr{J}(\psi, \Delta\psi) + \Xi_x &= 0, \\ \mathscr{J}(\psi, \Xi) &= 0. \end{aligned} \tag{21}$$

- RE

$$\begin{aligned} \mathscr{J}(\psi, \Delta\psi) + M_z &= 0, \\ \mathscr{J}(\psi, M) &= 0. \end{aligned} \tag{22}$$

Hence $\Xi = \Xi(\psi)$, $M = M(\psi)$, respectively, and

$$\Delta\psi + \Xi'(\psi)z = F(\psi), \tag{23}$$

$$\Delta\psi + M'(\psi)z = G(\psi), \tag{24}$$

where $\Xi(\psi), M(\psi), F(\psi), G(\psi)$ are arbitrary functions to be determined from boundary conditions.

Remarks:

The well-known Long's waves (e.g. [1]) in SB belong to this class. "Long's waves" in RE may be obtained by replacements $\Xi \to M$, $x \to z$, $F \to G$ giving *vertically*

propagating stationary waves from the same equations. Hydrostatic limit, much studied for mountain waves is analogous to geostrophic limit in this context. Long's waves may have *recirculation cores* [1].

3.2.2 Stationary solutions in MHD

Stationary solutions of MHD obey the equations:

$$\begin{aligned} \mathscr{J}(\psi,\Delta\psi)-\mathscr{J}(a,\Delta a)&=0,\\ \mathscr{J}(\psi,a)&=0. \end{aligned} \tag{25}$$

Hence $a=A(\psi)$ and

$$\left(1-\left[A'(\psi)\right]^2\right)\Delta\psi - A'(\psi)A''(\psi)\left(\nabla\psi^2\right)=H(\psi), \tag{26}$$

where $A(\psi),H(\psi)$ to be determined from b.c.

4 Similarity between models II: geometry

4.1 Hamiltonian structure

The similarity between the models becomes transparent if one considers their Hamiltonian strudture. The first observation is that in all three models the energy is a quadratic functional and the *Casimir invariants* are conserved

$$\int dxdz\,(\mathscr{F}(\mathscr{V})+\zeta\mathscr{G}(\mathscr{V}))=\text{const}, \tag{27}$$

where $\mathscr{V}$ is Ξ, M, and a in SB, RE, and MHD respectively, and $\mathscr{F}(\mathscr{V}),\mathscr{G}(\mathscr{V})$ are arbitrary functions.

All models have the same Hamiltonian structure [2; 3] given by the Hamiltonian, which is the energy functional, and the following *non-canonical Poisson bracket (PB)* for any pair of functionals $\mathscr{A}(\zeta,\mathscr{V}),\mathscr{B}(\zeta,\mathscr{V})$:

$$\begin{aligned} \{\mathscr{A}(\zeta,\mathscr{V}),\mathscr{B}(\zeta,\mathscr{V})\}=\int dxdz\,\zeta\,\mathscr{J}\left(\frac{\delta\mathscr{A}}{\delta\zeta},\frac{\delta\mathscr{B}}{\delta\zeta}\right)+\\ \mathscr{V}\left[\mathscr{J}\left(\frac{\delta\mathscr{A}}{\delta\zeta},\frac{\delta\mathscr{B}}{\delta\mathscr{V}}\right)+\mathscr{J}\left(\frac{\delta\mathscr{A}}{\delta\mathscr{V}},\frac{\delta\mathscr{B}}{\delta\zeta}\right)\right] \end{aligned} \tag{28}$$

The equations of motion, thus, are:

$$\zeta_t=\{\zeta,H\},\quad \mathscr{V}_t=\{\mathscr{V},H\}. \tag{29}$$

This Hamiltonian structure is *degenerate*. Degeneracy is lifted on the hypersurface of constant Casimirs, which constitutes the true phase-space.

4.2 Geometry of the phase space and nonconstrained dynamical variables

The underlying geometry follows from the symmetry with respect to the group of transformations [2]:

$$\begin{aligned} \zeta &\to \zeta(X(x,z),Z(x,z)) - \mathscr{J}(\Lambda(x,y),\mathscr{V}(X(x,z),Z(x,z)),\\ \mathscr{V} &\to \mathscr{V}(X(x,z),Z(x,z), \quad \mathscr{J}(X,Z)=1, \end{aligned} \tag{30}$$

which leaves the Casimirs invariant and sweeps the phase-space starting from arbitrary initial conditions $\zeta_0(x,z), \mathscr{V}_0(x,z)$. Hence the parameters of *area-preserving diffeomorphisms* (i.e. their generating functions), and Λ are true dynamical variables. The PB is still non-canonical in these variables, its recursive (skew-)diagonalisation using Lagrangian variables was proposed in [3] for strong stratification (rotation/magnetic field). This transformation obviously renders the Hamiltonian non-quadratic. Below, we will use a related, but more general method developed in [4] for the systems of this kind.

4.3 Casting PB to the canonical form

We sketch here the method of [4], as applied to SB, extension to RE and MHD is straightforward. The approach consists in diagonalization of PB order by order in inverse stratification (or rotation, or magnetic field), although all parameters are taken to be unity in the rest of this section to simplify the formulae (the details will be presented elsewhere).

The operator of the Poisson bracket in ζ, ξ variables for SB is

$$\mathbf{J} = -\partial_x \begin{pmatrix} 0 & 1 \\ 1 & 0 \end{pmatrix} + \begin{pmatrix} \mathscr{J}(\zeta,\cdot) & \mathscr{J}(\xi,\cdot) \\ \mathscr{J}(\xi,\cdot) & 0 \end{pmatrix} \equiv S + A_1. \tag{31}$$

A change of dependent variables $\mathbf{u} = (u_1,u_2) \equiv (\zeta,\xi) \to \mathbf{v}$:

$$\mathbf{v} = \mathbf{u} - \mathbf{f}_1[\mathbf{u},\mathbf{u}] - \mathbf{f}_2[\mathbf{u},\mathbf{u},\mathbf{u}] + O(\mathbf{u}^4), \tag{32}$$

gives the skew-diagonal (canonical) PB operator:

$$\mathbf{J}_2 = -\begin{pmatrix} 0 & \partial_x \\ \partial_x & 0 \end{pmatrix} + O(\mathbf{v}^3). \tag{33}$$

The inverse change of variables is needed in order to calculate the Hamiltonian, it is given by:

$$\mathbf{u} = \mathbf{v} + \mathbf{f}_1[\mathbf{v},\mathbf{v}] + \mathbf{f}_1[\mathbf{f}_1[\mathbf{v},\mathbf{v}],\mathbf{v}] + \mathbf{f}_1[\mathbf{v},\mathbf{f}_1[\mathbf{v},\mathbf{v}]] + \mathbf{f}_2[\mathbf{v},\mathbf{v},\mathbf{v}] + O(\mathbf{v}^4). \tag{34}$$

Here

$$\mathbf{f}_1[\mathbf{u},\mathbf{u}] = \frac{1}{3} A_1 \mathbf{u} S^{-1} \mathbf{u}. \tag{35}$$

and

$$\mathbf{f}_2[\mathbf{u},\mathbf{u},\mathbf{u}] = \frac{1}{4} I_2[\mathbf{u},\mathbf{u}] S^{-1} \mathbf{u}, \tag{36}$$

with

$$\begin{aligned} I_2[\mathbf{u},\mathbf{u}] &= A_1 T^* + T A_1 + T S T^* \\ &= -\frac{5}{9} A_1 S^{-1} A_1 + \frac{2}{9}\left(B_1 \partial_x S^{-1} A_1 - A_1 S^{-1} \partial_x B_1\right) - \frac{1}{9} B_1 S B_1, \end{aligned} \tag{37}$$

where

$$B_1 = \begin{pmatrix} \mathscr{J}(\partial_x^{-1} u_1, \cdot) & \mathscr{J}(\partial_x^{-1} u_2, \cdot) \\ \mathscr{J}(\partial_x^{-1} u_2, \cdot) & 0 \end{pmatrix}, \tag{38}$$

and

$$T = -\frac{1}{3} A_1 S^{-1} + \frac{1}{3} B_1 \partial_x S^{-1}, \quad T^* = -\frac{1}{3} S^{-1} A_1 - \frac{1}{3} S^{-1} \partial_x B_1. \tag{39}$$

This construction allows to rewrite SB, RE and MHD in canonical form and to calculate, order by order, the cubic, quartic etc corrections to the Hamiltonian, describing wave interactions.

5 Triad and quartet wave interactions and wave turbulence (WT)

The canonical Hamiltonian structure allows to understand underlying dynamics in standard terms of coupled oscillators and gives a fast track for obtaining stationary spectra of ensembles of weakly nonlinear waves under the standard WT hypotheses.

5.1 The WT algorithm

Let us remind that WT approach consists in:

- Analyzing the dispersion relation and checking whether the dispersion law is of the *decay* (3-wave resonances) or *non-decay* (4-wave resonances only) type
- Taking a system in canonical Hamiltonian form and applying the standard recipes (e.g [6]), i.e.: random-phase approximation, quasi-Gaussian closure,

- Getting *kinetic equation (KE)* for average wave-density using these recipies.
- Looking for stationary spectra annihilating the collision integral in KE.

Remarks:
The collision integral in the KE for a *decay spectrum* is entirely defined by the cubic part of the Hamiltonian. The collision integral in the KE for a *non-decay spectrum* is defined from both cubic and quartic parts of the Hamiltonian.

5.2 Known situations leading to get-it-by-hand solutions for stationary energy spectra in WT

Although solutions of the kinetic equation can be always sought numerically, if the dispersion law and interaction coefficients are *scale invariant*, stationary *power-law* spectra may be found "by hand" by factorizing the collision integral and looking for spectra annihilating each factor. There is a number of situations studied in literature when this is possible, falling in 3 classes:

1. Homogeneous isotropic dispersion (decay and non-decay): $\omega \propto |\mathbf{k}|^a$
2. Directionally homogeneous decay dispersion: $\omega \propto k^a m^b$
3. Non-decay dispersion of the form: $\omega \propto const + |\mathbf{k}|^a$, $\omega \propto const + k^a m^b$.

The methods of factorization of the collision integral in the corresponding cases use conformal transformations either in the frequency space [5], or in the wavenumber space [7] in cases 1,2, and conformal transformation in the wavenumber space [8; 9] in case 3. The solutions always contain a Rayleigh-Jeans equipartition spectrum, the constant energy-flux spectrum and, in the non-decay case, the constant wave-momentum flux spectrum.

5.3 WT: decay spectra for gravity, gyroscopic and Alfvèn waves

By applying the technique sketched above to the dispersion relations (16) - (20), we get the stationary spectra for weakly nonlinear waves in all three of our models:

- Internal gravity waves in the limit $k \ll m$.
  Energy spectrum
  $$\varepsilon \propto k^{-\frac{3}{2}} m^{-\frac{3}{2}} \tag{40}$$
- Gyroscopic waves in the limit $m \ll k$.
  Energy spectrum
  $$\varepsilon \propto k^{-\frac{3}{2}} m^{-\frac{3}{2}} \tag{41}$$
- Alfvèn waves
  - Limit $k \ll m$:

Energy spectrum

$$\varepsilon \propto k^{-\frac{3}{2}} m^{-1} \tag{42}$$

– Limit $m \ll k$:
Energy spectrum

$$\varepsilon \propto k^{-\frac{1}{2}} m^{-2} \tag{43}$$

Comments:
The spectrum of internal gravity waves (40) was obtained before without using the Hamiltonian structure (i.e. using *constrained* origainal variables) with the same result [10; 11]. This gives a proof that constraints are inessential for 3-wave interactions. The spectrum of gyroscopic waves (41) obtained recently in [12] follows *without calculation* from those of gravity waves in the corresponding limit. The spectra of Alfvèn waves are apparently new.

5.4 WT: non-decay spectra for gravity and gyroscopic waves

Similarly, in the non-decay case we get the spectra which are apparently new for internal gravity waves and gyroscopic waves:

- Internal gravity waves in the limit $m \ll k$:
  1. Energy spectrum corresponding to a constant energy flux:

$$\varepsilon \propto k^{-1} m^{-\frac{7}{3}} \tag{44}$$

  2. Energy spectrum corresponding to a constant wavenumber flux:

$$\varepsilon \propto k^{-\frac{5}{3}} m^{-\frac{5}{3}} \tag{45}$$

- Gyroscopic waves $k \ll m$:
  The spectra are obtained by exchanging k and m in previous formulae.

A discussion of physical realisability and applications of thus derived wave-spectra is beyond the scope of the present paper.

6 Conclusions

Thus we have shown that 2D SB and 2.5D RE system are *identical*, up to replacements: geostrophic momentum $\leftrightarrow$ buoyancy, and $x \leftrightarrow z$. The results for structures (nonlinear waves with or without vortex cores) and wave turbulence obtained in one model are immediately transposable for the other. The 2D MHD is close yet different due to the different form of the Hamiltonian, although the PB bracket is the same. The unified treatment of 2D SB, RE and MHD models, especially in what

concerns their canonical Hamiltonian structure, allowed us to understand and systemize the previous results on wave-turbulence spectra in these models and obtain some new ones.

It is worth noting that similar results and conclusions may be obtained in another "symmetric" 2D situation, namely *axisymmetric flows*, where translational invariance of the above-considered models is replaced by rotational invariance.

References

[1] Derzho, O., Grimshaw, R., Solitary waves with a vortex core in a shallow layer of stratified fluid, 1997, Phys. Fluids, **9**, p. 3378–3385.

[2] Zeitlin, V., On the structure of the phase space, Hamiltonian variables and statistical approach to description of the 2 dimensional hydrodynamics and magnetohydrodynamics, 1992, J. Phys. A, **25**, p. 171–175.

[3] Zeitlin, V., Vorticity and waves: geometry of phase-space and the problem of normal variables, 1992, Phys. Lett. A, **164**, p. 177–183.

[4] Medvedev, S.B., The method of normal forms and fast-slow splitting, p. 121–188, in *Nonlinear dynamics of rotating shallow water: methods and advances*, V. Zeitlin, ed, Springer, 2007.

[5] Zakharov V.E., Lvov V.S., Falkovich G.E., Kolmogorov spectra of turbulence, Springer, 1992.

[6] Zeitlin, V., 2005, Wave turbulence with applications to atmospheric and oceanic waves, p. 133–168, in *Nonlinear waves in fluids: recent advances and modern applications*, R. Grimshaw, ed. Springer, 2005.

[7] Kats, A.V., Kontorovich, V.M., Symmetry properties of the collision integral and nonisotropic stationary solutions in weak turbulence theory, 1973, Sov. Phys. JETP, **37**, p. 80–85; Anisotropic turbulent distributions for waves with a nondecay dispersion law, 1974, Sov. Phys. JETP, **38**, p. 102–107.

[8] Volotsky, S.V., Kats, A.V., Kontorovich, V.M., Symmetry transformations of the collision integral of quasiparticles with close to linear dispersion law, 1980, Proceedings of the Ukranian Akademy of Science (in Russian), No. 11, p. 66–69.

[9] Medvedev, S.B., Zeitlin, V., Weak turbulence of short equatorial waves, 2005, Phys. Lett. A, **342**, p. 269–290.

[10] Daubner, S., Zeitlin, V., On the Kolmogorov spectra for unidirectional internal gravity waves, 1996, Phys. Lett. A, **214**, p. 33–39.

[11] Caillol, P., Zeitlin, V., Kinetic equations and stationary energy spectra of internal gravity waves in flows with and without mean potential vorticity, 2000, Dyn. Atmos. Ocean, **32**, 81–112.

[12] Galtier, S., Weak inertial-wave turbulence theory, 2003, Phys. Rev. E, **68**, 015301.

Generation of an internal tide by surface tide/eddy resonant interactions

M.-P. Lelong and E. Kunze

Abstract The interaction of surface tidal currents and baroclinic geostrophic eddies is considered to determine whether energy can be transferred to baroclinic tides by this process. Theoretical and numerical analyses reveals that when the surface tide is uniform in the horizontal, the interaction is identically zero, even under resonant conditions. The resonant interaction results in maximum internal wave excitation when the horizontal scale of the tide is comparable to that of the eddies. Thus, this process is not an efficient mechanism for internal wave excitation in the deep ocean where barotropic tides vary over much larger scales than the eddies, but it may provide an additional wave source at low latitudes and in coastal regions where tidal horizontal modulation by topography can be significant.

1 Introduction

A series of surface-drifter observations in the western boundary current of the subpolar North Pacific found intense near-inertial/near-diurnal frequency motions trapped within anticyclonic warm-core rings (Rogachev *et al.*, 1992; Rogachev *et al.*, 1996; Rogachev and Carmack, 2002). The authors speculated that the lower bound of the internal wave frequency band had been locally decreased by the rings' negative vorticity (Kunze, 1985), thereby trapping near-inertial waves within the rings. The proximity of near-inertial and near-diurnal frequencies led them to conjecture that the observed waves might have resulted from a diurnal-tide/eddy interaction. However, given their limited data, they could not rule out the role of wind-forcing or subinertial instability, and the evidence for the suspected role of

M.-Pascale Lelong
NorthWest Research Associates, P.O. Box 3027 Bellevue WA 98009-3027,
e-mail: pascale@nwra.com

Eric Kunze
University of Victoria, e-mail: kunze@uvic.ca

D. Dritschel (ed.), *IUTAM Symposium on Turbulence in the Atmosphere and Oceans*,
IUTAM Bookseries 28, DOI 10.1007/978-94-007-0360-5_4,

the barotropic tide was circumstantial. Nor was the interpretation of these observations substantiated by any rigorous theoretical arguments.

Research into tidal generation of linear internal waves in the deep ocean has largely focused on the interaction of surface tidal currents with topography (e.g. Cox and Sandstrom, 1962; Wunsch, 1975; Simmons *et al.*, 2004; Garrett and Kunze, 2007), but the mechanism of tide/eddy interaction has not, to our knowledge, been previously considered. The objective of our combined theoretical and numerical study is to assess conditions under which internal waves can be generated following interaction of an oscillating tidal current with a baroclinic geostrophic eddy field.

A summary of the weakly nonlinear theory, first presented in Lelong and Kunze (2009), is given in Section 2. Numerical results are presented in section 3. Section 4 includes a discussion of results and concluding remarks.

2 Problem definition

This section provides a mathematical description of the problem. Equations of motion are given in Sec. 2.1. The analogy between resonant wave triads and tide/eddy interactions is explained in Sec. 2.2, followed by a summary of the multiple-scale analysis in Sec. 2.3.

2.1 Governing equations

Because of their barotropic structure, tidal flow studies are typically formulated with the rotating shallow-water equations. Here, the focus on internal wave generation and the baroclinicity of the eddy field suggests instead that we use a 3D Boussinesq model with f-plane rotation,

$$\frac{\partial \mathbf{u_h}}{\partial t} + (\mathbf{u_h}\cdot\nabla_h)\mathbf{u_h} + w\frac{\partial \mathbf{u_h}}{\partial z} + \nabla_h p + f\hat{e_3}\times\mathbf{u_h} = \hat{e}_1 F(x,y,t) \tag{1a}$$

$$\frac{\partial w}{\partial t} + (\mathbf{u_h}\cdot\nabla_h)w + w\frac{\partial w}{\partial z} + \frac{\partial p}{\partial z} - b = 0 \tag{1b}$$

$$\frac{\partial b}{\partial t} + (\mathbf{u_h}\cdot\nabla_h)b + w\frac{\partial b}{\partial z} + N^2 w = 0 \tag{1c}$$

$$\nabla_h\cdot\mathbf{u_h} + \frac{\partial w}{\partial z} = 0, \tag{1d}$$

where $\mathbf{u_h} = \{u, v\}$ is the horizontal velocity, w the vertical velocity, $b = -g\rho/\rho_0$ the buoyancy and p the pressure. f is the Coriolis frequency and $N = \sqrt{-\frac{g}{\rho_0}\frac{d\overline{\rho(z)}}{dz}}$ the

constant buoyancy frequency, defined in terms of the mean density profile $\overline{\rho(z)}$. $\hat{e}_1$ and $\hat{e}_3$ are unit vectors in the x and z directions.

The effect of the barotropic tide is incorporated as a time-dependent forcing term

$$F(x,y,t) = U(x,y)\frac{\omega_1^2 - f^2}{\omega_1}\cos\omega_1 t$$

on the right-hand-side of the x-momentum equation. This forcing represents a parameterization of the variation of sea-surface slope with the tidal cycle and is chosen to elicit a response of the form $u = U(x,y)\sin\omega_1 t$ where ω_1 denotes the tidal frequency. In the following analysis, we will assume that U is a function of y only, $U = U(y)$.

The eddy field, consisting of an array of 3D Taylor-Green vortices, is introduced as an initial condition in geostrophic and hydrostatic balance,

$$u(t=0) = U_e(t=0)\cos k_2 x \sin l_2 y \cos m_2 z \tag{2a}$$

$$v(t=0) = -\int \frac{\partial u}{\partial x}\,|_{t=0} dy \tag{2b}$$

$$w(t=0) = 0 \tag{2c}$$

$$b(t=0) = \int \frac{\partial v}{\partial z}|_{t=0} dx \tag{2d}$$

$$p(t=0) = \int v(t=0) dx. \tag{2e}$$

2.2 Wave-triad interactions

The interaction between a barotropic tide and an eddy field bears similarities with internal wave-triad interactions where the resonant interaction of two waves leads to the excitation of a third (McComas and Bretherton, 1977; Müller *et al.*, 1986), and with the resonant interaction between wind-forced pure inertial oscillations and a turbulent mesoscale eddy field that results in the excitation of a propagating near-inertial internal wave (Danioux and Klein, 2008).

To illustrate the analogy, we consider a barotropic semidiurnal tide with wavevector $\boldsymbol{\kappa_1} = \{0, l_1, 0\}$ and frequency ω_1 in the presence of an eddy field characterized by wavevector $\boldsymbol{\kappa_2} = \{k_2, l_2, m_2\}$ and advective time-scale $1/(\boldsymbol{\kappa_2}\cdot U_e) \gg 2\pi/\omega_1$ where U_e is a typical eddy velocity and $\kappa_2 = \sqrt{k_2^2 + l_2^2 + m_2^2}$. The nonlinear quadratic interaction of the tide with the eddies excites motions with functional form

$$e^{\imath[k_2 x \pm (l_1 \pm l_2)y \pm m_2 z \pm \omega_1 t]}.$$

As in the wave-wave interaction problem, the resulting signal is weak under most conditions. However, if the scales of the barotropic tide and eddy field are such that resonance conditions,

$$\kappa_1 \pm \kappa_2 = \kappa_3 \tag{3a}$$

$$\omega_1 = \omega(\kappa_1 \pm \kappa_2). \tag{3b}$$

where ω is the internal wave dispersion relation

$$\omega(\kappa_3) = \sqrt{\frac{N^2(k_3^2+l_3^2)+f^2m_3^2}{k_3^2+l_3^2+m_3^2}}, \tag{4}$$

then resonance conditions are satisfied and stronger interaction possible, exciting an inertia-gravity wave (IGW) whose frequency ω_3 matches that of the tide ω_1 and wavevector $\kappa_3 = \{k_3, l_3, m_3\} = \{k_2, l_1 \pm l_2, m_2\}$. In this case, the resonant triad is comprised of the barotropic tide, eddy field and IGW components with characteristic scales given above.

2.3 Multiple-scale analysis

The interaction has been examined with a weakly nonlinear multiple-scale perturbation method based on a fast wavelike timescale $T_0 \sim 1/f$, and a much longer, advective eddy timescale $T_1 \sim L/U_e$ where L is a typical eddy radius (Lelong and Kunze, 2009). The ratio of the two timescales defines a small parameter, $U_e/fL = \varepsilon$, known as the Rossby number. In the usual fashion, all variables are expressed as power series expansions in ε (Kevorkian and Cole, 1981), e.g. for velocity,

$$\mathbf{u}(\mathbf{x};t_0,t_1) = \mathbf{u}^{(0)}(\mathbf{x};t_0,t_1) + \varepsilon\mathbf{u}^{(1)}(\mathbf{x};t_0,t_1) + O(\varepsilon^2)$$

where t_0 and t_1 denote nondimensionalized fast and slow times respectively such that $\partial/\partial t = \partial/\partial t_0 + \varepsilon\partial/\partial t_1$.

The next step consists in delineating the triad components. To lowest order in ε, we assume that both tide and eddy velocities are entirely horizontal.

The barotropic tide velocity is defined to be the vertically averaged horizontal velocity over the domain depth H

$$\mathbf{u}_{BT} = \overline{\overline{\mathbf{u_h}(\mathbf{x};t_0,t_1)}} = \frac{1}{H}\int_0^H \mathbf{u_h}(\mathbf{x};t_0,t_1)\,dz. \tag{5}$$

The tide oscillates on the fast timescale but its amplitude may be modulated on the slower timescale. Tidal equations are obtained by vertically averaging Eqs. 1a-d.

The eddy velocity is independent of the fast timescale and defined as the temporally averaged horizontal velocity

$$\mathbf{u}_e(\mathbf{x},t_1) = \overline{\mathbf{u_h}(\mathbf{x};t_0,t_1)} = \frac{1}{\tau}\int_{t_0}^{t_0+\tau} \mathbf{u_h}(\mathbf{x};\tau_0,t_1)\,d\tau_0 \tag{6}$$

where $T_0 \ll \tau \ll T_1$. Eddy field equations are obtained by temporally averaging Eqs. 1a-d.

The residual horizontal velocity which is ascribed to internal waves possesses vertical structure and is a function of both timescales. To lowest order, the vertical velocity is entirely assigned to the wave component,

$$\mathbf{u}_{wave} = \{\mathbf{u_h} - \mathbf{u}_{BT} - \mathbf{u}_e, w\}. \tag{7}$$

Therefore, the internal wave evolution is best described by a forced wave equation for w, derived from Eqs. 1a-d through algebraic manipulation. In nondimensional form, it is

$$\varepsilon^2\frac{\partial^2}{\partial t_0^2}\nabla_h^2 w + \frac{\partial^2}{\partial t_0^2}(\frac{\partial^2 w}{\partial z^2}) + \nabla_h^2 w + \frac{\partial^2 w}{\partial z^2} = \varepsilon(F_1+F_2+F_3+F_4+F_5) + \varepsilon^3 F_6 + \varepsilon^4 F_7 \tag{8}$$

where the right-hand-side forcing terms

$$F_1 = \frac{\partial^2}{\partial t\partial z}\nabla_h\cdot[(\mathbf{u}_h\cdot\nabla_h)\mathbf{u}_h] \tag{9a}$$

$$F_2 = \frac{\partial^2}{\partial t\partial z}\nabla_h\cdot[w\frac{\partial \mathbf{u}_h}{\partial z}] \tag{9b}$$

$$F_3 = -\nabla_h^2[\mathbf{u}_h\cdot\nabla_h b] \tag{9c}$$

$$F_4 = -\nabla_h^2[w\frac{\partial b}{\partial z}] \tag{9d}$$

$$F_5 = \frac{\partial}{\partial z}\{\mathbf{e_3}\cdot[\nabla\times(\mathbf{u}\cdot\nabla)\mathbf{u}_h)]\} \tag{9e}$$

$$F_6 = -\frac{\partial}{\partial t}\nabla_h^2[\mathbf{u}_h\cdot\nabla_h w] \tag{9f}$$

$$F_7 = -\frac{\partial}{\partial t}\nabla_h^2[w\frac{\partial w}{\partial z}]. \tag{9g}$$

The scaling is based on the requirements that (i) Coriolis and pressure-gradient terms be of the same order and present in the lowest-order equations, (ii) buoyancy and pressure fields be in hydrostatic balance. We make the additional reasonable assumption that $H \sim \varepsilon L$ and $W \sim \varepsilon U_e$ where W is the vertical velocity scale.This sets $H/L = O(\varepsilon)$. Typical oceanic values for f/N are O(10^{-2}), of the same order as

ε based on a midlatitude $f = 10^{-4}s^{-1}$, U_e of O($0.1ms^{-1}$) and L of O(10^5m). Therefore, the Burger number $Bu = (NH/fL) \sim O(1)$.

Homogeneous solutions of Eq. 8 are of the form $exp[\pm\imath(kx+ly+mz\pm\omega t)]$ where $\omega^2 = 1+(k^2+l^2)/m^2$ is the nondimensional form of Eq. 4 when $m \gg (k^2+l^2)$.

At $O(1)$ and $O(\varepsilon)$, all solutions to Eq. 8 are trivial, implying that $w^{(0)}$ and $w^{(1)}$ are 0. Hence, only forcing terms F_1, F_3 and F_5 contribute at $O(\varepsilon^2)$.

Not all solutions of Eq. 8 represent propagating IGWs, but our present focus will be on forced solutions that exhibit propagating internal-wave

$$exp[\pm\imath(k_2x+(l_1\pm l_2)y+m_2z\pm\omega_1t)]$$

behaviour, described in Sec. 2.2. Forcing terms which satisfy the homogeneous equation elicit a resonant response, similar to the resonance of a harmonic oscillator forced at its natural frequency. Resonant solutions can only be excited if the F_i terms project onto matching frequency and wavenumber ranges (Ford *et al.*, 2000). This implies that eddy/eddy interactions, which occur on very long time-scales, cannot excite an internal tide since their projection onto the IGW-frequency band is zero. Similarly, barotropic tide/tide interactions cannot project onto IGW vertical scales which are much smaller. Therefore, for the purpose of studying IGW generation, we need only consider tide/eddy contributions These terms are of the form $\sin\theta_\pm$ and $\cos\theta_\pm$ where

$$\theta_\pm = k_2x\pm(l_1\pm l_2)y\pm m_2z-\omega_1t_0 = k_3x\pm l_3y\pm m_3z\pm\omega_3t_0.$$

We assume, without loss of generality, that terms with phase

$$\theta = k_1x+(l_1+l_2)y+m_2z-\omega_1t_0$$

excite a resonant response.

Coefficients C_s and C_c corresponding to resonant eddy/tide forcing terms $\sin\theta$ and $\cos\theta$ in Eq. 9a-g are then readily computed,

$$C_s(t_1) = u_e^{(0)}(t_1)u_{BT}^{(0)}(t_1)\frac{k_2l_1m_2}{4}(1+\frac{3l_1}{4l_2}) \tag{10}$$

$$C_c(t_1) = u_e^{(0)}(t_1)u_{BT}^{(0)}(t_1)\frac{l_1m_2}{16\omega_1}(-l_1+\frac{k_2^2}{l_2}-l_2+\frac{2k_2^2\omega_1^2}{l_2}). \tag{11}$$

For circularly shaped eddies ($k_2 = l_2$), C_s and C_c achieve a maximum when $l_1 = -\frac{2}{3}l_2$ and $l_1 = \frac{l_2}{\omega_1^2}$ respectively, which implies that l_1/l_2 must be $O(1)$ for resonant forcing to be most effective.

When barotropic tidal wavenumber $l_1 = 0$, $F_1^{(0)} \equiv 0$ since $\nabla_h\cdot\mathbf{u}_e^{(0)} = 0$. Moreover, the sum of $F_3^{(0)}$ and $F_5^{(0)}$ exactly cancels due to thermal-wind balance. Therefore, if

the barotropic tide velocity is uniform, no waves can be excited since all tide/eddy forcing terms vanish. This result is independent of whether resonance conditions are satisfied or not. Physically, this situation corresponds to a periodic advection of the entire water column by the tidal current. Without any horizontal modulation, this type of motion cannot transfer horizontal energy to vertical motions.

Additional details of the weakly nonlinear solutions are given in Lelong and Kunze (2009).

3 Numerical simulations

Numerical simulations were performed to check the weakly nonlinear theory. The numerical model solves the three-dimensional Boussinesq equations on the f-plane (Winters et al., 2004) in a domain of dimension $L_x \times L_y \times L_z$. Boundary conditions are periodic in both horizontal directions and free-slip in the vertical. To assess the role of the barotropic tide, we compare the evolution of two different simulations (Runs A and B) that differ only in their tidal forcing. In both cases, the initial condition consists of a field of vortices in geostrophic and hydrostatic equilibrium, modulated by Gaussian (in x) and exponential (in z) envelope functions to confine the eddy field to upper and middle regions of the domain. This configuration allows generated waves to radiate away from the presumed eddy source region. The initial vorticity distribution for Run B is shown in Fig. 1.

Tidal forcing is ramped up to full strength over five tidal cycles to ensure smoothness of solutions. Principal run parameters are given in Table 1. Coriolis and buoy-

Table 1 Simulation parameters for domain size $L_x \times L_y \times L_z$, tidal wavelength λ_1 and eddy wavelength λ_2.

Run	Tide	L_y	L_x	L_z	λ_1	λ_2
A	$0.03m\,s^{-1}$	6.25×10^4m	2.5×10^5m	$2400m$	∞	3.12×10^4m
B	$0.03m\,s^{-1}$	4×10^4m	1.6×10^5m	$2400m$	1.33×10^4m	2×10^4m

ancy frequencies are $f = 10^{-4}s^{-1}$ and $N = 5\times10^{-3}s^{-1}$ respectively. This yields $N/f = 50$, somewhat smaller than typical oceanic values. Using a reduced value of N/f while simultaneously reducing horizontal scales of eddies and tide preserves dynamical similarity with oceanographically relevant parameter regimes in situations such as this one where the large range of spatial and temporal scales that must be resolved becomes prohibitively expensive (e.g. Lelong and Sundermeyer, 2005).

Runs A and B differ in the horizontal scale, $\lambda_1 = 2\pi/l_1$, of the tidal forcing. In Run A, λ_1 is much larger than the scale of the dominant eddies $\lambda_2 = 2\pi/l_2$, a case

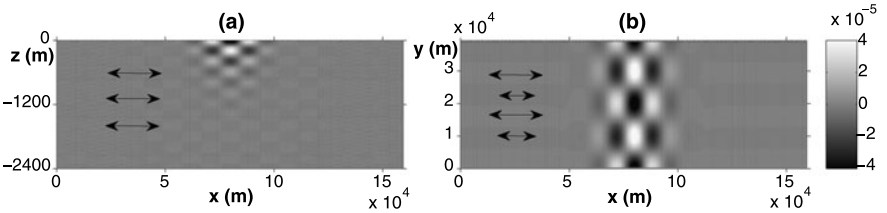

Fig. 1 vertical (a) and horizontal (b) cross-sections of vorticity field at $t = 0$ for Run B. Arrows indicate the direction and spatial variation of the barotropic tidal forcing.

characteristic of deep-ocean conditions. In contrast, in Run B, $\lambda_1 = O(\lambda_2)$, as might occur on the continental shelf or at low latitudes. In both Runs A and B, eddy and tide parameters are chosen to satisfy resonance conditions Eqs. 3a,b.

All runs, including one in which the tide was turned off (not shown), exhibit some degree of initial low-level internal wave radiation. Some weak radiation occurs because the balance of the initial flow is inherently limited by finite numerical resolution. This was confirmed by noting a decrease in initial wave radiation with increasing numerical resolution (not shown). Another source of waves arises because the initial array of localized vortices is not a rigorously exact solution of the nonlinear equations (in contrast to the periodic array of vortices defined in Eq. 2). Over time, nonlinear effects act to distort the initial state, resulting in some wave radiation. This was verified numerically by performing a linear simulation in which nonlinear terms and tidal forcing were set to zero. In this case (not shown), the vortices retained their initial balanced state and the resulting early-time wave radiation was several orders of magnitude lower than in the nonlinear case.

In Run B, eddy and tidal scales are chosen to maximize the strength of the forcing terms in Eq. 10. L_y encompasses exactly two λ_2 and three λ_1. To allow for horizontal and vertical wave propagation, $L_x = 4L_y$, and in the vertical $L_z = 6\lambda_{z_2}$ where $\lambda_{z_2} = 2\pi/m_2$.

If residual u and v (defined by Eq. 7) and w indeed represent linear internal waves of frequency ω_1 with wavevector κ_3, then u and v components should be $\pi/2$ out of phase and their amplitudes should differ by a factor of ω_1/f. Similarly, w will be π out of phase with residual u and scale as $(\kappa_{h_3}/m_3)u$. Residual u, $(\omega_1/f)v$ and $-(m_3/\kappa_{h_3})w$ are plotted for each simulation in Fig. 2. In Run A (Fig. 2a), corresponding to the case where $l_1 = 0$ in the theory, residual horizontal velocities are inertial oscillations (Lelong and Kunze, 2009). The residual velocities in Run B, for which resonant forcing is maximum, are an order of magnitude larger than in Run A and have phase behavior consistent with propagating internal waves. The velocities, which are initially zero, begin to grow in response to the strong interaction between

tidal and eddy fields. (Fig. 2b). They oscillate with the tidal frequency and their amplitudes grow on the slow time scale.

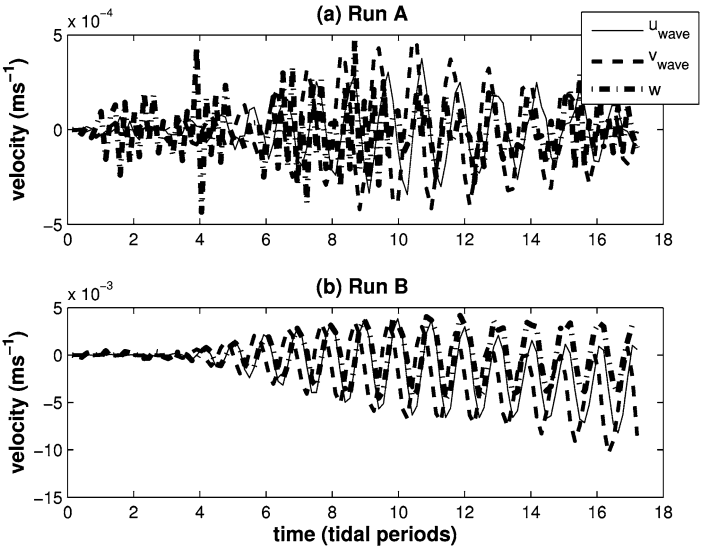

Fig. 2 Time evolution of u, $(\omega_1/f)v$ and $-(m_3/\kappa_{h_3})w$ for (a) Run A ($\lambda_1 >> \lambda_2$) and (b) Run B ($\lambda_1 \approx \lambda_2$), at a point away from the eddy field.

Cross-sections of w at three different times for Run B are shown in Fig. 3. The first emitted waves, visible on the outer edges of Fig. 3 (a,d) are barotropic and lack horizontal structure. These weak waves radiate in response to the initial adjustment discussed above. The next set of emitted waves, visible on the flanks of the eddy region by $t = 7T$ [Fig. 3 (b,e)], are much stronger and exhibit well defined vertical and horizontal structure. By $t = 10T$ (Fig. 3(c,f), definite mode-1 horizontal wavelength in y and mode-6 vertical wavelength are evident (Fig. 3(b,e)], corresponding to $l_3 = l_1 - l_2$ and $m_3 = m_2$, as predicted by the theory for resonantly forced waves. Analysis shows that the energy source for the waves is the eddy field rather than the tide (Lelong and Kunze, 2009). This is quite different from the resonant forcing of internal waves by interaction of near-inertial oscillations and geostrophic eddies (Danioux and Klein, 2008), in which the eddy field acts as a catalyst in transferring near-inertial energy to waves.

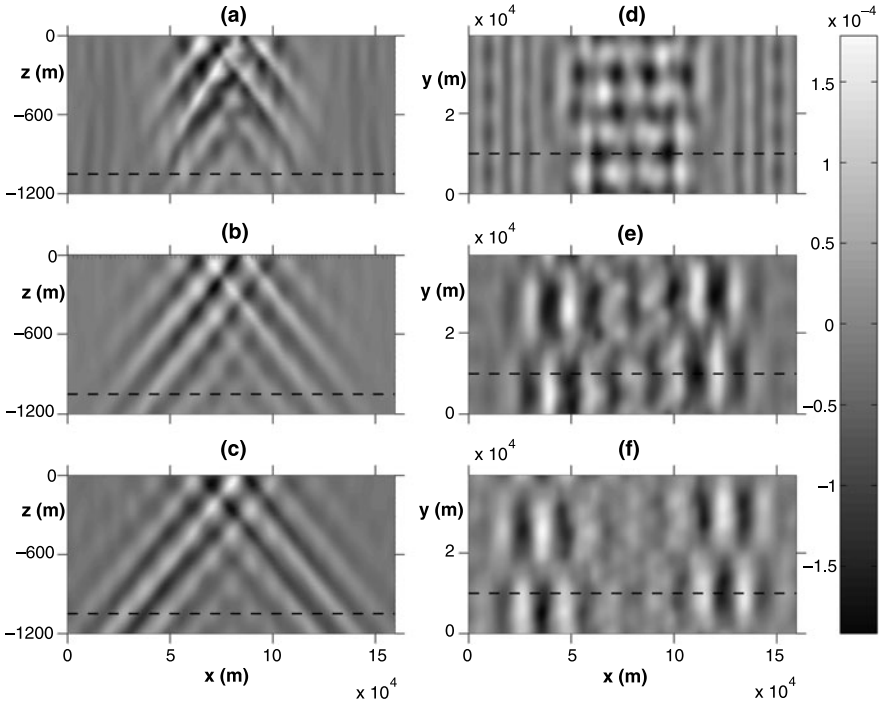

Fig. 3 Cross-sections of w in Run B at t=3.5 T (a,d), t=7 T (b,e) and 10 T (c,f); T is the tidal period. Left panels represent vertical cross-sections (only top half of domain is shown), right panels horizontal cross-sections; dashed lines indicate corresponding positions of horizontal and vertical planes. Displayed data spans $\pm 2 \times 10^{-4} m\ s^{-1}$.

4 Conclusions

The interaction of a barotropic tide with a geostrophic eddy field as a potential internal wave source has been examined theoretically and numerically. As predicted by the theory, interaction is negligible when the tidal wavelength is much larger than the eddies' even when resonance conditions are met. When the tide varies on lengthscales comparable to the eddy field's, resonant interaction is maximized. This is unlikely to occur in the mid- and high-latitude open ocean where barotropic tidal lengths are O(1000 km) while dominant eddy lengthscales are at the Rossby lengthscale $U/f \sim$ O(100 km). These two lengthscales become more comparable on the continental shelf and at low latitudes. We conclude that the mechanism of eddy/tide interaction, conjectured by Rogachev *et al.* (1992) to explain the intense near-inertial waves observed in western North Pacific anticyclonic vortices, is unlikely. The observed oscillations were more likely wind-generated near-inertial waves.

Though there is little barotropic variance outside of tidal frequencies, higher frequencies with lengthscales matching those of the eddy field will more efficiently transfer energy to internal waves than tidal frequencies (Lelong and Kunze, 2009).

Acknowledgements Support from the Office of Naval Research for the original phase of this study is gratefully acknowledged.

References

[1] Bell, T.H., 1975: Topographically generated internal waves in the open ocean. *J. Geophys. Res.*, **80**, 320-327.

[2] Cox, C., & H. Sandstrom, 1962: Coupling of internal and surface waves in water of variable depth. *J. Oceanogr. Soc. Japan*, **18**, 499-513.

[3] Danioux, E. & P. Klein, 2008: A resonance mechanism leading to wind-forced motions with a 2f frequency *J. Phys. Oceanogr.*, submitted.

[4] Ford, R., M.E. McIntyre & W.A. Norton, 2000: Balance and the Slow Quasi-manifold: Some Explicit Results. *J. Atmos. Sci.*, **57**, 9, 1236-1254.

[5] Garrett, C., & E. Kunze, 2007: Internal tide generation in the deep ocean. *Ann. Rev. Fluid Mech.*, **39**, 57-87.

[6] Kevorkian, J. & J.D. Cole, 1981: Perturbation methods in applied mathematics. *Applied Mathematical Sciences*, 34, Springer.

[7] Kunze, E., 1985: Near-inertial wave propagation in geostrophic shear. *J. Phys. Oceanogr.*, **15**, 544-565.

[8] Lelong, M.-P. and E. Kunze, 2009: Can barotropic current/geostrophic eddy interactions excite internal waves?, manuscript in preparation for *J. Fluid Mech.*

[9] Lelong, M.-P. and M.A. Sundermeyer, 2005: Geostrophic adjustment of an isolated diapycnal mixing event and its implications for small-scale lateral dispersion. *J. Phys. Oceanogr.*, **35**, 2352-2367.

[10] McComas, C.H., & F.P. Bretherton, 1977: Resonant interaction of oceanic internal waves. *J. Geophys. Res.*, **83**, 1397-1412.

[11] Müller, P., G. Holloway, F. Henyey & N. Pomphrey, 1986: Nonlinear interactions among internal gravity waves. *Rev. Geophys.*, **24**, 493-536.

[12] Rogachev, K.A., E. Carmack, M. Miyaki, R. Thompson & G.I. Yurasov, 1992: Drifting buoy in an anticyclonic eddy of the Oyashio Current. *Doklady Rossiyskoy Akademii Nauk*, **326**, 547-550.

[13] Rogachev, K.A., A.S. Salomatin, V.I. Yusupov & E.C. Carmack, 1996: On the internal structure of the Kuril Current anticyclonic eddies. *Okeanologiya*, **36**, 247-354.

[14] Rogachev, K.A. & E.C. Carmack, 2002: Evidence for the trapping and amplification of near-inertial motions in a large anticyclonic ring in the Oyashio. *J. Oceanogr.*, **58**, 673-682.

[15] Simmons, H.L., R.W. Hallberg & B.K. Arbic, 2004: Internal wave generation in a global baroclinic tidal model. *Deep-Sea Res. II*, **51**, 3043-3068.

[16] Winters, K.B., J.A. MacKinnon and B. Mills, 2004: A spectral model for process studies of rotating, density-stratified flows. *J. Atmos. Ocean. Technol.*, **21**, 69-94.

[17] Wunsch, C., 1975: Internal tides in the ocean. *Rev. Geophys. Space. Phys.*, **13**, 167-182.

Generation of harmonics and sub-harmonics from an internal tide in a uniformly stratified fluid: numerical and laboratory experiments

Ivane Pairaud, Chantal Staquet, Joël Sommeria and Mahdi M. Mahdizadeh

Abstract This paper focuses on the internal tide emitted from a continental slope in a uniformly stratified fluid. Results from numerical simulations using the MITgcm and from laboratory experiments performed on the Coriolis platform in Grenoble are compared. Due to their peculiar dispersion relation, internal gravity waves organize into localized beams of energy. We show that the beam structure is well-predicted by the viscous theory of [10], assuming that the internal gravity wave field is emitted by a horizontally oscillating cylinder whose radius is the radius of curvature of the topography at the beam emission. The wave beam can bear a sub-harmonic parametric instability whose vertical scale is recovered from resonant interaction theory. Reflection of the wave beam on the bottom leads to the generation of harmonic beams, consisting of free and trapped waves.

1 Introduction

The oceanic tide can be considered as a barotropic (vertically uniform) oscillating current. In the presence of density stratification, the upward motion induced by bottom topography generates an internal tide. This mechanism is active at mid-ocean ridges and at continental slopes (such as the Bay of Biscay), as documented from

Ivane Pairaud
LEGI, CNRS & Université de Grenoble, France [Present address: IFREMER, La Seyne sur Mer, France, e-mail: Ivane.Pairaud@ifremer.fr]

Chantal Staquet
LEGI, CNRS & Université de Grenoble, France, e-mail: Chantal.Staquet@hmg.inpg.fr

Joël Sommeria
LEGI, CNRS & Université de Grenoble, France, e-mail: Sommeria@coriolis-legi.org

Mahdi M. Mahdizadeh
LEGI, CNRS & Université de Grenoble, France [Present address: Hormozgan University, Bandar Abbas, Iran, e-mail: mehdizadeh@hormozgan.ac.ir]

D. Dritschel (ed.), *IUTAM Symposium on Turbulence in the Atmosphere and Oceans*, IUTAM Bookseries 28, DOI 10.1007/978-94-007-0360-5_5,

satellite altimetry and moored current meter data. Internal tide has been given much attention for the last ten years in relation with their role in deep ocean mixing, as reviewed by [3]. The magnitude and distribution of mixing indeed influences the whole process of oceanic thermohaline circulation ([2]). Mixing is produced from the internal tide by the degradation of the internal tide into turbulence through a sequence of instabilities, involving resonant interactions (such as parametric instability [8; 17; 4]) or shear or buoyancy induced instabilities.

Several laboratory experiments of internal wave generation by oscillating bodies have been performed since the pioneering work of [18]. The case of a horizontally oscillating cylinder has been recently studied by [25] as a simple model of internal tide generation. Indeed, in a frame of reference attached to the barotropic tide, the topography oscillates horizontally and the active part of the topography may be modeled as a cylinder. [19] considered an isolated topography while the case of a continental slope was addressed by [1], [6] and [21].

The numerical modelling of the internal tide first relied on the hydrostatic approximation and solved the equations of motions in an oceanic context (f.i. [9]). To our knowledge, the first non-hydrostatic numerical simulation of internal tide emission was performed by [12] with the MITgcm, focusing upon energy transfer from the barotropic tide to internal tides for an isolated topography. Further works were conducted along the same lines by [13] and [14] for the same topography. The case of a continental slope was considered by [5] and [4]. All these numerical works were performed in a two-dimensional vertical plane and for an idealized topography. The case of a three-dimensional realistic topography with non-hydrostatic equations was tackled by [11].

In the present paper, the internal tide is generated by a simple two-dimensional continental slope in a uniformly stratified ocean and modeled by joint numerical simulations and laboratory experiments. Their set-ups are described in Sect. 2. The internal tide emission is discussed and illustrated from our results in Sect. 3. The main features of the internal tide are presented in the next sections: (i) its spatial structure close to the emission region is well predicted by a viscous theoretical model of internal wave emission by a horizontally oscillating cylinder (Sect. 4), (ii) it can bear a sub-harmonic instability of small vertical scale (Sect. 5), (iii) harmonic components can be generated from the bottom reflexion region (Sect. 6). We conclude in Sect. 7.

2 Experimental set-ups

2.1 Laboratory experiments

A tidal current is forced along a channel, 4 meter wide, built inside the circular tank of the Coriolis platform, 13 meters in diameter (see Fig. 1). The results of the present paper are obtained in the absence of rotation. The barotropic tide is produced by the

horizontal oscillation of a piston, filling the whole section of the channel. At the opposite end, the channel is open, so that the flow can escape side-way over the topography. Let d and ω be the amplitude and frequency of the motion of the piston respectively. In the present paper, the values for d and $2\pi/\omega$ are 0.6 cm and 26 s respectively, except in Sect. 5 where $d = 2$ cm.

A linear density stratification is introduced by salinity while the tank is filled. Since there is no flux of salinity through the surface and through the bottom of the tank, the linear density profile is slowly eroded by mixed layers developing from these boundaries. Nevertheless their thickness remains limited to a few cm during a whole set of experiments (several weeks) with no significant evolution of the stratification in the interior. The data presented here correspond to a stratification with uniform Brunt-Väisälä frequency $N_{exp} = 0.71 \pm 0.2$ rad/s^{-1}, except for a bottom mixed layer $\simeq 9$ cm thick and a surface mixed layer $\simeq 3$ cm thick.

The laboratory configuration is designed by similarity with a typical oceanic configuration, as described in the numerical simulations of the internal tide by [5]. To reach regimes of inertial dynamics, with weak viscous damping, we need a sufficiently deep water, so we choose a total depth of $H = 90$ cm, with a shelf height equal to 76.5 cm. The topography is made of a constant slope 0.5, with inclination angle 30^o, matched with the flat continental shelf through a section with radius of curvature $R = 180$ cm. If this is assumed to represent an ocean 4.5 km deep, the vertical scaling factor is $1/5000$. At this scale, the available channel length of 10 m represents 50 km. To simulate the process over a distance of 250 km, allowing space for internal tide propagation, reflection and breaking, we need to apply a distortion of aspect ratio by a factor 5. Hence, the slope is five times larger in the experiment than in the ocean (typical value 0.1). We expect that such a distortion has only a weak influence on the dynamics. Note that within the hydrostatic approximation, the dynamics is strictly invariant by a change of aspect ratio in the absence of viscosity effect or turbulence parameterisation.

The main measurement tool is Particle Image Velocimetry (PIV) providing velocity fields in a vertical plane. Polystyrene particles (300 μm in diameter) sorted in density are used to get a uniform seeding over the fluid depth. The vertical laser sheet is obtained by a 6 watt continuous Yag laser and an oscillating mirror while

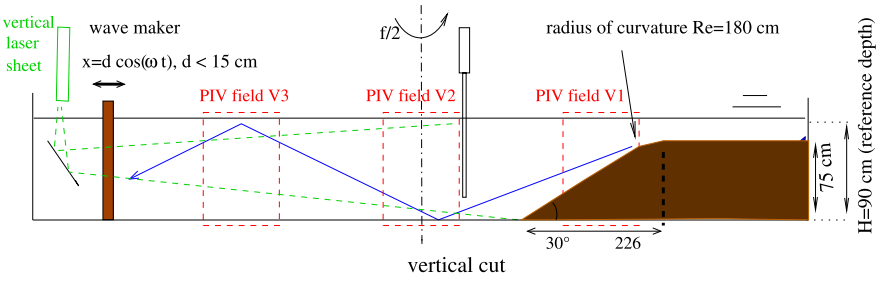

Fig. 1 Sketch of the laboratory experiment.

the images are obtained by two CCD cameras looking through windows on the side of the channel. A few velocity fields have been also obtained from a top view with a horizontal laser plane.

2.2 Numerical simulations

The simulations are based on the numerical model developed at MIT by [16], which we adapted to the experimental configuration. The code solves the nonlinear non-hydrostatic Navier-Stokes equations in the Boussinesq approximation using a finite volume method and a Cartesian coordinate system. Since the topography in the laboratory experiment is two-dimensional and the Coriolis platform is non rotating, we assume that the flow dynamics is two-dimensional in a vertical plane. The horizontal and vertical dimensions of the numerical domain are exactly those of the laboratory experiment as is also the topography we impose. The coordinate system (O,x,z) we use is such that x increases from the shelf to the piston and $z = 0$ at the bottom. The position of O along the x-axis is located at the crossing of the line $z = 76.5$ cm (on the shelf) and the line of maximum slope tangent to the topography.

We performed direct numerical simulations that is, no subgrid scale modelling is used. The value of the viscosity is set to 10^{-2} cm^2/s, as in the laboratory experiments, while the Prandtl number is set to 1 (against 700 in the experiments).

The MITgcm has an implicit free-surface formulation and no-flux boundary conditions are applied to the density field at the surface and at the bottom. Free-slip boundary conditions are applied to the velocity components.

We chose $N = 0.72$ rad/s in the simulation which we impose from the free surface down to a height $z = 9$ cm, below which the density is uniform. Thus, we ignored the thin surface mixed layer of the experiments but reproduced the bottom mixed layer.

The forcing generated by the piston is modeled by imposing a barotropic flux at the two vertical boundaries. This flux is oscillating in time at the excitation frequency ω. Measurements of the barotropic component in the experiment indicate that it is partly blocked by the topography, so that the forcing amplitude decreases from the piston to the shelf-break by typically 50 %. The constant barotropic flux introduced in the computation is therefore adjusted to match the measured value over the topography, in the region of internal tide generation. Thus, in the numerical simulation, $d = 0.24$ cm except in Sect. 5 where $d = 0.5$ cm.

We use a resolution of 1202 grid points along the horizontal direction, with $dx = 0.91$ cm. Along the vertical, the grid size is constant and equal to $dz = 0.28$ cm, implying that the number of grid points is 320 over the plain and 48 over the shelf. This resolution may be considered as large since, in an ocean model, it would correspond to a horizontal resolution of 45 m and to a vertical direction of 14 m. One tidal period is simulated by 200 time steps, with $dt = 0.1305$ s.

All simulations are started from rest and run over 40 forcing periods.

3 Emission of the wave beam

Internal gravity waves are dispersive waves with an anisotropic dispersion relation (f.i. [15]). For a plane wave in a stratified medium with constant N, the wave vector $\mathbf{k}$ and frequency ω are indeed related by $\omega^2 = N^2 \sin^2\theta$, where θ is the angle of $\mathbf{k}$ with the vertical. The group velocity is perpendicular to $\mathbf{k}$, therefore aligned with the fluid velocity. As a consequence, any object oscillating at a frequency ω smaller than N emits internal gravity waves, which carry the energy along directions with angle θ with respect to the horizontal. Energy is concentrated along these directions within wave beams. This striking property is nicely illustrated by the laboratory experiments of [18]. The experiments also show that the beams are tangent to the object as a consequence of the impermeability condition. Beams are thus emitted from 'critical' points, where the boundary is perpendicular to $\mathbf{k}$. The slope is referred to as being 'critical' there. In the case of a cylinder, the energy of the source distributes among four beams, associated with upward and downward (as well as leftward and rightward) propagation.

The theory of wave emission by a cylinder has been derived in the far-field by [24] and later in the near-field by [10]. In the latter, the structure of the wave beam depends both upon the ratio s/R, where s is the distance along the beam from the object and R the radius of the cylinder, and on the ratio δ/R, where $\delta = \sqrt{\nu/\omega}$ is the thickness of the viscous boundary layer on the object. It is assumed that δ is much smaller than R. In this case, near the cylinder, the energy of each beam actually possesses two maxima, which eventually merge into a single one away from the cylinder under the action of viscosity. For a very large cylinder, the two maxima are well pronounced, which results in two distinct wave beams on each side of the object.

The internal tide can be viewed as the wave emission from an horizontally oscillating topography, in a frame of reference attached to the barotropic tide. In the case of a continental slope, the energy will be able to propagate in two directions only. This result is illustrated in Fig. 2 where color maps of the along-beam velocity are displayed for the laboratory experiment (frame a) and for the numerical simulation (frame b). Our study is focused on the beam propagating toward the deep ocean, and the beam propagating leftward (toward the shelf) is not shown in these figures.

A good agreement is observed between the simulation and the experiment, the emission location, thickness and amplitude of the wave beams being the same. Note that, already after 8 periods, the maximum amplitude of the velocity field is 1 cm/s that is, at least three times larger than the forcing amplitude.

Fig. 2 shows that the most active part of the topography is the region where the beam is tangent to the slope that is at the critical point. Hence, we may compare our results for wave emission to the theoretical predictions of [10] for a cylinder with radius R=1.80 tangent to the slope at the critical point. Such a comparison was also made by [25], [19] and [6] using data from their laboratory experiments.

4 Spatial structure of the wave beam

In the theory of [10], the linear Boussinesq equations of motions are solved in a two-dimensional vertical plane and for a constant N fluid, for a solution which is harmonic in time. The key assumptions of the model lie in the boundary conditions for the velocity field. This field vanishes at infinity, as expected. On the cylinder, the thickness of the viscous boundary layer δ is assumed to be much smaller than the cylinder radius so that free-slip boundary conditions can be set. As a result, an analytic expression for the stream function can be obtained, from which the along-beam velocity field U_{HK} can be inferred. Following [10], let s and η be the along- and cross-beam coordinates respectively, the origin of the coordinate system being at the center of the cylinder (hence $\eta/R = 1$ at the beam center). Omitting time harmonic dependence, $U_{HK}(s,\eta)$ is expressed as

$$U_{HK}(s,\eta) = -\frac{U_0}{2} e^{-i\theta} \int_0^{+\infty} \mathrm{J}_1(k) \exp\left(-k^3\lambda \frac{s}{R} + ik\frac{\eta}{R}\right) dk, \tag{1}$$

where $s \geq 0$, U_0 is the velocity amplitude of the cylinder, $\lambda = (\tan\theta/2)(\delta/R)^2$ and $\mathrm{J}_1(k)$ is the first order Bessel function.

In the present work, we compute in the absolute frame of reference the velocity filtered at the forcing frequency, which therefore involves the baroclinic and

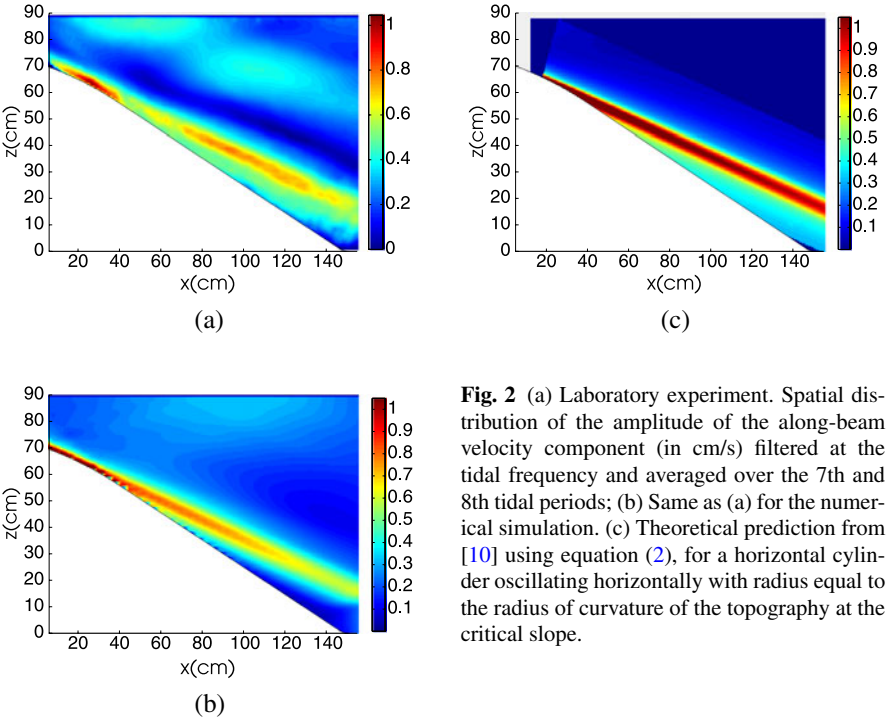

Fig. 2 (a) Laboratory experiment. Spatial distribution of the amplitude of the along-beam velocity component (in cm/s) filtered at the tidal frequency and averaged over the 7th and 8th tidal periods; (b) Same as (a) for the numerical simulation. (c) Theoretical prediction from [10] using equation (2), for a horizontal cylinder oscillating horizontally with radius equal to the radius of curvature of the topography at the critical slope.

barotropic tidal signals. The corresponding analytical expression of the along-beam velocity component, denoted U_s, is therefore (omitting again time dependence)

$$U_s(s,\eta) = -U_{HK}(s,\eta) + U_{BT}, \tag{2}$$

where U_{BT} is the barotropic component of the velocity, which depends upon x. U_{BT} is computed as the vertical average of the horizontal velocity component. When used in equation (2), the factor U_0 in equation (1) is taken as the amplitude of the barotropic velocity at the critical point.

Maps of U_s are plotted in Fig. 2c. The topography has been added to facilitate comparison with the results from the numerical simulations and laboratory experiments (but we recall that waves are emitted by a horizontally oscillating cylinder in the theory). The agreement between the three approaches is quite good, the beam amplitudes differing by 20% at most.

5 Parametric instability of the wave beam

It has been known since [7] and [20] that plane monochromatic internal gravity waves may be unstable through parametric subharmonic instability (PSI). This instability is a special case of resonant interactions which occur among a wave triad. Let $(\mathbf{k}_0, \omega_0)$, $(\mathbf{k}_1, \omega_1)$ and $(\mathbf{k}_2, \omega_2)$ denote the wave vector and frequency of each member of the triad. Since the waves form a triad, $\mathbf{k}_0 + \mathbf{k}_1 + \mathbf{k}_2 = 0$. Resonance occurs when a temporal resonance relation is also satisfied : $\omega_0 + \omega_1 + \omega_2 = 0$. In the case of PSI, one wave of small amplitude, referred to as the primary wave, interacts with two waves of much smaller amplitude such that $|\omega_1| \simeq |\omega_2| \simeq |\omega_0|/2$, where index 0 refers to the primary wave. The instability promotes the growth of small scale waves with respect to the primary wave scale.

As discussed above, the internal tide is emitted as a wave beam, which can be viewed as a plane wave whose amplitude is modulated across the beam ([22]). This implies that a wave beam of infinite extent is a solution of the Boussinesq equations in the absence of viscosity, as is a plane wave in an infinite medium. Hence, such a wave beam could bear a PSI. This was shown indeed by [4] from numerical simulations of internal tide emission at a continental slope in an oceanic context.

In the present case of joint numerical and laboratory experiments, no PSI was detectable for the forcing amplitude used in Fig. 2. Since the growth rate of PSI is proportional to the amplitude of the wave beam, we ran a computation doubling the forcing amplitude. The result is displayed in Fig. 3a, where we plot the time average amplitude of the horizontal velocity component filtered at half the forcing frequency. Quasi-horizontal structures (actually whose direction makes the angle $\mathrm{asin}(\omega/2N)$ with the horizontal) appear. These structures are of alternate sign along the vertical (it is not visible since the amplitude of the velocity field is plotted). The same spatial pattern was obtained by [4]. We performed this filtering operation on the experimental data, for the same forcing amplitude (frame 3b): similar quasi-

horizontal structures appear, with comparable amplitude, demonstrating for the first time in a laboratory experiment that PSI can appear in a wave beam. Note that the maximum amplitude of the perturbation is only 4 times smaller than the maximum amplitude of the wave beam from which the perturbation developed.

The spatial structure of this perturbation displays a well-defined vertical scale, which can be computed from resonant interaction theory. Fig. 3c displays the growth rate of the instability as a function of the vertical component of the wave vector k_z, for the parameters of the computation. In the absence of viscous effects, the growth rate saturates as $k_z \to \infty$ so that viscous effects, in damping the largest wavenumbers, introduce a scale selection. The value of k_z for which the growth rate is maximum should provide the scale of the instability visible in Fig. 3a and 3b. We find from Fig. 3c that this vertical wavelength is about 8 cm, which compares well with that of the quasi-horizontal structures displayed in frames a) and b). This result confirms that the instability is of parametric sub-harmonic type.

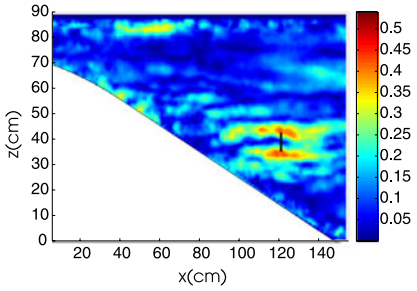

(a)

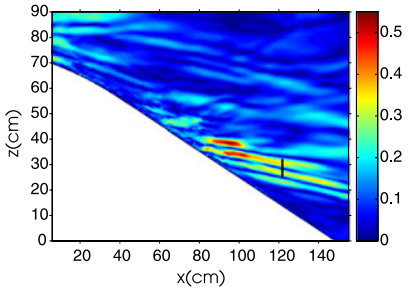

(b)

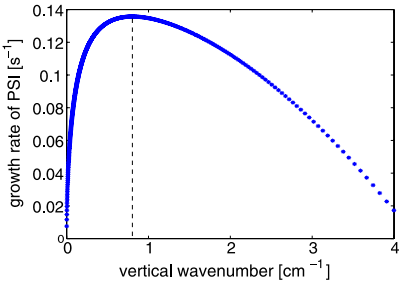

(c)

Fig. 3 (a) Laboratory experiment. Amplitude of the horizontal velocity (in cm/s) filtered at half the forcing frequency and averaged over forcing periods 22 to 25; (b) Same as (a) for the numerical simulation. (c) Growth rate of PSI predicted by resonant interaction theory for the parameters of the simulation and experiment, as a function of the vertical wavenumber of the perturbation. The vertical wavenumber with maximum growth rate is indicated with a dashed line and the corresponding wave length is drawn on frames (a) and (b) with a vertical black line.

6 Generation of harmonics

When the wave beam hits the bottom mixed layer, a reflected beam is created. While no harmonic wave is generated by the reflection of a plane internal gravity wave on a flat bottom, this result does not hold any longer for a wave beam ([23]). This theoretical prediction was verified by [5] and is also found in the present numerical simulation, as shown in Fig. 4b. This figure displays the time average amplitude of the horizontal velocity component filtered at twice the forcing frequency (which is smaller than N). The harmonic wave reflects also at the top boundary of the mixed layer and on the piston, which accounts for the perturbed signal for x larger than about 4 m. Fig. 4a shows that a similar harmonic wave is created in the laboratory experiment. It is noteworthy that, both in the laboratory and numerical experiments, a harmonic wave is also trapped in the primary reflected wave beam.

7 Conclusion

The purpose of this short paper was to provide the main characteristics of the weakly nonlinear dynamics of the internal tide emitted at a continental slope in a uniformly

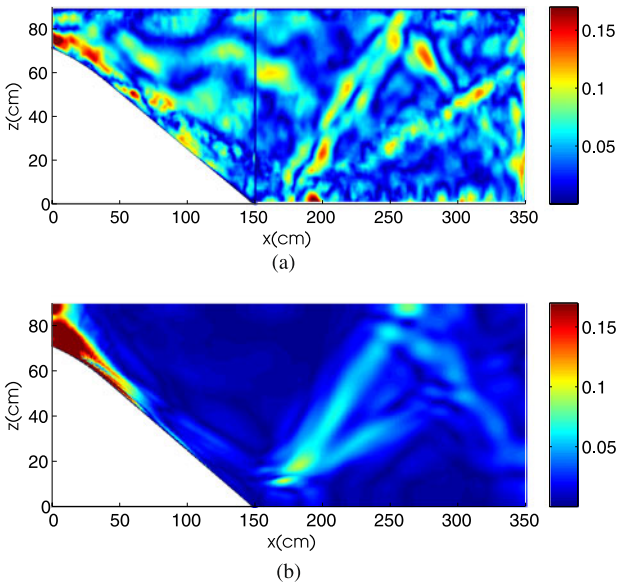

Fig. 4 (a) Laboratory experiment. Amplitude of the horizontal velocity component filtered at twice the forcing frequency and averaged over forcing periods 18 to 21; (b) Same as (a) for the numerical simulation.

stratified non rotating fluid. These are the spatial structure of the wave beam and two processes of energy transfer toward smaller scales. Large scale laboratory experiments were performed on the Coriolis platform, so that inertial dynamics can be reached, and compared with well-resolved numerical simulations using the non hydrostatic MITgcm for the same sets of parameters.

We analysed the emission of the wave beam in light of the theory of [10], when the oscillating source is a cylinder with radius equal to the radius of curvature of the topography at the critical slope. A very good agreement is found between the laboratory and numerical experiments and the theory, with differences not larger than 20%. This shows that the radius of curvature of the topography at the critical slope, along with viscosity, control the beam formation and possibly the beam width. The theory of [10] should provide such dependencies.

The beam can be unstable to parametric sub-harmonic instability (PSI) if the time scale of the instability (namely, the inverse growth rate) is smaller than the viscous time at the scale of the instability. A PSI was observed both in the laboratory and in the numerical experiments, associated with strikingly quasi-horizontal phase lines of comparable amplitude. We checked that the vertical wavelength of the perturbation matches the prediction from resonant interaction theory. When extrapolated to the ocean, using a simple similarity argument, this vertical wavelength is 400 m, associated with layers of half that height. The much higher value of the Reynolds number in the ocean compared to the present experiments would actually select an even smaller scale. If these layers become unstable (through buoyancy induced instability), an appreciable vertical part of the ocean would be mixed.

We also showed that harmonic beams can be created when the incident wave beam interacts with the reflected beam at the bottom mixed layer, a part of the harmonic wave field being trapped in the reflected beam. The same behavior is observed in the numerical simulation and, for the first time again, in the laboratory experiments.

Acknowledgements We thank Louis Gostiaux and Bruno Voisin for fruitful interaction. The laboratory experiments and the post-doctoral grant of Ivane Pairaud were supported by ANR (Agence Nationale de la Recherche) through contract ANR-05-BLAN-0176-01. Numerical simulations were performed on the computers of IDRIS (Institut du Développement et des Ressources en Informatique Scientifique) under contract 070580.

References

[1] Baines, P.G., Fang, X.H.: Internal tide generation at a continental shelf/slope junction: A comparison between theory and a laboratory experiment. Dynamics of Atmospheres and Oceans **9**, 297–314 (1985).

[2] Ferrari, R., Wunsch, C: Ocean circulation kinetic energy: reservoirs, sources, and sinks. Ann. Rev. Fluid Mech. **41**, 253–282 (2009).

[3] Garrett, C, Kunze, E.: Internal tide generation in the deep ocean. Annu. Rev. Fluid Mech. **39**, 57–87, 2007.
[4] Gerkema T., Staquet C., Bouruet-Aubertot, P.: Nonlinear effects in internal tide beams and mixing. Geophysical Research Letters **33**, L08604 (2006).
[5] Gerkema T., Staquet C., Bouruet-Aubertot, P.: Nonlinear effects in internal tide beams and mixing. Ocean Modelling **12**, 302–318 (2006).
[6] Gostiaux, L, Dauxois, T. Laboratory experiments on the generation of internal tidal beams over steep slopes. Physics Fluids **19**(1), 1–4 (2007).
[7] Hasselmann, K: A criterion for nonlinear wave stability. J. Fluid Mech. **30**, 737 (1967).
[8] Hibiya, T., Nagasawa, M., Niwa, N.: Nonlinear energy transfer within the oceanic internal wave spectrum at mid and high latitudes. J. Geophys. Res. **107**(C11), 3207 (2002).
[9] Holloway, P.E., Merrifield, M.A.: Internal tide generation by seamounts, ridges, and islands. J. Geophys. Res. **104**(C11), 25937–25951 (1999).
[10] Hurley, D.G., Keady, K.: The generation of internal waves by vibrating elliptic cylinders. Part 2. Approximate viscous solutions. J. Fluid Mech. **351**, 11 (1997).
[11] Jachec, S.M., Fringer, O.B., Gerritsen, M.G., Street, R.L.: Numerical simulation of internal tides and the resulting energetics within Monterey Bay and the surrounding area. Geophys Res. Lett. **33**, L12605 (2006).
[12] Khatiwala, S.: Generation of internal tides in an ocean of finite depth: analytical and numerical calculations. Deep Sea Research, **50**, 3–21 (2003).
[13] Lamb, K.B.: Nonlinear interaction among internal wave beams generated by tidal flow over supercritical topography. Geophys. Res. Lett. **31**, doi:10.1029/2003GL01939 (2004).
[14] Legg, S., Huijts, K.M.H: Preliminary simulations of internal waves and mixing generated by finite amplitude tidal flow over isolated topography. Deep Sea Research-II, **53**, 140-156, 2006.
[15] Lighthill, J.: Waves in fluids. Cambridge University Press (1978).
[16] Marshall, J., Adcroft A., Hill C., Perelman L., Heisey, C: A finite-volume, incompressible navier-stokes model for studies of the ocean on parallel computers. Journ. Geophys. Res. 102:5753–5766 (1997).
[17] MacKinnon, J.A., Winters, K.B.: Subtropical Catastrophe: significant loss of low-mode tidal energy at 28.9 degrees. Geophys. Res. Lett. **32**, L15605, doi:10.1029/2005GL023376 (2005).
[18] Mowbray, D.E., Rarity, B.S.H.: The internal wave pattern produced by a sphere moving vertically in a density stratified liquid. J. Fluid Mech. **30**, 489–495 (1967).
[19] Peacock, T., Echeverri, P., Balmforth, N.J.: An experimental investigation of internal wave beam generation by two-dimensional topography. J. Phys. Ocean. **38**, 235–242 (2008).
[20] Phillips, O.M.: The dynamics of the upper ocean. Cambridge University Press (1966).

[21] Staquet, C., Sommeria, J., Goswami, K., Mehdizadeh, M.: Propagation of the internal tide from a continental shelf: laboratory and numerical experiments. Proceedings of the Sixth International Symposium on Stratified Flows, Perth, Australia, 11-14 December (2006).

[22] Tabaei, A., Akylas, T.R.: Nonlinear Internal Gravity Wave Beams. J. Fluid Mech. **482**, 141–161 (2003).

[23] Tabaei, A., Akylas, T.R., Lamb, K.G.: Nonlinear Effects in Reflecting and Colliding Internal Wave Beams. J. Fluid Mech. **526**, 217–243 (2005).

[24] Thomas, N.H., Stevenson, T.N.: A similarity solution for viscous internal waves. J. Fluid Mech. **54**, 495–506 (1972).

[25] Zhang, H.P., King, B., Swinney, H.L.: Experimental study of internal gravity wvaes genarated by supercritical topography. Physics Fluids **19**, 096602 (2007).

Deep ocean mixing by near-inertial waves

Victor I. Shrira and William A. Townsend

Abstract We consider a novel mechanism of deep ocean mixing caused by breaking of near inertial waves propagating poleward beyond the inertial latitude. On the non-traditional beta plane a noticeable portion of incident inertial waves is not reflected at the inertial latitude but goes through; these waves propagate several hundred kilometers further poleward trapped in three narrowing waveguides. Most of the wave energy passing through becomes trapped into the waveguide adjacent to the ocean bottom. The focus of the paper is on describing the wave evolution in this guide and mixing it causes. First we find an asymptotic analytic solution describing the linear evolution of a wave packet of finite bandwidth taking into account its viscous dissipation. As the wavelength and waveguide width decrease with the distance from the inertial latitude the vertical shear increases sharply. Assuming total mixing in the areas where the Richardson number is less than 1/4 and neglecting the relaxation and turbulent diffusion at the boundaries of the mixed region we find the domain of mixed fluid created by the chosen wave packet. The mixing changes the basic stratification in such a way that in the modified density structure each subsequent packet propagates faster and correspondingly with a weaker spatial decay, thus extending the mixed fluid domain further poleward. The process continues until a balance is reached between the decrease in buoyancy and increase in viscosity inside the mixed domain.

Victor I. Shrira
Department of Mathematics, EPSAM, Keele University, Keele, Staffordshire ST5 5BG, UK
e-mail: v.i.shrira@maths.keele.ac.uk

William A. Townsend
Department of Mathematics, EPSAM, Keele University, Keele, Staffordshire ST5 5BG, UK
e-mail: w.a.townsend@epsam.keele.ac.uk

D. Dritschel (ed.), *IUTAM Symposium on Turbulence in the Atmosphere and Oceans*,
IUTAM Bookseries 28, DOI 10.1007/978-94-007-0360-5_6,

1 Introduction

The existing ocean circulation models heavily depend on the parameterisation of the subgrid motions. To reproduce the existing pattern of global circulation the abyssal basin-average vertical diffusivity K_v should be quite high, which implies existence of intense mixing in the deep ocean [4]. The experimental data suggest much stronger diffusivity near the bottom [9]. The required mixing is widely believed to be provided by internal wave breaking, however, specific mechanisms (apart from the critical reflection by bottom relief) leading to wave breaking have not even been identified. In [2] it was found that near inertial waves pass through the inertial latitude and then tend to focus, primarily, near the bottom. It was then hypothesized that such a focussing of near inertial waves might lead to wave breaking and thus provide the mixing in the deep ocean. In this work we elaborate this idea by developing quantitative description of the processes leading to wave breaking and thus suggest a plausible mechanism of wave breaking in the abyssal ocean. The paper just briefly outlines the mechanism; details of the analytic derivations and discussion of parameter space will be reported elsewhere.

2 Basic Equations and WKB

We start with the Boussinesq equations for a density-stratified viscous fluid on the non-traditional β-plane in a standard Cartesian frame with coordinates x (eastwards), y (northwards) and z (vertical, upwards), with corresponding velocity $\mathbf{u} = (u, v, w)$, reduced pressure p, and buoyancy b. We assume the bottom to be flat. The linearized equations of motion are

$$u_t - fv + \tilde{f}w = -p_x + \nu u_{zz} \tag{1a}$$

$$v_t + fu = -p_y + \nu v_{zz}, \tag{1b}$$

$$w_t - \tilde{f}u = -p_z + b + \nu w_{zz} \tag{1c}$$

$$u_x + v_y + w_z = 0, \tag{1d}$$

$$b_t + N^2(z)w = \kappa b_{zz}, \tag{1e}$$

where N is the buoyancy frequency, ν and κ are the eddy viscosity and diffusivity. The horizontal and vertical Coriolis parameters $\tilde{f}$ and $f = f_0 + \beta y$ are given at a fixed latitude ϕ by

$$(\tilde{f}, f_0) = 2|\Omega|(\cos\phi, \sin\phi), \qquad \beta = \frac{2|\Omega|\cos\phi}{R}, \tag{2}$$

with Ω and R being the Earth's angular velocity and radius respectively. The system has two boundaries, a rigid boundary at the bottom of the ocean $z = 0$ with the no-slip condition $u(0) = v(0) = 0$, and a free surface at the top of ocean of the depth H

where we use the 'rigid lid' approximation, i.e., $w(H) = 0$.

We are primarily interested in poleward propagation of near-inertial waves. Since for such waves with any initially arbitrary wavevector its meridional component tends to become infinite [2], we confine our consideration to strictly meridional wave propagation, that is $\partial_x \equiv 0$. Starting with the linear inviscid problem with no diffusion simplifies the boundary conditions to

$$w(0) = w(H) = 0. \tag{3}$$

By introducing stream-function Ψ defined as

$$v = \Psi_z, \qquad w = -\Psi_y, \tag{4}$$

the system of equations (1a-1e) reduces to

$$\Delta\Psi_{tt} + N^2\Psi_{yy} + f^2\Psi_{zz} + \tilde{f}^2\Psi_{yy} + 2f\tilde{f}\Psi_{yz} + \beta\tilde{f}\Psi_z = 0, \tag{5}$$

while the boundary conditions (3) become

$$\Psi_y(0) = \Psi_y(H) = 0. \tag{6}$$

After Fourier transform with respect to time the system (5, 6) represents a mixed type (Tricomi) type problem with complicated geometry and, correspondingly, there is no standard method of solving it. Nevertheless it is straightforward to find its characteristics for a harmonic in time component. They are plotted in Fig. 1 for a typical oceanic stratification, which gives an idea on the character of wave evolution. Characteristics could be interpreted as wave rays (e.g. [6]). At the inertial latitude some rays are reflected, while some go through. Those which go through are trapped in one of three narrowing waveguides centred at the minima of N. The picture suggests that there is no reflection beyond the inertial latitude. In this paper we examine waves in the bottom wave guide beyond the inertial latitude, while the reflection and propagation in the immediate vicinity of this latitude (shaded in grey) is not considered. In itself the analysis of characteristics carried out for the bottom waveguide in [3] does not allow one to construct the solution. However, the large separation of scales between the inhomogeneity due to the β-plane and the wavelengths under consideration at the core of the beta-plane concept, prompts us to apply the WKB approach.

Consider a near-inertial wave on the non-traditional β-plane ($\tilde{f} \neq 0$) beyond the inertial latitude and assume there are no other large scale ambient wave-motions, leaving the only large scale inhomogeneity to be caused by the meridional variation of the vertical Coriolis parameter f. This inhomogeneity has characteristic length $L \sim \frac{f_0}{\beta} = R\tan\phi \sim R$. As we are interested in waves of much smaller characteristic wavelength $\lambda_0 \ll L$ there is a natural small parameter ε

$$\varepsilon = \frac{1}{l_0 L} \ll 1. \tag{7}$$

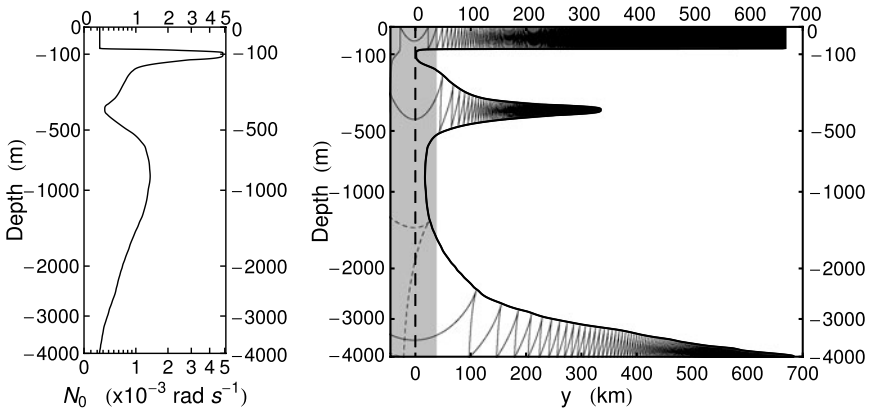

Fig. 1 (a) A typical ocean stratification profile $N(z)$. (b) Characteristics: thin solid – characteristics going through, thin dashed – reflected characteristics, thick solid – boundary of the hypebolicity/ellipticity domains, thick dashed vertical line – inertial latitude. Solution is sought to the right of the grey zone.

where l_0 is the characteristic wavenumber. Rewriting equation (5) in terms of appropriately scaled variables we get

$$\Delta\Psi_{tt} + N^2\Psi_{yy} + f(\varepsilon y)^2\Psi_{zz} + \tilde{f}^2\Psi_{yy} + 2f(\varepsilon y)\tilde{f}\Psi_{yz} = -\varepsilon\beta\tilde{f}\Psi_z. \tag{8}$$

The limit $\varepsilon \to 0$ represents the situation where the Coriolis parameter f ceases to depend upon the meridional coordinate y, and thus becomes the case of the non-traditional f-plane considered in detail in [2]. In the f-plane limit a simple solvable boundary-value problem specifying wavenumber l for a given frequency σ can be found by substituting

$$\Psi = \psi(z, l, \sigma)e^{i(ly - \sigma t + \delta z)}, \qquad \text{where } \delta = \frac{lf\tilde{f}}{\sigma^2 - f^2}. \tag{9}$$

This gives a Sturm-Liouville boundary value problem for ψ:

$$\psi'' + l^2\left[\frac{N^2(z) - \sigma^2}{\sigma^2 - f^2} + \left(\frac{\sigma\tilde{f}}{\sigma^2 - f^2}\right)^2\right]\psi = 0; \qquad \psi(0) = \psi(H) = 0, \tag{10}$$

for a given stratification profile $N(z)$. As we are looking for mechanisms of mixing in the deep ocean, here we consider only the bottom waveguide following [2], where the profile can be approximated by $N^2(z) = N_0^2 + \gamma_1 z$. For this stratification profile the boundary value problem (10) reduces to the Airy equation, then on simplifying the upper boundary condition by moving it to $z = \infty$, we find solution in terms of the Airy function

$$\psi = a_{(\psi)}\mathrm{Ai}\left(\tilde{l}^{2/3}\left[z - \frac{\Delta}{\gamma_1 C}\right]\right), \tag{11}$$

$$\text{where} \quad \tilde{l}^2 = \frac{l^2\gamma_1}{C}, \quad C = f^2 - \sigma^2; \quad \Delta = (f\tilde{f})^2 - (N_0^2 - \sigma^2 + \tilde{f}^2)C,$$

and $a_(\psi)$ is amplitude of the chosen eigenmode [2]. The bottom boundary condition gives the wavenumbers l_n in terms of the zeros of $\mathrm{Ai}(\zeta)$ denoted $-s_n$, where n is the vertical mode number and s_n are known positive constants (e.g. [1], §10.4):

$$l_n = \pm\gamma_1 C^2\left(\frac{s_n}{\Delta}\right)^{3/2}. \tag{12}$$

The group velocity is given by

$$\frac{\partial\sigma}{\partial l} = \frac{\mp\Delta^{5/2}}{\gamma_1\sigma C s_n^{3/2}[4\Delta + 3C(N_0^2 - \sigma^2 + \tilde{f}^2 + C)]}. \tag{13}$$

At the tip of the hyperbolicity domain we have a singularity: $l_n \Rightarrow \infty$; in some vicinity of the singularity the asymptotics in terms of the distance to the singularity $\hat{y}$ acquire the following simple form

$$l_n(y) \sim \hat{y}^{-3/2}, \qquad \frac{d\sigma}{dl} \sim \hat{y}^{5/2}. \tag{14}$$

Importantly these asymptotics imply that the WKB approach becomes more accurate as the wave approaches the singularity, and in the limit when it reaches the singularity the expansion becomes exact! When ε is small but nonzero in equation (8) we can apply a WKB expansion

$$\Psi = \Phi_{n(0)}(z, \varepsilon y)\exp i[\int_{y_i}^{y} l_n(\varepsilon y_1)dy_1 - \sigma t] + \sum_{m,s=1} \varepsilon^m \Psi_{s(m)}(z, \varepsilon y). \tag{15}$$

where y_i is the initial position of the wave. Substituting this into (8) and taking only the n-th mode gives to leading order the f-plane solution (10), while to $O(\varepsilon)$ the orthogonality conditions lead to the conservation of wave action equation which explicitly gives the amplitude of ψ as

$$a_{(\psi)} = a_0\left(\tilde{l}^{-2/3}\int_0^{\infty}[l(N_0^2 - \sigma^2 + \tilde{f}^2) + f\tilde{f}\delta + \tilde{l}^{-2/3}l\gamma_1 z]\mathrm{Ai}(z - s_n)^2 dz\right)^{-1/2}, \tag{16}$$

where a_0 sets the initial amplitude. The small $\hat{y}$ asymptotics for the amplitude near the singularity are

$$a_{(\psi)} \sim l^{1/6} \sim \hat{y}^{-1/4}. \tag{17}$$

It can be shown that these asymptotics provide a good description of wave amplitude evolution over the entire range of the WKB validity. So far we have considered a

single Fourier harmonic inside the waveguide, however, in reality the waves exist in the form of finite bandwidth packets. Since each Fourier component has a singularity at a different position, as the packet moves poleward it will be spread out as its harmonics move towards their own singular point, while at the same time the packet will be vertically focussed by the narrowing waveguide. By adopting the approach by [5] it is possible to show that a packet will become focussed at the singularity of its central frequency, although the harmonic spreading has a restraining effect on the amplitude growth: the small $\hat{y}$ asymptotics for the amplitude of stream function becomes $a_{(\psi)} \sim \hat{y}^{5/4}$. The decrease of $a_{(\psi)}$ does not prevent infinite (albeit slower) growth of velocities and vertical shear.

The inviscid and non-diffusive form of the equations (1a-1e) enabled us to find the dispersion law and amplitude evolution. These results however need to be revisited with viscosity and diffusion taken into account. To find the first order contribution due to the viscous and diffusion terms an asymptotic procedure was applied based upon small characteristic value of the eddy viscosity $\bar{\nu}$ and the diffusivity (presumed to be of the same order). This provided an $O(\nu)$ correction to the frequency. When the Ekman layer at the ocean bottom was also accounted for, this gives an $O(\sqrt{\nu})$ correction to the frequency. We select an initial value of y already at some distance y^* past the inertial latitude so that the WKB expansion becomes valid (at a latitude of 45° with a stratification given by $N_0 = 2.5 \times 10^{-4} s^{-1}$, $\gamma_1 = 4 \times 10^{-10} m^{-1} s^{-2}$ this distance was $\sim 11km$), and set this to be our origin in the y direction. To explore the potential for mixing we calculate the vertical shear and the Richardson number $Ri(z,y)$, $Ri = N^2(z)/(u_z^2(z,y) + v_z^2(z,y))$.

The necessary condition for loss of stability by a density stratified parallel shear flow is $Ri < 1/4$ [7],[8] and, since the waves we are interested in are reasonably close to being a parallel flow, we look for regions with large vertical shear. We make a strong assumption that whenever the Richardson number drops below the critical value the wave breaks and total mixing of the highly sheared domain resulting in complete homogenization of density takes place. We introduce the initial Richardson number by $Ri_0 = Ri(z = 0, y = 0)$. Recall that here $y = 0$ corresponds to the initial position y^* of the wave packet chosen to be at the boundary of the WKB validity range, typically the initial point is about $10km$ past the inertial latitude. Figure 2(a) illustrates meridional evolution of wave parameters. We calculated various amplitudes at the bottom of the ocean ($z = 0$) and normalized them with respect to their initial value at $y = 0$. The inverse Richardson number growth is the fastest but that it is also the first to fall off due to viscous effects. Note that there is a wide range of parameters where the Richardson number is well below the critical value of 1/4 while the nonlinearity parameter is still small, which *a posteriori* justifies the use of linear theory in this range. Figure 2(b) shows vertical dependence of normalized shear on depth and meridional coordinate. The vertical shear of a wavepacket is the highest at the bottom of the ocean for small y; it is in this region we would expect to see wave-breaking and mixing. This is illustrated by figure 3: there is a domain at the bottom of thickness varying from zero to a maximum and then back to zero where this condition is satisfied which we refer to as the 'mixed layer' or 'mixed domain'. From initial examination of parameter space it appears that the thickness

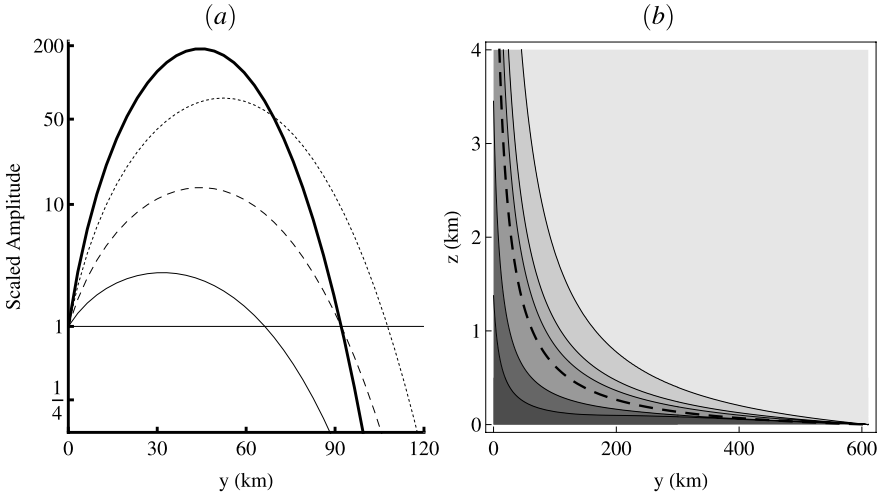

Fig. 2 (a): Amplitudes of the velocities u and v (thin line), vertical shear (dashed line), nonlinearity (dotted line) and inverse Richardson number (thick line) with respect to meridional coordinate y, relative to their initial values at $y = 0$. (b): Distribution of vertical shear normalized with respect to the shear at the bottom of the ocean, $z = 0$. Isolines for the amplitude are 0.99, 0.9, 0.5, 0.1, 0.001 (from bottom to top). The thick dashed black line shows the hyperbolicity condition (the waveguide). The parameter values are: $\phi = 45°$, $N_0 = 2.5 \times 10^{-4} s^{-1}$, $\gamma_1 = 4 \times 10^{-10} m^{-1} s^{-2}$, $\nu = 10^{-5} m^2 s^{-1}$.

of the mixed layer is increased by decreasing the initial Richardson number Ri_0, or decreasing the bottom value of buoyancy frequency N_0. Inside the mixed layer the effect of wave-breaking would homogenize the density, decreasing the local buoyancy frequency to the limit specified by the compressibility, and, crucially, increase the eddy viscosity in the layer. Since the decrease of N decreases the Richardson number for subsequent waves passing through the mixed region, the area of the mixed domain tends to increase, on the other hand, the increased viscosity decreases the wave amplitude and shear, which acts to shrink the mixed domain. To try to understand how this would effect potential wave-breaking we incorporated the mixed domain into our model.

3 Mixed Bottom Layer

We now consider a two layer system with a common boundary at $z = z_0(y)$. In the upper region we have the usual equations of motion (1a-1e) with velocities $\boldsymbol{u} = (u, v, w)$ and a reduced pressure p. In this region N^2 remains unperturbed ($N^2 = N_0^2 + \gamma_1 z$) and we neglect viscosity and diffusion. In the lower 'mixed' layer, again we have equations (1a-1e) but with velocities $\boldsymbol{u} = (\hat{u}, \hat{v}, \hat{w})$, and a reduced pressure $\hat{p}$. The buoyancy is $N(z)^2 = N_1^2 < N_0^2 + \gamma_1 z_0$ where N_1 is constant. The 'rigid lid'

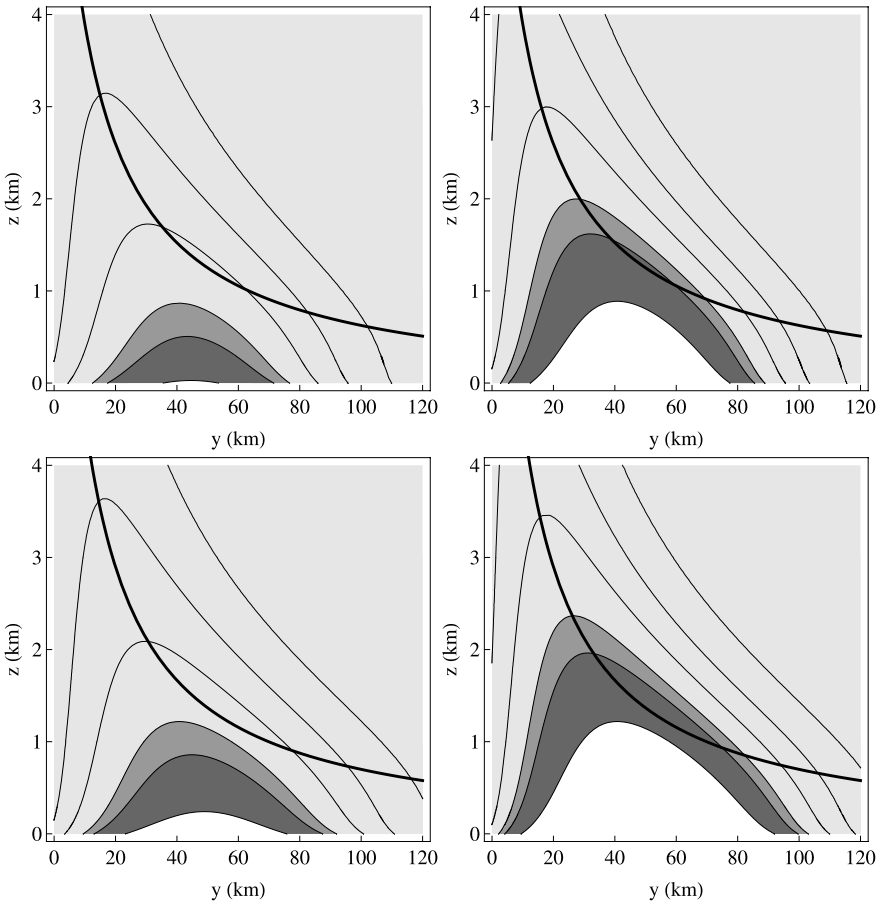

Fig. 3 Contour plots of Ri with isolines for $Ri = 1/4, 1, 2, 10, 10^2, 10^4$ (bottom to top respectively). Left Figures: $R_0 = 40$; Right Figures: $R_0 = 5$; Top Figures: $N_0 = 2.5 \times 10^{-4} s^{-1}$; Bottom Figures: $N_0 = 2 \times 10^{-4} s^{-1}$; All Figures: $\gamma_1 = 4 \times 10^{-10} m^{-1} s^{-2}$, $\nu = 10^{-5} m^2 s^{-1}$.

condition at $z = H > z_0$, and lower boundary at $z = 0$ remain and in addition the usual matching condition is applied at the interface $z = z_0$: the vertical velocity and pressure in both layers should be equal on the boundary, that is

$$w(z_0) = \hat{w}(z_0) \tag{18a}$$

$$p(z_0) = \frac{\rho_{0T}}{\rho_{0B}} \hat{p}(z_0), \tag{18b}$$

where ρ_{0T} and ρ_{0B} are the characteristic density in the top and bottom layers respectively. The equations of motion for the upper layer reduce to the Airy-equation and by extending again the upper boundary condition to infinity give the solution

$$\psi = T_1 \mathrm{Ai}(\hat{z}), \qquad \text{where} \quad \hat{z} = \tilde{l}^{2/3}\left(z + \frac{\Delta}{\gamma_1(\sigma^2 - f^2)}\right), \; T_1 = \text{constant}. \tag{19}$$

The equations for the bottom layer admit a solution of the form $\hat{\psi} = B_1 \sin\lambda z + B_2 \cos\lambda z$, with B_1 and B_2 constant in z, then the application of the bottom boundary condition yields

$$\hat{\psi} = B_1 \sin\lambda z, \qquad \lambda = \sqrt{l^2\left[\frac{\sigma^2 - N_1^2}{f^2 - \sigma^2} + \frac{\sigma^2 \tilde{f}^2}{(\sigma^2 - f^2)^2}\right]}. \tag{20}$$

The matching conditions (18a, 18b) specify the new dispersion relation in the implicit form

$$\tilde{l}^{2/3} \tan\lambda z_0 = \lambda \frac{\mathrm{Ai}(\hat{z_0})}{\mathrm{Ai}'(\hat{z_0})}, \tag{21}$$

where Ai' denotes the derivative of the Airy function Ai with respect to its argument and $\hat{z_0} = \hat{z}$ at $z = z_0$. When $z_0 = 0$ this condition reduces to that of the single layer problem, $\mathrm{Ai}(\hat{z_0}) = 0$. To find the new dispersion relation this equation is solved numerically. The new dispersion found by solving (21) numerically modifies the system in two ways. First, the change in wavenumber l_n affects the amplitude growth of ψ and, crucially, the increase of the group velocity decreases the time it takes for a packet to reach any particular point y. The latter is particularly important since this determines how far poleward the packet could advance before the increased eddy viscosity decreases shear to insignificant levels.

4 Discussion

First we summarize in plain words what has been done and then discuss some perspective directions of further studies.

It is well known that shoaling surface waves almost always break at surf zone because of their shortening and steepening in the process. Our key result is that for near-inertial waves at moderate latitudes a similar 'surf zone' is everywhere: at any point there are near-inertial waves which due to inhomogeneity provided by the beta effect experience shortening and steepening strong enough for wave breaking to occur. Note that the mechanism of wave breaking is entirely different and quite peculiar: waves develop very strong vertical shear remaining essentially linear. This allowed us to describe in great detail the evolution of wave packets (up to the breaking) taking into account all essential factors while remaining within the framework of linearized problem. The greatest uncertainty in our analysis is due to the value of eddy viscosity which is presumed to be constant in time and prescribed. To be on the safe side we took quite large values of viscosity, which nevertheless did not prevent development of strong vertical shear. Therefore our main conclusion about the existence of 'surf zones' at the bottom is quite robust. However the size

of the domain with high shear is sensitive to the value of viscosity and should be treated with caution. It is possible to develop a coupled quasi-linear model where wave evolution remains linear while the eddy viscosity is specified by local time dependent shear produced by the wave; the eddy viscosity will affect slow evolution of wave amplitude and hence shear, thus closing the feedback loop. A lesser but still essential element of uncertainty is the link between the 'initial amplitudes' of wave packets we take as our starting point at a distance y^* past the inertial latitude and the incident inertial waves. A preliminary analysis in terms of characteristics was done in [3], where a share of the incident wave energy going through was estimated to be 10-30%. Our analysis of sensitivity of evolution to the initial Richardson number illustrated by figure 3, where the Richardson numbers were initially one order of magnitude different, suggests that the outcome is robust.

The adopted model of mixing is very basic and relies entirely on the critical Richardson number reasoning. It neglects local adjustment of eddy viscosity to vertical shear and relaxation processes. It seems reasonable to assume that wave breaking which is expected to occur regularly as in the surf zone, makes by far the greatest contribution to mixing. Such a model enables us to find the domain of fluid mixed by breaking and its dependence on relevant parameters. The present model is deterministic. One of the most interesting and relatively straightforward extensions would be to consider mixing caused by random incoming waves. Taking into account relaxation of small scale turbulence would certainly enrich the model. However at the moment it is not clear whether an analytical advance is possible or numerical simulation is the only option. It is worth noting that direct numerical simulation (DNS) is not an easy option: so far even the evolution of a linear wave packet beyond the inertial latitude has not been reproduced numerically. The unresolved difficulty seems to be in ensuring much lower level of numerical viscosity than it is common for other applications. An additional difficulty for DNS is the high sensitivity of the outcome to the parametrization of eddy viscosity. Hence the hybrid models incorporating analytical results and insights of this work but still requiring numerics might prove a perspective way forward.

References

[1] Abramowitz, M., Stegun, I.A.: Handbook of Mathematical Functions. Dover (1965).
[2] Gerkema, T., Shrira, V. I.: Near-inertial waves in the ocean: beyond the "traditional approximation". J. Fluid Mech. **529**, 195–219 (2005).
[3] Gerkema, T., Shrira, V. I.: Near-inertial waves on the "non-traditional" β-plane. J. Geophys. Res. **110**, C01003, doi:10.1029/2004JC002519 (2005).
[4] Garrett, C., St. Laurent, L.: Aspects of deep ocean mixing. J. Oceanogr. **58**, 11–24 (2002).
[5] Gnevyshev, V. G., Shrira, V. I.: Monochromatic rossby wave transformation in zonal flow critical layers. Izv. Atmos. Ocean Phys. **25**, 628–635 (1989).

[6] Harlander, U., Maas, L. R. M.: Characteristics and energy rays of equatorially trapped, zonally symmetric internal waves. Meteorologische Zeitschrift. **15:44**, 439–450 (2006).
[7] LeBlond, P. H., Mysak, L. A.: Waves in the ocean. Elsevier (1978).
[8] Miropol'sky, Yu. Z.: Dynamics of internal gravity waves in the ocean. Kluwer (2001).
[9] Polzin, K. L., Toole J. M., Ledwell J. R., Schmitt R. W.: Spatial Variability of Turbulent Mixing in the Abyssal Ocean. Science **276**, 93–96 (1997).

Part II
Turbulence and Convection

Eddies and Circulation: Lessons from Oceans and the GFD Lab

Peter B. Rhines

Abstract This is a discussion of aspects of the energy-dominant eddies/waves of the global ocean emphasizing their finite-amplitude dynamics in the upper levels of the ocean and their reshaping of the deep branches of the general circulation. We rely heavily on observations which, only in the past few years have achieved the status of a global quasi-synoptic observing system, making possible an increasingly complete understanding of the time-dependent oceans. In stratified oceans and atmospheres a significant fraction of the baroclinic energy is captured in mesoscale structures which resist the classic cascades of geostrophic turbulence toward barotropic (depth-independent) states and thence to larger horizontal scale. Eddies both stir the deep ocean, shape its PV field, transfer surface momentum downward to drive large recirculation gyres, and greatly alter the western boundary currents. In effect, eddies redefine the general circulation.

1 Introduction

Planetary fluids inherit the angular momentum of their planets. Concentrated and diluted, and fragmented into a complex potential vorticity (PV) field, the polar angular momentum controls the circulation under a limited budget of energy. In particular, wherever energy decays, planetary PV takes control of the dynamics and atmospheres and oceans tend to flow along latitude circles. This control is manifested in the 'stiffness' and 'PV elasticity' of rotating fluids which leads to many kinds of wave motion, and to extreme limitation of turbulent mixing. It works most strongly in the vertical, as resistance to stretching of planetary vorticity (the vorticity contributed by the mean rotation of the Earth). In the horizontal the gradient of the vertical component of planetary vorticity, $f = 2\Omega \sin(\text{latitude})$, provides elastic-

Peter Rhines
University of Washington, School of Oceanography, Seattle 98195 WA, USA, e-mail: rhines@uw.edu

D. Dritschel (ed.), *IUTAM Symposium on Turbulence in the Atmosphere and Oceans*, IUTAM Bookseries 28, DOI 10.1007/978-94-007-0360-5_7,

ity which yields Rossby waves. This elasticity is strongly controlling only for large horizontal scales. When PV variations are no longer dominated by their large-scale gradient, the variability evolves as geostrophic turbulence, yet it seems never to be far out of reach of wave dynamics. The time-averaged circulation of the upper ocean (Fig. 1a) corresponds to the large scale PV field, yet both vary greatly beneath the surface. PV is a conservable quantity (conserved following fluid elements in absence of external forcing and dissipation), giving great importance to maps of mean PV. Motivated by theory, we constructed the first extensive PV maps in the early 1980s (McDowell et al. 1982), and yet the interplay of circulation and PV is only now coming clear.

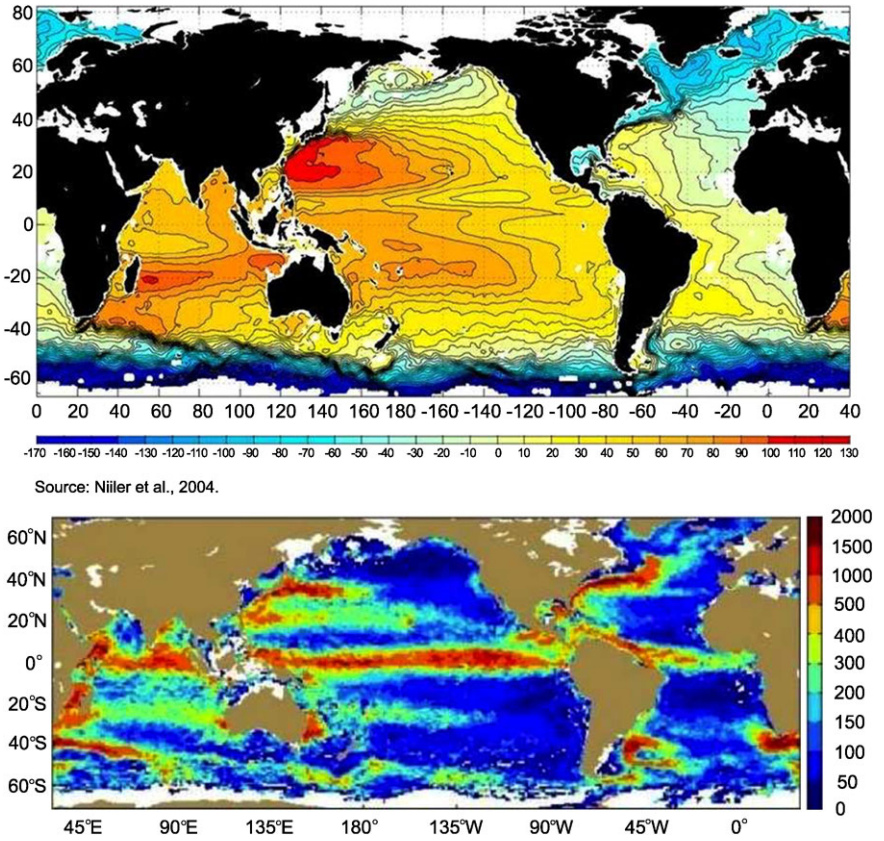

Fig. 1 (a, above) Time-mean surface circulation of the oceans (expressed in cm. of sea-surface elevation, Maximenko and Niiler, 2004; (b, below), eddy kinetic energy ($cm^2 sec^{-2}$) at the ocean surface, averages formed from surface drifting buoy data (Lumpkin, 2003).

Ocean eddies are distinctly smaller in scale than the dominant eddies of Earth's atmosphere (roughly 1/10 as wide, $\sim$ 100km diameter), leading to difficulties in observation and simulation. Yet, we anticipate that their smallness may lead to bulk effects on ocean gyres and global overturning which could be somewhat insensitive to phase and other detail. The mean circulation of the fluid, together with the planetary vorticity, determines curves of constant PV, which cover the nearly horizontal surfaces of constant potential density. If we imagine the energy of the system decreasing toward zero, fluid can then only circulate along these curves of constant mean PV. It is a highly constrained system, in which fluid motion both responds to and reshapes the PV field. Rigid boundaries (the solid Earth) and fluid layers with strong stratification contribute an extra, concentrated contribution, acting as delta-function sheets of PV.

The fluid finds ways of dealing with limited energy and with control by the large-scale PV gradient: for example sculpting PV 'staircases' in the smoothly sloping meridional variation of planetary vorticity, f. PV gradients are concentrated at the 'risers', promoting both long-lived solitary vortices and attendant jet streams on the 'treads' of the staircase. As a result we see numerous zonal jets and semi-permanent eddies on the great gas-giant planets which rotate rapidly and are subject to strong β-control. Weaker β-control exists in Earth's eddy-enhanced atmospheric subpolar jet streams (estimates of globally averaged kinetic energy density are 10^6 J m^{-2} for the atmosphere and 0.8 x 10^4 J m^{-2} for the oceans, Oort et al. 1994). [1] There are other ways to overcome the PV constraint, in particular in the development of intense, 'hard-core', cyclones and anticyclones.

The basic cascades of stratified, rotating turbulence toward large lateral scale and toward barotropic (tall or depth-independent) form (e.g., Rhines, 1977, 1979) can be resisted, and indeed much of the world ocean is dominated by eddies that are neither barotropic nor particularly large in the horizontal. This does not mean, however, that nonlinear effects are negligible. The ocean eddy spectrum takes on three interesting limits: geostrophic turbulence at the mesoscale, sub-mesoscale turbulence enhanced at top and bottom boundaries, and super-mesoscale eddies, actually nonlinear Rossby waves, particularly in the upper half of the water column.

The extensive research into the wave/turbulence dynamics of the energy containing eddies is beyond the scope of this review. However, there is considerable evidence for both nonlinear transformations inherent in the enstrophy cascade, and their limitation by quasi-linear dynamics of Rossby waves/baroclinic instability. In both oceans and atmosphere, topographic PV is strongly active. Solid-Earth topography, like energy, has a broad, red wavenumber spectrum. This acts to scatter energy toward high wavenumber (accelerating the enstrophy cascade) yet also to stabilize energy in topographic/Rossby waves. A primary effect at the mesoscale is the form-stress interaction, in which Rossby-wave drag exerts a westward force on the fluid at scales comparable to or greater than that of the topography. In ocean basins with topographic large-scale PV this becomes a cyclonic force inducing basin-scale circulation. The quasi-geostrophic wave/turbulence problem initially developed for

[1] A 2006 Chapman Conference focused on 'Jets and Annular Structures' is recorded in a highlighted collection of Journal of Atmospheric Sciences (2008); see Baldwin et al. (2008).

the simple β-plane relates not only to the wave/eddy field but also to poleward heat-flux and the formation of the basic stable density stratification. This applies to the atmospheric troposphere (e.g. Schneider, 2005) and, potentially to the ocean, which is usually cast as a problem in laminar overturning with microscopic mixing.

Frontogenesis near the surface and bottom boundaries of the fluid yields the energetic sub-mesoscale (eddy diameters from a few km to a few tens of km). This has become a subject of great interest in the ocean surface layers (e.g. Klein et al., 2008). It emerges in models as lateral resolution is increased. In the 3200 km-wide square ocean basin simulations of Siegel et al. (2001), driven by wind-stress at the surface, there is a factor of ten increase in near-surface eddy kinetic energy at 1.5 km resolution, compared with, say, 25 km resolution. Northward PV flux by near-surface eddies also increases by roughly 50% over this range of lateral resolution. Surface geostrophic turbulence is an idealized limit of this near-boundary, sub-mesoscale turbulence, and was proposed by Bretherton (private communication, 1965) and developed by Blumen (1978) and Held et al. (1995). In this limit a zero-PV interior is slaved to the horizontal advection of density anomalies (a.k.a. delta-function PV anomalies) at the surface of the fluid. Computationally, it is an elegantly simple two-dimensional calculation. More advanced models show that restratification occurs near the surface when ageostrophic velocities allow sloping density surfaces to relax toward the horizon, as in geostrophic adjustment. The observed ocean has some of the characteristics of these three limits:

- near-surface sub-mesoscale eddies with Rossby numbers that are not small (for example ranging from f to $3f$ in the Siegel et al., (op. cit.) simulations)
- mesoscale eddies with large vertical scale, including barotropic eddies (tall mesoscale eddies reaching from top to bottom, steered and possibly generated by the topography of the bottom, particulary prevalent at high, subpolar latitudes where f is strong and stratification is weak), and,
- nonlinear Rossby waves, often manifested as 'super-mesoscale' cores of water and PV propagating westward across subtropical and tropical oceans.

The key distinguishing feature of these three limits is the source of PV structure: at the smallest scale, the PV expressing surface density variations; at the mesoscale the PV relating to the thickness variations and relative vorticity of the mean circulation, and finally the larger eddy scales for which planetary PV (the β-effect) organizes eddy activity. The distinctions between near-surface eddy fields and those filling the rest of the water column carry over to wavenumber spectra which tend to be flat (typically varying like k^{-2}) near the surface and steeply red (typically k^{-3} to k^{-4}) through the interior of the fluid (Klein et al. (op. cit.)).

Eddies in the oceans range widely in amplitude, and this greatly influences the competition between turbulent and wave- dynamics. At the ocean surface we know this field better than anywhere else. Ridges of eddy kinetic energy (Fig. 1b) reflect the major jet-like currents. Secondary maxima may be connected with topographic enhancement, coastal upwelling zones, wind forcing and deep convective forcing at high latitude. Eddy generation is favored also in latitudes of westward upper-ocean flow, where the meridional PV gradient of the ocean gyres can oppose β,

thus allowing baroclinic instability. This may explain the ridges of eddy energy near latitude 20° in most oceans. The lateral sizes of eddy/wave activity also range widely, and are strongly correlated with latitude. Baroclinic instability theory and its generalization as geostrophic turbulence favors scales near the Rossby deformation scale $L \sim L_D = c_0/f \sim NH/f$ or ratio of phase speed c_0 of long gravity waves in the vertical mode of interest, to the Coriolis frequency f. N is the buoyancy frequency and H the vertical height scale of the eddy. L_D decreases strongly toward high latitude, doubly so, as both f^{-1} and N decrease poleward. For this reason, barotropic eddies are more prevalent at high latitude.

Surprisingly, the ratio of kinetic energy in the eddies to that in the time-averaged circulation greatly exceeds unity in the 'quiet' parts of the oceans, whereas the ratio is of order unity in the most energetic jets. More usually, classical turbulence is bounded in amplitude by the mean flow that generates it. This surprise suggests that the Peclét number of the ocean circulation gyres, the ratio Pe = UL_m/κ of mean advection U to eddy stirring (with Taylor Lagrangian diffusivity κ) of some scalar conservable quantity, is not far from unity, even in the 'quiet mid-ocean'. Here L_m is the width of the mean ocean gyre. Maps of this quantity (Rhines & Schopp, 1991) from models agree, estimating Pe $\sim$ 3 to 5 in mid-ocean, somewhat larger in boundary currents. Observations of the wide dispersal of passive chemical tracers throughout gyres support these numbers. Similarly, the nonlinearity parameter, the wave steepness (current speed/phase speed or lateral peak-to-trough particle displacement/wavelength), varies greatly with position and latitude. For barotropic Rossby waves of scale L this is $(U'/\beta L^2)^{1/2}$, U' being the rms horizontal fluid velocity. Baroclinic Rossby waves at the deformation radius scale have phase speed $\beta L_D^2 = \beta N^2 H^2/f^2$, and their wave steepness $U/\beta L_D^2$ varies greatly with latitude as f^{-2}, β and N^2 all decrease poleward. The tropics tend to be wavelike, and higher latitudes to be turbulent for these reasons.

Despite all the study by the fluid dynamics community, and numerous hard-cover monographs and textbooks (some even available on your Kindle) there is little clear insight as to what eddies actually do and how they behave in Nature. Too much of the dialogue on large-scale turbulence ignores the rich observational database. We saw in this symposium debate over basic questions of general ocean circulation: for example: where is the turbulence that brings the dense cold waters of the abyss back to the sea surface in the oceanic meridional overturning circulation? Very recently a global observing system for the oceans has reached full strength. Satellite altimetry provides global coverage of the surface geostrophic circulation each 10 days or so. The ARGO array of 3000 neutrally buoyant, vertically profiling, subsurface floats was completed in November 2007. Symbolic of the diverse array of remarkable instruments drifting, moored, self-propelled, launched or towed from ships, or looking down from Space, the ARGO network and its companion instruments give us global, somewhat synoptic observations of oceanic hydrography (temperature, salinity) and currents, and they begin to provide chemical and biological fields such as dissolved oxygen, chlorophyll and nitrate. Descending down the 10 decades of length scale that mark ocean velocity and scalar property fields (10^4 km to 1 mm) we now have articulate 'cat-scans' of ocean microscale turbulence, the rich texture

of submesoscale eddies and their fine-structure decoration (through geoseismics, optical imaging and microstructure probes on freely falling profiles and gliders).

The 'geography' of PV involves several disparate scales (PV = $(f+\zeta)/h$, where ζ is vertical vorticity and h is the vertical thickness of a layer bounded by two nearby potential density surfaces, with special amendment at solid boundaries). The disparate scales arise from the planetary vorticity (with vertical component f), vertical thickness (h) of the larger gyres and jets of circulation, relative vorticity (ζ) related to zonal currents, and the turbulent PV of eddies and waves themselves. Even in the PV of a turbulent flow there are distinct differences in scale between thickness-PV and relative vorticity-PV, the latter tending to have smaller scale and more localized flux divergence.

2 Deep pathways in the oceanic overturning circulation

The energy flow-chart for the climate 'heat-engine' involves meridional transports of heat and fresh-water. Global meridional overturning circulations of oceans and atmospheres (MOCs) are full of subtlety, and are challenging to theory, models and observations alike. The Coriolis constraint reduces the strength of these circulations, relative to unfettered convection of a non-rotating fluid. Oceans benefit from topographic basins which promote meridional flow without the severe constraint of polar angular momentum conservation: the water can lean on the continents to balance the east-west Coriolis force. The up-down part of the MOC is equally difficult to observe and understand: where do cold, dense waters rise back to the sea surface to close the circulation? Here we have the modest goal of describing one piece of the global oceanic overturning: the southward flow of cold, dense waters from the headwaters of the MOC in the far northern Atlantic and Arctic to the south, joining the southern sources from around Antarctica. This southward flow has long been portrayed as a narrow, deep western boundary current in the 'conveyor belt' idealization of the MOC.

When the eddy form-stress mechanism for transferring momentum vertically through the fluid was understood it became apparent that this is a potent mechanism for driving deep ocean circulation. Form stress is simply the horizontal pressure force (per square m) exerted by fluid on a sloping surface, either sloping bottom topography or a sloping density interface. It yields the general-circulation-scale version of barotropization in fields of geostrophic turbulence. Form-stress is also related to the lateral eddy transport of the thickness part of PV, and has become codified in the Eliassen-Palm momentum flux. In the vicinity of intense jet-like currents form stress drives deep countercurrents and in basin geometries these close to form deep recirculation gyres (Rhines & Holland, 1979).

At the same time stirring by the eddies produces a Lagrangian circulation very different from the laminar models in textbooks. A recent example came from theory to early circulation models and finally to direct Lagrangian observations of Bower et al. (2009). The southward flowing branch of the MOC in the Atlantic forms a clas-

sic western boundary current visible along the continental rise of the US. However this deep artery is not a conveyor belt but is stochastically occupied by cold, dense waters from far north. Deep RAFOS floats, launched in the subpolar latitudes at locations carefully chosen to correspond to the dense outflows from the Labrador Sea, drift like water parcels, yet do not simply follow the western boundary southward (Fig. 2). Instead, many of them recirculate at high latitude before entering the broad gyres of the Newfoundland Basin. They populate the entire western basin of the N. Atlantic, traveling in the recirculations induced by the Gulf Stream overhead. The figure combines 40 float trajectories, all launched near the western boundary near Newfoundland with numerical model simulations showing the widely spread, averaged southward transport across latitude lines (thick solid curves). The circles in the deep western boundary current show by their size the transport of water of far northern origins. At Cape Hatteras (36°N) only 3% of the modeled transport lay in the boundary current, and 0.1% had arrived there along the direct boundary pathway. This picture was anticipated through chemical tracer data (e.g., tritium and CFCs (chlorofluorocarbons); Jenkins and Rhines (1980), Lebel et al. (2008) which show the dense waters to have western boundary current cores, yet also be distributed widely across the western basin).

Eddies affect the deep circulation in many ways. Here we see them drive deep gyres of mean circulation from above, largely by inviscid form stress. Stirring by eddies also forms a stochastic Lagrangian circulation; and, quite separately, the mean PV fields shaped by eddy PV flux (as well as by mean advection) provide continuous pathways for circulation connecting subpolar and subtropical latitudes. In yet another form of eddy/mean-flow interaction, the source of eddy energy comes from instability of the time-averaged circulation, which is favored in regions where the mean PV gradient has opposing directions at different depths.

Wind and buoyancy flux at the sea-surface combine to drive the circulation. Eddy effects cause the wind-driven and buoyancy-driven circulations to interact and overlap in ways unforeseen in classical portrayals of ocean dynamics. In fact, the very definition of ocean circulation requires some acuity in the presence of eddies. There are single Eulerian time-averaged mean velocity and mass fields, yet an infinity of Lagrangian-mean circulations (since the Lagrangian particle trajectories $X(t;X_0,t_0)$ depend on the launch location X_0 and time t_0). Perhaps more relevant to the MOC and climate are the transports of heat, salt, mass and chemical tracers by the velocity field, and these can be displayed on the key phase plane of physical oceanography, the potential temperature/salinity plane (e.g., Bailey et al. 2005).

3 Eddies and Rossby waves in the upper ocean

A dynamic life-cycle which has received much attention is the generation of zonal jets by PV stirring due to mesoscale eddies, and conversely the basic instabilities of jets and boundary currents yielding such eddies. In ocean basins there are other life-cycles of great interest, owing to the gyres of mean circulation which are not

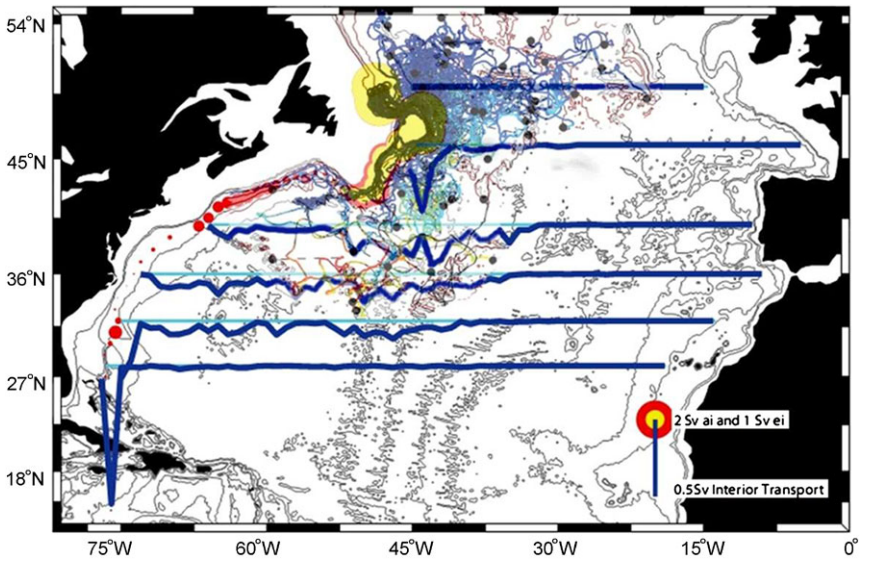

Fig. 2 RAFOS float tractories (chaotic curved trajectories) at the depths of Labrador Sea Water, launched at 700m and 1500m depths at roughly 50°N, at the western boundary of the subpolar Atlantic Ocean (Bower et al., 2009). The floats are dominated by eddy activity, and over time indicate widespread pathways to the south. Numerical simulations with the high-resolution FLAME model (solid blue curves) show the transport of simulated floats offshore of the 4000m isobath in the same region. The transport is distributed across the western one-half of the ocean, carried in eddy-driven gyres of recirculation, yet the flow rejoins the classic western boundary pathway at latitude 27°N, far to the south. Coloured circles indicate transport associated with modeled floats exclusively inshore of the 4000m isobath (ei, yellow), floats moving both inshore and offshore of that isobath (ai, red) where the circle radius is proportional to volume transport.

purely zonal. Kim (1974) and Rhines (1977) showed how meridional mean circulations are baroclinically unstable to zonal-jet-like disturbances which are not inhibited by the β-effect. The simplest example is a baroclinic Rossby wave with purely meridional velocities, either propagating or made stationary on a gentle eastward barotropic flow. The instability evolves toward L_D-scale (Rossby deformation scale-) eddies; some of this energy will barotropize, and the eddies then jump from slow baroclinic to much faster barotropic Rossby wave propagation. Generation of alternating zonal flows can then occur. But if the energy level is not sufficient to be free of β-control (and if the stratification is concentrated in the upper ocean, or if bottom topography is present) the cascade into the barotropic mode is incomplete, and nonlinear baroclinic eddies remain viable for long times. This life-cycle helps us to understand the world-wide existence of something like nonlinear baroclinic Rossby waves somewhat larger in lateral scale than L_D (Chelton et al. 2007). Does β-control arrest turbulence cascades in the baroclinic mode, when $U'/(\beta L_D^2) \sim 1$, as has been demonstrated for barotropic flows? Theiss (2007) argues in favor, apply-

ing familiar wave-steepness/turbulence cascade arguments. Surprisingly, a decisive numerical study does not yet seem to have been made. Yet once closed PV contours have formed (the eddies reaching large-enough amplitude to overcome β) then we know that long-lived westward drifting vortices can occur.

These baroclinic eddies occupy the upper few hundred metres of the world ocean and are clearly visible with satellite altimetry. They were first observed in the MODE and POLYGON experiments of the early 1970s (MODE group, 1978). Temperature and velocity time-series (Fig. 3) show such an eddy passing westward by the central mooring of MODE-1, at 28°N, 70°W. The PV distribution in this same eddy (Fig. 4, McWilliams, 1980) shows the dominance of the thickness component of PV, with markedly smaller contribution from relative vorticity. This helps us to understand the apparently long life of these baroclinic eddies, as tending toward the planetary-geostrophic limit ($L \gg L_D$) in which thickness dominates, PV = f/h_σ where h_σ is isopycnal layer thickness. Maps of ocean-wide PV, for example, are strongly dominated by f/h_σ.

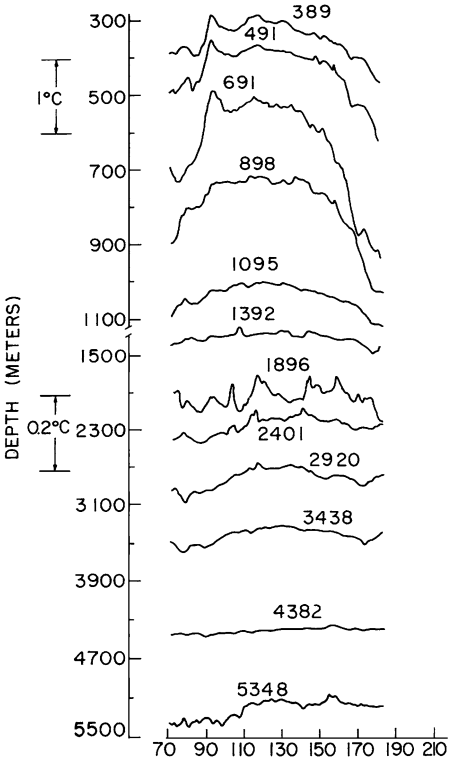

Fig. 3 Time series of temperatures at a fixed mooring on the Hatteras Abyssal Plain, 28°N, 70°W (depths below surface indicated), vs. year-day of 1973. The strong, warm anticylonic eddy is most intense in the upper km of the ocean, yet it excites higher frequency oscillations below.

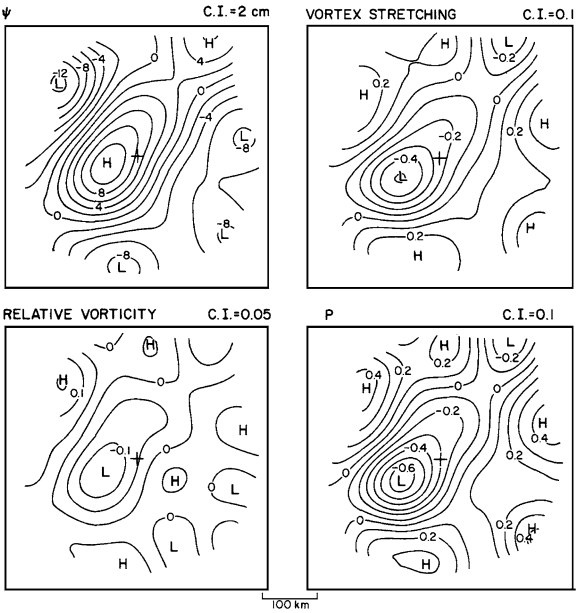

Fig. 4 Potential vorticity (PV) in the MODE-1 eddy (1973 day 140 at 150m depth) in the western N Atlantic. Clockwise from top left: streamfunction, thickness contribution to PV, relative vorticity contribution to PV, total PV. The + sign indicates the position of the central mooring, Fig. 3 from McWilliams (1977).

While detailed evaluation of advection of PV in McWilliams' study suffered from sampling limitations, the PV itself was uncontrovertibly dominated by the eddy scale. This was guaranteed by the diameter of the eddies, which at $\sim$ 250km was significantly greater than L_D. The structure of the eddy differed from a 1st-baroclinic-mode linear Rossby wave in several respects: the wave-steepness was roughly 5 (the ratio U/c); the currents above and below the thermocline were not in anti-phase; the surface density perturbation did not vanish, and, as we shall discuss, the eddy transported mass westward.

A modern reconstruction can be seen (Fig. 5) in eddy-resolving numerical models; here the Japan Earth Simulator fields (OFES), 54 levels, 1/10 degree horizontal resolution, 97-year integration) show the dominance of eddy PV in the upper ocean, yet as one descends the β-gradient (with larger values toward the north) asserts itself in the less energetic deep water (Nakamura & Kagimoto, 2006). In the upper ocean mixed layer (upper left panel), frontal structures appear which are associated with the dominant baroclinic eddies and can be enhanced by wind-forcing.

Modern observations have now revealed similar structures in the surface elevation field (hence in the sub-surface pressure) throughout the world ocean. Altimetry satellites, for example the TOPEX-Poseidon and JASON series from NASA, and European Space Agency satellites, map the elevation field with resolution of a few

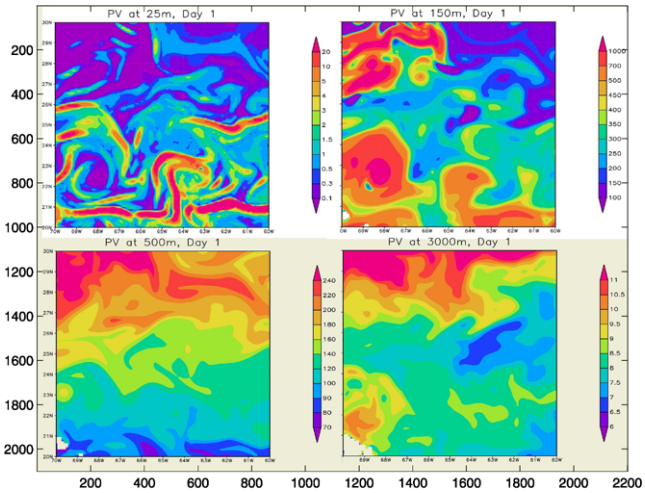

Fig. 5 PV fields at 25m, 150m, 500m and 3000m (clockwise from upper left) in the OFES Japan Earth Simulator ocean model, 20–30°N, 60–70°W (Dr. M. Nakamura, personal communication). This much larger region shows several MODE-type eddies, as well as the background β gradient (PV increasing northward). The strongest eddy, in the southwest region, has size and intensity similar to the observations. PV is wrapped into an isolated core at 150m depth and deeper, while at the surface small-scale fronts intensity round the periphery of the eddies. These eddies move predominantly westward, transporting fluid with them.

cm. vertically, and can resolve eddies with diameter greater than 50 to 100 km, when they are sufficiently energetic. Surface elevation is a geostrophic streamfunction, ψ, for the upper ocean, and animations show a dimpled pattern of ψ that drifts westward almost everywhere, at latitudes less than about 45°. (Fig. 6, Chelton et al., 2007). The major exception to this rule is in the Antarctic Circumpolar Current which is broad and swift, and lies at high latitude: it creates topographically locked stationary eddies and eastward-advected eddies. Even the Gulf Stream, Kuroshio and Somali boundary currents are hard-pressed to advect patterns downstream and exhibit nearly stationary meanders.

The magnificent animation of Fig. 6, showing the world ocean's surface pressure field (extending from 1992 to the present) is full of waves, el Nino events and instabilities as well as the ubiquitous mesoscale eddies/waves. Using two or more satellites, these features are convincingly resolved and there is much verification from *in situ* observations. Of particular relevance here is the likelihood (or near certainty) that eddies with these amplitudes can carry fluid with them. The PV field is dominated by the layer thickness, and using observed vertical structure, the PV features are seen to propagate with the eddies; barring an unlikely form of local forcing and dissipation this tells us that the enclosed cores are indeed moving water. Dramatic verification has been made in a few cases: the MODE-1 eddy was itself the first; RAFOS floats launched by Dr. C. Collins off the California coast became repeatedly trapped in (predominantly anticyclonic eddies) which marched westward

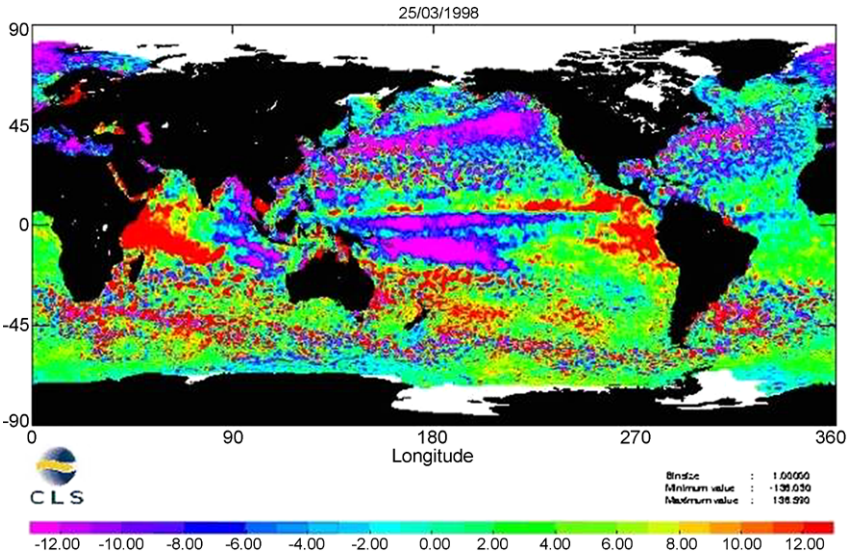

Fig. 6 Sea-surface height anomaly map for 25 March 1998, from the Topex/POSEIDON and ERS-1 satellite altimeters, which provide sampling of the world ocean approximately every 10 days. Chelton et al. analyze the thousands of baroclinic, generally westward propagating eddies visible here. They generally mark strong generation sites or strong mean circulation features. Only in the Antarctic Circumpolar Current and the western boundary currents is the eastward flow fast enough to make the eddies stationary or eastward propagating. A strong el Nino event yields high pressure (warm ocean) in the eastern tropical Pacific.

and were closely identified with altimetrically observed eddies (Chelton, personal communication). In addition there are examples of biological communities embedded in this family of eddies (e.g., Nicholson et al. 2008).

Upper ocean mesoscale eddies propagate westward with speeds close to βL_D^2, the long-wave linear Rossby wavespeed, and they also migrate gradually poleward (if cyclonic) or equatorward (if anticyclonic); Chelton et al. (2007). There is no shortage of theoretical reasons for the small excess in westward propagation speed observed by the satellite altimeters, relative to linear theory. However, the manifestly nonlinear nature of these eddies is a more compelling challenge to theory and modelling. At length scales greater than L_D, long-lived eddies are increasingly likely. With simple layered stratification there are characteristic solutions for Rossby waves in which nonlinearity is retained for the finite layer thickness variations, yet not for ageostrophic effects (e.g., Anderson & Killworth, 1979; Rhines 1989). Typically, for stratification concentrated in the upper half of the fluid, wave steepening occurs at leading, westward side of a warm anticyclone; oppositely for a cold cyclone. The theory allows closed PV cores and eddy transport of fluid, with westward propagation. However these reduced gravity '1 1/2 layer' models ignore the interaction of barotropic and baroclinic modes which are demonstrably active for realistic models of the oceanic stratification (and in observations of the vertical structure of

velocity in mesoscale eddies, Fig. 3b). Typical simulations starting with single isolated baroclinic vortices (e.g., Matsurra 1995, Chassignet & Cushman-Roisin 1991) show lateral radiation of barotropic Rossby waves, including excitation of the deeper layers beneath the vortex as part of this process. Complex evolution of PV occurs, involving shedding of the slowly-flowing outer sheath of the vortex, while the remaining eddy core propagates westward.

Understanding of the generation of the Rossby wave/eddies of the upper ocean remains incomplete. The prime suspect has always been the instability of western boundary currents which themselves dominate the kinetic energy of the ocean. However, these cannot readily explain the westward propagating eddies which seem to require energy sources at latitudes distant from, and far east of, the boundary currents. We know of some sources: radiation from the eastern boundaries of the oceans, from instabilities or seasonal pulsation of the near-boundary circulation, or large-scale flow past topographic features, for example. Just as we see in the MODE-1 observations, models of initially isolated eddies show generation of fast barotropic Rossby waves by the baroclinic vortex, and these are manifested as higher frequencies and phase speeds at deeper levels. LeCointre et al. (2008) show in model studies a variation in mean phase propagation with depth, in this same sense.

In addition, eddy-energy maps (e.g., Fig. 1b) show stripes of high energy appearing in mid-ocean. In the Antarctic Circumpolar Current and detached western boundary currents, bottom topography can create unstable wake vortices. West of Hawaii, there is a ridge of elevated eddy activity that extends across several thousand km. High-resolution wind-stress maps show in fact that Hawaii leaves a wind-wake in the same region, and the island topography itself can shed eddies. Mid-ocean baroclinic instability, particularly in the North- and South Equatorial currents (the westward limbs of the subtropical gyres) has long been suspected. With increasing resolution, models are beginning to yield clear portraits of eddy generation by such forcing.

Finally, we reproduce Lagrangian portraits of flow close to the actual movement of fluid parcels in the deep ocean, from RAFOS floats in the North Atlantic (Fig. 7a) and from ARGO floats in the Pacific (Fig. 7b). Neutrally buoyant floats developed by John Swallow and Thomas Rossby gave us the first animated views of the flow of the deep ocean. It is immediately evident from these figures that this is a turbulent ocean, in which the displacement of marked particles is comparable with the mesoscale size of the dominant eddies, and in which jet-like deep zonal currents emerge at low to moderate latitude. The archive for this data is at Woods Hole Oceanographic Institution, http://wfdac.whoi.edu/.

4 Notes from the GFD Lab

While numerical experiments dominate our field, laboratory simulations of nonlinear Rossby waves provide high spatial resolution, non-hydrostatic effects, interaction of geostrophically balanced circulations with ageostrophic internal waves and

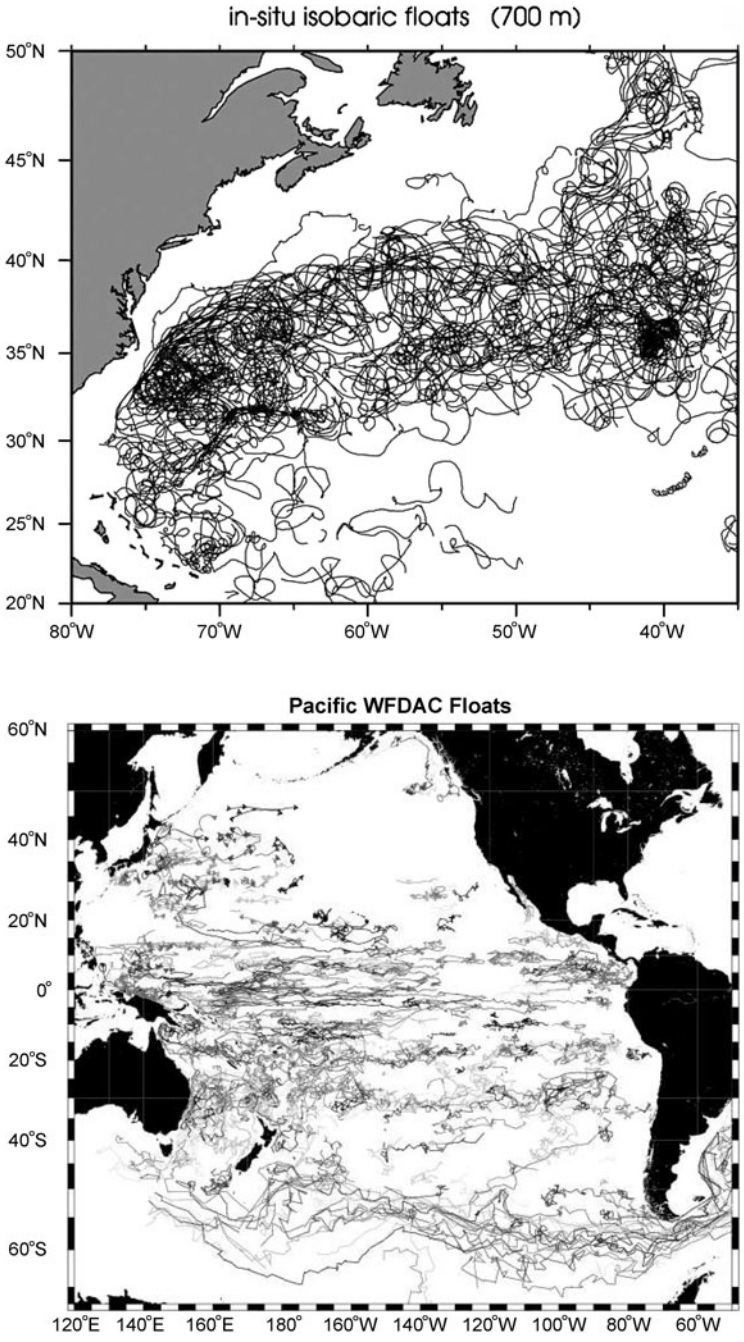

Fig. 7 (a), above: isobaric RAFOS float trajectories at 700m depth in the North Atlantic; (b), below: ARGO floats with depths ranging from 750m to 1550m (mostly between 800 and 900m). Note the prevalence of zonally extended Lagrangian circulation features, and the generally turbulent appearance of the particle trajectories.

submesoscale eddies, and a rich array of turbulent mixing. A new measurement technique, reminiscent of satellite altimetry, yields 'global' fields of fluid surface elevation, hence of surface circulation (Rhines et al., 2007, Afanasyev et al., 2009). In stratified experiments at the Geophysical Fluid Dynamics lab of University of Washington, we include also simultaneous imaging of layer thicknesses which yields baroclinic velocity fields and potential vorticity. In Fig. 8 we show the field of pressure (surface elevation; surface ψ), particle trajectories and vertical vorticity for a flow on a polar β-plane (North Pole at the center). This particular experiment is not a complete ocean analog because the basin-scale depth variation mimicking β is confined to the lower layer. A source of buoyant fluid (fresh water) is injected steadily onto a bed of denser salt water from a point source at 9 o'clock in the figures (at the end of the radial arm). In time this forms a β-plume, that is, a gyre of circulation elongated by Rossby-wave propagation westward from the source. This gyre is unstable to mesoscale eddies which populate its periphery. As the particle trajectories show, the wave steepness of these eddies is near unity. They propagate with barotropic 'roots' as Rossby waves yet participate in fluid transport. The vorticity of the upper layer (Fig. 8e) is accurately recovered, and exhibits intense cores which move with the fluid. Cyclones migrate poleward, anticyclones equatorward as in Nature. Two velocity and ψ cross-sections are plotted in the lower right panels f and g (their locations are marked in Figs. 8b and 8c).

5 Conclusion

Nonlinear Rossby waves in the upper ocean represent a novel mode of ocean circulation: they carry fluid westward in their cores. The Chelton et al., op. cit. analysis of their nonlinear nature is convincing, yet we anticipate a fuller understanding of their generation and interaction with the mean circulation. More generally, we see multiple modes of interaction between eddies and the general circulation, including fully dynamic feedbacks. The geography of the time-averaged PV field, mapped on isopycnal surfaces, together with its top and bottom boundary singular-sheets, is a key control over, and consequence of, these feedbacks. Despite arguments that the atmospheric circulation is not far from quasi-linear dynamics (e.g. Schneider et al., op. cit.) we find the ocean to depend on geostrophic turbulence in many ways. The linear/nonlinear interplay in the atmosphere itself can be essential even where the enstrophy cascade is not active. Further progress may come quickly, from the newly established global observing system recently put into place, and from a wide spectrum of innovative measurement techniques already in the field. We now have the observational and model-based tools with which to gain a much more complete understanding of the ocean circulation and its variable climate.

Acknowledgements This work is funded by the National Science Foundation Physical Oceanography Program and the NASA Ocean Surface Topography Science Team. My thanks to many collaborators and the small but intense community who think about PV.

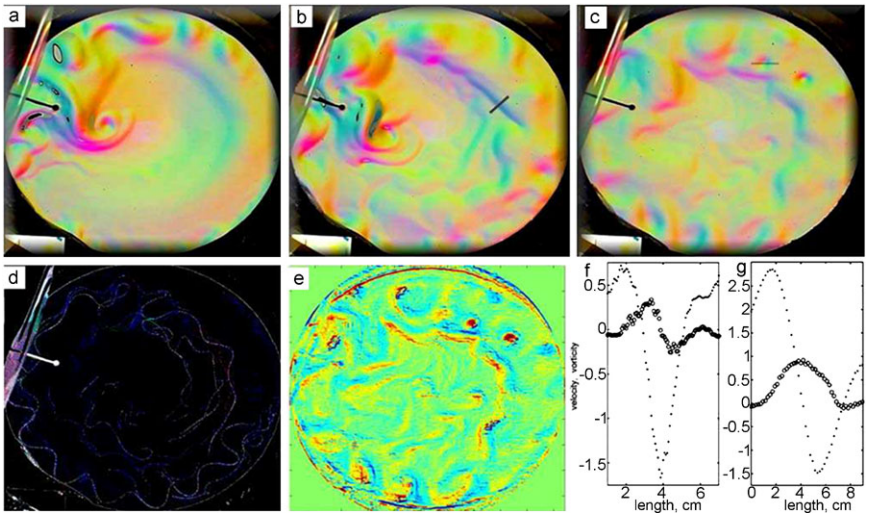

Fig. 8 Circulation on a laboratory polar β-plane observed (as fluid surface elevation) from above with optical altimetry. The source is at 10 o'clock. (a): Large vortices formed by baroclinic meanders are slowly moving along the wall of the tank in the clockwise direction. The Northern flank of the beta-plume is visible as a jet-like flow. (b): The plume extends to the entire tank. Small scale jets are formed. (c): Two small eddies (at 1 and 2 o'clock) are pinched-off from the jet, t = 380 s (125 rotations of the table). (d): Traces left by particles floating on the surface during the interval of 100 s. (e): Relative vorticity field. (f): Velocity (points) and vorticity (circles) profiles measured along the line across the jet as shown in plate b. (g): Profiles of y-component of velocity and vorticity along the line parallel to the x-axis through the centre of the frontal eddy visible at 2 o'clock in plate c. (Afanasyev et al. 2009).

References

[1] Afanasyev YD, Rhines PB, Lindahl EG (2009) Velocity and potential vorticity fields measured by Altimetric Imaging Velocimetry in a rotating two-layer fluid. Exps in Fluids. doi:10.1007/s00348-009-0689-3

[2] Anderson DLT, Killworth PD (1979) Nonlinear propagation of long Rossby waves. Deep-Sea Res 26:1033-1050

[3] Bailey D, Rhines PB, Hakkinen S (2005) Pathways and formation of North Atlantic Deep Water in a coupled ice-ocean model of the Arctic-North Atlantic Oceans. Clim Dyn. doi:10.1007/s00382-005-0050-3

[4] Baldwin M, Rhines PB, Huang H-P, McIntyre ME (2007) The jet-stream conundrum. Science 315: 467-468

[5] Blumen W (1978) Uniform potential vorticity flow, I. J Atmos Sci 35: 774-783

[6] Bower AS, Lozier MS, Gary SF, Bōning C (2009) Interior pathways of the North Atlantic meridional overturning circulation. Nature. doi:10.1038/nature07979

[7] Chassignet E, Cushman-Roisin B (1991) On the influence of the lower layer in the propagation of ocean eddies. J Phys Oceanogr 21: 939-957
[8] Held I, Pierrehumbert RT, Garner ST, Swanson KL (1995) Surface quasi-geostrophic dynamics. J Fluid Mech 282: 1-20
[9] Jenkins WJ, Rhines PB (1980) Tritium in the deep North Atlantic Ocean, Nature 286: 877-880.
[10] Keffer T (1983) The ventilation of the world ocean: the potential vorticity field. J Phys Oceanogr 15: 509-523
[11] Kim K (1978) Instability of baroclinic Rossby waves; energetics in a two-layer ocean. Deep Sea Res 25: 795-814
[12] Klein P, Hua B-L, Lapeyre G, Capet X, Le Gentil S, Sasaki H (2008) Upper ocean turbulence from high-resolution 3-D simulations. J Phys Oceanogr 38: 1748-1763
[13] Lebel DL, Smethie WM, Rhein M, Kieke D, Fine RA, Bullister JL, Min D-H, Roether W, Weiss RF, Andrie C, Smythe-Wright D and Jones EP (2008) The formation rate of North Atlantic Deep Water and Eighteen Degree Water calculated from CFC-11 inventories observed during WOCE. Deep-Sea Res I, 55: 891-910
[14] Lecointre A, Penduff T, Cipollini P, Tailleux R and Barnier B (2008) Depth dependence of westward-propagating North Atlantic features diagnosed from altimetry and a numerical 1/6°model. Ocean Sci 4: 99-113
[15] Lumpkin R (2003) Decomposition of surface drifter observations in the Atlantic Ocean. Geophys Res Lett. doi:10.1029/2003GL017519
[16] McDowell S, Rhines PB, Keffer T (1982) North Atlantic potential vorticity and its relation to the general circulation, J. Phys. Oceanogr. 12: 1417-1436
[17] McWilliams J (1977) Maps from the Mid-Ocean Dynamics Experiment: Part II. Potential vorticity and its conservation. J Phys Oceanogr 6: 828-846
[18] Matsuura T (1995) The evolution of frontal-geostrophic eddies in the ocean. J Phys Oceanogr 25: 2298-2318
[19] Maximenko NA, Niiler PP (2004) The Global Ocean: A 10-year portrait of the near-surface circulation. IPRC Climate, 4: 4-5
[20] MODE Group (1978) The Mid-Ocean Dynamics Experiment. Deep-Sea Res 25: 859-910
[21] Nakamura M, Kagimoto T, (2006) Potential vorticity and eddy potential enstrophy in the North Atlantic Ocean simulated by a global eddy-resolving model. Dyn Atmos Oceans 41: 28-59
[22] Nicholson D, Emerson S, Eriksen CE (2008) Net community production in the deep euphotic zone of the subtropical North Pacific gyre from glider surveys. Limnology & Oceanogr 53: 2226-2236
[23] Oort A, Anderson LA, Peixoto JP (1994) Estimates of the energy cycle of the oceans. J Geophys Res 99(C4): 7665-7688
[24] Rhines PB (1977) The dynamics of unsteady currents. In: Goldberg ED (ed) The Sea, V6, Wiley-Interscience, New York
[25] Rhines P (1979) Geostrophic turbulence. Ann Revs Fluid Mech 11: 404-441

[26] Rhines, PB (1989) Deep planetary circulation over topography: simple models of mid-ocean flows. J Phys. Oceanogr 19: 1449-1470
[27] Rhines PB, Holland WR (1979) A theoretical discussion of eddy-driven mean flows. Dyn Atmos Ocean 3: 289-325
[28] Rhines PB, Schopp, R (1991) Wind-driven circulation: theory and quasi-geostrophic simulations for non-symmetric winds. J Phys Oceanogr 21: 1438-1469
[29] Rhines PB, Lindahl EG, Mendez AH (2007) Optical Altimetry: a new method for observing rotating fluids with applications to Rossby waves on a polar beta-plane. J Fluid Mech 572: 389-412
[30] Schneider T, Walker CC (2005) Self-organization of atmospheric macroturbulence into critical states of weak nonlinear eddy-eddy interactions. J Atmos Sci 63: 1569-1586
[31] Siegel A, Weiss JB, Toomre J, McWilliams J, Berloff P, Yavneh A (2001) Eddies and vortices in ocean basin dynamics. Geophys Res Lett 16: 3183-3186
[32] Theiss J (2006) A generalized Rhines effect and storms on Jupiter. Geophys Res Lett. doi:10.1029/2005GL025379

Observations on Rapidly Rotating Turbulence

P A Davidson, P J Staplehurst and S B Dalziel

Abstract Experiments on rapidly rotating turbulence have been reported in recent years in which the Rossby number, Ro, drifts down towards unity as the energy of the turbulence decays [1; 2]. The experiments were performed in a large vessel, approximately 35 integral scales in each direction. Moreover, any mean flow was carefully suppressed and so the resulting motion constitutes a good approximation to homogeneous turbulence. In line with other experiments, and certain numerical simulations, four robust phenomena were observed: (i) when Ro reaches a value close to unity, columnar eddies start to form and these eventually dominate the large, energy-containing scales; (ii) during the formation of these columnar eddies, the integral scale parallel to the rotation axis grows linearly with time; (iii) more cyclones than anticyclones are observed; and (iv) the rate of energy decay is reduced by rotation. The experiments also show that, despite the fact that $Ro \sim 1$, the columnar eddies form through simple linear wave propagation, in which inertial waves pump energy along the rotation axis. In this paper we explain: (i) why columnar vortices form in such experiments; (ii) why linear behaviour dominates the dynamics in [2], even though $Ro \sim 1$; and (iii) why cyclones are more frequently observed than anticyclones. We also re-examine the energy decay data in [2] and show that, to a reasonable approximation, it takes the form $u^2 \sim (\Omega t)^{-1}$. We offer one possible explanation for this behaviour.

1 Introduction

We consider rapidly-rotating turbulence in which the fluctuating velocity in the rotating frame, $\mathbf{u}$, is smaller than, or of the order of, $|\boldsymbol{\Omega}|\ell$, where $\boldsymbol{\Omega} = \Omega\hat{\mathbf{e}}_z$ is the bulk rotation vector and ℓ a suitably defined integral scale. It is well known that such turbulence is characterised by the presence of large columnar eddies aligned with

University of Cambridge, Department of Engineering, Trumpington Street, Cambridge, CB2 1PZ, UK, e-mail: pad3@eng.cam.ac.uk

D. Dritschel (ed.), *IUTAM Symposium on Turbulence in the Atmosphere and Oceans*, IUTAM Bookseries 28, DOI 10.1007/978-94-007-0360-5_8,

the rotation axis [1]–[5], and there has been much discussion as to the mechanism by which these columnar structures form. The various theories differ in detail but all agree that inertial waves play an important role. Nearly all theories focus on the case $Ro = u/\Omega\ell \ll 1$ and suggest that anisotropy results from a weak non-linear coupling of the waves (so-called resonant triads), operating over a long period of time [6]–[9].

However, a quite different, and simpler, explanation for the growth of the columnar eddies was put forward in [1]. It too is posed in the context of $Ro \ll 1$, but does not require non-linearity. Rather, it relies on the idea that eddies can elongate along the rotation axis by radiating energy in the form of linear inertial waves. This leads to the prediction, which can be tested in the laboratory, that the eddies, and hence the integral scale parallel to $\boldsymbol{\Omega}$, will elongate at a rate set by the group velocity of inertial waves. The idea is the following. Consider unforced turbulence which decays from an initial condition composed of a sea of spatially compact blobs of vorticity (eddies). This is a reasonable idealisation of an experiment in which the fluid is stirred up by a grid and then left to itself. For $Ro \ll 1$, each blob of vorticity present in the initial condition will spontaneously radiate energy in the form of inertial waves, and that energy will propagate in a direction set by the group velocity,

$$\mathbf{c}_g = \pm 2\mathbf{k} \times (\boldsymbol{\Omega} \times \mathbf{k})/|\mathbf{k}|^3. \tag{1}$$

Now a blob of vorticity of arbitrary shape should yield, on being Fourier transformed, an energy distribution which varies in an arbitrary fashion across the wavevectors, $\mathbf{k}$. Since the orientation of $\mathbf{c}_g$ depends on $\mathbf{k}$ in accordance with 1, we might anticipate that the energy of each eddy will disperse in all directions, showing no particular preference to propagate along the rotation axis, and so no tendency to elongate the eddy into a columnar vortex. However, it was pointed out in [1] that this dispersion of energy is subject to certain integral constraints, and that consequently, it is not quite as random as might at first be thought. In particular, it was noted that, within the framework of linear dynamics ($Ro \ll 1$), the axial components of linear and angular impulse of a vortex blob, which are measures of the linear and angular momentum of the eddy, are confined for all time to the cylindrical region of space which circumscribes the vortex at $t = 0$. In short, the axial components of linear and angular momentum can disperse along the rotation axis only. This, in turn, constrains the way in which energy can radiate away from a blob of vorticity, focussing the dispersion of energy onto the rotation axis. Thus each vortex blob present in the initial condition will spontaneously convert itself into a columnar structure through linear wave propagation, with the length of each columnar eddy growing at a rate set by 1, i.e. $\ell_z \sim \delta\Omega t$, where δ is the initial scale of the blob.

It turns out that this process is exactly what is observed in the experiments of [2], and we shall review briefly the theory of [1] in §2 and the experiments of [2] in §3. Curiously, though, the theory of [1] was developed for $Ro \ll 1$, whereas the experiments of [2] show columnar growth via linear wave propagation at $Ro \sim 1$. It is natural to ask why a low-Ro theory persists in practice up to $Ro \sim 1$. We shall provide an explanation for this in §4, as well as for the observed asymmetry between

cyclones and anti-cyclones. Finally, in §6, we re-examine the energy decay data of [2] and show that, to a good approximation, it takes the form $u^2 \sim (\Omega t)^{-1}$. We offer one possible explanation for this behaviour.

2 How Columnar Eddies Form at Low *Ro*

Let us start by summarizing the linear theory of [1], which offers a simple explanation for the growth of columnar structures at low Ro. Consider the initial value problem consisting of a localised blob of vorticity sitting in an otherwise quiescent, rapidly-rotating fluid. Let the characteristic scale of the blob be δ and a typical velocity be u. If $Ro = u/\Omega\delta \ll 1$ then the inertial force in the rotating frame, $\mathbf{u}\cdot\nabla\mathbf{u}$, is much weaker than the Coriolis force, $2\mathbf{u}\times\boldsymbol{\Omega}$, and the governing equation of inviscid motion can be linearized to give

$$\frac{\partial \mathbf{u}}{\partial t} = 2\mathbf{u}\times\boldsymbol{\Omega} - \nabla(p/\rho). \tag{2}$$

The subsequent motion then consists of a spectrum of linear inertial waves whose group velocity is dictated by the initial distribution of $\mathbf{k}$ in accordance with 1. Thus the energy will disperse in all directions with a typical speed of $|\mathbf{c}_g| \sim \Omega\delta$. However, this radiation of energy is subject to a powerful constraint, which systematically favours dispersion of energy along the rotation axis. Let V_R be a cylindrical volume of radius R and infinite length that encloses the vorticity field $\boldsymbol{\omega}$ at $t = 0$; the so-called tangent cylinder. Then it is shown in [1] that the axial component of the angular impulse, $\frac{1}{3}\int [\mathbf{x}\times(\mathbf{x}\times\boldsymbol{\omega})]_z\, dV$, which is equal to the angular momentum held in the tangent cylinder, $\int_{V_R} [\mathbf{x}\times\mathbf{u}]_z\, dV$, is conserved for all time. In short, angular momentum can disperse along the rotation axis only.

This constraint systematically biases the dispersion of energy. For example, as the energy radiates to fill a volume whose size grows as $(c_g t)^3 \sim (\delta\Omega t)^3$, we would expect that conservation of energy requires the velocity outside the tangent cylinder to fall as $|\mathbf{u}| \sim |\mathbf{u}_0|(\Omega t)^{-3/2}$. However, inside the tangent cylinder the angular momentum is confined to a cylindrical region of volume, $c_g t\delta^2 \sim \Omega t\delta^3$, and so the characteristic velocity inside the cylinder falls more slowly, as $|\mathbf{u}| \sim |\mathbf{u}_0|(\Omega t)^{-1}$. It follows that the energy density inside the tangent cylinder is significantly greater than that outside, and so the dominant influence of inertial wave radiation is to spread the energy of the vortex along the rotation axis. (If the eddy happens to have zero angular impulse, we arrive at exactly the same conclusions by considering the conservation of linear impulse.) Moreover, these two scalings, $|\mathbf{u}| \sim |\mathbf{u}_0|(\Omega t)^{-1}$ inside V_R and $|\mathbf{u}| \sim |\mathbf{u}_0|(\Omega t)^{-3/2}$ outside, can be confirmed by detailed calculation using stationary phase.

A simple, almost trivial, example illustrates the point. Suppose our initial condition consists of

$$u = \Lambda r \exp\left[-\left(r^2+z^2\right)/\delta^2\right]\hat{\mathbf{e}}_\theta \tag{3}$$

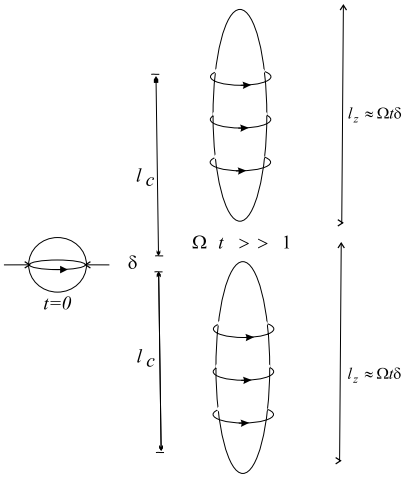

Fig. 1 An initial blob of vorticity converts itself into a pair of columnar eddies (Taylor columns) via inertial wave propagation, $Ro \ll 1$.

in cylindrical polar coordinates, where Λ as a measure of the initial vortex strength. Then 2 yields the axisymmetric wave equation

$$\frac{\partial^2}{\partial t^2}\left[r\frac{\partial}{\partial r}\frac{1}{r}\frac{\partial \Gamma}{\partial r}+\frac{\partial^2 \Gamma}{\partial z^2}\right]+(2\Omega)^2\frac{\partial^2 \Gamma}{\partial z^2}=0, \tag{4}$$

where $\Gamma = ru_\theta$. This may be solved using a Hankel-cosine transform, which yields

$$u_\theta \approx \Lambda\delta\int_0^\infty \kappa^2 e^{-\kappa^2} J_1\left(\frac{2\kappa r}{\delta}\right)\left\{\exp\left[-\left(\frac{z}{\delta}-\frac{\Omega t}{\kappa}\right)^2\right]+\exp\left[-\left(\frac{z}{\delta}+\frac{\Omega t}{\kappa}\right)^2\right]\right\}d\kappa, \tag{5}$$

where J_1 is the usual Bessel function and $\kappa = k_r\delta/2$. Evidently, the kinetic energy disperses along the z-axis forming two columnar structures of radius δ and length $\ell_z \sim \delta\Omega t$, and whose centres are located at $z = \pm\delta\Omega t$. This is illustrated in figure 1. Of course these two lobes of vorticity are just transient Taylor columns. The precise form of 5 for $\Omega t \gg 1$ may be found by insisting that the arguments in the exponentials remain of order unity at $\Omega t \to \infty$. At location $z = \delta\Omega t$, for example, we find

$$u_\theta(t\to\infty) \approx \Lambda\delta(\pi^{1/2}/e)J_1(2r/\delta)(\Omega t)^{-1}, \tag{6}$$

yielding $u_\theta \sim \Lambda\delta(\Omega t)^{-1}$ inside the tangent cylinder and $u_\theta \sim \Lambda\delta(\Omega t)^{-3/2}(r/z)^{-1/2}$ outside the cylinder, in line with the discussion above.

Now consider an initial condition consisting of many such eddies randomly but uniformly distributed in space. It is readily confirmed (see [2]) that, for $Ro \ll 1$, the two-point velocity correlation $Q_\perp(\mathbf{r}) = \langle \mathbf{u}_\perp(\mathbf{x}) \cdot \mathbf{u}_\perp(\mathbf{x}+\mathbf{r}) \rangle$ takes the form

$$Q_\perp \approx Q_\perp^{(s)} + \frac{1}{2}\langle \mathbf{u}^2 \rangle \int_0^\infty \kappa^3 e^{-\kappa^2} J_0\left(\frac{2\kappa r_\perp}{\delta}\right) \left\{ \exp\left[-\left(\frac{r_{//}}{\delta} - \frac{2\Omega t}{\kappa} \right)^2 \right] + \exp\left[-\left(\frac{r_{//}}{\delta} + \frac{2\Omega t}{\kappa} \right)^2 \right] \right\} d\kappa$$

where $\kappa = k_\perp \delta/2$, $\perp$ and $//$ indicate components perpendicular and parallel to the rotation axis, and $Q_\perp^{(s)}$ is a steady contribution to $Q_\perp$ which need not concern us here. The time-dependent part of the correlation is centred on $r_{//} \sim \pm \delta \Omega t$ and its characteristic axial length-scale grows as $\ell_z \sim \delta \Omega t$, as shown schematically in figure 2. Evidently $Q_\perp$ mimics, albeit in a statistical sense, the behaviour of the individual eddies shown in figure 1.

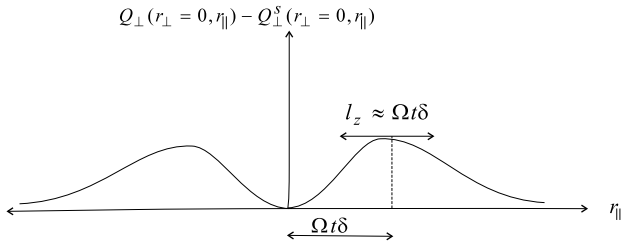

Fig. 2 Schematic illustration of the time-dependent term in the autocorrelation Q for $Ro \ll 1$.

For $\Omega t \gg 1$ the autocorrelation $Q_\perp$ is self-similar if $r_{//}$ is scaled by $2\Omega\delta t$, which admits the simple physical interpretation that all of the eddies grow in the axial direction at the rate $\ell_z \sim \delta \Omega t$. It is readily confirmed that the parallel velocity correlation $\langle \mathbf{u}_{//}(\mathbf{x}) \cdot \mathbf{u}_{//}(\mathbf{x}+\mathbf{r}) \rangle$ behaves in exactly the same way, as do the equivalent two-point vorticity correlations. In [2] it is argued that this behaviour is not particular to the model eddy described by 3, but rather generalises to any kind of eddy; i.e. in all cases we would expect the autocorrelations to be self-similar at large times when $r_{//}$ is normalised by $2\Omega\delta t$. We may think of this as the hallmark of energy dispersion by linear inertial waves propagating from a sea of compact vortex blobs.

Note, however, that it is important in this analysis that we start with spatially compact blobs of vorticity, which is typical of the vorticity field behind a grid. It is this particular initial condition which provides an arrow of time and ensures that we move from spherical-like objects to columnar structures. This is important, because many numerical simulations have initial conditions in which the phase information

is scrambled, so that there is no phase coherence, and hence no coherent structures in physical space. Such atypical initial conditions may behave quite differently.

3 The Experimental Evidence at $Ro \sim 1$

We now turn to the experiments of [2]. Here Ro drifts down towards unity as the energy of the flow decays. The high initial value of Ro ensures that no waves are generated by the grid used to create the turbulence, and so those waves which do appear arise from the turbulence itself. The experiments were performed in a large vessel, 35 integral scales across, and any mean flow was suppressed so that the resulting motion is a good approximation to homogeneous turbulence. Four robust phenomena were observed:

- when $Ro = u/\Omega\ell$ reaches a value close to unity, columnar eddies start to form and these eventually dominate the large, energy-containing scales;
- during the formation of these columnar eddies, the integral scale parallel to $\boldsymbol{\Omega}$ grows linearly in time, $\ell_z \sim \ell_0 \Omega t$, where ℓ_0 is the initial integral scale;
- more cyclones than anticyclones are observed, as in other experiments;
- the rate of energy decay is reduced by rotation.

We shall discuss items (iii) and (iv) shortly. Here we focus on the first two observations. The fact that the integral scale grows as $\ell_z \sim \delta\Omega t$ is highly suggestive that the columnar eddies form by linear wave propagation, and not by resonant triad interactions. This is perhaps surprising, since $Ro \sim 1$. In order to check this hypothesis, two-point autocorrelations where measured as a function of $r_{//}$ and t. This was done for four different experiments which had varying values of $\boldsymbol{\Omega}$ and ℓ_0, but were otherwise similar. According to linear theory, the autocorrelations from all four experiments and at all times in each experiment should collapse onto a single universal curve, provided $r_{//}$ is normalised by $\Omega\ell_0 t$. This is exactly what was found, so there is no doubt that the columnar vortices seen in [2] were formed by linear wave propagation, despite the fact that $Ro \sim 1$.

Note, however, that it is only the large energy-containing vortices which form columnar vortices. Most of the enstrophy, on the other hand, is held in much smaller vortices. Moreover, since $Ro \sim 1$ based on the large scales, the effective Rossby number for these smaller enstrophy-containing eddies will be large. This suggests that we have two types of dynamics occurring simultaneously in the turbulence: the large eddies form columnar structures through linear wave propagation, but these columnar eddies are immersed in a sea of smaller vortices which continue to evolve in a highly non-linear way. Of course, the anisotropy created at the large scales by linear inertial wave propagation can then feed non-linearly into the smaller eddies, because these sit in the shadow of the large columnar vortices and so are subject to a strain field whose axial length scale grows as $\ell_z \sim \ell_0 \Omega t$.

4 Why Linear Behaviour at $Ro \sim 1$?

Let us now consider the curious observation that linear wave propagation can persist up to a Rossby number of $Ro \sim 1$. A sequence of numerical simulations were undertaken in [10] to investigate this very point, in which a single eddy was allowed to evolve in the presence of background rotation. In the rotating frame the eddy had an initial condition very similar to 3 and the Rossby number was defined as $Ro = |u_{\max}|/2\Omega\delta$. A wide range of initial values of Ro were considered, from 0.1 to 4.0, and both cyclones and anticyclones were computed. For small Ro the eddies evolved into columnar structures as shown in figure 1, and of course there is no difference between the behaviour of cyclones and anticyclones in the linear regime. At high Ro, on the other hand, the vortices burst radially outward under the influence of the centrifugal force, generating a secondary flow which sweeps all of the vorticity into a thin axisymmetric vortex sheet. The sheet then thins exponentially fast [11]. This is illustrated schematically in figure 3. Evidently, the fate of a vortex is very different depending on whether the flow is dominated by linear inertial waves or by non-linear dynamics.

Perhaps the most surprising aspect of the computations is that the transition from almost purely linear to fully non-linear behaviour is abrupt. In the case of cyclones the transition occurs in the narrow range $1.4 < Ro < 3.0$, with columnar vortex formation below $Ro = 1.4$ and centrifugal bursting for $Ro > 3.0$. The equivalent range for anticyclones is also surprisingly narrow, $0.4 < Ro < 1.6$. Of course these findings relate to a very particular initial condition, but they do at least illustrate how quasi-linear inertial wave propagation can persist up to Rossby numbers of $Ro \sim 1$, which is consistent with the experiments of [2].

5 Why a Cyclone-Anticyclone Asymmetry?

The results of [10] are also interesting from the point of view of the observed dominance of cyclones over anticyclones. Notice that the transition range of Ro is different for cyclones and anticyclones, with the anticyclones requiring a lower value of Ro to form columnar structures. It is argued in [10] that this is not just an artefact of the particular initial condition used, but is in fact a generic feature of cyclones and anticyclones. The point is this: centrifugal bursting is driven by regions in which, in an inertial frame of reference, Rayleigh's discriminant is negative, $\partial\hat{\Gamma}^2/\partial r < 0$. (Here $\hat{\Gamma}$ is the angular momentum in the inertial frame, $\hat{\Gamma} = ru_\theta + \Omega r^2$.) The physical significance of the criterion $\partial\hat{\Gamma}^2/\partial r < 0$ is most readily understood in terms of the well-known analogy between swirling and stratified fluids, in which $\partial\hat{\Gamma}^2/\partial r < 0$ corresponds to heavy fluid imbedded within a region of light fluid [10]. In any event, loosely speaking, the numerical simulations in [10] show that columnar vortices form provided that, everywhere in the initial condition, we satisfy $\partial\hat{\Gamma}^2/\partial r > 0$. Conversely, the vortex will burst radially outward if there is a significant region in which $\partial\hat{\Gamma}^2/\partial r < 0$. Moreover, it is shown in [10] that, if we consider a sequence of

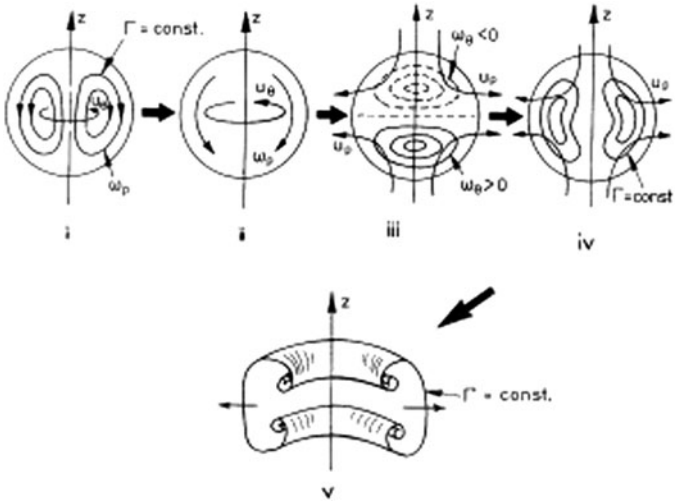

Fig. 3 Schematic illustration of the radial bursting of a vortex under the influence of the centrifugal force. The vortex generates a secondary poloidal flow which sweeps all of the vorticity into a thin axisymmetic vortex sheet. The sheet then thins exponentially fast. $Ro \gg 1$. (i) Initial condition, (ii) generation of azimuthal vorticity by differential rotation, (iii) poloidal motion, (iv) poloidal motion sweeps the angular momentum radially outward, (v) eventually a vortex sheet forms

initial conditions in which Ro increases progressively from $Ro \ll 1$ up to $Ro \sim 1$, anticyclones will exhibit regions of negative $\partial \hat{\Gamma}^2/\partial r$ before cyclones. In short, the fact that the transition range of Ro noted in [10] is lower for anticyclones than cyclones is not particular to initial condition 3, but rather is a generic feature of anticyclones.

Let us now return to the experiments of [2]. Initially, we have a high value of Ro, but as Ro drifts down towards $Ro \sim 1$, columnar eddies start to appear. From the asymmetry described above, we might expect the first columnar structures to be cyclones, with significantly lower values of Ro needed to generate anti-cyclonic columns. Note, however, that while this cartoon is consistent with the experimental evidence, several other explanations for the dominance of cyclones have been put forward (see, e.g. [12]).

6 The Rate of Energy Decay

We conclude by discussing the rate of energy decay in rotating turbulence, which is known to be suppressed by the rotation. It is shown in [13] that, subject to certain caveats, such as the spectral tensor, Φ_{ij}, taking the form $\Phi_{ij}(k \to 0) \sim k^2$, homogenous turbulent flows which are statistically axisymmetric posses the Loitsyanky-like invariant

$$I = -\int r_\perp^2 Q_\perp(\mathbf{r}) d\mathbf{r} = \text{constant} \tag{7}$$

This includes MHD, stratified and rotating turbulence. If the large scales in such a flow are self-similar, and they usually are, then this requires $u_\perp^2 \ell_\perp^4 \ell_{//} =$ constant, where $\ell_\perp$ and $\ell_{//}$ are suitably defined transverse and longitudinal integral scales. Moreover, we have already seen that, once the Rossby number falls below $Ro \sim 1$, $\ell_{//}$ grows as $\ell_{//} \sim \ell_0 \Omega t$. It follows that, in freely-decaying, rapidly-rotating turbulence, $u_\perp^2 \ell_\perp^4 \ell_0 \sim (\Omega t)^{-1}$. This is interesting because the decay data of [2], which has been replotted in figure 4, seems to follow a power law reasonably close to $u_\perp^2 \sim (\Omega t)^{-1}$. Given that $\ell_\perp$ does not change significantly during the rapid growth of $\ell_{//}$, this is reasonably consistent with $u_\perp^2 \ell_\perp^4 \ell_0 \sim (\Omega t)^{-1}$.

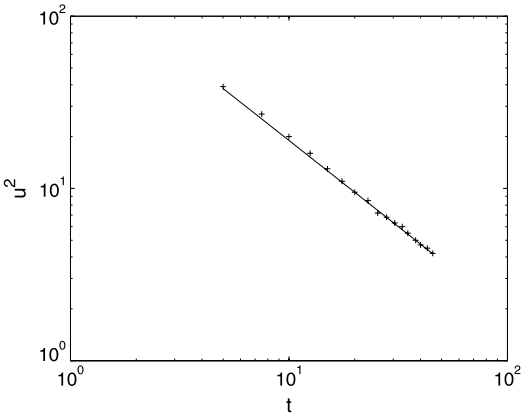

Fig. 4 Plot of energy versus time from the experiments of [2]. The solid line is $u^2 \sim (\Omega t)^{-1}$

References

[1] Davidson, P.A., Staplehurst, P.J. & Dalziel S.B., 2006, On the evolution of eddies in a rapidly rotating system. *J Fluid Mech.* **557**, 135-144.
[2] Staplehurst P.J., Davidson P.A. & Dalziel S.B., 2008, Structure formation in homogeneous freely decaying rotating turbulence. *J. Fluid Mech.* **598**, 81-105.
[3] Hopfinger, E.J., Browand, F.K. & Gagne, Y., 1982, Turbulence and waves in a rotating tank. *J. Fluid Mech.* **125**, 505-534.
[4] Morize, C., Moisy, F. & Rabaud, M., 2005, Decaying grid-generated turbulence in a rotating tank. *Phys. Fluids* **17**, 095105.
[5] Morize, C. & Moisy, F., 2006, Energy decay of rotating turbulence with confinement effects. *Phys. Fluids* **18**, 065107.
[6] Waleffe, F., 1993, Inertial transfers in the helical decomposition. *Phys. Fluids A* **5** (3), 667-685.

[7] Smith, L.M. & Waleffe, F., 1999, Transfer of energy to two-dimensional large scales in forced, rotating three-dimensional turbulence. *Phys. Fluids* **11** (6), 1608-1622.

[8] Smith, L.M. & Lee, Y., 2005, On near resonances and symmetry breaking in forced rotating flows at moderate Rossby number. *J. Fluid Mech.* **535**, 111-142.

[9] Cambon, C., Mansour, N.N. & Godeferd, F.S., 1997, Energy transfer in rotating turbulence. *J. Fluid Mech.* **337**, 303-332.

[10] Sreenivasan, B. & Davidson, P.A., 2008, On the formation of cyclones and anticyclones in a rotating fluid. *Phys. Fluids* **20** (8), 085104.

[11] Davidson, P.A., Sreenivasan, B. & Aspden, A.J., 2007, Evolution of localized blobs of swirling or buoyant fluid with and without an ambient magnetic field. *Phys. Rev. E* **75**, 026304.

[12] Gence, J.-N. & Frick C., 2001, Naissance des correlations triple de vorticite dans une turbulence homogene soumise a une rotation. *C. R. Acad. Sc. Paris, Ser. IIB* **329**, 351-362.

[13] Davidson, P.A., 2004, Turbulence, an introduction for scientists and engineers, *Oxford University Press*.

Equilibration of Inertial Instability in Rotating Flow

Daan D.J.A. van Sommeren, George F. Carnevale, Rudolf C. Kloosterziel and Paolo Orlandi

Abstract Unstable vortices in a rotating environment may breakup due to the combined effect of inertial and barotropic instabilities. Recent advances in the theory of inertial instability of vortices provide a prediction of the equilibrated state if inertial instability acts alone. This prediction combined with what is known about barotropic instability gives the possibility of predicting the end state of a vortex breakup subject to both inertial and barotropic instability.

1 Introduction

Through a series of laboratory experiments, Kloosterziel and van Heijst (1991) explored the breakup and restabilization of freely evolving unstable vortices in a rotating flow. Although the breakup of unstable anticyclones involved a highly three-dimensional turbulent stage, in the end the effect of rotation dominated and the final by-products of the breakup were combinations of stable monopolar, dipolar and tripolar vortices with the axes of the vortices aligned along the axes of the ambient rotation. These experiments were performed in a rotating tank of water. The initial vortex was created by placing a hollow cylinder within the tank, with its axis aligned

Daan D. J. A. van Sommeren
Technische Universiteit Eindhoven,
Eindhoven, the Netherlands, e-mail: d.d.j.a.v.sommeren@student.tue.nl

George F. Carnevale
University California San Diego, La Jolla, CA, USA, e-mail: gcarnevale@ucsd.edu

Rudolf C. Kloosterziel
University of Hawaii, Honolulu, HI, USA, e-mail: rudolf@soest.hawaii.edu

Paolo Orlandi
Università di Roma, "La Sapienza," Rome, Italy, e-mail: orlandi@kolmogorov.ing.uniroma1.it

D. Dritschel (ed.), *IUTAM Symposium on Turbulence in the Atmosphere and Oceans*,
IUTAM Bookseries 28, DOI 10.1007/978-94-007-0360-5_9,

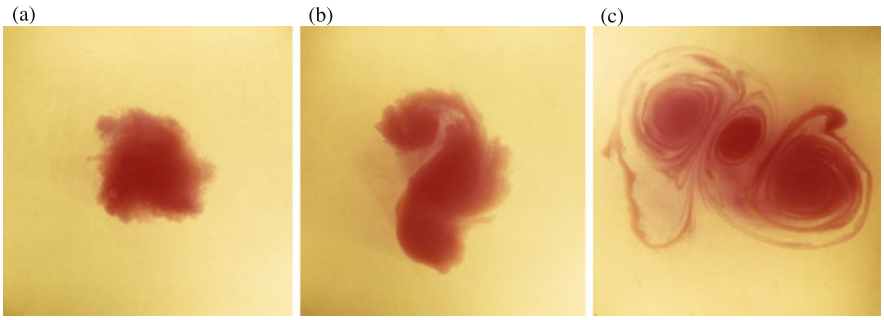

Fig. 1 Vortex breakup leading to a tripole in a laboratory experiment. The evolution takes place in 30 cm of water in a rotating tank. The photographs are taken from above with a camera mounted in the rotating frame on the axis of rotation.

along the axis of rotation. The water in the cylinder was stirred anticyclonically, dye was added for visualization, and then the cylinder was removed vertically, thus releasing the vortex. The subsequent evolution was then photographed from above by a camera mounted in the rotating frame of the tank. In figure 1, we see the results of such an experiment. In panel (a) we see the early stage of the breakup of the vortex in which the flow is very three-dimensional. As time evolves, the ambient rotation suppresses vertical motion and the flow becomes more two dimensional. In panel (c) the flow has organized into a tripolar vortex with an anticyclone in the center and two cyclones for satellites. Another example is shown in figure 2 where the final result is a pair of dipoles (compact cyclone-anticyclone pairs) moving away from each other. Kloosterziel and van Heijst (1991) hypothesized that the complex three-dimensional evolution of the unstable anticyclones was a result of combined inertial (i.e. centrifugal) and barotropic instabilities. Three-dimensional numerical simulations by Orlandi and Carnevale (1999) confirmed this hypothesis. At that point, the theory of barotropic instability of vortices, essentially a two dimensional process, had already been highly developed, and it became clear that barotropic instability was responsible for the final phase of the breakup that produced the monopolar, dipolar and tripolar by-products. It was also demonstrated numerically that it was centrifugal instability that led to the intense vertical overturning motion that created the initial turbulent phase of breakup, and that this phase primed the flow for subsequent barotropic instability. However, a theory of the long term tendency of the inertial instability was lacking, and this prevented prediction of the combined effects of the two instabilities. Recently Kloosterziel et al (2007) returned to this problem and have provided a theory of saturation of inertial instability that fills the gap. We are now in a position to predict the outcome of the breakup of the vortices under certain circumstances based on the combination of the theory of inertial instability and simple two-dimensional simulations of barotropic instability.

In their pure form, these instabilities are not fully three-dimensional. The barotropic instability is an instability on horizontal shear and can be understood in terms of two-dimensional dynamics in a plane perpendicular to the ambient rotation axis. Inertial instability is an axisymmetric instability producing perturbations symmet-

Fig. 2 Vortex breakup leading to two dipoles.

ric about the axis of the main vortex. The relevant features of how these instabilities evolve in pure form is discussed in sections 2 and 3. In section 4, we will propose and test a way of combining those theories to yield a prediction for the final state resulting from the breakup of a given unstable anticyclone under fully three-dimensional dynamics.

2 Pure Barotropic Instability

The criterion for barotropic instability was originally given by Rayleigh (1880) for planar flows. This is a necessary criterion that requires the vorticity to have an extremum somewhere in the flow (Rayleigh's inflection point theorem, see e.g. Drazin and Reid, 1984). The generalization to a circularly symmetric vortex is straightforward and requires that the radial gradient of vorticity vanish somewhere in the flow. We are directly concerned with isolated vortices (i.e. vortices with zero net circulation). Such vortices, necessarily having both positive and negative relative vorticity, always satisfy the criterion for barotropic instability. A simple model of a zero circulation vortex that is amenable to analytical progress from the point of view of stability is the two-patch model consisting of an inner core of constant vorticity and an annulus of opposite signed vorticity. This model was explored with linear stability theory by Flierl (1988). Through normal-mode analysis, he was able to give growth rates for various azimuthal modes. He demonstrated that if the outer annulus is sufficiently broad, the flow is stable, even though the Rayleigh necessary criterion for instability is satisfied. Thus there is a threshold for instability and this involves the size of the jump in vorticity between the core and the annulus. Kloosterziel and Carnevale (1992) confirmed this by considering the extremal properties of a linear combination of the total energy and angular momentum. Carton et al (1989) studied the stability of a family of zero-circulation anticyclones with smooth vorticity profile which in non-dimensional form is

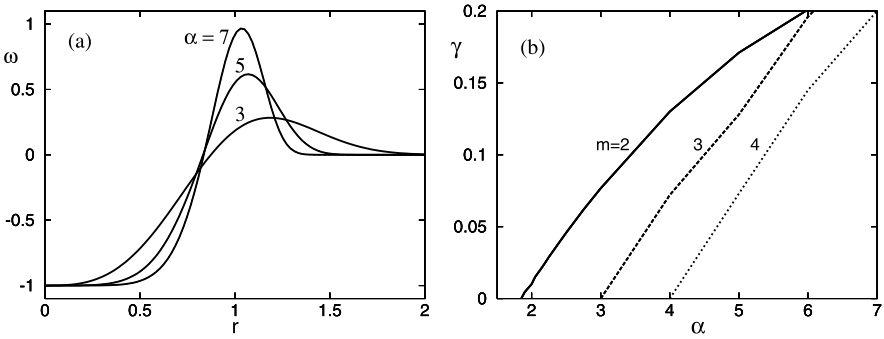

Fig. 3 (a) Profiles of vorticity for different α. (b) Growth rate for azimuthal modes m =2,3,4.

$$\omega = -(1 - \frac{1}{2}\alpha r^{\alpha})e^{-r^{\alpha}}, \tag{1}$$

where r is the radial distance from the center of the vortex. This family is parameterized by α which is known as the steepness parameter. The vorticity distribution for this family is shown in figure 3a for a few values of α. The higher the value of α, the higher are the gradients of vorticity on each side of the peak.

Linear stability analysis was used to calculate the growth of perturbations of azimuthal wavenumber m (Carton et al, 1989; Carnevale and Kloosterziel, 1994). There are no growing modes for $\alpha \lesssim 1.85$. As α is increased above this critical value, the $m = 2$ mode is the first to go unstable. The instability of this mode leads to tripole formation. As α is increased further, higher azimuthal modes become unstable. The growth rates of the first three unstable azimuthal modes are shown in figure 3b, drawn from data taken from Kloosterziel and Carnevale (1999). The result of this succession of an increasing number of unstable modes with increasing α is that the evolution is increasingly more complex with higher α. Because barotropic instability is two-dimensional, it is easily simulated numerically. The results of the instability for any profile and any initial perturbation are readily predicted by numerical simulation. For small-scale small-amplitude initial perturbations, the vortex evolves into a tripole for $1.85 \lesssim \alpha \lesssim 3$ (Carton and Legras, 1994; Kloosterziel and Carnevale, 1999). For higher values, the vortex can go through a remarkable array of forms depending on how many azimuthal modes are unstable. The final result is typically made up of monopoles, dipoles and tripoles. Although Carnevale and Kloosterziel (1994) demonstrated that a quadrapole is also possible, this is very weakly stable and rarely observed as a final state (Kloosterziel and Carnevale, 1999).

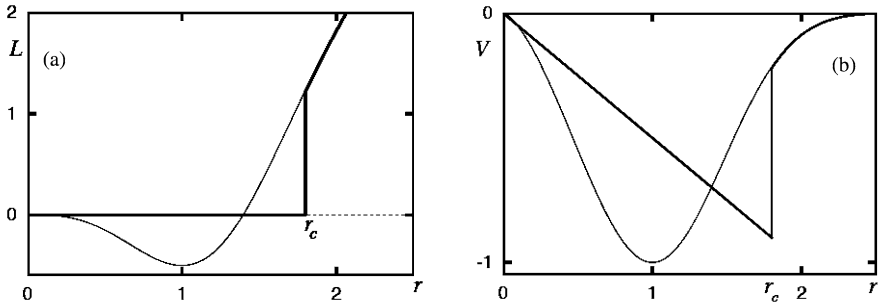

Fig. 4 (a)The construction used to determine the new angular momentum resulting from inviscid mixing of momentum for an anticyclone. The thin curve is the angular momentum of the original anticyclonic vortex. The thick curve is the equilibrated angular momentum. (b) The azimuthal velocity field based on the equilibrated angular momentum shown in panel (a).

3 Pure Inertial Instability

Inertial instability of a vortex in ideal form is an axisymmetric flow problem. The instability appears as rings of perturbation vorticity that surround the main vortex. The necessary and sufficient criterion for centrifugal instability is that the magnitude of the absolute angular momentum decreases somewhere in the flow (Rayleigh, 1916; Kloosterziel and van Heijst, 1991). The absolute angular momentum is $L = r(V + \Omega r)$ where V is the azimuthal velocity of the flow, Ω the ambient rotation rate, and r the radial distance from the center of the vortex. Inertial instability will occur in the inviscid case if and only if $\mathrm{d}L^2/\mathrm{d}r < 0$ somewhere in the flow. This is an inviscid criterion; sufficiently high viscosity (small Reynolds number) can prevent the instability from developing.

In Kloosterziel et al (2007), we studied the unfolding of inertial instability and the subsequent evolution of the vortex. We were trying to understand the tendency of the inertial instability acting alone. In order to isolate the effects of this instability from all others, we ran axisymmetric simulations. The simulations were run long enough to see the linear instability saturate by non-linear effects and the restabilization of the vortex.

Through a series of such simulations, we were able to deduce general rules for predicting the final state of a vortex that underwent inertial instability. The effect of the instability is to redistribute angular momentum in such a way that the resulting vortex is inertially stable. In some sense, this is obviously necessary, yet the form that the final profile of angular momentum would take and, in particular, the radial range over which the angular momentum would be distributed were not obvious *a priori*. The initial instability region is the radial range over which $\mathrm{d}L^2/\mathrm{d}r < 0$. However, the rib vortices that grow from the instability propagate beyond the boundaries of this region. Through the synthesis of the results of all of our simulations, we obtained a method for predicting, in the high Reynolds number limit, the final velocity

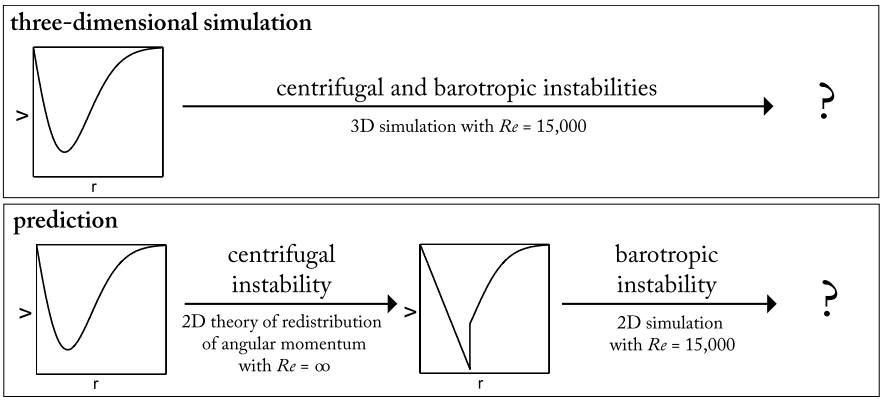

Fig. 5 Schematic showing the basics of the prediction method proposed here.

profile with a simple rule based on total absolute angular momentum conservation. This prediction can be understood in terms of the diagram shown in figure 4a. The effect of the instability is to thoroughly mix the negative absolute angular momentum with the positive from the axis of the vortex out to a point $r = r_c$ that is just as far as necessary to make the total or net absolute angular momentum within that radius zero. For any initial given anticyclonic profile $V_0(r)$, the value of r_c can determined from the following formula:

$$\int_0^{r_c} L_0(r) r \mathrm{d}r = 0 \tag{2}$$

where $L_0(r) = r(V_0(r) + \Omega r)$.

The prediction then is that for inviscid flow the inertial instability will be stabilized with the flow reaching a distribution such that $L(r) = 0$ for $0 < r < r_c$, while $L(r) = L_0(r)$ for $r_c < r$. This profile for L is shown as the dark line in figure 4a. The corresponding prediction for the equilibrated velocity field is

$$\begin{aligned} V(r) &= -\Omega r \qquad 0 < r < r_c \\ &= V_0(r) \qquad r_c < r. \end{aligned} \tag{3}$$

The profile for the equilibrated V is shown as the dark line in figure 4b.

4 Full 3D Simulation vs. Prediction

Now that we finally have 'theories' for the equilibration of both barotropic and inertial instability, we can try to put the both of these together to predict the outcome of a fully three-dimensional representation of the breakup of a vortex that involves both instabilities. The situation that is most amenable for this kind of prediction would be the case in which the vortex is initially barotropically stable but inertially un-

stable. This would test the scenario proposed by Kloosterziel and van Heijst (1991) and Orlandi and Carnevale (1999) in which there is a fast inertial instability that transforms the flow into a barotropically unstable flow after which two-dimensional processes tear the vortex apart creating the final combinations of monopoles, dipoles and tripoles. Since we do not have an analytic prediction for the result of barotropic instability for a general unstable profile, we will use a two-dimensional simulation as a substitute. Thus the overall prediction is obtained by first taking an initial velocity profile and determining the result of inertial instability acting alone by using equation (3). Then that inertially equilibrated profile, with an added random small-scale perturbation, is used as the basis for a two-dimensional simulation of the barotropic instability acting alone. Our program is schematically represented in figure 5. The top part of the figure indicates the 3D simulation, the bottom the prediction method consisting of the analytic prediction for the result of inertial instability followed by the application of 2D simulation of the barotropic instability to obtain the resulting profile. We then compare the results to see how faithful the prediction can be. For this study we will consider a vortex from the family of vortices introduced in section 2 above.

In equation (1), we gave a non-dimensional form of the vorticity field for this family. The dimensional form of the velocity profile can be written as

$$V(r) = \frac{\alpha}{2}\mathscr{U}\rho e^{(-\rho^{\alpha})}, \tag{4}$$

where $\rho = r/\mathscr{L}$, $\mathscr{L}$ is the length scale of the vortex, and $\mathscr{U}$ is the signed velocity amplitude. We define the Rossby and Reynolds numbers for this flow as

$$\mathrm{Ro} = \mathscr{U}/f\mathscr{L} \quad \text{and} \quad \mathrm{Re} = \mathscr{U}\mathscr{L}/\nu, \tag{5}$$

respectively, where $f = 2\Omega$ is the Coriolis parameter.

As explained in section 2, this profile is barotropically stable for $\alpha \lesssim 1.85$. For the rest of the paper, we will consider only the case with $\alpha = 1.8$. The initial condition for this problem is barotropically stable, although not far from the barotropic stability boundary. As explained in section 3, the flow will be inertially unstable where $\mathrm{d}L^2/\mathrm{d}r < 0$. For the anticyclonic profile with $\alpha = 1.8$, this condition can only be met for $\mathrm{Ro} < -1$. We have performed many three-dimensional simulations sweeping through a range of Rossby numbers. The three-dimensional numerical simulations were performed using a finite difference code in cylindrical geometry (see Orlandi, 2000 for details). The code allows coordinate stretching in the radial direction, and this stretching was used to maximize the resolution in the region $0 < r/\mathscr{L} < 2$, where most of the important evolution takes place. The domain has a maximum radius at $r/\mathscr{L} = 6$. There was no stretching in the azimuthal or vertical directions. The 3D simulations reported here are based on a resolution of 128 points for each coordinate. The simulations are performed with $\mathrm{Re} = 15000$. For the barotropic part of the prediction, we used the same cylindrical code but in a two-dimensional mode. The resolution in the radial and azimuthal directions was kept as in the fully three-dimensional simulations. For the two-dimensional simulations,

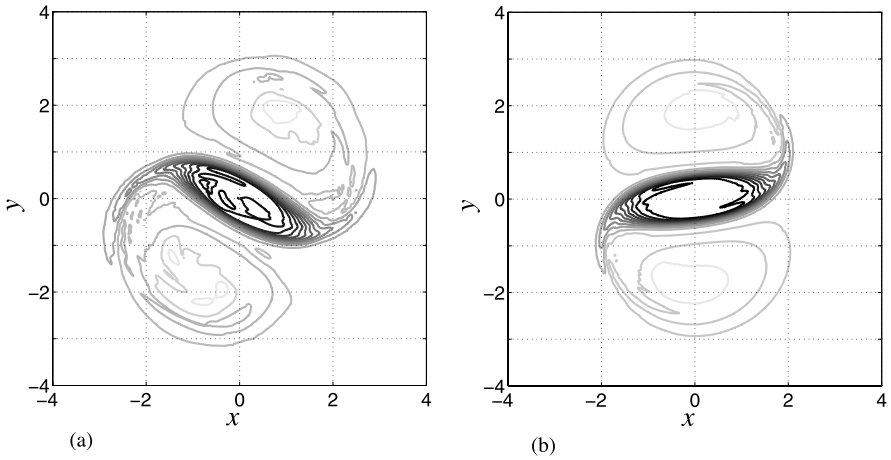

Fig. 6 Comparison of the results of the three-dimensional simulation with the prediction. (a) Vorticity field at the midplane at time $t = 160f^{-1}$ in the fully three-dimensional simulation. (b) Predicted vorticity field at time $\tau = 140f^{-1}$ in the two-dimensional simulation of the barotropic part of the prediction. The isolevels increase from -1.15f (black) to 0.65f (grey) with increments of 0.1f. The coordinates (x, y) are scaled with $\mathscr{L}$. ($\alpha = 1.8$, Ro $= -2.35$, Re $= 15000$).

Re $= 15000$ was also used. A random variation of one percent was added to the amplitude of the initial azimuthal velocity at every point in the flow.

An example of how well the prediction can do is shown in figure 6. The prediction for this Rossby number (Ro $= -2.35$) is for the formation of a tripole, as in the laboratory experiment shown in figure 1. In figure 6a we show the vorticity field on the mid-level horizontal plane at time $t = 160$. The result is a tripole as predicted. The vorticity field compares well with the vorticity field from the prediction at time $\tau = 140$ shown in figure 6b. In the 3D simulation the time t is the time from when the initial perturbed condition is allowed to evolve freely. In the prediction, τ is the time after which the barotropic simulation has been initiated based on a randomly perturbed version of the inertially equilibrated profile. The prediction and the 3D result correspond very closely in form, and they are not very far off quantitatively, although the 3D simulation does have a minimum vorticity about 10 percent more negative than found in the prediction. The orientation of the final structure is not very important since this depends on the orientation of the initial small-scale perturbation field. For example, if we took the perturbation field used in the prediction for this case and simply rotated it by ϕ degrees, the final image of the prediction would be rotated by that much. Since the random perturbation used in the 3D simulation and in the 2D perturbation are unrelated except in scale and amplitude, but not in phase, the relative orientation of the final results is irrelevant.

Another example is shown in figure 7. The prediction for this Rossby number (Ro $= -3.0$) is for the formation of two dipoles propagating away from each other as in the laboratory experiment shown in figure 2. The result from the 3D simulation

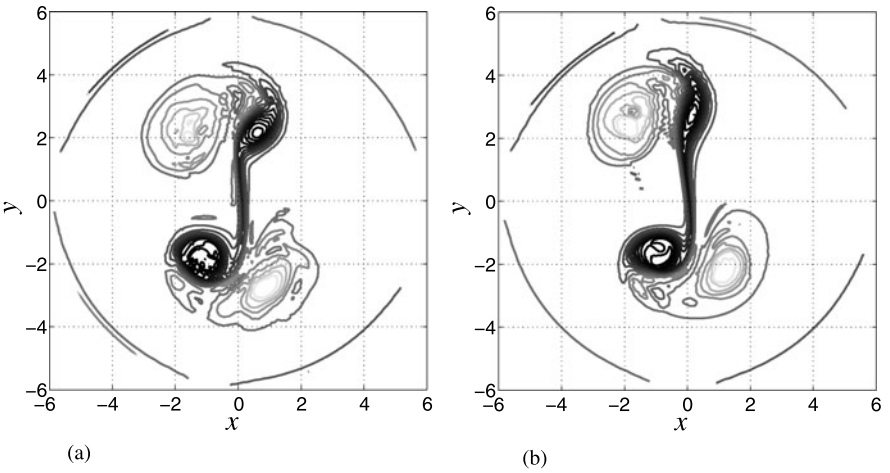

Fig. 7 Comparison of the results of the three-dimensional simulation with the prediction. (a) Vorticity field at the midplane at time $t = 120f^{-1}$ in the fully three-dimensional simulation. (b) Predicted vorticity field at time $\tau = 80f^{-1}$ in the two-dimensional simulation of the barotropic part of the prediction. The isolevels increase from -1.15f (black) to 0.65f (grey) with increments of 0.1f ($\alpha = 1.8,\ \mathrm{Ro} = -3.0,\ \mathrm{Re} = 15000$).

SIMULATION	FINAL STRUCTURE	PREDICTION
-3.5 < Ro < -2.4	**TWO DIPOLES**	**-3.5 < Ro < -2.3**
-2.4 < Ro < -2.2	**TRIPOLE**	**-2.3 < Ro < -2.1**
-2.2 < Ro < -1.0	**MONOPOLE**	**-2.1 < Ro < -1.0**

Table 1 Comparison of regime boundary predictions with results from 3D simulations for the anticyclone with $\alpha = 1.8$.

is a set of dipoles as predicted. The image for the 3D simulation is the vorticity field at the mid plane at time $t = 120$. This field compares well with the vorticity in the prediction at time $\tau = 80$. Here too, the prediction and the 3D result correspond very closely.

The skill of our predictions can also be tested by considering the ranges of Ro over which different outcomes occur. Simulations were performed for Ro ranging from -1 down to -3.5. The results are shown table 1. The predicted regime boundaries are at Ro= -2.1 and -2.3. These are reasonably close to the values found in the 3D simulations, i.e. Ro= -2.2 and -2.4.

5 Discussion

The comparison between the simulations and the prediction for the case $\alpha = 1.8$ is very promising. It suggests that for flows in which the inertial instability is much faster than the barotropic, we can separate their effects for prediction purposes. However, this will not be the case for all vortices. For example, as we increase the value of α above 1.85 the barotropic instability will occur simultaneously with the centrifugal instability from the initial time and the ratio of the barotropic instability growth rate to the inertial instability growth rate will decrease with increasing α. It is reasonable to suspect that the higher the value of α the less skill this prediction method will have. We are in the process of testing this limit.

The type of analysis used here may someday be useful in parameterizing the effect of vortex instabilities on the evolution of vortices in general circulation models where those vortices are under-resolved.

Acknowledgements RCK acknowledges support from National Science Foundation grant OCE 07-26866. GFC acknowledges support from National Science Foundation grant OCE 07-26482 and the Ministero Istruzione Universita e Ricerca (MIUR D.M. 26.01.01 n. 13).

References

Carnevale G, Kloosterziel R (1994) Emergence and evolution of triangular vortices. J Fluid Mech 259:305–331

Carton X, Legras B (1994) The life-cycle of tripoles in two-dimensional incompressible flows. J Fluid Mech 267:53–82

Carton X, Fierl G, Polvani L (1989) The generation of tripoles from unstable axisymmetric isolated vortex structures. Europhys Lett 9:339–344

Drazin P, Reid W (1984) Hydrodynamic Stability. Cambridge University Press

Flierl G (1988) On the instability of geostrophic vortices. J Fluid Mech 197:349–388

Kloosterziel R, Carnevale G (1992) Formal stability of circular vortices. J Fluid Mech 242:249–278

Kloosterziel R, Carnevale G (1999) On the evolution and saturation of instabilities of two-dimensional isolated circular vortices. J Fluid Mech 388:217–257

Kloosterziel R, van Heijst G (1991) An experimental study of unstable barotropic vortices in a rotating fluid. J Fluid Mech 223:1–24

Kloosterziel R, Carnevale G, Orlandi P (2007) Inertial instability in rotating and stratified fluids: barotropic vortices. J Fluid Mech 583:379–412

Orlandi P (2000) Fluid flow phenomena: a numerical toolkit, vol 55. Kluwer Academic Publishers, Dordrecht, The Netherlands

Orlandi P, Carnevale G (1999) Evolution of isolated vortices in a rotating fluid of finite depth. J Fluid Mech 381:239–269

Rayleigh L (1880) On the stability, or instability, of certain fluid motions. Proc London Math Soc 11:57–70
Rayleigh L (1916) On the dynamics of revolving fluids. Proc R Soc London Ser A 93:148–154

Quasigeostrophic and stratified turbulence in the atmosphere

Peter Bartello

Abstract New simulations of rotating and stratified turbulence are presented. The goal of simulating a large-scale régime dominated by quasigeostrophic flow and a small-scale régime consistent with recent simulations of stratified turbulence was successfully achieved. Interestingly, the transition scale exhibited a scaling break in the energy spectrum much like that observed in the Gage-Nastrom atmospheric data. An attempt is made to situate objectively these results amongst a variety of others. The latter were obtained with atmospheric numerical models and observations and employed different techniques to separate the turbulence into quasigeostrophic (large-scale) and more general (small-scale) motions. Although the present idealised simulations agree with observations at this level, much of the atmospheric context is missing, there are other ways to produce the spectral scaling break and more observations are required.

1 Introduction

In the late 1970's the Global Atmospheric Sampling Program (GARP) produced wind and temperature data that allowed for the calculation of the atmospheric kinetic and potential energy spectra over the range from $O(10^4)$ km down to $O(1)$ km. It became apparent that the large-scale k_h^{-3} spectrum, where k_h is the horizontal wavenumber, became more shallow at scales between 100 to 1000 km ([12, 13]). Since these horizontal scales are far from being isotropic in the troposphere, initial speculation in [12, 21] suggested that the shallow mesoscale range was due to an inverse cascade, along the lines of that observed in two-dimensional flow, from small convective scales towards larger scales. On the other hand [39] argued that the shallow range was dominated by inertial gravity waves resulting from the larger-scale

Peter Bartello
Institute for Mathematical Sciences, Imperial College London, e-mail: bartello@math.mcgill.ca (Permanent address: McGill University, Montréal)

D. Dritschel (ed.), *IUTAM Symposium on Turbulence in the Atmosphere and Oceans*, IUTAM Bookseries 28, DOI 10.1007/978-94-007-0360-5_10,

motion. [10] provided the conceptual framework in terms of a spectrum of gravity waves, each on the threshold of breaking, radiating from either convective or shear instabilities. Unfortunately, their framework predicted the form of the vertical energy spectrum, while the Gage-Nastrom data yielded only the horizontal spectrum.

The Gage-Lilly inverse cascade mechanism was subsequently explored numerically in [15] in idealized fluid dynamical simulations of stratified turbulence. They found that an inverse cascade was not observed in stratified Boussinesq simulations without rotation. Since the energy reached statistical stationarity with only small-scale dissipation, it must have been transferred to smaller scales (see also the recent work in [19]). Several simulations were performed in the 1990's by several authors, as reviewed in [30]. Of relevance here is the study [28], which showed that an inverse cascade, along with a $k_h^{-5/3}$ spectrum could be obtained when sufficient rotation was added. It was shown in [1] that this régime corresponded to low-Rossby, low-Froude dynamics leading to quasigeostrophy in the large scales, but could not be invoked at convective scales.

Since then more data have become available supporting the shallowing of the spectrum in the mesoscale, with spectral slopes in the -5/3 to -2 range. [23] calculated the structure functions of MOZAIC aircraft data (similar to those of GARP) to deduce the cascade directions. It was found in [9, 26] that the mesoscale -5/3 range occured in conjunction with a downscale cascade, also in contradiction to the Gage-Lilly phenomenology.

More recently, three studies have emerged that present further attempts to describe the mesoscale atmospheric spectrum from very different theoretical perspectives. First is [38], claiming that both the steep large-scale spectrum and the shallow mesoscale spectrum can be simulated using a two-layer quasigeostrophic model. [33] showed that the small-scale spectrum could be the result of insufficient numerical dissipation, whereupon [37] replied that it was correctly scaled to the atmosphere.

The second recent study is [25], where it is argued that stratified Boussinesq turbulence forced at large scales leads to a downscale cascade with horizontal wavenumber spectrum proportional to $\varepsilon^{2/3}k_h^{-5/3}$. Based on [24], it was reasoned that such a stratified-only cascade could prevail as long as the velocity-based Rossby number was greater than 0.1. It would seem reasonable to expect that rotational effects are at least present, if not predominant, over part of the mesoscale range as it includes scales up to $O(10^2 - 10^3)$ km. We aim to extend Lindborg's study by attempting to reproduce the transition to the large-scale steep spectrum, where rotation is important.

Finally, the third and most recent set of studies are described in [35, 36]. They have argued from the completely different perspective that the kink in the atmospheric energy spectrum can be explained within quasigeostrophic theory, using a more realistic top and bottom boundary. They suggest that the coupling between surface quasigeostrophic flow, with no potential vorticity in the interior, and the interior flow, naturally leads to a break in the slope of the energy spectrum. In the first approximation they view the tropopause as a frictionless surface of constant z with no normal flow. If surface quasigeostrophy on the tropopause plays an important role

in the atmosphere, it would suggest that at different heights between the ground and the tropopause, the spectral transition occurs at different horizontal wavenumbers. The observational record is currently unable to confirm or deny this as commercial airplanes fly near the tropopause. Unfortunately, as the present study employs periodic boundary conditions in the vertical, these results cannot be used to shed any light on the role of surfaces in a context more general than quasigeostrophy.

[1] presented numerical simulations of rotating stratified Boussinesq turbulence in which the flow was decomposed into geostrophic and ageostrophic normal modes. The simulations were initialized isotropically and allowed to decay under the influence of hyperviscosity. The contribution to the total energy from the geostrophic (low-frequency) and ageostrophic (high linear frequency) modes was then calculated. At large times there emerged a steep geostrophic spectrum and a much more shallow ageostrophic spectrum, such that they crossed at an intermediate wavenumber. Following [43], the simulation results were intrepeted as a first-order decoupling of the QG flow from the linear wave modes, implying a QG inverse cascade of energy as in [8]. Statistical mechanical arguments, verified by simulations, pointed to a downscale cascade of wave energy. Since this paper was published fourteen years ago, the author has often speculated that this is the mechanism for the shallow mesoscale atmospheric spectrum. This picture is consistent with the earlier work [39].

There has been recent interest in the mesoscale spectrum as realistic models now resolve these scales cleanly. Although idealised fluid dynamical models and realistic atmospheric models seemed irreconcilable in [22], there was an early hint of the spectral transition in the Sky-Hi model in [18]. More recently, the WRF model has clearly shown the break in [32]. When "divergence damping" was applied, the shallow mesoscale spectrum became steep, near k_h^{-3}, lending support to the idea this spectral zone is not completely dominated by rotational modes. [14] shows clear spectral transitions in extensive sensitivity tests with a high-resolution global model. Below the transition scale, rotational modes are more energetic than horizontally divergent ones, but only by an order one factor. [42] also observed a spectral transition in dry simulations of a baroclinic life cycle. They find a significant decrease in the mesoscale range's amplitude and a transition at higher wavenumbers than in the observations and conclude, in agreement with [14], that moist processes are required to obtain the correct energy. It should be noted that scales below the transition scale in all these realistic models are rather influenced by uncertain physics parameterisations and model diffusion. In addition, recent work on stratified turbulence has identified vertical resolution requirements (see e.g. [34, 19]) that are at best marginally attained with current realistic models. Finally, the ECMWF forcast model shows the steep large-scale spectrum continuing down to its dissipation range and truncation. This is likely due to semi-Lagrangian advection being too dissipative at third-order interpolation (see [5]). [31] proposed making up the energy deficiency by stochastically forcing a white-noise spectrum in rotational modes.

It is worth noting that these results show similarities to recent work in realistic ocean modelling, where [7] also noted a transition to a less steep spectrum at scales well below the deformation radius. Such a transition was confirmed in the simu-

lations of [17], where surface ageostrophic energy spectra were considerably less steep than those of the total velocity.

[3] showed that the interplay between rotational and divergent modes was completely spurious when semi-implicit and split-explicit numerics were combined with large time steps. In order to reproduce the resonance phenomena that determine the interactions and hence the cascades, accurate temporal resolution of the linear wave frequencies is required. In addition, [2] showed that excessive vertical diffusion could result in a spurious inverse energy cascade resembling the Gage-Lilly phenomenology. For these reasons it is important to understand the dry dynamics in the mesoscale, both as a first step in formulating a theory, and as it will surely aide in optimizing numerical approaches.

The main goal of this contribution is therefore to explore whether both ranges of the atmospheric spectrum can be simulated at statistical stationarity in forced Boussinesq flow and interpreted in terms of the cascades of geostrophic and ageostrophic modes. If so, this implies that divergent energy may play a significant role in the mesoscale energy spectrum. We also seek to determine the wavenumber dependence of this spectum. Indeed, a steep geostrophic modal spectrum can be obtained in conjunction with a more shallow divergent modal spectrum at statistical stationarity. Given large-scale geostrophy and a sufficiently large scale separation, the two cross. Towards smaller scales, the two types of modes display parallel spectra, indicating the linear terms defining them are no longer predominant. Although this picture is consistent with the observations, caution is required since the simplicity of the context does not capture much of the atmosphere.

2 Divergent and geostrophic modes

As a first approximation to atmospheric flow, we examine the rotating stratified Boussinesq equations. In this section important features of the normal-mode decomposition presented in [1] are pointed out. In terms of the velocity u_i and the buoyancy variable b the inviscid equations on an f-plane are,

$$\frac{\partial u_i}{\partial t} + u_j \frac{\partial u_i}{\partial x_j} + f\varepsilon_{ijk}\delta_{j3}u_k = -\frac{\partial p}{\partial x_i} + \delta_{i3}b,\ \frac{\partial u_i}{\partial x_i} = 0,\ \frac{\partial b}{\partial t} + u_j \frac{\partial b}{\partial x_j} = -N^2 u_3,$$

where f is the Coriolis parameter and N is the Brunt-Väisälä frequency. The Rossby number is $Ro = U/fL$, where U and L are characteristic velocity and horizontal length scales. The Froude number is $Fr = U/NH$, with H being a characteristic vertical scale. (Only the vertical Froude number will be referred to here.) Forcing and viscous terms have been omitted, but the numerical section below discusses the forcing, hyperviscosity and Rayleigh damping employed in this study.

The variables that diagonalise the linear terms are composed of the zero-frequency geostrophic mode and two inertia-gravity modes whose frequencies are $\pm\sigma$, where $\sigma^2 = (f^2 k_z^2 + N^2 k_h^2)/k^2$. The total energy can be written $E_T = E_G + E_A$, where E_G is

the geostrophic energy and E_A is the ageostrophic energy. Applying the projection onto the new variables is straightforward for both the usual variables and the various terms in their tendency equations. Definitions of spectra follow in the standard way (see e.g. [20]).

It was shown in [41] that to leading order when the Froude number is small, the mean-square potential vorticity (potential enstrophy) is $V \approx V_G$. In other words, only the geostrophic modes contribute to the linear PV (see also [11]). Both vertical vorticity and vertical buoyancy gradients contribute to the geostrophic mode (as in the PV). The ageostrophic modes account for all horizontal divergence, vertical velocity and the inertial-wave component of the vertical vorticity. The latter underlines differences between these 3D normal modes and the more usual vorticity and divergence decomposition on a constant vertical level. Since both geostrophic and ageostrophic modes contribute to the vertical vorticity on a 2D surface, recent observational and model results concerning relative energies of rotational and divergent motions must be interpreted with caution as these do not possess the linear PV-based dynamical distinction of our decomposition. More work needs to be done to facilitate such comparisons.

Finally, there is the delicate issue of "balance" in large-scale atmospheric flow. Since balance is more subtle than simple geostrophy, there is a contribution to the ageostrophic modes that describes higher-order corrections to balance rather than high-frequency waves. For example, [41] compared model vertical velocities to those obtained with the "omega equation" and the geostrophic modes (see e.g. [16]). They found the true variance exceeded the QG level by a factor of over seven at a velocity-based Rossby number of 0.09, implying that the unbalanced contribution far exceeds the correction to geostrophy at typical mesoscale Rossby numbers. There are of course higher order definitions of balance, but for the purpose at hand it is sufficient simply to avoid using the term "waves" to describe the ageostrophic modes in a nonlinear context.

3 The numerical configuration

The Boussinesq equations were integrated using a pseudo-spectral method in triply-periodic cartesian f-plane geometry. This configuration is standard in turbulence studies and, while it does not resemble the atmosphere, the aim is to see if it contains the necessary ingredients for the spectral transition, i.e. the modal interplay in turbulence that is sufficiently QG at large scale.

Given the atmospheric ratio N to f is most often quoted as 100 to one, we would have preferred to integrate the model on a domain whose vertical periodicity length was one one hundredth of its horizontal length. The approach would then be to use $N/f = 100$ and to force a set of quasigeostrophic baroclinic Fourier modes whose length scale ratio was also 100 to one. This represents the large-scale injection of quasigeostrophic energy from baroclinic instability. From these QG large scales we wish to simulate the transition(s) to the mesoscale régime, where rotation is less

important, down to the almost isotropic scales required for accurate simulation of stratified turbulence, as described in [34]. The latter requires an isotropic resolution.

Unfortunately, the available computing resources make this impossible. In numerical simulations that resolve the dissipation explicitly, scales below $O(10)$ grid points, at least, are dominated by dissipation. If we require approximately 50 vertical grid points to ensure that at least some of the dynamics are not swamped by model dissipation (this would require hyperviscosity), then we would need 5000 horizontal grid points. It is possible that this is, or shortly will be, at the limit of today's computers. In any event, the same logic and strategy was adopted, but the ratio N/f was reduced to ten. As a result we must sacrifice any hope of exact atmospheric scaling of the results.

The model employs the de-aliased pseudo-spectral method with leap-frog time stepping and a weak Robert filter. The buoyancy variable b and the vorticity are integrated with the normal-mode projections being applied only at output times. The collocation grid was $500 \times 500 \times 50$. The vertical domain size was one tenth that of the horizontal domain such that $\Delta x = \Delta y = \Delta z$.

The forcing takes the form $\hat{F}_{\mathbf{k}}^{(j)} = C^{(j)}(\mathbf{k}) G_{\mathbf{k}}^{(j)}(t)$, where j specifies the normal mode being forced, $C^{(j)}(\mathbf{k})$ is the constant-in-time wavevector-dependent amplitude, and $G_{\mathbf{k}}^{(j)}(t)$ is a random process that gives the time dependence. $G_{\mathbf{k}}^{(j)}(t)$ satisfies $\langle G_{\mathbf{k}}^{(j)}(t) \rangle = 0$ and $\langle G_{\mathbf{k}}^{(j)}(t_0) G_{\mathbf{p}}^{(n)}(t_0 + t) \rangle = \delta_{jn} \delta_{\mathbf{kp}} e^{-t/\tau}$, where the decorrelation time, τ, is set at 25 timesteps in order to inhibit computational $2\Delta t$ oscillations. $G_{\mathbf{k}}^{(j)}(t)$ was computed by drawing a Gaussian random number f_n (with zero mean and unit variance) at every time level n, setting $G_{\mathbf{k}}^{(j)}(n\Delta t) = \alpha G_{\mathbf{k}}^{(j)}((n-1)\Delta t) + \beta f_n$, and requiring $\alpha = e^{\Delta t/\tau}$ and $\alpha^2 + \beta^2 = 1$.

The horizontally-isotropic forcing was applied to a band of wavenumbers centred on horizontal wavenumber two and was active only at vertical wavenumbers ± 20. A set of baroclinic geostrophic modes was forced such that $C^{(j)}(\mathbf{k})$ is non-zero only if $|k_h - 2| \leq 1$, $|k_z| = 20$ and $j = 0$ in which case it was $C^{(0)}(\mathbf{k}) = a(k_h - 1)(3 - k_h)$, with $a = 0.09$. This forcing term is added to the nonlinear version of the normal-mode amplitude equation.

At the numerical resolutions employed in this study, the use of the Laplacian dissipation operator would preclude an inertial range. One solution is to employ a sub-grid scale parameterization. Another is to use an iterated Laplacian (i.e. hyperviscosity), which restricts the effects of dissipation to a narrow range of scales and is trivially implemented in a pseudo-spectral model. [4] discusses the relationship between hyperviscosity and eddy viscosity in rotating stratified turbulence.

Cylindrical hyperviscosity was employed to be consistent with the spectral truncation. The dissipation of momentum and buoyancy are given by identical operators $D_u = D_b = \nu_h (-1)^{n+1} \nabla_h^{2n} + \nu_z (-1)^{n+1} \partial^{2n} / \partial z^{2n}$. In all simulations $n = 4$ and $\nu_h = \nu_z = 8.4 \times 10^{-17}$, yielding a dissipation range of at least a decade in all runs. In addition, since most of the simulations involve low Rossby and Froude numbers, there is an approximate decoupling of geostrophic modes from ageostrophic modes, at least in the large scales. In this case a strong inverse cascade of geostrophic energy results and we have dealt with it by including a Rayleigh damping term in all vari-

ables with coefficient of 0.1, corresponding to an e-folding time of approximately 200 eddy turnover times, based on rms total vorticity. Physically, this corresponds to the simplest representation (Ekman) of a boundary layer.

4 Results

A rather inefficient QG model can be obtained by setting the ageostrophic modal amplitudes to zero at every time step in the present model (see e.g. [29]). This truncation was applied to the baroclinic forcing described above and spun up to statistical stationarity, providing a quasigeostrophic initial condition for all the simulations described below. They were simply the continuations of the QG spin-up simulation at various values of f and N after ceasing to project the results onto the geostrophic modes only.

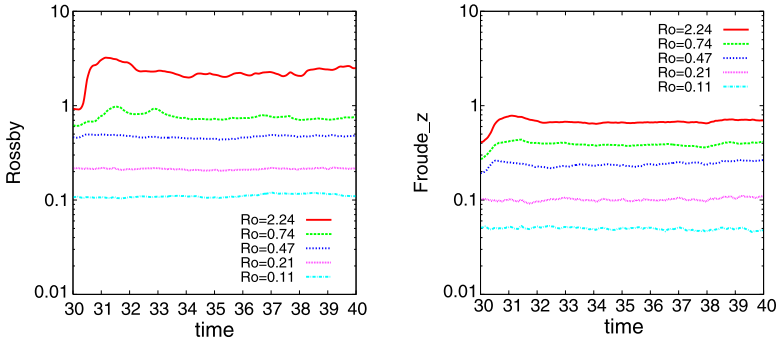

Fig. 1 Time series of the Rossby (left) and vertical Froude (right) numbers. All simulations were initialised with statistically stationary fields from a quasigeostrophic model. Quantities discussed below were averaged over the period beginning at $t = 33$.

In Figure 1 we display time series of the Rossby and Froude numbers. Vorticity-based quantities ($Ro = \langle \omega_z^2 \rangle^{1/2}/f$, $Fr = \langle \omega_h^2 \rangle^{1/2}/N$) were employed to emphasise the small-scale dynamics in this search for a spectral kink. It has been pointed out that, when the spectrum is shallow, vorticity-based quantities are dependent on the Reynolds number. The simulations presented below are rather dominated by quasigeostrophic large-scale flows and this was not a problem.

The figure shows that statistical stationarity in the presence of ageostrophic modes has been achieved. Note there is little change from the curves' initial values at low Ro and Fr, as the ageostrophic modes saturate at relatively low amplitudes. As these curves are normalised vorticities, not even the small scales of the flow are much affected. At large Ro and Fr, there is an initial adjustment, followed by a longer stationary régime. Average quantities were obtained over $33 \leq t \leq 40$.

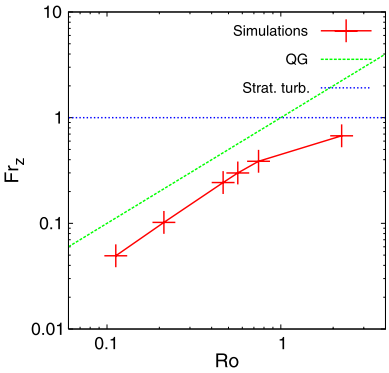

Fig. 2 The average Froude number versus the average Rossby number. Quasigeostrophic scaling implies $Ro \sim Fr$, whereas recent work on stratified turbulence suggests $Fr \sim 1$ when rotation is not important.

It is important to know the extent to which quasigeostrophic scaling holds. Large-scale quasigeostrophy may be the result of the forcing, with $\frac{N}{f} \sim \frac{L}{H}$ or $Ro \sim Fr$, but does this extend down to the small scales and the vorticity field? In Figure 2 we plot the average vertical Froude number versus Rossby number for all simulations. Quasigeostrophic scaling is evident over the low-Ro range in that the two stay proportional to each other. Recently, [6], [40] and [25] have noted the tendency for stratified turbulence to adjust to $Fr \sim 1$ when rotation is absent or negligible. This seems consistent with the single point at the largest Rossby number. For a more complete look at this transition see [41].

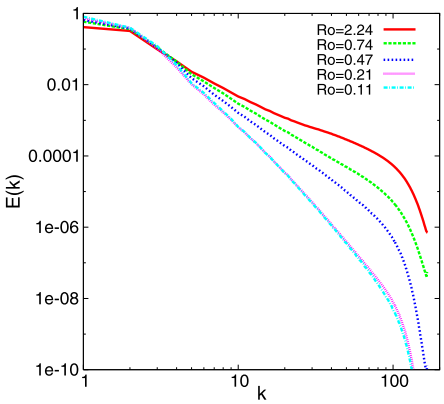

Fig. 3 The average horizontal energy spectrum at various Rossby numbers.

Figure 3 displays the time-average total energy spectrum as a function of horizontal wavenumber for a variety of Rossby numbers. A small kink resembling the atmospheric spectrum is apparent at the larger Rossby numbers. At very small Rossby numbers the spectrum is very steep and shows only a weak dependence on *Ro*. In this limit it is indistinguishable from the quasigeostrophic spin-up simulation (not shown).

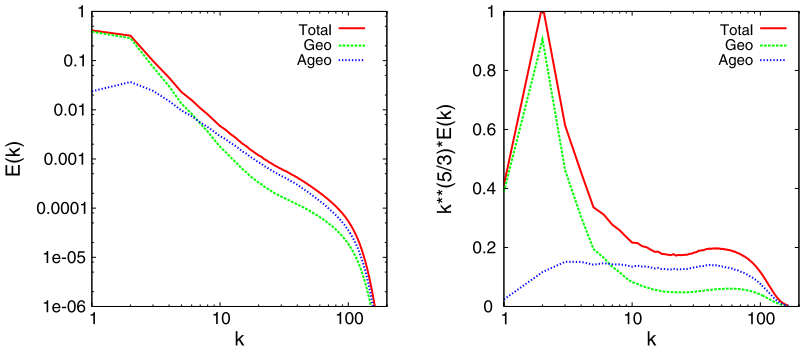

Fig. 4 The averaged total energy spectrum of the simulation at the highest *Ro*, along with its contributions from geostrophic modes and ageostrophic modes. Left: the usual log-log plot, Right: lin-log plot compensated by $k^{5/3}$.

Given the results of Figures 2 and 3, in Figure 4 we take a closer look at the simulation with the highest *Ro*. Here, we decompose the energy into geostrophic and ageostrophic parts. Also displayed is a lin-log spectrum compensated by $k_h^{5/3}$. It appears the ageostrophic spectrum is quite close to being proportional to $k_h^{-5/3}$. At higher k_h, if *Re* is large enough, geostrophic and ageostrophic spectra are expected to become parallel in the ratio of 1:2 as their quasi-linear dynamical basis is undermined at these scales. Note that this simulation was repeated with a Rayleigh dissipation extending from the minimum wavenumber out to only the third wavenumber bin, beyond which it was set to zero. Apart from slightly higher energies near the transition scale, the results were qualitatively similar with an equally clear spectral transition.

In Figure 5 horizontal (top panel) and vertical (bottom panel) cross sections of *local* $Ro = \omega_z/f$ are displayed for the simulation at the largest *global* $Ro = \langle \omega_z^2 \rangle^{1/2}/f$. In the early stages of ageostrophic modal growth, anticyclonic regions showed more small-scale activity than cyclonic ones, consistent with inertial instability (see also [27]). After statistical stationarity was reached (as in the figure), the vorticity field appeared as a mixture of small-scale structure superimposed on the long filaments of QG and 2D turbulence. Note that, while the Rossby number based on the rms vertical vorticity was only approximately 2.2, point values exceed ± 25. As in many other simulations of turbulence, the histogram of grid-point vorticities showed close to exponential tails.

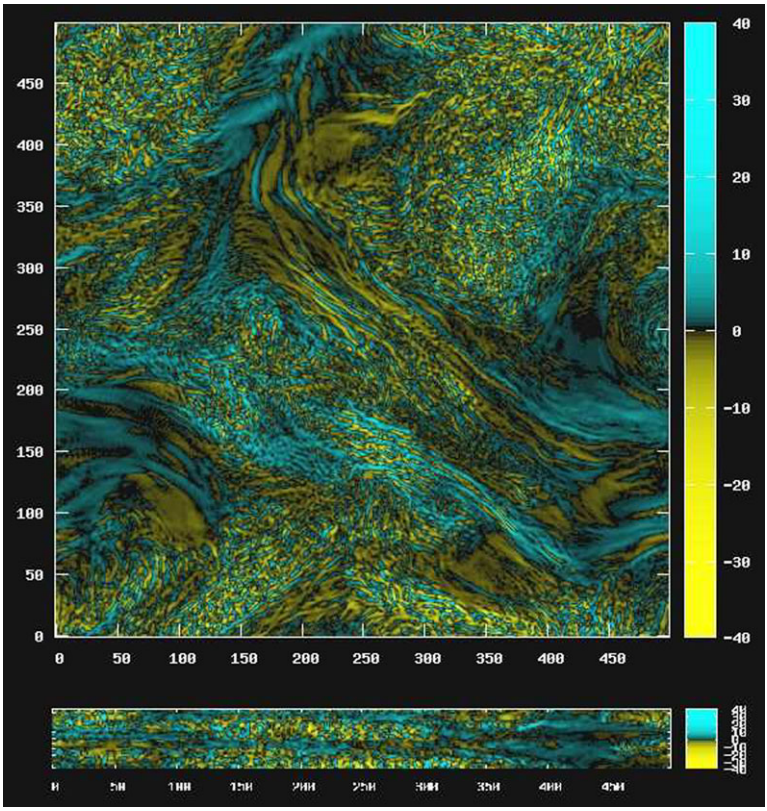

Fig. 5 The final vorticity field normalised by the Coriolis parameter, f, for the simulation with largest global Rossby number, $Ro \approx 2.24$. Top panel: xy-plane, Bottom panel: xz-plane.

In Figure 6 the time-average flux of total energy is shown. At low Ro this is very negative at low k_h, indicating a transfer to larger scales. Since the forcing is at horizontal wavenumber two, this is absorbed by the Rayleigh dissipation term. At larger k_h the flux returns to zero downscale of the forcing, but the wavenumber at which it does so is an increasing function of Ro. Ultimately, at the highest Ro simulated, the flux is significant and downscale until the dissipation is reached near the truncation scale. The spectral transition around $k_h \approx 20$ that is clearly visible in the energy spectrum is much less obvious in the flux spectrum.

5 Conclusions

Although many elements of the atmospheric context are missing in this highly idealized study, we have clearly managed to simulate a robust spectrum with a large-

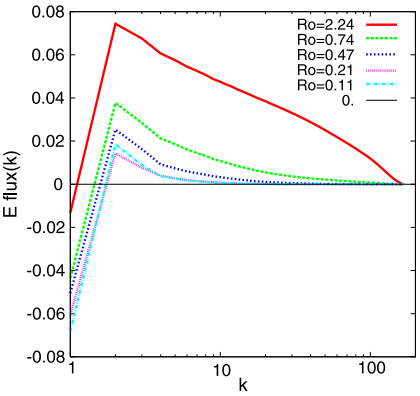

Fig. 6 Spectral energy flux as a function of horizontal wavenumber at various Rossby numbers. Positive (respectively negative) fluxes imply a transfer to smaller (respectively larger) scales.

scale steep range and a small-scale shallow range. While at this resolution only one Rossby number could show the transition clearly, and only one low value of N/f was employed, the small-scale damping was well resolved and the result was insensitive to the Rayleigh dissipation at high wavenumbers. The interpretation in terms of the first-order decoupling of vortical from ageostrophic modes applies to the large scales at least. At larger Rossby number, this decoupling was not present in the small-scale shallow range, where statistics were consistent with stratified turbulence, as discussed in [25].

The relationship between the imbalance of the "interior flow" simulated here and surface processes discussed in a QG context in [35, 36] needs to be elucidated. In particular, in order to test their relative roles, it would be necessary to place upper and lower surfaces within a non-hydrostatic Boussinesq framework.

The issue of the exact spectral slopes also needs to be examined using more realistic values of N/f and at higher resolution. The latter would also permit testing the sensitivity of the transition simulated here to the Reynolds number, as well as a more careful examination of the extent to which the small-scale régime is consistent with recent studies of stratified turbulence. Two of these ([19] and [40]) noted spuriously steep horizontal energy spectra with insufficient vertical resolution. In light of this it seems surprising that hydrostatic GCM models are able to simulate the shallow mesoscale range. In order to determine whether the same dynamics are present in all models, work must be done on the relative roles of PV-possessing modes and those without PV in more realistic geometry. Finally, as stressed recently by [42], the analysis must be fully three-dimensional to account for vertical fluxes.

Acknowledgements I would like to express my heart-felt thanks to my new friends at the Isaac Newton Institute, CUED, DAMTP, the University of Warwick and to all the INI visitors, for making the INI Turbulence Programme a delightful experience.

References

[1] Bartello, P., Geostrophic adjustment and inverse cascades in rotating stratified turbulence. *J. Atmos. Sci.*, **52**, 4410–4428 (1995).

[2] Bartello, P., Potential vorticity, resonance and dissipation in rotating convective turbulence, in *Geophysical and Astrophysical Convection*, ed. by P. A. Fox and R. M. Kerr. (Gordon and Breach, NY, 2000), pp. 309–322.

[3] Bartello, P., A comparison of time discretization schemes for two-timescale problems in geophysical fluid dynamics. *J. Comp. Phys.*, **179**, 268–285 (2002).

[4] Bartello, P., O. Métais and M. Lesieur, Geostrophic versus wave eddy viscosities in atmospheric models. *J. Atmos. Sci.*, **53**, 564–571 (1996).

[5] Bartello, P. and Thomas, S. J., An update on semi-Lagrangian cost-effectiveness, Unpublished manuscript available at http://www.meteo.mcgill.ca/~bartello/old/b_and_thomas_1999_unpublished.pdf (1999).

[6] Billant, P. and J.-M. Chomaz, Self-similarity of strongly stratified inviscid flows. *Phys. Fluids*, **13**, 1645–1651 (2001).

[7] Capet, X., McWilliams, J. C., Molemaker, M. J. and Shchepetkin, Mesoscale to submesoscale transition in the California Current system. Part I: Flow structure, eddy flux, and observational tests. *J. Phys. Oceanogr.*, **38**, 29–43 (2008).

[8] Charney, J. G., Geostrophic turbulence. *J. Atmos. Sci.*, **28**, 1087–1095 (1971).

[9] Cho, J. Y. N. and E. Lindborg, Horizontal velocity structure functions in the upper troposphere and lower stratosphere: 1. Observations. *J. Geophys. Res.*, **106**, 10,223–10,232 (2001).

[10] Dewan, E. M. and R. E. Good, Saturation and the "universal" spectrum for vertical profiles of horizontal scalar winds in the atmosphere. *J. Geophys. Res.*, **91**, 2742–2748 (1986).

[11] Embid, P. F. and A. J. Majda, Low Froude number limiting dynamics for stably stratified flow with small or finite Rossby numbers. *Geophys. Astrophys. Fluid Dyn.*, **87**, 1–50 (1998).

[12] Gage, K. S., Evidence for a $k^{-5/3}$ law inertial range in mesoscale two-dimensional turbulence. *J. Atmos. Sci.*, **36**, 1950–1954 (1979).

[13] Gage, K. S. and G. D. Nastrom, Theoretical interpretation of atmospheric wavenumber spectra of wind and temperature observed by commercial aircraft during GASP. *J. Atmos. Sci.*, **43**, 729–740 (1986).

[14] Hamilton, K., Takahashi, Y. O. and Ohfuchi, W., Mesoscale spectrum of atmospheric motions investigated in a very fine resolution global general circulation model. *J. Geophys. Res.* **113**, D18110, doi:10.1029/2008JD009785.

[15] Herring, J. R. and O. Métais, Numerical experiments in forced stably stratified turbulence. *J. Fluid Mech.*, **202**, 97–115 (1989).

[16] Hoskins, B. J., Draghici, I. and Davies, H. C., A new look at the omega-equation. *Q. J. R. Met. Soc.*, **104**, 31–38 (1978).

[17] Klein, P., Hua, B. L., Lapeyre, G., Capet, X., Le Gentil, S. and Sasaki, H., Upper ocean turbulence from high-resolution 3D simulations. *J. Phys. Oceanogr.*, **38**, 1748–1763 (2008).

[18] Koshyk, J. N., K. Hamilton and J. Mahlman, Simulation of the mesoscale spectral regime in the gfdl skyhi general circulation model. *Geophys. Res. Lett.*, **26**, 843–846 (1999).

[19] Laval, J.-P., McWilliams, J. C. and Dubrulle, B., Forced stratified turbulence: successive transitions with Reynolds number. *Phys. Rev. E*, **68**, 036308 (2003).

[20] Lesieur, M., *Turbulence in Fluids*. Kluwer, Dordrecht, The Netherlands, third edition (1997).

[21] Lilly, D. K., Stratified turbulence and the mesoscale variability of the atmosphere. *J. Atmos. Sci.*, **40**, 749–761 (1983).

[22] Lilly, D.K., G. Bassett, K. Droegemeier and P. Bartello, Stratified Turbulence in the atmospheric Mesoscales. *Theoret. Comput. Fluid Dyn.*, **11**, 139–153 (1998).

[23] Lindborg, E., Can the atmospheric kinetic energy spectrum be explained by twodimensional turbulence? *J. Fluid Mech.*, **388**, 259–288 (1999).

[24] Lindborg, E., The effect of rotation on the mesoscale energy cascade in the free atmosphere. *Geophys. Res. Lett.*, **32**, L01809, doi:10.1029/2004GL021319 (2005).

[25] Lindborg, E., The energy cascade in a strongly stratified fluid. *J. Fluid Mech.*, **550**, 207–242 (2006)

[26] Lindborg, E. and J. Y. N. Cho, Horizontal velocity structure functions in the upper troposphere and lower stratosphere. 2. Theoretical considerations. *J. Geophys. Res.*, **106**, 10,233–10,242 (2001).

[27] McWilliams J. C., M. J. Molemaker and I. Yavneh, Ageostrophic, anticyclonic instability of a geostrophic, barotropic boundary current. *Phys. Fluids*, **16**, 3720–3725 (2004).

[28] Métais, O., P. Bartello, E. Garnier, J. J. Riley and M. Lesieur, Inverse cascade in stably stratified rotating turbulence. *Dyn. Atmos. Ocean*, **23**, 193–203 (1996).

[29] Ngan, K., P. Bartello and D. N. Straub, Dissipation of synoptic-scale flow by small-scale turbulence, *J. Atmos. Sci.*, **65**, 766–791 (2008).

[30] Riley, J. J. and M.-P. Lelong, Fluid motions in the presence of strong stable stratification. *Annu. Rev. Fluid Mech*, **32**, 613–657 (2000).

[31] Shutts, G., A stochastic kinetic energy backscatter algorithm for use in ensemble prediction systems. *European Centre for Medium-Range Weather Forecasts Technical Report*, **449**, 1–50 (2004).

[32] Skamarock, W. C., Evaluating mesoscale nwp models using kinetic energy spectra. *Mon. Wea. Rev.*, **132**, 3019–3032 (2004).

[33] Smith, K. S., Comments on "the k^{-3} and $k^{-5/3}$ energy spectrum of atmospheric turbulence: Quasigeostrophic two-level model simulation". *J. Atmos. Sci.*, **61**, 937–942 (2004).

[34] Smythe, W. D. and Moum J. N., Anisotropy of turbulence in stably stratified mixing layers. *Phys. Fluids*, **12**, 1343–1362.

[35] Tulloch, R. and K. S. Smith, A theory for the atmospheric energy spectrum: Depth-limited temperature anomalies at the tropopause. *Proc. Nat. Acad. Sci.*, **103**, 14690–14694 (2006).
[36] Tulloch, R. and K. S. Smith, Quasigeostrophic turbulence with explicit surface dynamics: Application to the atmospheric energy spectrum. *J. Atmos. Sci.*, **66**, 450–467 (2009).
[37] Tung, K. K., Reply. *J. Atmos. Sci.*, **61**, 943–948 (2004).
[38] Tung, K. K. and W. W. Orlando, The k^{-3} and $k^{-5/3}$ energy spectrum of atmospheric turbulence: Quasigeostrophic two-level model simulation. *J. Atmos. Sci.*, **60**, 824–835 (2003).
[39] Van Zandt, T. E., A universal spectrum of buoyancy waves in the atmosphere. *Geophys. Res. Lett.*, **9**, 575–578 (1982).
[40] Waite, M. L. and P. Bartello, Stratified turbulence dominated by vortical motion. *J. Fluid Mech.*, **517**, 281–308 (2004).
[41] Waite, M. L. and P. Bartello, The transition from geostrophic to stratified turbulence. *J. Fluid Mech.*, **568**, 89–108 (2006).
[42] Waite, M. L., and C. Snyder, The mesoscale kinetic energy spectrum of a baroclinic life cycle. *J. Atmos. Sci.*, **66**, 883–901 (2009).
[43] Warn, T., Statistical mechanical equilibria of the shallow water equations. *Tellus*, **38A**, 1–11 (1986).

A Perspective on Submesoscale Geophysical Turbulence

James C. McWilliams

1 The Dynamical Regime of Submesoscale Turbulence

Define the submesoscale regime as the geophysical fluid dynamics that arise from advective processes and that have a marginal degree of dynamical control by planetary rotation and stable density stratification. The degrees are conventionally measured by a Rossby number, $Ro = V/fL$ (V a horizontal speed, f the Coriolis frequency, L a horizontal length), and a Froude number, $Fr = V/NH$ (N a stratifica-

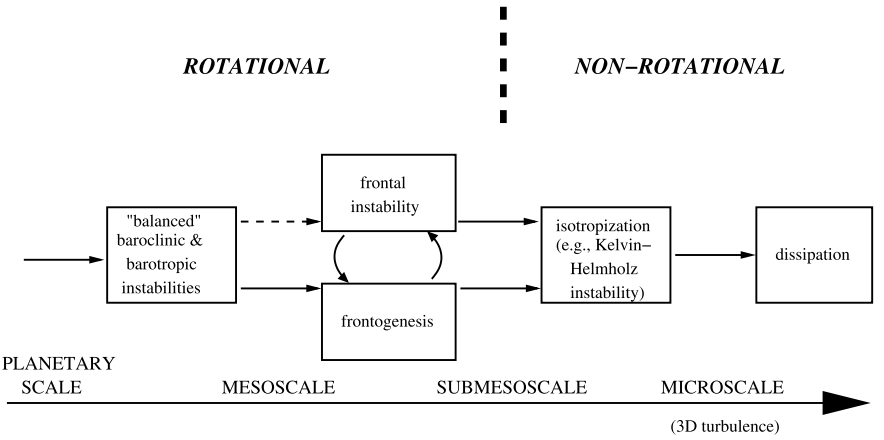

Fig. 1 Sketch of the flow of dynamical control and energy from the global forcing of the general circulation through the balanced mesoscale and partially-balanced submesoscale ranges down to the isotropic microscale where dissipation occurs.

James C. McWilliams
Institute of Geophysics and Planetary Physics, University of California, Los Angeles, CA 90095-1567, USA, e-mail: jcm@atmos.ucla.edu

D. Dritschel (ed.), *IUTAM Symposium on Turbulence in the Atmosphere and Oceans*, IUTAM Bookseries 28, DOI 10.1007/978-94-007-0360-5_11,

tion frequency, H a vertical length), respectively; small $Ro,\ Fr$ imply strong control. This regime lies in between the highly anisotropic ($H \ll L$) planetary and mesoscale regimes on larger scales — with small $Ro,\ Fr$, hence approximate diagnostic force balances: geostrophic in the horizontal direction and hydrostatic in the vertical direction — and the more isotropic microscale regime — with large $Ro,\ Fr$, hence little or no rotational, stratified control and frequent violations of diagnostic force balance. The activation of the submesoscale is primarily by energy transfer from mesoscale flows. Submesoscale turbulence occurs in both the ocean and atmosphere on horizontal scales $\leq\ \mathcal{O}(10)$ km and time scales $\leq\ \mathcal{O}(10^5)$ s. Inertia-gravity waves are considered a separate phenomenon since they have primarily non-advective generation and evolution, although they often co-populate the same space and time scales as submesoscale flows. Clouds are also considered as a separate phenomenon not considered here. Thus, the submesoscale regime is perhaps less simply matched to the atmosphere than the ocean, though relevant for both. My focus below is oceanic.

Much of our dynamical understanding of larger-scale dynamics comes from the asymptotic approximation with $Ro\ Fr\ \rightarrow\ 0$, called quasigeostrophy or, more generally, balanced dynamics. Two important properties of quasigeostrophic turbulence [4] are (1) inverse energy cascade and vanishing energy dissipation rate when the Reynolds number $Re = VL/\nu$ (ν the viscosity)) is large, and (2) asymptotic consistency of the foundational assumptions of small $Ro,\ Fr$ in turbulent spectra even in the large horizontal and vertical wavenumber ranges.

Inverse cascade poses a conundrum about the energy balance of the general circulation: how is climate equilibrium achieved with sufficient dissipation to balance continual large-scale forcing by planetary radiation and surface wind stress? Quasigeostrophic asymptotic consistency says there is no relief from this conundrum in the small-scale limit, apart from whatever dissipation might occur in parameterized turbulent boundary layers. However, another answer might come from the partial invalidity of these two properties of balanced, large-scale flows if there were mechanisms for forward energy cascade as a route to unbalanced turbulence and viscous dissipation as in Kolmogorov's theory (Fig. 1). This possibility is now known to be true, and submesoscale turbulence is the collective term for its occurrence. We are still in an early phase of learning about submesoscale turbulence, as previous computational and observational limitations (plus a few mental ones as well) are now being overcome.

There is certainly the possibility that submesoscale flows, as defined here, might interact with inertia-gravity waves because of their scale overlap. Similarly, as part of their loss of geostrophic, hydrostatic balance, submesoscale flows can sometimes exhibit "spontaneous emission" of subsequently propagating inertia-gravity waves [24; 26]. However, this is not an evident feature of the illustrative flows presented in this essay, where the transfer of energy from the mesoscale into the submesoscale is primarily a local advective process.

2 The Frontogenetic Route

Two computational testbed problems for the possibility of submesoscale turbulence are sketched in Fig. 2. In each problem, as with the general circulation itself, there is a mean, large-scale forcing of a mean circulation that is unstable to approximately quasigeostrophic mesoscale eddies that evolve into turbulence. Calculations are made with large computational grids and large Re, and they are integrated to a period of stationary statistical equilibrium.

With increasing Re and grid size, each of these simulations spontaneously exhibits a submesoscale transition evident in much bigger small-scale variances in velocity, buoyancy (temperature), and vorticity than are consistent with quasigeostrophic turbulent cascades. The initiating mechanism is frontogenesis, locally acting much as originally described in the atmospheric synoptic regime [10], but in the oceanic context it is much more pervasive than historically envisioned in the weather context: near-surface temperature gradients in the presence of horizontal deformation flows (*e.g.*, $u_d = -\alpha x,\ v_d = \alpha y,\ w_d = 0$, with 2α the rate of strain) have super-exponentially growing vertical and horizontal gradients in combination with a geostrophic along-front flow and an ageostrophic secondary circulation in the cross-frontal section. In these flows mesoscale eddies provide the important deformation flows around their periphery, and the submesoscale variances are largest

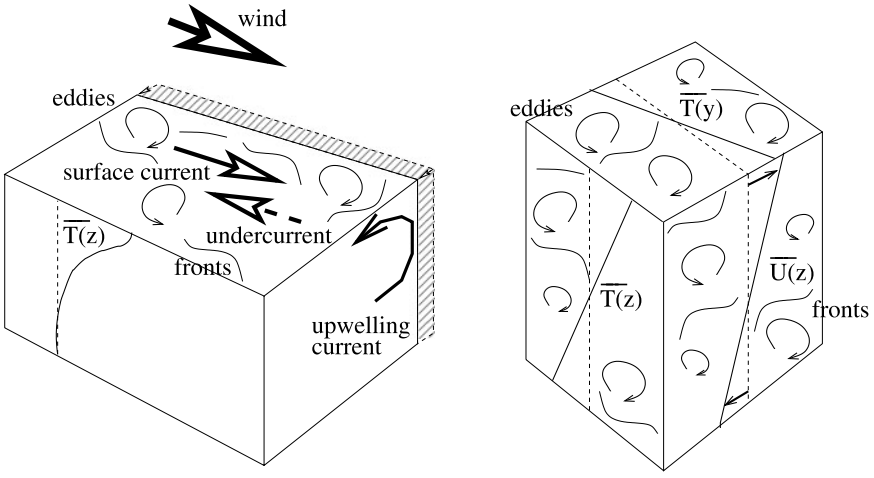

Fig. 2 Idealized problems for investigating the transition from mesoscale to submesoscale turbulence. The Eastern Boundary Current has an equatorward wind forcing, flat bottom, straight coastline, variable $f(y)$, open lateral boundaries (except at the coast), and a shallow thermocline. Offshore surface Ekman transport causes coastal upwelling. Eady's problem has an artificially-maintained uniform vertical shear flow with uniform N and f, horizontal periodicity, and flux-free top and bottom boundaries. [2; 20]

there (Fig. 3). Ro and Fr become locally $\mathcal{O}(1)$ or larger because of their large horizontal and vertical shears, even while Ro, Fr remain small for the mean and mesoscale flow components. For example, the vertical vorticity ω^z is larger than f many places in Fig. 3, and this is a local measure of $Ro > 1$. Frontogenesis often leads to submesoscale frontal instability [18] (Fig. 4), generating frontal meanders and fragmentation, and giving rise to coherent vortices. These mechanisms develop positive (cyclonic) skewness in ω^z and negative (downwelling) skewness in vertical velocity w, both as expected from frontogenesis theory. The w magnitudes are much larger than those associated with larger flow scales, indicating that the submesoscale will dominate vertical material and buoyancy fluxes near the surface [11]. The vertical buoyancy flux ($w'T' > 0$) has a restratifying effect on the mean vertical buoyancy profile, thus working against the destratifying microscale turbulent fluxes (*i.e.,* mixing) in the surface boundary layer; it also converts potential energy to kinetic. Overall dissipation in the upper ocean is enhanced by the surface concen-

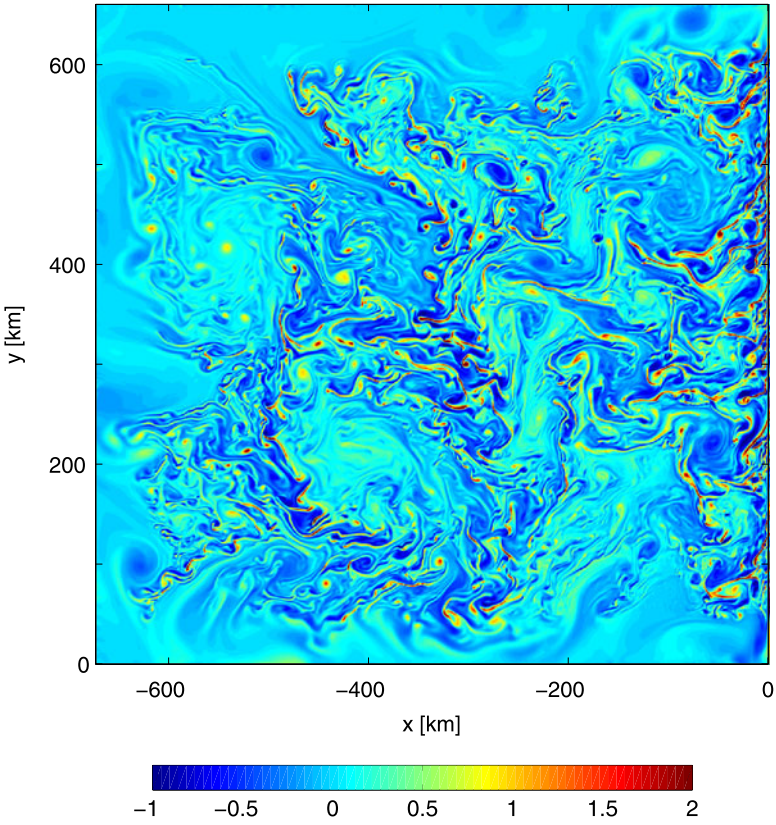

Fig. 3 Snapshot of surface vertical vorticity ω^z normalized by f in an idealized Eastern Boundary Current. Intense submesoscale activity — fronts, frontal instabilities, and coherent vortices — occurs near the boundary and surrounding the mesoscale eddy centers. [2]

tration of submesoscale frontogenesis coincident with wind-driven boundary-layer turbulence.

Diagnostic force balances are only partially valid in the submesoscale range, consistent with the theoretically predicted conditions for loss of temporal integrability with purely balanced dynamics [27].

Following the path of Kolmogorov for isotropic, homogeneous (non-rotating, unstratified) turbulence, basic descriptions of turbulence are often made with wavenumber spectra and spectral fluxes[1]. In the submesoscale regime the kinetic energy (KE) is primarily horizontal, and the most relevant potential energy is the available com-

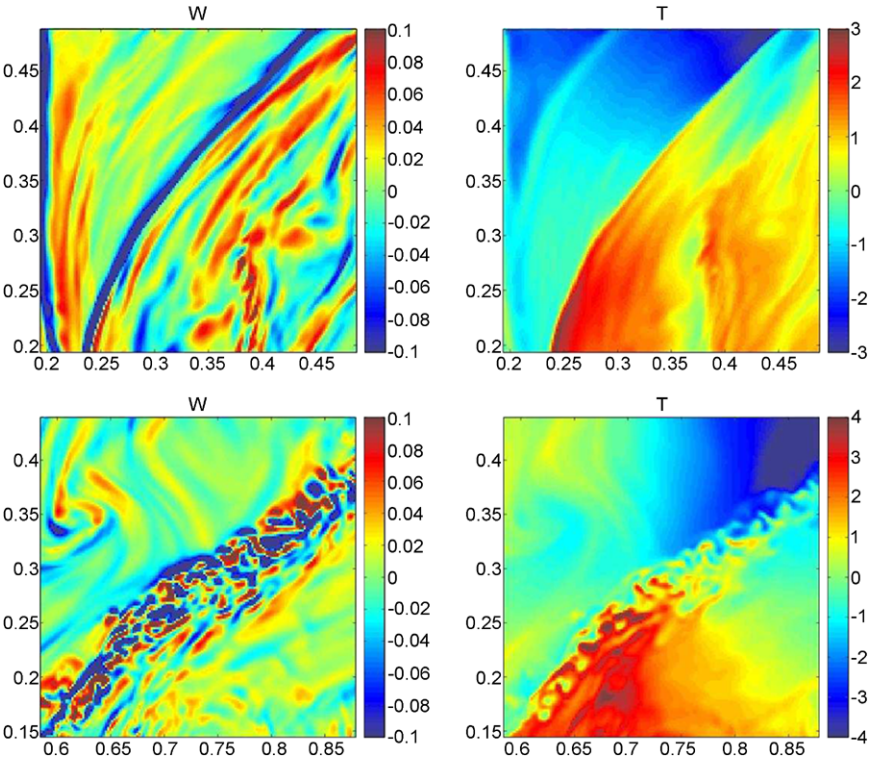

Fig. 4 Instantaneous horizontal maps of vertical velocity w (left column) and temperature T (right column) in Eady's flow at an interior vertical level. Units for the dependent variables and coordinate axes are non-dimensional. The spatial extent of the subdomain is a small fraction of both the total domain and the first baroclinic deformation radius. In the top row the dominant submesoscale front in T is stable and has a frontogenetic secondary circulation in w (downward on the dense side and upward on the light side). In the bottom row the dominant front is actively unstable (primarily by horizontal shear instability). [20]

[1] Most natural systems are inhomogeneous and exhibit intermittency in the form of spatially sparse coherent structures (*e.g.,* fronts). So a spectral description of turbulent dynamics is only a partial characterization at best.

ponent (APE) [9]. In the range of wavenumbers dominated by submesoscale frontogenesis, the horizontal wavenumber k_h spectra for horizontal velocity (KE) and temperature have approximately k_h^{-2} shapes (shallower than the quasigeostrophic enstrophy inertial-range shape of k_h^{-3}). This is consistent with ship-survey and satellite measurements [7] in the relevant wavenumber range. For even smaller scales, which we associate with the arrest of frontogenesis through frontal instability, both the KE and APE spectra shallow slightly toward a $k_h^{-5/3}$ shape, with the KE spectrum amplitude about 3 to 4 times larger than for APE [21]. Advective spectral energy fluxes show forward APE flux at almost all k_h and show inverse flux for KE in the mesoscale and larger submesoscale ranges, reversing to forward flux at larger wavenumbers [2; 20]. The spectral fluxes are nearly independent of k_h in the sub-frontal range, consistent with the concept of a constant-flux, inertial-cascade range. Thus, at the smallest scales, both KE and APE exhibit forward energy cascades that plausibly continue down through the microscales to viscous and diffusive energy dissipation and provide significant energy for diapycnal material mixing (often attributed to breaking inertia-gravity waves). These idealized problems give a qualitatively sufficient answer to the conundrum of balanced inverse energy cascade and a turbulent route to dissipation (Sec. 1), though it has yet to be quantified for the general circulation.

Geophysical fluid dynamicists have found the asymptotic model called surface quasigeostrophy (SQG) a useful paradigm. SQG is defined as geostrophic, hydrostatic balance for flows with nonzero surface horizontal buoyancy gradient and zero interior potential vorticity [8]. It manifests frontogenesis, shallow wavenumber spectra, and forward cascade of APE near the surface. On the other hand, SQG does not allow the types of frontal instability that seem most relevant, violations of diagnostic force balance, ω^z and w skewness, nor forward energy flux for volume-integrated KE + APE.

3 Other Submesoscale Generation Routes

Mixed-Layer Instability

Because of boundary-layer mixing, near-surface stratification is often weak. This implies that the quasigeostrophic baroclinic instability of a vertically sheared current occurs with a smaller horizontal scale than the baroclinic deformation radius typical of mesoscale currents [1]. This mechanism is therefore a source of submesoscale energy in the upper ocean. It is not an important process in the two flows in Sec. 2, neither of which have a thick mixed layer that favors this type of instability; nevertheless, once generated, these submesoscale currents may undergo analogous frontogenetic and frontal instability on even smaller scales. However, in a simulation of wintertime circulation over the Argentinian shelf [3], outbreaks of submesoscale mixed-layer instability arise even in the presence of parameterized boundary-layer turbulence.

Wakes and Topography

Flows past islands and headlands develop narrow lateral boundary layers whose instabilities may spawn mesoscale and submesoscale eddies after separation [6]. More generally, Earth's topography has a broad k_h spectrum, so adjacent mesoscale flows can transfer energy directly into the submesoscale range, either through balanced dynamics or as lee or boundary-trapped waves (quasi-stationary inertia-gravity waves). This mechanism is as yet little explored for turbulent flows, but it seems likely to be an important source of submesoscale energization, loss of diagnostic force balance, and forward energy cascade.

Localized Diapycnal Mixing

In a rotating, stratified fluid, a localized diapycnal mixing event in the interior is followed by adjustment toward a balanced, isolated, anticyclonic vortex after radiating inertia-gravity waves [17]. The plausible sources of mixing are bottom boundary interactions (*e.g.,* a detaching turbulent boundary layer) or breaking inertia-gravity waves [13]. The oceanic interior is known to be full of sparsely distributed, long-lived anticyclones [16].

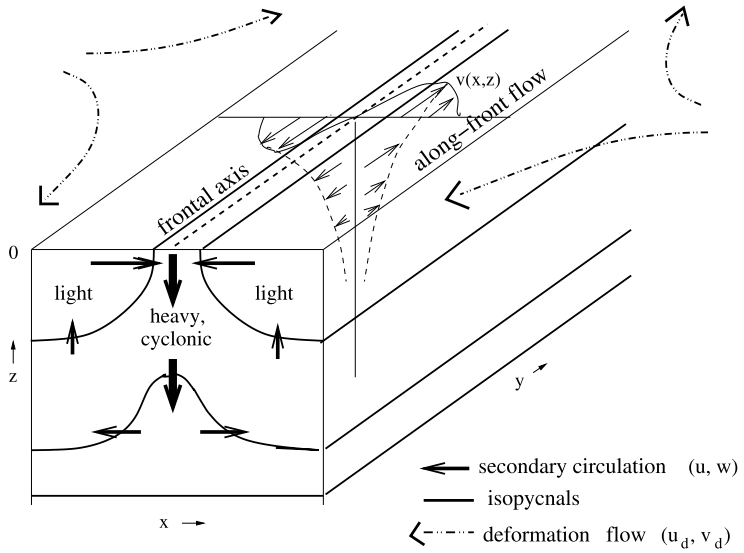

Fig. 5 Sketch of the configuration for 2D filamentogenesis in a horizontal deformation flow $(u_d, v_d, 0)$. Lateral and vertical scales of the filament shrink with time; the buoyancy field b and along-filament flow v stay close to hydrostatic, geostrophic balance. The secondary circulation $(u, 0, w)$ has two cells with intense central surface convergence and downwelling. [19]

Filamentogenesis

Balanced mesoscale dynamics are effective at generating elongated filaments in potential vorticity and material concentrations (tracers) along interior isopycnal surfaces and in temperature or other tracers along the surface. The filaments themselves have an essentially passive dynamics in quasigeostrophy, including in SQG, when they are under the influence of a strong strain field associated with the larger mesoscale eddies; nevertheless, they do have an associated ageostrophic secondary circulation that may have large w near the surface [11]. In more general dynamics the filamentary gradients can grow super-exponentially in a deformation flow, analogous to frontogenesis, and exhibit stronger secondary circulations with an asymmetric dependence on the sign of the buoyancy (temperature) anomaly in the filamentary core [19]. A surface cold filament (Fig. 5) has intense surface convergence and central downwelling. Since surface convergence concentrates buoyant surfactants, which in turn suppresses short surface gravity waves, filamentogenesis is a plausible explanation for the abundant lines visible in reflectance images (*e.g.,* sun glint and Synthetic Aperture Radar) with approximately submesoscale spacing.

Spirals on the Sea

An old mystery is the spiral patterns of surfactant lines frequently seen in reflectance images; from the spiral-arm orientation, they are interpreted as cyclonic vortices, although this has never been confirmed with measurements *in situ* [22]. In a regional

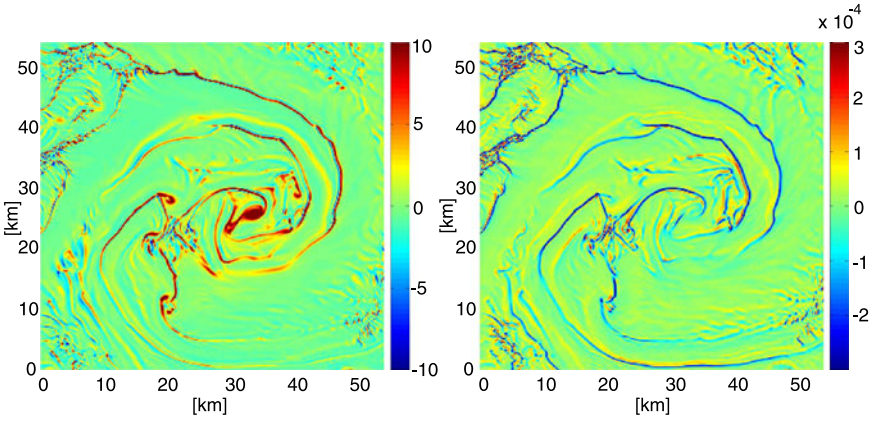

Fig. 6 Snapshot of a subdomain from a regional simulation of the upwelling circulation off Peru [5] showing a submesoscale surface cyclonic spiral vortex with frontal and filamentary arms seen in ω^z/f (left) and w (right) in a near-surface horizontal plane. Notice the mixture of two-signed frontal and one-signed filamentary lines in the secondary circulation outside the vortex core.

simulation of the equilibrium upwelling circulation off Peru [5], the use of aggressive grid-refinement into the submesoscale range allows spontaneous development of submesoscale spiral eddies through cyclogenesis by the roll-up of antecedent frontal and filamentary lines. In their mature stage the vortices show active vertical velocity and surface convergence along the spiral arms left over from the vortex generation event (Fig. 6). An unresolved question is why near-surface submesoscale activity is dominated by different mixtures of frontogenesis, mixed-layer instability, filamentogenesis, or spiral eddy generation in different situations; our present hypothesis is that the upper-ocean stratification profile has a strong role in this selection.

4 Stratified, Non-Rotating Turbulence

Strong stratification even in the absence of rotation supports two distinct classes of flow: internal gravity waves and stratified turbulence. The latter has anisotropic flows with small w, sometimes referred to as pancake vortices, and its available diagnostic force balance state is hydrostatic and cyclostrophic (not geostrophic since $f = 0$). The two classes often evolve with little mutual interaction. For a long time the energy cascade in stratified turbulence was poorly determined, but recent simulations with large Re show that the cascade is almost entirely in the forward direction and furthermore leads to large vertical shear with local $Fr \approx 1$ (*i.e.,* $H \approx V/N$) and to overturning motions at small scales reminiscent of Kelvin-Helmholtz instability [23; 12]. When $Fr_h = V/NL$ is small enough, an inertial-cascade range develops with nearly constant energy flux and a wavenumber spectrum shape of $k_h^{-5/3}$ for both KE and APE, with the KE spectrum amplitude about 3 to 4 times larger than APE [14]. There is a striking phenomenological similarity between the energy cascade behaviors in stratified turbulence and in rotating, stratified turbulence in the sub-frontal range (Sec. 2). Extending from the purely stratified regime with $F_h \ll 1$, increased f initiates a transition to some inverse energy cascade at larger scales [25]. These results suggest a rather seamless continuity from the submesoscale regime down to the isotropization events that terminate the stratified regime and initiate the microscale regime (Fig. 1). The inertial-range in stratified turbulence is a possible explanation for measured wavenumber spectra [15]. However, in a space of possible (Ro, Fr_h) values, it remains to be determined when, with increasing k_h in the energy cascades toward smaller scales, rotational dynamical control wanes before stratified control does. For example, centrifugal instability (*i.e.,* due to a change in sign of potential vorticity) is a process that may make a direct transition from rotational control to microscale turbulence without an intervening stratified turbulence regime.

5 Summary

In a rotating, stratified fluid, submesoscale turbulence may arise despite the strictures implied by quasigeostrophic dynamics. Submesoscale turbulence is characterized by forward energy cascade and partial violation of diagnostic force balance, providing a conduit from the planetary general circulation down to microscale mixing and dissipation. The variety of possible submesoscale phenomena in the atmosphere and ocean is still being explored.

Given a sustained fluctuation energy through-put (*e.g.,* from mean-flow instability) and dynamical equilibration away from solid boundaries and with large enough Re, then the following propositions seem to be valid:

- **rotating, stratified turbulence:** for any energy-peak $Ro,\ Fr \ll 1$ — no matter how small — frontogenesis and other mechanisms induce a submesoscale transition to an anisotropic, unbalanced forward energy cascade with local $Ro, Fr \sim 1$ and increasing with k_h.
- **non-rotating, stratified turbulence:**
  For any energy-peak $Fr_h, H/L \ll 1$ — no matter how small — the forward energy cascade extends in k_h to Kelvin-Helmholtz overturning with local $Fr, H/L \sim 1$, hence a transition to Kolmogorov's isotropic regime.

These are non-uniform $Ro,\ Fr \to 0$ asymptotic behaviors for multi-scale rotating, stratified turbulence at large Re, and are contrary to historical understanding.

Acknowledgements I greatly appreciate the collaborations with Xavier Capet, Francois Colas, Jeroen Molemaker, and Sasha Shchepetkin that made much of this research possible. I also appreciate support from the National Science Foundation and Office of Naval Research.

References

[1] Boccaletti, G., Ferrari, R., Fox-Kemper, B.: Mixed layer instabilities and restratification. J. Phys. Ocean. **37**, 2228–2250 (2007)
[2] Capet, X., McWilliams, J., Molemaker, M., Shchepetkin, A.: Mesoscale to submesoscale transition in the California Current System: (I) Flow structure and eddy flux. (II) Frontal processes. (III) Energy balance and flux. J. Phys. Ocean. **38**, 29–43, 44–64, 2256–2269 (2008a)
[3] Capet, X., Campos, E.J., Paiva, A.M.: Submesoscale activity over the Argentinian shelf. Geophys. Res. Lett. **35**, L15605 (2008b)
[4] Charney, J.: Geostrophic turbulence. J. Atmos. Sci. **28**, 1087–1095 (1971)
[5] Colas, F., Capet, X., McWilliams, J., Shchepetkin, A.: 1997-98 El Niño off Peru: A numerical study. Prog. in Ocean. **79**, 138–155 (2008)
[6] Dong, C., McWilliams, J., Shchepetkin, A.: Island wakes in deep water. J. Phys. Ocean. **37**, 962–981 (2007)

[7] Ferrari, R., Rudnick, D.: Thermohaline variability in the upper ocean. J. Geophys. Res. **105**, 16857–16883 (2000)
[8] Held, I., Pierrehumbert, R., Garner, S., Swanson, K.: Surface quasi-geostrophic dynamics. J. Fluid Mech. **282**, 1–20 (1995)
[9] Holliday, D., McIntyre, M.: On potential energy density in an incompressible, stratified fluid. J. Fluid Mech. **107**, 221–225 (1981)
[10] Hoskins, B., Bretherton, F.: Atmospheric frontogenesis models: Mathematical formulation and solution. J. Atmos. Sci. **29**, 11–37 (1972)
[11] Klein, P., Lapeyre, G.: The oceanic vertical pump induced by mesoscale and submesoscale turbulence. Ann. Rev. Marine Science **1**, 351–375 (2009)
[12] Laval, J., McWilliams, J., Dubrulle, B.: Forced stratified turbulence: Successive transitions with Reynolds number. Phys. Rev. E **68**, 036308, 1–8 (2003)
[13] Lelong, M., Sundermeyer, M.: Geostrophic adjustment of an isolated diapycnal mixing event and its implications for small-scale lateral dispersion. J. Phys. Ocean. **35**, 2352–2367 (2005)
[14] Lindborg, E.: The energy cascade in a strongly stratified fluid. J. Fluid Mech. **550**, 207–242 (2006)
[15] Riley, J., Lindborg, E.: Stratified turbulence: A possible interpretation of some geophysical turbulence measurements. J. Atmos. Sci. **65**, 2416–2424 (2008)
[16] McWilliams, J.: Submesoscale, coherent vortices in the ocean. Rev. Geophys. **23**, 165–182 (1986)
[17] McWilliams, J.: Vortex generation through balanced adjustment. J. Phys. Ocean. **18**, 1178–1192 (1988)
[18] McWilliams, J., Molemaker, M., Olafsdottir, E.: Linear fluctuation growth during frontogenesis. J. Phys. Ocean., in press (2009a)
[19] McWilliams, J., Colas, F., Molemaker, M.: Cold filamentary intensification and oceanic surface convergence lines. Geophys. Res. Lett. **36**, L18602 (2009b)
[20] Molemaker, M., McWilliams, J., Capet, X.: Balanced and unbalanced routes to dissipation in an equilibrated Eady flow. J. Fluid Mech., in press (2009a)
[21] Molemaker, M., McWilliams, J.: Available Potential Energy spectrum and spectral budget in rotating, stratified flows. J. Fluid Mech., in press (2009b)
[22] Munk, W., Armi, L., Fischer, K., Zachariassen, F.: Spirals on the sea. Proc. R. Soc. London **A456**, 1217–1280 (2000)
[23] Riley, J., de BruynKops, S.: Dynamics of turbulence strongly influenced by buoyancy. Phys. Fluids **15**, 2047–2059 (2003)
[24] Viudez, A., Dritschel, D.G.: Spontaneous generation of inertia-gravity wave packets by balanced geophysical flows. J. Fluid Mech. **553**, 107–117 (2006)
[25] Waite, M., Bartello, P.: The transition from geostrophic to stratified turbulence. J. Fluid Mech. **568**, 89–108 (2006)
[26] Wang, S., Zhang, F., Snyder, C.: Generation and propagation of inertia-gravity waves from vortex dipoles and jets. J. Atmos. Sci. **66**, 1294-1314 (2009)
[27] Yavneh, I., Shchepetkin, A., McWilliams, J., Graves, P.: Multigrid solution of rotating, stably stratified flows: The balance equations and their turbulent dynamics. J. Comp. Phys. **136**, 245–262 (1997)

Spectra and Distribution Functions of Stably Stratified Turbulence

Jackson R. Herring & Yoshifumi Kimura

Abstract We examine homogeneous stably stratified turbulence both freely decaying and randomly forced cases. Our principal focus is the scale size distribution of the eddies and waves (spectra) comprising the flow. We also present results for the rate of decay for unforced flows. The tools used in both spectral and decay studies are direct numerical simulations (DNS), combined with elements of the statistical theory of turbulence. For situationally maintained flows, our results are consistent with spectra that are steeper than Kolmogorov at large scales but fair over into the normal isotropic inertial range at smaller scales. The DNS decay rate of freely decaying strongly stratified turbulence is consistent with t^{-1}. For stratified flow, our simulations are consistent with a near equilibration between waves and vortical eddies.

1 Equations of Motion and their Economical Representation

The Navier–Stokes equations under the Boussinesq approximation may be nondimensionalized as:

$$(\partial_t - \nabla^2)\mathbf{u} = -\nabla p - \mathbf{u}\cdot\nabla\mathbf{u} - \hat{\mathbf{g}}N\theta + 2\boldsymbol{\Omega}\times\mathbf{u} \tag{1}$$

$$(\partial_t - \sigma\nabla^2)\theta = Nw - \mathbf{u}\cdot\nabla\theta \tag{2}$$

$$\nabla\cdot\mathbf{u} = 0. \tag{3}$$

Jackson R. Herring
N.C.A.R., P.O. Box 3000, Boulder, CO 80307, USA
e-mail: jackson.herring8@gmail.com

Yoshifumi Kimura
Graduate School of Mathematics, Nagoya University,
Furo-cho, Chikusa-ku, Nagoya 464-8602, Japan
e-mail: kimura@math.nagoya-u.ac.jp

D. Dritschel (ed.), *IUTAM Symposium on Turbulence in the Atmosphere and Oceans*,
IUTAM Bookseries 28, DOI 10.1007/978-94-007-0360-5_12,

Here $\mathbf{u} = (u, v, w)$ and θ is the deviation of the temperature field from its mean, which has constant vertical gradient. We shall study the solutions to the N-S system numerically in the homogeneous context in which the Fourier transforms of the fields in (1), (2), (3) are the variables advanced Forward in time from their initial values. We find it convenient to represent the velocity field $\mathbf{u}(\mathbf{k})$ by:

$$\left\{ \begin{array}{c} \mathbf{u} \\ \mathbf{e}_1 \\ \mathbf{e}_2 \end{array} \right\} = \left\{ \begin{array}{c} \mathbf{e}_1(\mathbf{k})\phi_1(\mathbf{k}) + \mathbf{e}_2(\mathbf{k})\phi_2(\mathbf{k}) \\ (\mathbf{k}\times\hat{\mathbf{g}})/|\mathbf{k}\times\hat{\mathbf{g}}| \\ \mathbf{k}\times(\mathbf{k}\times\hat{\mathbf{g}})/|\mathbf{k}\times(\mathbf{k}\times\hat{\mathbf{g}})| \end{array} \right\} \tag{4}$$

where $\mathbf{e}_\lambda$ is:

$$\left\{ \begin{array}{ccc} e_1^1 & e_1^2 & e_1^3 \\ e_2^1 & e_2^2 & e_2^3 \end{array} \right\} = \left\{ \begin{array}{ccc} \sin\varphi & -\cos\varphi & 0 \\ \cos\vartheta\cos\varphi & \cos\vartheta\sin\varphi & -\sin\vartheta \end{array} \right\} \tag{5}$$

We may replace the Fourier transforms of $\mathbf{u}(\mathbf{k},t), \theta(\mathbf{k},t)$ by $(\phi_1, \phi_2, \theta) \equiv \Psi_i$ (i=1,2,3):

$$\partial_t \Psi + L\Psi = NL \tag{6}$$

where

$$L = \left\{ \begin{array}{ccc} 0 & -\mathscr{C} & 0 \\ \mathscr{C} & 0 & \mathscr{S} \\ -0 & -\mathscr{S} & 0 \end{array} \right\} \tag{7}$$

Here, $\mathscr{C} = 2\Omega\cos\vartheta$, $\mathscr{S} = N\sin\vartheta$, and NL represents the nonlinear terms: $NL = (F_1, F_2, F_3)$. Eigenvalues of L are $\lambda = i(\pm\sigma, 0)$, $\sigma = \sqrt{N^2\sin^2\vartheta + 4\Omega^2\cos^2\vartheta}$.

In the discussion to follow, we shall sometimes find it convenient to employ a representation of (6) in which the linear part is diagonal. The transformation that diagonalizes (6) and (7) is:

$$\left\{ \begin{array}{c} \psi_1 \\ \psi_2 \\ \psi_3 \end{array} \right\} = \left\{ \begin{array}{ccc} ic/\sqrt{2} & -ic/\sqrt{2} & s \\ 1/\sqrt{2} & 1/\sqrt{2} & 0 \\ is/\sqrt{2} & -is/\sqrt{2} & -c \end{array} \right\} \left\{ \begin{array}{c} \chi_1 \\ \chi_2 \\ \chi_3 \end{array} \right\}, \tag{8}$$

where, $\chi_i \equiv \langle L_i|\psi\rangle$, and $c = \mathscr{C}/\sigma$, $s = \mathscr{S}/\sigma$. Here $|L_i\rangle$ are the eigen vectors of L. The matrix above has its inverse as its conjugate adjoint. The equations for χ_i are then:

$$\left\{ \begin{array}{ccc} \partial_t + i\sigma & 0 & 0 \\ 0 & \partial_t - i\sigma & 0 \\ 0 & 0 & \partial_t \end{array} \right\} \left\{ \begin{array}{c} \chi_1 \\ \chi_2 \\ \chi_3 \end{array} \right\} = \left\{ \begin{array}{ccc} -ic & 1 & -is \\ ic & 1 & is \\ s & 0 & -c \end{array} \right\} \left\{ \begin{array}{c} F_1 \\ F_2 \\ F_3 \end{array} \right\} \tag{9}$$

with

$$\left\{ \begin{array}{c} \chi_1 \\ \chi_2 \\ \chi_3 \end{array} \right\} = \left\{ \begin{array}{ccc} -ic & 1 & -is \\ ic & 1 & is \\ s & 0 & c \end{array} \right\} \left\{ \begin{array}{c} \phi_1 \\ \phi_2 \\ \theta \end{array} \right\} \tag{10}$$

Recall $(\phi_1, \phi_2, \theta) = (\psi_1, \psi_2, \psi_3)$ and (8) which says:

$$\psi_1 = \frac{ic}{\sqrt{2}}(\chi_1 - \chi_2) + s\chi_3, \psi_2 = \frac{1}{\sqrt{2}}(\chi_1 + \chi_2), \psi_3 = \frac{is}{\sqrt{2}}(\chi_1 - \chi_2) - c\chi_3 \quad (11)$$

2 Some Historical Comments

Large scale atmospheric motion is largely two–dimensional both because of geometrical constraints and because its stable stratification and rotation combine to give a dynamics that is to first order layered two-dimensional flow. The observed horizontal spectrum in the mesoscale range has been measured by Nastrom, Gage, & Jasperson (1984) to be near $k_\perp \sim k^{-5/3}$. Here, $\mathbf{k}_\perp \equiv (k_x, k_y, 0)$. This suggested to the above authors that the dynamics could be an inverse cascade range which is forced at small thunder-storm scales. One problem with this interpretation is that the assumption underlying quasi-geostrophy become progressively weaker as the scale of the flow becomes smaller; the Rossby number, whose smallness is needed to assure the validity of the quasi-geostrophic theory, becomes of order unity in the scale–region where needed.

Nonetheless, it could be that strongly stratified turbulence could be in some sense two dimensional so that the violation of the quasi-geostrophic constraints is not a problem. Here we note the work of Riley *et al.* (1982), and Lilly (1983). Their research indicated that two-dimensional flow in *decoupled* horizontal layers emerged as the leading order description in the limit as the (inverse N) Froude number vanishes. Their approximation was re-formulated by Grote and Majda (1997), with essentially the same result but more rigor.

Early attempts to confirm an inverse cascade numerically were not successful. One such study is reproduced in Fig. 1 (from Herring & Métais 1989). Here, the two-dimensional small scale forcing and spectral range (64^3) is identical to that of Lilly (1971). During the initial 2-D phase, the total energy gradually grows, typical of forced flows without large scale damping. At t=1, a small three dimensional perturbation (Φ_2) is introduced. It grows exponentially in approximate accord with the empirical rule of Rotta (1951). Spectra for Φ_1 are shown in in the top part of the figure after these components have reached their stationary values. Several values of N are shown, but for none of these is there a significant inverse cascade.

We note that $\Phi_1(k_\perp)$ is a rough measure of the two-dimensional energy.[1] Apparently the two dimensional layers which move in opposing direction as proposed

[1] $\Phi_2(k_\perp)$ also contributes to the horizontal energy. We have,

$$\langle \mathbf{u}_\perp(\mathbf{x}) \cdot \mathbf{u}_\perp(\mathbf{x} + \hat{n}\zeta) \rangle = \int \exp(i\zeta \hat{n} \cdot \mathbf{k}) dk_z k_\perp dk_\perp \cdot \{\Phi_1(k_\perp, k_z) + \Phi_2(k_\perp, k_z) \cos^2 \vartheta\} \quad (12)$$

Similarly,

$$\langle w(\mathbf{x}) w(\mathbf{x} + \hat{n}\zeta) \rangle = \int \exp(i\zeta \hat{n} \cdot \mathbf{k}) dk_z k_\perp dk_\perp \cdot \Phi_2(k_\perp, k_z) \sin^2 \vartheta = \mathscr{F}(k_\perp, k_z) \quad (13)$$

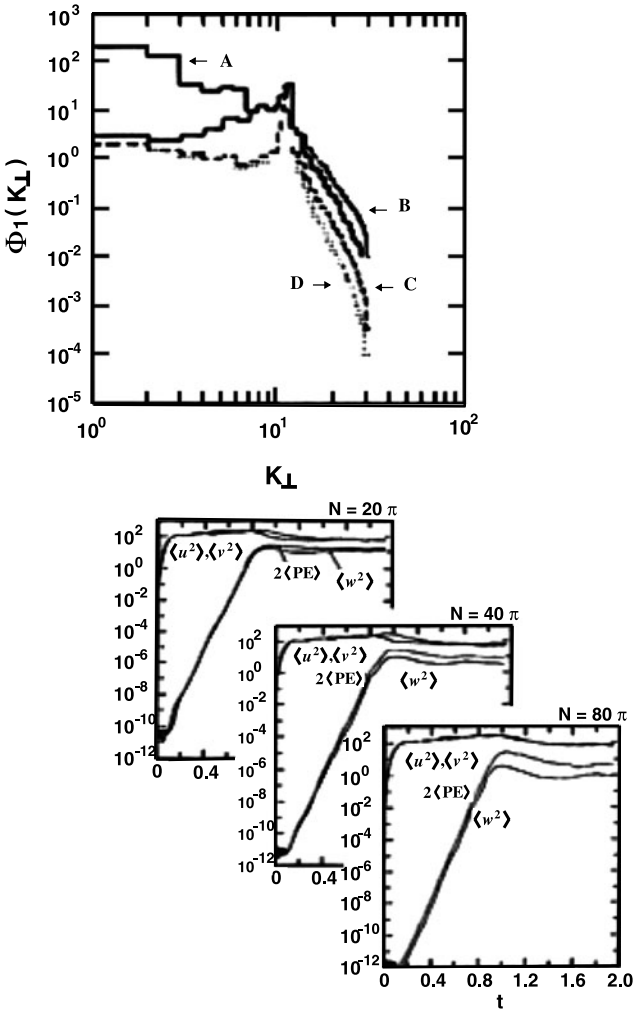

Fig. 1 Upper panel: $\Phi_1(k_\perp)$ energy spectra for differing values of $N = \pi(0, 10, 20, 30)$. Curve A is unperturbed 2-D turbulence randomly forced at $k_\perp = 12$. Curves marked B, C, & D are progressive the larger N. Three lower panels: evolution of total horizontal (top curves); potential energy and vertical kinetic energy, lower two. The vertical motion is introduced as a small initial perturbation. Three stratifications are shown, as labeled in the top right-hand corner of the panels.

by Riley *et al.* (1982) exert sufficient friction on each other to arrest any possible inverse cascade.

We should note that the characterization of the spectra of stratified turbulence with their horizontal or vertical projections is an inadequate characterization. In

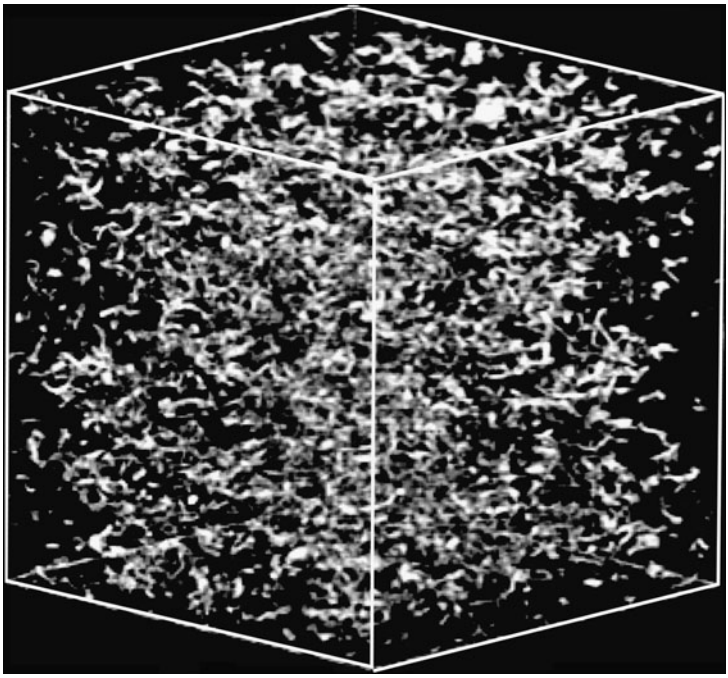

Fig. 2 Enstrophy distribution just before stratification is switched on at the time of maximum total enstrophy. From Herring *et al.* (2006).

these crude early simulations we recorded the number of spherical harmonics $P_n(\cos\vartheta)$ needed to describe the three dimensional spectra. We estimated (unpublished) $n \simeq 10$.

3 More Recent Numerical Results

Higher resolution DNS affords a more detailed glimpse into the structures of stratified flows. This is illustrated in Fig. 2 and Fig. 3, as taken from Herring *et al.* (2006), for which the resolution is 512^3.

Fig. 2 show (for decaying turbulence) the enstrophy distribution for unstratified flow. The usual vortex "worms" are seen. Fig. 3 shows the enstrophy distribution after a new equilibrium with strong stratification is established. The vortex tubes or "worms" are now replaced by "scattered pancakes". There seems to be an occasional pairing of vortex patches, and indicated by the arrow in Fig. 3.

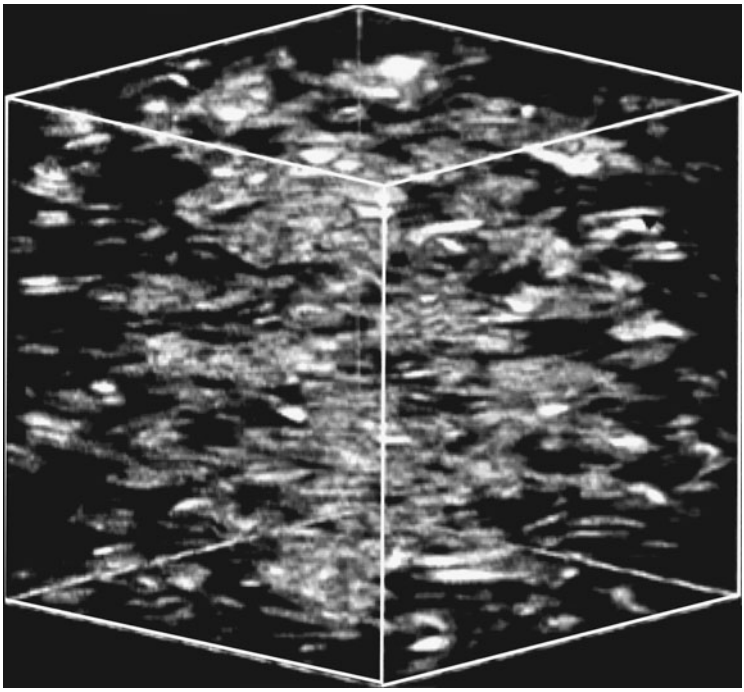

Fig. 3 Enstrophy distribution several eddy circulation times after stratification ($N^2 = 100$) is switched on. From Herring *et al.* (2006).

Isotropic turbulence is known to have strong departures from Gaussianity. Thus although the distribution function for the velocity field is near Gaussian that for its gradients is more nearly exponential or even more more "fat tailed". It is interesting in this connection that stratification seems to restore a Gaussianity. This is demonstrated in Fig. 4 which shows the PDF for $\partial u/\partial z$ (from Métais & Herring 1987). We remark that the same "Gaussianization" applies to the Eulerian acceleration: for isotropic turbulence, the PDF of the acceleration is broader than exponential, while that for strongly stratified turbulence more nearly Gaussian. The approximate picture of stratified flow as layered two dimensional flow is certainly born out in these simulations but the strongly intermittent character of two dimensional turbulence is not a feature of stratified turbulence. Some insight into why this is so has been suggested by Fincham *et al.* (1994), who argued that by tracing a vortex line that connects to adjacent vortices one can see that the strong isolated vortices often found in two-dimensional turbulence are prohibited.

For strong stratification one could argue that rapid distortion theory (RDT) may be invoked as a suitable basis for understanding the flow. In fact, Kaneda and Ishida

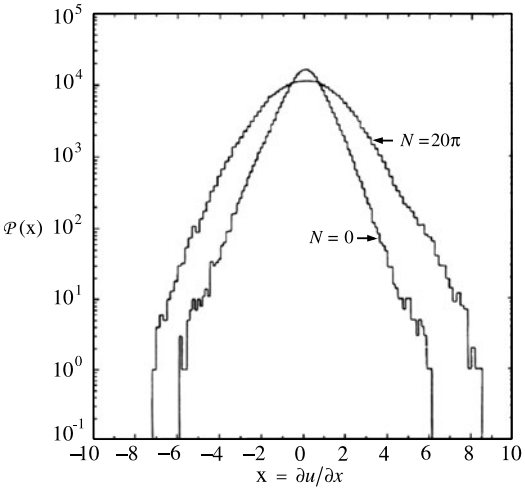

Fig. 4 PDF of $\partial u_\perp/\partial z$ for stratified turbulence as compared to unstratified. From Métais & Herring (1989).

(2000) have proposed this as a procedure to estimate the suppression on vertical diffusion in stratified turbulence. Our simulations give satisfactory results for the case in which both rotation and strong stratification are present. However, if only stratification is present, RDT tends to over estimate the suppression of vertical diffusion. This is shown in Fig. 5. Thus RDT tends to underestimate the squashing of vortex patches, which means that non-linear effects must play a significant role in enhancing two-dimensionality.

Finally we present spectra $\Phi_1 = \langle|\phi|^2\rangle$, $\Phi_2 = \langle|\phi_2|^2\rangle$ and $\Theta = \langle|\theta|^2\rangle$. These quantities are anisotropic and we show here only their cylindrically accumulated values $(\Phi(k_\perp)\cdots)$ and spherically accumulated spectra $(\Phi(|\mathbf{k}|)\cdots)$. The first of these relates to the spectra that measure the horizontal covariance.[2] The cylindrically accumulated spectra are depicted in Fig. 6, while those spherically accumulated are in Fig. 7. Here, $N = 10$, a quite strong stratification. We note that Φ_2 and Θ are quite similar, with $\Theta \sim \Phi_2$ for $N = 10$.[3] For the spherically accumulated spectra (Fig. 8) there seems little evidence of a power law, except at large $|\mathbf{k}|$, where one may argue for $|\mathbf{k}|^{-3}$. The $k_\perp$ spectra, however show evidence for $\Phi_1(k_\perp) \sim k_\perp^{-3}$ and $\Phi_2(k_\perp) \sim k_\perp^{-2}$.

[2] We note here that the second order structure function,

$$\mathscr{S}_f(d) = \langle(u_x(\mathbf{x}) - u_x(\mathbf{x}+\hat{\mathbf{i}}d))^2\rangle \tag{14}$$

$$\sim \pi \int_0^\infty [\{J_1(x)/x\}_{x\to 0} - J_1(x)/x]\Phi_1(k_\perp)k_\perp dk_\perp + \mathscr{O}\{\Phi_2(k_\perp,k_z)\},\ x = k_\perp d \tag{15}$$

[3] The non dimensionalization used in the DNS has the N removed from equation (1), and the Nw of (2) replaced by $N^2 w$.

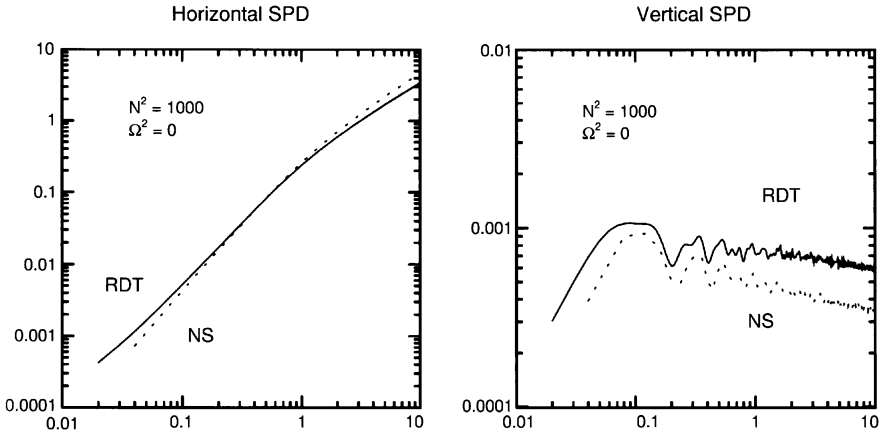

Fig. 5 Single particle diffusion, DNS solid line, RDT dashed line.

We should remark that spectra of these figures are at resolution 512^3. More recent higher resolution simulations at 1024^3 show a similarity to these spectra. They are at higher Reynolds number and both the -3 and -2 power laws fair over into an approximate -5/3 law at higher $k_\perp$.

4 Interpretation of DNS

The random pancake structures of Fig. 3 may be partially understood in terms of standard perturbation theory for the the spectra, $\langle \mathbf{u}(\mathbf{k})\mathbf{u}(-\mathbf{k})\rangle$. Consider stratified flow in the diagonal representation of (9) and (10). If we take the forcing terms as random driving force, then a standard estimate of the resulting magnitude of (χ_2, χ_3) (w and θ, essentially) would say that those amplitudes with minimum σ would be strongest. One way of achieving this is to have most of the participating wave vectors horizontal. If these vectors point in different directions at different heights, the flow is layered. Such an argument does not distinguish between horizontal streaks and flattened pancakes. Another possible arrangement is simply two dimensional flow, but as seen from Fig. 1, such is unstable.

Our results found here are consistent with $\Phi_1(k_\perp) \sim k_\perp^{-3}$ and $\Phi_2(k_\perp) \sim k_\perp^{-2}$. As noted earlier, at larger $k_\perp$, the 1024^3 simulations indicate that these fair over into -5/3, as indicated by Fig. 8 (Kimura & Herring 2010). A possible explanation for these results may be found in examining the normal mode analysis as in (9) and (10). A closure approximation to these equations would suggest that the eddy viscosity

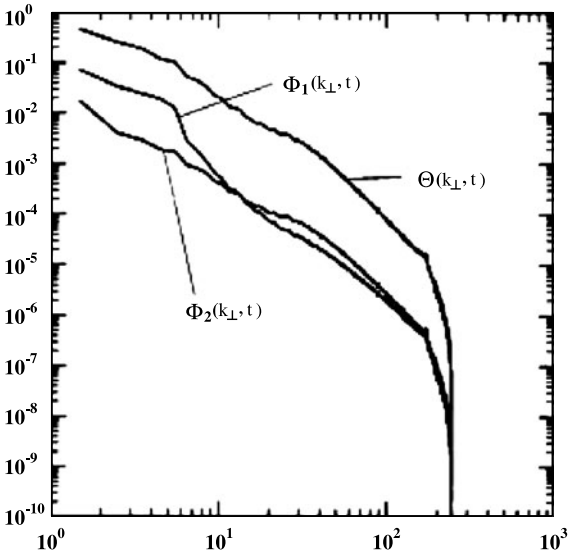

Fig. 6 Snapshot of $\Phi_1(k_\perp)$, $\Phi_2(k_\perp)$ and $\Theta(k_\perp)$ spectra for the case in which Φ_1*is* randomly forced at $k_\perp$=5. Time of snapshot: $t = 27.5$ eddy circulation times; stratification, $N = 10$; viscosity, $\nu = 0.001$.

that would determine the steady state intensities for isotropic turbulence should be augmented by the factor $\sigma = N\sin\vartheta$ for stratified flow. Of course that makes the eddy damping complex, but the dispersive nature of gravity wave would impart a real damping effect when averaged over the polar angle. We have suggested in the past (Kimura & Herring 1996) that such an analysis implies a spectrum

$$\Phi_2(k) = \gamma\sqrt{\varepsilon N}k^{-2} \tag{16}$$

provided N is much larger than the eddy turnover frequency. For Φ_1 the case is less clear since the frequency for ϕ_1 in (9) and (10) is zero. Notice that here we have not distinguished between $|\mathbf{k}|$ and $k_\perp$, since our rough argument does not take into account the degree of anisotropy. Other proposals for the dependence of the energy spectrum on stratification are by Holloway (1988) and Carnevale *et al.* (2001).

5 Concluding Comments

Our DNS indicates that stratified turbulence to be much less intermittent than isotropic turbulence. The vortex tubes of the later are replaced by "scattered pancakes" of the former. For strong stratification, we have suggested two spectral re-

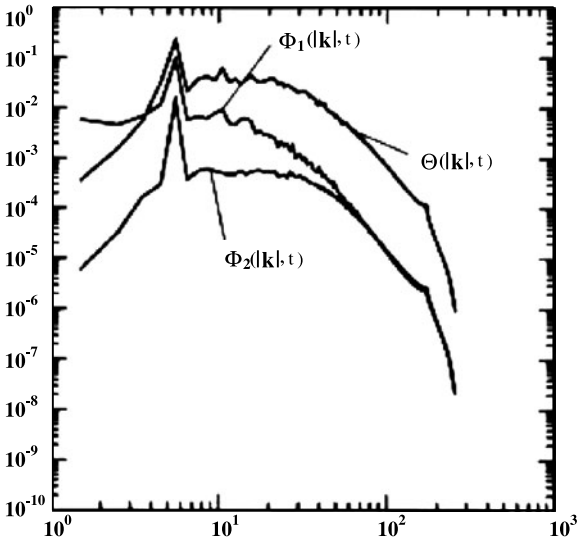

Fig. 7 Snapshot of $\Phi_1(|\mathbf{k}|)$, $\Phi_2(|\mathbf{k}|)$ and $\Theta(|\mathbf{k}|)$. Conditions as in the previous figure.

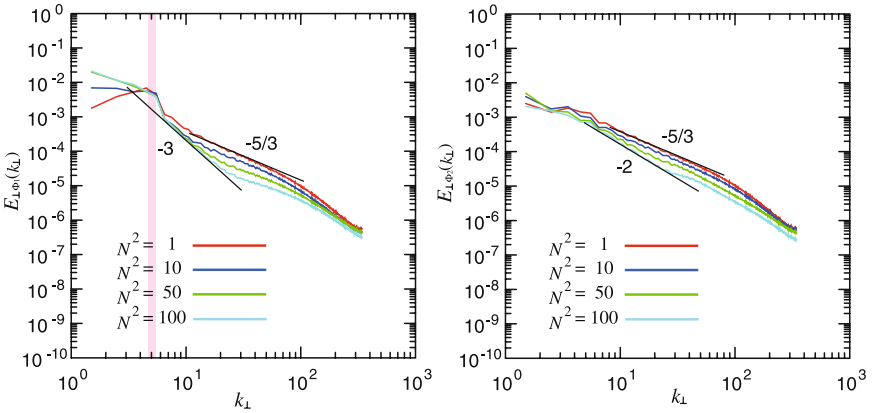

Fig. 8 $\Phi_1(k_\perp)$ (left panel) and $\Phi_2(k_\perp)$ (right) at late time after stationary state is reached. Vertical stripe indicates forcing scales for $\phi_1(\mathbf{k})$. $\phi_2(\mathbf{k})$ is unforced.

gions: a large-scale k^{-2} followed by $k^{-5/3}$. We have found preliminary evidence for such power laws, but only for the horizontally gathered vertical spectrum, and only for $\Phi_2(k_\perp)$. For the horizontal spectrum, we suggest $\Phi_1(k_\perp \sim k^{-3}$ followed by $k^{-5/3}$. Such is indicated by the spectra of Fig. 8, at (1024^3). In this way–perhaps–our DNS are reconciled with other theories and simulations such as those of Linborg (2006), Brethouwer, Billant, Lindborg & Chomez (2007), and Riley (2008) and the

theoretical results of Godeferd & Cambon (1994), and of Sukoriansky & Galperin, (2006) However, there is clearly a need for higher resolution to confirm these conclusions. We remark that our proposal that $E(k) \sim k^{-2}$ implies a lessening of the decay turbulence rate to (t^{-1}) or less is an asymptotic suggestion. That is, given any ν, $\exists$ an N $\ni E(k) \sim k^{-2}$ followed by a $k^{-5/3}$ range for sufficiently small ν. If a substantial $k^{-5/3}$ range exists, then the decay rate would be determined by the -5/3 range, and a standard decay rate $(t^{-10/7})$ should follow.

References

[1] Nastrom, G.D., Gage, K.S., Jasperson, W.H.: Atmospheric kinetic energy spectrum, $10^0 - 10^4$ km. Nature, **310**, 36–38 (1984)

[2] Riley, J.J., Metcalfe, R.W., Weissman, M.A.: Direct numerical simulations of homogeneous turbulence in density stratified fluids. *Proc. AIP Conf. on Nonlinear Properties of Internal Waves*, (ed. Bruce J. West), 79–112 (1982)

[3] Lilly, D.K.: Stratified turbulence and the mesoscale variability of the atmosphere. J. Atmos. Sci. **40**, 749–761(1983)

[4] Majda, A.J., Grote, M.J.: Model dynamics and collapse in decaying strongly stratified flows. Phys. Fluids **9** (10), 2932–2940 (1997)

[5] Herring, J.R., Métais, O.: Numerical experiments in forced stably stratified turbulence. J. Fluid Mech. **202**, 97–115 (1989)

[6] Lilly, D.K.: Numerical simulation of developing and decaying two-dimensional turbulence. J. Fluid Mech. **45**, 395–415 (1971)

[7] Rotta, J.: Statistische Theorie nichthomogener Turbulenz. Z. Phys. **129**, 127–147 (1951)

[8] Herring, J.R., Kimura, Y., James, R., Davidson, P., Clyne, J.: Statistical and Dynamical Questions in Stratified Turbulence, in *Mathematical and Physical Theory of Turbulence, Proceedings of the 2002 International Turbulence Workshop*, J. Cannon and B. Shivamoggi Eds., Chapman & Hall/CRC, Taylor & Francis Group, Boca Raton London New York (2006)

[9] Métais, O., Herring, J.R.: Numerical studies of freely decaying homogeneous stratified turbulence. J. Fluid Mech. **202**, 117–148 (1989)

[10] Fincham, A.M., Maxworthy, T., Spedding, G.R.: The horizontal and vertical structure of the vorticity field in freely-decaying, stratified grid–turbulence. *Preprints, 4th Symposium on Stratified Flows* **Vol. 2**, Sec. A4 (1994)

[11] Kimura, Y., Herring, J.R.: Energy spectra of stably stratified turbulence. Preprint, to be submitted to J. Fluid Mech. (2010)

[12] Kaneda, Y., Ishida, T.: Suppression of vertical diffusion in strongly stratified turbulence. J. Fluid Mech. **402**, 311–327 (2000)

[13] Kimura, Y., Herring, J.R.: Diffusion in stably stratified turbulence. J. Fluid Mech. **328**, 253–263 (1996)

[14] Holloway, G.: The buoyancy flux from internal gravity wave breaking. Dyn. Atmos. Oceans **12**, 107–125 (1988)

[15] Carnevale, C., Briscolini, M. & Orlandi, P.: Buoyancy-to-inertial-range transition in forced stratified turbulence. J. Fluid Mech. **427**, 205–239 (2001)
[16] Linborg, E.: The energy cascade in a strongly stratified fluid. J. Fluid Mech. **550**, 207–242 (2006)
[17] Brethouwer, G., Billant, P., Lindborg, E., Chomaz, J.-M.: Scaling analysis and simulation of strongly stratified turbulent flows. J. Fluid Mech. **585**, 343–368 (2007)
[18] Godeferd, F.S., Cambon, C.: Detailed investigation of energy transfer in homogeneous stratified turbulence. Phys. Fluids **6** (6), 2084–2100 (1994)
[19] Sukoriansky, S., Galperin, B.: Nonlinear Processes in Geophysics. Proc. London Math. Soc. **20**, 10–25 (2006)

Modeling mixing in two-dimensional turbulence and stratified fluids

Antoine Venaille and Joel Sommeria

Abstract A phenomenological model for turbulent mixing in a stratified fluid is presented. This model describes the evolution of the local probability distribution for the fluid density. It is based on an analogy between the mixing of vorticity in 2D turbulent flows and the mixing of density in (3D) turbulent flows.

1 Introduction

Models of turbulent mixing in stratified fluids are of wide interest in the context of oceanic and atmospheric flows, especially for sub-grid scale parameterization [5]. Although the processes of turbulent density mixing occur at small scales and short time scales, they considerably influence large scale dynamics by controlling water mass properties and the global stratification. It is therefore compulsory to describe carefully these processes.

We propose in this paper a new approach to describe the evolution of the local probability density function (PDF) for the fluid density. The advantage of such a statistical approach is to predict a coarse grained evolution of the system, without describing the complicated fine grained dynamics, but while keeping track of the conserved quantities of this dynamics, which are important physical constraints.

The most commonly used models for small scale density mixing are based on variations around the $k-\varepsilon$ models (see part I and III of [1] for a review). In those approaches, turbulence is represented locally by two parameters for which a dy-

Antoine Venaille
GFDL-AOS Princeton University, Princeton NJ, 08540, USA, e-mail: venaille@princeton.edu

Joel Sommeria
LEGI UMR 5519 (CNRS-Univ. Grenoble) BP 53, 38041 Grenoble, France, e-mail: joel.sommeria@legi.grenoble-inp.fr

D. Dritschel (ed.), *IUTAM Symposium on Turbulence in the Atmosphere and Oceans*, IUTAM Bookseries 28, DOI 10.1007/978-94-007-0360-5_13,

namical equation based on turbulent diffusivity is proposed: the turbulent kinetic energy and either a length or a time scale of the flow. In those models, the effect of density fluctuations are ignored, and their ability to describe properly mixing process strongly relies on parameterization of turbulent diffusion coefficients from the (locally) averaged quantities. Refinement of those models take into account higher order moments of the density (up to the fourth), and in some cases nonlocal effects [14; 5].

In parallel to those approaches, an idealized stochastic model (referred to as one-dimensional turbulence) has been applied for mixing in stratified flows [4]. This model mimics the effects of turbulent cascade, buoyancy and advection on a vertical realization of the density field.

Surprisingly, there has been no attempt to combine the classical modeling of mixing in terms of turbulent diffusion, with a model for the temporal evolution for the probability distribution of density. Beyond the advantage of describing the temporal evolution of the density distribution, such a model can give insight into the role played by density fluctuations in mixing processes. The density in a turbulent stratified flow, as vorticity in a 2D turbulent flow, is a scalar quantity that needs to satisfy conservation laws. Those constraints prevent complete mixing of the scalar. The idea of equilibrium statistical mechanics that are well known for the case of vorticity in 2D flows have been recently applied for stratified fluids in an idealized case [12]. We propose in this paper a phenomenological approach for the (out of equilibrium) turbulent mixing in stratified flows, on the basis of this analogy between the mixing of vorticity in 2D turbulent flows and the mixing of buoyancy in 3D turbulent stratified flows.

The paper is organized as follows: i) We briefly review the statistical theory of 2D flow, and then present the analogy with stratified flows. ii) We propose relaxation equations toward the equilibrium states for stratified flows, based on a work developed previously in the context of 2D flows. Two physical mechanisms are taken into account: turbulent diffusion and buoyancy effects, that tend to drive back the system toward a background "sorted" density profile (which minimizes the potential energy for a given global distribution of density). iii) We incorporate to those relaxation equations a mechanism of dissipation of the density fluctuations, due to turbulent cascade effects that tend to smooth out the density field by transfers from large to small scales iv) we discuss simple limit cases of the previous model v) we explain how the dynamical equations proposed in this paper could be adapted in a more general and realistic context.

2 An analogy between statistical mechanics of 2D flows and density stratified fluids

2.1 Statistical mechanics of 2D flows

The Euler equations can be expressed as a transport equation of the vorticity $\omega(x,y,t)$ in a domain $\mathscr{D}$

$$\partial_t \omega + \mathbf{u}\cdot\nabla\omega = 0 \quad with \quad \mathbf{u} = \left(-\frac{\partial\psi}{\partial y}\,,\,\frac{\partial\psi}{\partial x}\right) \quad and \quad \omega = \Delta\psi\,, \tag{1}$$

where the (non-divergent) velocity field is expressed in terms of a stream function ψ. The transport equation conserves the energy functional $E = \frac{1}{2}\int_{\mathscr{D}}(\nabla\psi)^2\,dxdy = -\frac{1}{2}\int_{\mathscr{D}}\omega\psi dxdy$ and the global distribution of vorticity levels $g(\sigma) = \int_{\mathscr{D}}\delta(\omega-\sigma)dxdy$ (equivalent to the conservation of the infinite number of Casimir functionals $\mathscr{C}_g[q] = \int_{\mathscr{D}} g(q)dxdy$, where g is any continuous function on $\mathscr{D}$).

The Euler equations are known to develop complex vorticity filaments at finer and finer scales as time goes on. Rather than describing the fine-grained structures of the flow, equilibrium statistical theories of two dimensional turbulent flows predict final organization of the flow at a coarse grained level [10; 8]. The *macroscopic state* is given by a field $\rho(x,y,\sigma)$ representing the probability density of finding the vorticity level σ in a small neighborhood of the position (x,y). From this field, one can compute the coarse-grained vorticity field and stream function by inverting the Laplacian with appropriate boundary conditions

$$\overline{\omega} = \int \rho\sigma d\sigma\,, \quad \overline{\omega} = \Delta\overline{\psi} \tag{2}$$

The rationale of the theory is that most accessible microscopic states will approach the macroscopic state which maximizes the mixing entropy $\mathscr{S}[\rho] = -\int_{\mathscr{D}}\int \rho\ln\rho dxdyd\sigma$. Assuming ergodicity, the equilibrium statistical theory provides a variational problem: the most probable (or equilibrium) macroscopic state ρ maximizes the mixing entropy with the constraints provided by the conservation of the energy and the global distribution of fine-grained vorticity levels (both quantities can be theoretically computed from the initial condition):

$$\mathscr{E}[\rho] = \int_{\mathscr{D}}\int \rho\sigma\overline{\psi}dxdyd\sigma \quad \forall\sigma\,,\, d_\sigma[\rho] = \int_{\mathscr{D}}\rho dxdy. \tag{3}$$

Notice that the energy of the fluctuations are supposed to tend to zero due to the dominance of small scale fluctuations. The variational problem can be summarized as follows:

$$S(E,g) = \max_{\{\rho\,|\,N[\rho]=1\}}\{\mathscr{S}[\rho]\mid \mathscr{E}[\rho] = E\ \&\ d_\sigma[\rho] = g(\sigma)\} \tag{4}$$

Much effort has been devoted to the study of the equilibrium states of the RSM theory. It has been applied in particular to explain the robustness of the Great Red Spot in the Jovian atmosphere [2].

2.2 Statistical mechanics of stratified fluids

Let us consider now the mixing of the density anomaly $b = g\left(\rho_{fluid} - \rho_0\right)/\rho_0$ in the framework of the Boussinesq approximation (b is the opposite of the buoyancy). This is a tracer advected by a (3D) turbulent non divergent velocity field $\mathbf{v}$:

$$\partial_t b + \mathbf{v}\nabla b = \kappa \Delta b \tag{5}$$

$$\partial_t \mathbf{v} + \mathbf{v}\nabla \mathbf{v} = -\nabla P - b\mathbf{k} + \nu \Delta \mathbf{v} + \mathbf{F} \tag{6}$$

where $\mathbf{F}$ is a mechanical forcing and $\mathbf{k}$ is the vertical unit vector.

In the absence of forcing and dissipation ($\mathbf{F} = 0$, $\kappa = \nu = 0$), the total energy of the flow $E = \int_{\mathscr{V}} \left(\frac{1}{2}\mathbf{v}^2 + bz\right) dxdydz$ and the global distribution of density levels $g(\sigma) = \frac{1}{|\mathscr{V}|}\int_{\mathscr{V}} \delta(b-\sigma)dxdydz$ are conserved. We suppose in addition that the mean value of the velocity field at any location is zero: there is no mean flow.

We define a *microscopic state* as a given fine grained density field $b(x,y,z)$ and velocity field $\mathbf{v}(x,y,z)$. From the knowledge of a microscopic configuration, one can compute the conserved quantities $E, g(\sigma)$. The problem is assumed to be statistically homogeneous on horizontal planes $\mathscr{P}_z$ (parallel to Oxy). An integration over the directions x and y will be considered as an ensemble average, and denoted by an upper bar: $\overline{b}(z) = \frac{1}{|\mathscr{P}_z|}\int_{\mathscr{P}_z} b dxdy$.

A *macroscopic state* of the system is given by the field $\rho(z,\sigma,\mathbf{v})$ that describes the probability to measure a given scalar and velocity value at height z. As for the mixing of the vorticity in 2D flows, the most probable macroscopic state is the one that maximize the mixing entropy $\mathscr{S} = -\int_{[0\ H]}\int_{]-\infty\ +\infty[^3}\int_{[\sigma_{min}\ \sigma_{max}]} \rho \ln\rho d\sigma d\mathbf{v}dz$ (the bounds of integration will be dropped for simplicity) among all the states that satisfy the constraints of the problem, namely the energy conservation

$$\mathscr{E}[\rho] = \mathscr{E}_c[\rho] + \mathscr{E}_p[\rho] = \int\int\int \rho\left(\frac{\mathbf{v}^2}{2} + \sigma z\right) dzd\sigma d\mathbf{v} = E, \tag{7}$$

and the conservation of the global scalar distribution:

$$\mathscr{H}_\sigma[\rho] = \int\int \rho dzd\mathbf{v} = g(\sigma) \tag{8}$$

where H is the total height of the domain. We make at this point the strong assumption that each microscopic state is accessible, and compute the most probable macroscopic state satisfying the constraints of the problem, as in the case of vorticity in 2D flows.

In order to compute critical points of the variational problem, we introduce the Lagrange multipliers β and $\gamma(\sigma)$ associated respectively with the energy (7) and with the constraints of the global vorticity distribution (8), and then compute first variations with respect to ρ:

$$\delta\mathscr{S} - \beta\delta\mathscr{E} + \int \gamma(\sigma)\delta\mathscr{H}_\sigma d\sigma = 0\,. \tag{9}$$

This gives $\int\int\int \left(-1-\ln(\rho)-\beta\mathbf{v}^2-\beta z\sigma+\gamma\right)\delta\rho d\mathbf{v}d\sigma dz = 0$. Since this equality holds for any variation $\delta\rho$, we obtain

$$\rho = A\exp\left(-\beta\mathbf{v}^2/2-\beta\sigma z+\gamma(\sigma)\right) \tag{10}$$

The value of the Lagrange multipliers β and $\gamma(\sigma)$ are determined by the expression of the constraints $\mathscr{E}[\rho] = E$ and $\mathscr{H}_\sigma[\rho] = g(\sigma)$, and A is a normalization factor.

Notice that the PDF (10) of the statistical equilibrium can be expressed as a product of a PDF for density and velocity, which means that b and $\mathbf{v}$ are two independent quantities. The predicted velocity distribution is Gaussian, and is isotropic. The predicted isotropy is not likely to be observed in a real flow, in which vertical motion is inhibited by stratification. However, a careful examination of the flow structure at the interface of two turbulent layers of different density shows that mixing occurs mainly by the occurrence of intermittent (both in time and space) turbulent patches that break the interface, stir and mix the density of the patches [6]. At the early stage of those mixing events, the distinction between vertical and horizontal velocities is not obvious.

The predicted velocity profile does not depend on z; the kinetic energy profile $e(z)$ is therefore constant along the vertical axis, with

$$e = \frac{1}{2}\int\int \mathbf{v}^2\rho d\sigma d\mathbf{v} = \frac{3}{2}\beta^{-1}. \tag{11}$$

The inverse of β (a "temperature" of the turbulent field) is thus proportional to the variance of the velocity fluctuations. This implies that $\beta > 0$. In the following, we shall focus on the density distribution $\rho(\sigma,z)$ (and the associated moments), ignoring the independent distribution in velocity.

$$\rho(\sigma,z) = B\exp\left(-\beta\sigma z+\gamma(\sigma)\right)\,, \quad \overline{b^n} = \int \sigma^n\rho d\sigma \tag{12}$$

We can then find another expression for β, which links this quantity with a form of potential energy, related to density fluctuations:

$$\beta^{-1} = \frac{\int_0^H \left(\overline{b^2}-\overline{b}^2\right)dz}{-\int_0^H \partial_z\overline{b}dz} = \frac{\int_0^H \left(\overline{b^2}-\overline{b}^2\right)dz}{\overline{b}(0)-\overline{b}(H)}\,. \tag{13}$$

Let us consider as an example an initial state composed of two density values ($b = 0$ and $b = \sigma_0$). Let us first assume that both values are in equal proportions. According to equation (12), the probability p to measure $b = \sigma_0$ at height z is

$$p(z) = \frac{e^{-\beta\sigma_0(z-H/2)}}{1+e^{-\beta\sigma_0(z-H/2)}} \tag{14}$$

The vertical profile of the mean density at statistical equilibrium is then $\overline{b}(z) = \sigma_0 p(z)$, a Fermi-Dirac distribution, represented in figure (1). This expression has been proposed recently by [12], using similar arguments.

Assuming ergodicity, such an equilibrium state is expected to be reached if the inertial time scale $\tau \sim \beta^{1/2}H$ is smaller than time scales of forcing and dissipating mechanisms. Let us notice that in the limit of infinit boundaries ($H \to +\infty$), the inertial time scale tends to infinity, and one can not expect to reach the equilibrium state. More generally, real flows are out of equilibrium systems, and the computation of the equilibrium states is only a starting point before more complex approaches.

Another case of interest is the dilute limit, for which the global probability $\int pdz$ to measure the level σ_0 tend to zero while keeping constant $\sigma_0 \int pdz$. This would correspond to the case of a sediment suspension, for which the Boussinesq approximation done earlier is no more valid, but it would be straightforward to generalize this result to a non Boussinesq flow. In this limit, we recover the standard expression $p(z) \simeq \exp -\beta\sigma z$ for a gas in a uniform gravity field.

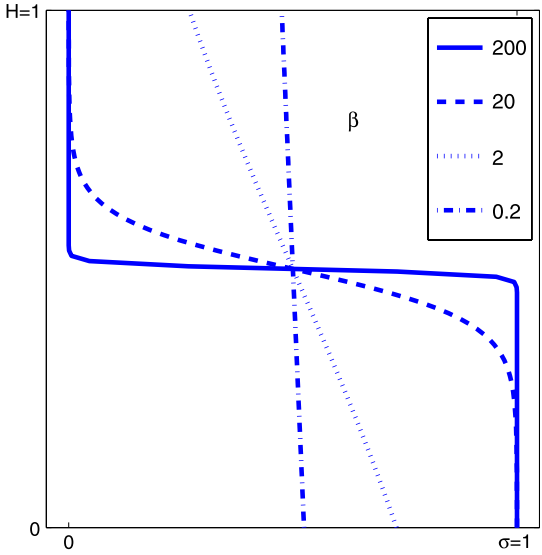

Fig. 1 Equilibrium profile for a two level system. We represent $\overline{b}(z) = \sigma p(z,t)$ where p is given by equation (14), for three different values of β.

3 Relaxation toward statistical equilibrium

We propose in this section an equation describing the relaxation toward the statistical equilibrium state. The general idea is that the system will evolve with increasing mixing entropy while preserving its conserved quantities.

We introduce the turbulent flux of probability $J(\sigma,z,t)$ (directed along z) and still consider that there are neither sinks nor sources for the density σ. The temporal evolution of the PDF $\rho(\sigma,z,t)$ thus satisfies the general conservation law

$$\partial_t \rho + \partial_z J = 0 \,, \tag{15}$$

with $J=0$ at lower and upper boundaries. This equation conserves the global density distribution, since $d_t\left(\int_0^H \rho dz\right)=0$. A convenient way to obtain an equation for the relaxation toward an entropy maximum is to assume that J maximizes the entropy production at fixed energy (with a condition of bounded fluxes). A similar approach has been previously applied to 2D and geostrophic turbulence [9; 3].

The entropy production reads $\dot{S} = -\int J(\partial_z \rho/\rho) d\sigma dz$, and the time derivative of the energy reads

$$\dot{\mathscr{E}} = d_t\left(\int_0^H e dz\right) + \int_0^H \sigma z \partial_t \rho d\sigma dz = d_t\left(\int_0^H e dz\right) + \int_0^H \sigma J d\sigma dz \tag{16}$$

We assume in addition that the flux J is bounded at each location, $\int (J^2/2\rho) d\sigma < C(z)$ (the quantity J^2/ρ can be considered as the square of a diffusion velocity, a natural quantity to bound). In order to ensure the conservation of the norm $\int \rho d\sigma = 1$, we impose the additional constraint $\int J d\sigma = 0$ at any height z. Then the first variation (with respect to the flux J) of the entropy production with the constraints of the problem gives

$$\delta\dot{S} - \beta\delta\dot{\mathscr{E}} - \int \frac{1}{D}\frac{J}{\rho}\delta J d\sigma dz - \int \zeta(z)\delta J d\sigma dz = 0, \tag{17}$$

where β, $\zeta(z)$ and $-1/D(z)$ are Lagrange parameters associated with the different constraints. A direct computation of those critical points gives

$$J = -D\left(\partial_z \rho + \beta\left(\sigma - \overline{b}\right)\rho\right), \tag{18}$$

where $\zeta(z)$ has been determined by using $\int J d\sigma = 0$. The coefficient D must be positive for the entropy production to be positive. We expect this diffusion coefficient to be related to the turbulent kinetic energy and a characteristic turbulent length scale l, $D \sim l e^{1/2}$.

We assume at this stage that l (hence D) is constant, and we make the strong assumption that velocity reaches its equilibrium distribution much faster that density, which means that the kinetic energy does not depend on z, with $e = \frac{3}{2}\beta^{-1}$. These hypothesis will be relaxed later on.

We distinguish two contributions to J in (18): a "down-gradient" diffusion term and a sedimentation term, which tends to drive back a fluid particle with density σ to its equilibrium position, where $\overline{b} = \sigma$.

When $J = 0$, turbulent diffusion and sedimentation cancel each other, yielding $\partial_z \rho = -\beta\rho\left(\sigma - \overline{b}\right)$, whose solution is the vertical profile (12) of the statistical equilibrium.

We use the energy conservation $\mathscr{E}^{\cdot} = 0$ and equation (16) to compute the kinetic energy:

$$e = \frac{3}{2}\beta^{-1}\,, \quad \frac{H}{D} d_t e = \frac{3}{2e}\int \left(\overline{b^2} - \overline{b}^2\right) dz - \left(\overline{b}(0) - \overline{b}(H)\right)\,. \tag{19}$$

At equilibrium ($d_t e = 0$), we recover equation (13) that links the kinetic energy e to the fluctuations of density. Since $e > 0$, we see that this equilibrium results from a competition between density fluctuations that tend to increase the kinetic energy and the (vertically integrated) stratification $\left(\overline{b}(0) - \overline{b}(H)\right)$ that tends to decrease the kinetic energy e if the profile is stable ($\overline{b}(0) > \overline{b}(H)$). Let us also notice that an unstable profile ($\overline{b}(0) < \overline{b}(H)$) cannot correspond to a stationary state, since the term $\left(\overline{b}(0) - \overline{b}(H)\right)$ acts then as a source of kinetic energy.

4 Dissipation of density fluctuations by turbulent cascade

The existence of a turbulent cascade implies that the global distribution of $g(\sigma)$ is actually not conserved: fluctuations are transferred to smaller and smaller scales, until molecular diffusive effects occur. For instance, in a system initially composed of two levels $\{0, \sigma_0\}$, this will create a third level $\frac{1}{2}\sigma_0$, and so on...

This effect has to be taken into account in relaxation equations toward equilibrium, by adding a dissipation term in the dynamical equation (15) of the density distribution:

$$\partial_t \rho + \partial_z J = s\mathscr{D}_c[\rho]\,, \tag{20}$$

where $s(z)$ is a straining rate depending mainly on the velocity field properties in each horizontal plane. At a given height z, the term $\mathscr{D}_c(\sigma)$ depends on the whole PDF $\rho(\cdot, z)$. This operator must conserve the norm and the mean of the distribution ($\int \mathscr{D}_c d\sigma = 0$ and $\int \mathscr{D}_c \sigma d\sigma = 0$), and should dissipate the fluctuations at a rate $s \sim e^{1/2}/l$ depending on the local strain of the flow. One should have $\partial_t \left(\overline{b^2} - \overline{b}^2\right) = -s\left(\overline{b^2} - \overline{b}^2\right)$ in the absence of other processes.

To estimate $\mathscr{D}_c$, several models have been developed in the context of mixing of reactive flows [11]. We choose here a simple model based on a self-convolution process:

$$\widehat{\mathscr{D}}_c(\kappa) = (\widehat{\rho}\ln\widehat{\rho} - \kappa\partial_\kappa\widehat{\rho}) \quad \widehat{\mathscr{D}}_c(\kappa) = \int e^{-\sigma\kappa}\mathscr{D}_c(\sigma)d\sigma\,, \tag{21}$$

where $\widehat{\rho}$ and $\widehat{\mathscr{D}_c}$ are Laplace transform of ρ and $\mathscr{D}_c$. In the absence of other processes, the model predict that an initial PDF will evolve by a succession of self convolutions of the PDF, corresponding to the addition of concentrations of independent scalar sheets becoming adjacent due to random turbulent motion, and simultaneously elongated by straining (see [13] for a more detailed presentation and discussion of the model).

Let us discuss the consequence of the addition of such a dissipation term $\mathscr{D}_c$, whatever its explicit form. The total energy $E = \frac{3}{2}H\beta^{-1} + \int \overline{b}z dz$ is still a conserved quantity in the presence of this dissipation term. Then equation (19) is still valid. If the initial condition is an equilibrium state, the dissipation will lower the contribution of the fluctuation term $\left(\overline{b^2} - \overline{b}^2\right)$ in equation (19), which will imply a decrease of the kinetic energy, and thus an increase of the potential energy of the system.

5 A simple example: mixing of a two layer stratified fluid

To illustrate the mechanisms presented in previous sections, we consider an idealized situation for which the kinetic energy (hence β) is fixed and study the time evolution of the PDF ρ by equations (18), (20) and (21). The unrealistic hypothesis of a fixed kinetic energy will be relaxed later on.

Since the diffusion coefficient D is assumed to be constant, the time unit can be always chosen such that $D = 1$, then the dynamical equation for the PDF is

$$\partial_t \rho = \partial_{zz}\rho + \beta \partial_z \left((\sigma - \overline{\sigma})\, \rho \right) + \tau_{diss}^{-1} \mathscr{D}_c \ , \tag{22}$$

where $\tau_{diss}^{-1} = s$. There are two independent parameters, namely β, linked to the imposed kinetic energy, and the time scale of the dissipation process τ_{diss}. The parameter β can be expressed as a sedimentation time scale $\tau_{sedim} = L/\beta\sigma_0$, where σ_0 is the density of the unmixed dense fluid, and L is a characteristic scale of the mean profile $\overline{b}(z)$. The behavior depends on the values of τ_{diss} and τ_{sedim} with respect to the diffusion time scale $\tau_{diff} = L^2$. We distinguish four limit cases:

- **i)** Diffusion and sedimentation dominate dissipation ($\tau_{diff} \sim \tau_{sedim} \ll \tau_{diss}$: The system relaxes toward the statistical equilibrium state corresponding to the (fixed) value of β. On a longer time scale, new density levels are created or destroyed by the dissipation mechanism. The system then goes through a sequence of equilibrium states until it reaches the homogeneous (fully mixed) state.
- **ii)** Dissipation dominates sedimentation and diffusion ($\tau_{diss} \ll \tau_{diff} \sim \tau_{sedim}$): The fluctuations of the initial state are first dissipated. Then the mean profile evolves through the diffusive mechanism $\partial_t \overline{b} = \partial_{zz}\overline{b}$ until complete mixing is achieved.

- **iii)** Diffusion dominates dissipation which dominates sedimentation ($\tau_{diff} \ll \tau_{diss} \ll \tau_{sedim}$). The mean profile evolves mainly by the diffusive process $\partial_t \overline{b} = \partial_{zz} \overline{b}$, until reaching an homogeneous mean vertical profile. Fluctuations around the mean are then dissipated.
- **iv)** Sedimentation dominates dissipation, which dominates diffusion ($\tau_{sedim} \ll \tau_{diss} \ll \tau_{diff}$). The system relaxes first toward the sorted profile (the potential energy minimum for a given global distribution of density levels). There are no more fluctuations in this state, and the vertical profile evolves by the diffusive process $\partial_t \overline{b} = \partial_{zz} \overline{b}$ until complete homogenization is achieved.

In cases **ii)** and **iii),** taking into account fluctuations around the mean profile is not particularly relevant, since the evolution of the mean vertical profile does not depends on these fluctuations. In case **iv),** the fluctuations are important in the early evolution of the flow, but the knowledge of the initial condition is sufficient to determine the sorted profile, and then the evolution equation does not imply any fluctuations.

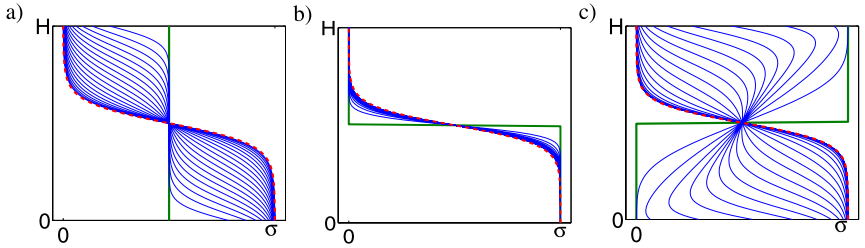

Fig. 2 Relaxation toward the equilibrium state (dashed red line) for a two level system, with $\beta = 20$, $H = 1$, $\sigma_0 = 1$, for three different initial profiles represented in bold plain green line. The thin plain blue curve represent the density profile at successive times with constant time interval.

Let us then consider case **i)**. We first display in figure 2 the relaxation toward an equilibrium state for a two level system ($b = 0$ or $b = \sigma_0 = 1$ in equal proportions), in a case without dissipation. The value of $\beta = 2/(3e)$ is still supposed to be fixed. Three different initial conditions are considered: a) the initial state is completely mixed ($\forall z$, $\rho(0,z) = \rho(\sigma_0,z) = 1/2$); b) the initial state is the sorted profile (the dense fluid is at the bottom) c) the initial state corresponds to the highest possible potential energy (the dense fluid is at the top, which is an instable initial condition).

Let us now consider the evolution of the density profile when the dissipation term is taken into account, figure 3. The initial condition is the equilibrium profile of the two level system for $\beta = 200$. The time scale for dissipation is $\tau_{diss} \sim 1000$, which is much greater than the characteristic time for relaxation toward equilibrium, of order one. The temporal evolution of the mean profile is represented in figure 3-a. Far from the interface (figure 3-b), the PDF is a sharp peak, there is almost no fluctuation, but the density of the peak decreases little by little. Closer to the interface (figure 3-c),

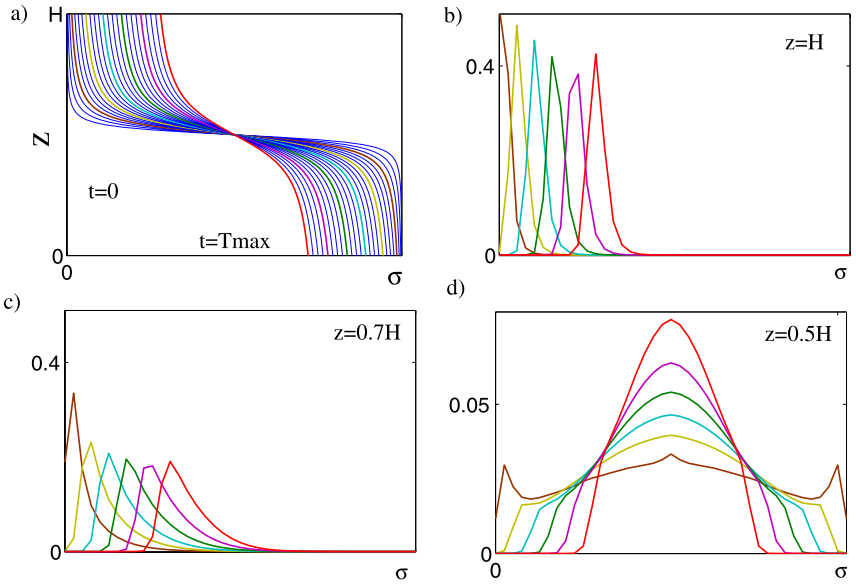

Fig. 3 a) Temporal evolution of the mean profile between $t = 0$ and $T_{max} = 1000$. The initial condition is the equilibrium profile of a two-level system characterized by $\beta = 200$, $\tau_{diss} = 1000$ b-c-d) Temporal evolution of the PDF at different altitudes z.

the PDF is asymmetric, with important fluctuations. Finally, at the middle of the interface (figure 3-d), the PDF is symmetric. The extreme values σ_{min} and σ_{max} of density progressively diminish.

Let us stress that the evolution of the vertical profile is not given by a classic turbulent diffusion: at leading order, diffusion is compensated by sedimentation. The temporal evolution is driven by the dissipation term that creates intermediate density levels, changing little by little the equilibrium profile.

6 Coupling the model with an equation for the kinetic energy

In the general case, the kinetic energy e (and then β) is not uniform, but should satisfy itself a diffusion equation. We assume that its diffusivity has a similar form as for density fluctuations, namely $D \sim le^{1/2}$. We furthermore introduce a dissipation term $a_4 l^{-1} e^{3/2}$ (the usual Kolmogoroff scaling for a turbulent cascade), a production term $\mathscr{P} = \mathbf{F}.\mathbf{v}$ and take into account the exchange with potential energy due to the buoyancy flux. This yields the energy equation

$$\partial_t e = a_3 \partial_z \left(l e^{1/2} \partial_z e \right) - \int \sigma J d\sigma - a_4 l^{-1} e^{3/2} + \mathscr{P} \,. \tag{23}$$

One can check that in the absence of production and dissipation, the total energy $E = \int_0^H (\overline{\sigma} z + e)\, dz$ is indeed conserved by equations (15) and (23).

Now that the kinetic energy e varies in space and time, let us assume that the kinetic energy still satisfies locally the link (11) with the inverse temperature β obtained at equilibrium: $e(z,t) = (3/2)\beta^{-1}(z,t)$.

Since the diffusion coefficient D in the buoyancy flux (18) depends on the kinetic energy, $D = a_1 l e^{1/2}$, it is also time and space dependent. The mean density flux is then

$$\int \sigma J d\sigma = -a_1 \left(l e^{1/2} \left(\partial_z \overline{b} \right) - \frac{3l}{2e^{1/2}} \left(\overline{b^2} - \overline{b}^2 \right) \right). \tag{24}$$

Notice that this buoyancy term has the same form as in the case of the "level 3 configuration" in the hierarchy of models by Mellor and Yamada [7].

Let us summarize the full model for the temporal evolution of the kinetic energy $e(z,t)$ and the density PDF $\rho(z,\sigma,t)$:

$$\partial_t \rho = -\partial_z J + a_2 l^{-1} e^{1/2} \mathscr{D}_c \tag{25}$$

$$J = -a_1 \left(l e^{1/2} \partial_z \rho + 3 e^{-1/2} \rho \left(\sigma - \overline{\sigma} \right) / 2 \right) \tag{26}$$

$$\widehat{\mathscr{D}} = \left(\widehat{\rho} \ln \widehat{\rho} - \kappa \partial_\kappa \widehat{\rho} \right) \quad \widehat{\mathscr{D}}_c = \int e^{-\sigma\kappa} \mathscr{D}(\sigma) d\sigma \tag{27}$$

$$\partial_t e = a_3 \partial_z \left(l e^{1/2} \partial_z e \right) + \int J \sigma d\sigma - a_4 l^{-1} e^{3/2} + \mathscr{P} \tag{28}$$

There are four intrinsic non-dimensional constants of order unity: i) a_1 and a_3 quantify the turbulent diffusivity for density fluctuations and kinetic energy (velocity fluctuations) respectively. ii) a_2 and a_4 quantify the rate of cascade of density and velocity fluctuations respectively. An additional relation should be given to determine the turbulent scale l. This could be done in the spirit of the k-ε model or mixing length theories. Finally the forcing term $\mathscr{P}$ could represent energy injection by external effects, like oscillating grid. Extension to shear driven turbulence should be proposed for more general cases.

7 Conclusion and perspectives

We have proposed a model for turbulent mixing in a stratified fluid. While most turbulence models deal with the mean and variance of fluctuating quantities, this model predicts the whole probability distribution of density fluctuations. It can deal with highly non-Gaussian distributions. The structure of the model is derived from conservation laws and general principles of entropy production maximization. It can account for re-stratification by gravity. Tests are needed for the validation in more realistic configurations.

References

[1] H. Z. Baumert, J. H. Simpson, and J. Sndermann. *Marine Turbulence: theories, observations, models*. Cambridge University Press, 1998.

[2] F. Bouchet and J. Sommeria. Emergence of intense jets and jupiter's great red spot as maximum entropy structures. *J. Fluid. Mech.*, 464:465–207, 2002.

[3] E. Kazantsev, J. Sommeria, and J. Verron. Subgrid-scale eddy parameterization by statistical mechanics in a barotropic ocean model. *Journal of Physical Oceanography*, 28:1017–1042, 1998.

[4] A. R. Kerstein. One-dimensional turbulence: model formulation and application to homogeneous turbulence, shear flows, and buoyant stratified flows. *Journal of Fluid Mechanics*, 392:277–334, August 1999.

[5] W. G. Large. Modeling and parameterizing vertical mixing. In E. Chassignet and J. Verron, editors, *Ocean modeling and parameterization*, 1998.

[6] J. L. McGrath, H. J. S. Fernando, and J. C. R. Hunt. Turbulence, waves and mixing at shear-free density interfaces. Part 2. Laboratory experiments. *Journal of Fluid Mechanics*, 347:235–261, September 1997.

[7] G. L. Mellor and T. Yamada. A hierarchy of turbulence closure models for planetary boundary layers. *Journal of Atmospheric Sciences*, 31:1791–1806, 1974.

[8] Jonathan Miller. Statistical mechanics of euler equations in two dimensions. *Phys. Rev. Lett.*, 65(17):2137–2140, Oct 1990.

[9] R. Robert, J. Sommeria. Relaxation towards a statistical equilibrium state in two-dimensional perfect fluid dynamics. *Phys. Rev. Lett.*, 69(19):2776, 1992.

[10] R. Robert and J. Sommeria. Statistical equilibrium states for two-dimensional flows. *J. Fluid Mech.*, 229:291–310, August 1991.

[11] S. B. Pope. An improved turbulent mixing model. *Prog. Energy Combust. Sci.*, 28:131, 1982.

[12] E. Tabak and F. Tal. Mixing in simple models for turbulent diffusion. *Comm. Pure Appl. Math.*, 57:563–589, 2004.

[13] A. Venaille and J. Sommeria. Is Turbulent Mixing a Self-Convolution Process? *Physical Review Letters*, 100(23):234506, June 2008.

[14] Y. Cheng, V. M. Canuto, A. Howard. Nonlocal convective pbl model based on new third- and fourth-order moments. *J. Atmos. Sci.*, 62:2189–2204, 2005.

The solar tachocline: a study in stably stratified MHD turbulence

Steven Tobias

Abstract In this paper I shall describe the dynamics of the solar tachocline. This region at the base of the solar convection zone is believed to play a key role in the generation of the solar activity cycle. Moreover it provides the motivation for a wide-ranging study of the properties of stably stratified rotating turbulence in the presence of a magnetic field. I shall discuss how the presence of even a weak large-scale magnetic field may lead to suppression of the turbulent correlations that drive zonal flows in neutral fluids.

1 Introduction

The dynamics of rotating stably stratified fluids has been investigated intensively over the past decades largely owing to its importance for understanding the behaviour of the Earth's atmosphere and oceans (see e.g. Pedlosky 1982) and the outer layers of the giant gas planets (see e.g. Marcus 1993). The presence of stratification and rotation leads to behaviour that is fundamentally different from that of homogeneous istropic flows. One of the central issues is the role of turbulence in such an environment – in particular the nature of transport. In neutral fluids turbulence may transport momentum or passive or active scalars and often the goal is to seek an understanding of the consequences for the large-scale fluid flows of such turbulence. The presence of rotation and stratification is known to introduce correlations within the turbulence that are not present for isotropic and homogeneous flows and it is the presence of these that can lead to counter-intuitive dynamics on the large scales.

In recent years there has been an increased interest in understanding the interactions of stably stratified rotating flows with magnetic fields. This is largely due to the importance of these interactions in determining the dynamics of stably stratified

Steven Tobias
Department of Applied Mathematics, University of Leeds, Leeds, LS2 9JT, e-mail: smt@maths.leeds.ac.uk

D. Dritschel (ed.), *IUTAM Symposium on Turbulence in the Atmosphere and Oceans*, IUTAM Bookseries 28, DOI 10.1007/978-94-007-0360-5_14,

stellar interiors and possibly the outer layers of extra-solar planets. In particular the dynamics of the solar tachocline, which is believed to play a key role in the generation of the solar magnetic activity cycle, is controlled by the complicated interactions of magnetic field and turbulence in a rotating stably stratified environment.

In this paper, I shall briefly summarise the physics of the solar tachocline (in section 2) and then discuss the modelling of the interaction of flows with magnetic fields that has been undertaken in this emerging discipline.

2 The Solar Tachocline

In this section I shall briefly describe the observations and physical processes of the solar tachocline, explain why an understanding of the dynamics is considered vital for models of the generation of the Sun's magnetic field, and also why this region can be considered an interesting test-bed for models of stratified rotating magnetohydrodynamic (MHD) turbulence. The physics of the tachocline is varied and complicated and so I shall only describe the observations and processes that support the case for an understanding of stably stratified MHD turbulence. A more complete picture can be obtained by the interested reader by examining the reviews by Tobias (2005), or Miesch (2005), or the collection of papers edited by Hughes, Rosner & Weiss (2007).

2.1 Properties of the solar tachocline

The sun's magnetic field is believed to be generated by a hydromagnetic dynamo operating in the solar interior. This dynamo is responsible for the large-scale eleven year activity cycle manifested in sunspots, solar flares and the solar corona. It is fair to say that no consensus has been reached on the precise ingredients that are necessary to explain solar magnetic activity, though it is commonly believed that the systematic activity arises via the interaction of rotation, turbulence, differential rotation and magnetic fields. For recent discussions of solar dynamo theory see the reviews of Ossendrijver (2003), Charbonneau (2005), Tobias & Weiss (2007) or Weiss & Thompson (2009). It is, however, widely believed that a crucial ingredient of solar dynamo action is the stretching of magnetic field lines via differential rotation. This process (often termed the ω-effect) is analogous to vortex stretching in neutral fluids. The differential rotation (or global azimuthal shear flow) leads to the generation of strong azimuthal (toroidal) magnetic field from weaker meridional (poloidal) magnetic field. It is this toroidal field that is believed to lose stability and rise through the solar interior to form sunspots at the solar surface.

Hence differential rotation is a key feature of solar dynamo models. It is well established that the Sun rotates differentially, with surface observations suggesting that the solar equator completes a rotation in approximately 25 days; and the poles

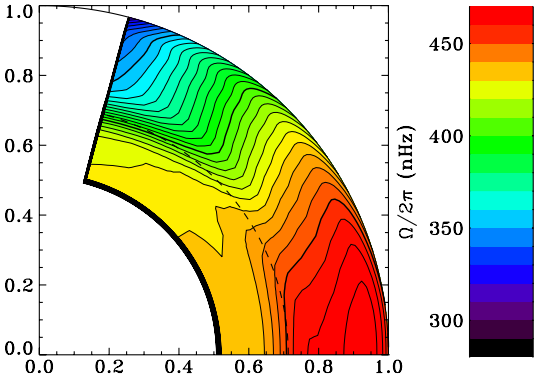

Fig. 1 The solar interior rotation profile as determined by helioseismology (courtesy M.J. Thompson)

30 days. This latitudinal differential rotation has been included in dynamo models for many years. However, the rotation profile of the solar interior has only been determined in the past twenty-five years using the science of helioseismology. Here continuous observation of acoustic oscillations at the solar surface leads to the determination of the the pattern of differential rotation (as shown in Figure 1). The data is consistent with the surface differential profile being largely maintained throughout the solar convection zone on radial lines; the solar convection zone comprises the outer 30% of the Sun by radius. Beneath the convection zone lies the stably stratified radiative zone, which appears to rotate largely as a solid body at an intermediate rate found at mid-latitudes in the convection zone. These two differential rotation profiles are matched via a thin radial shear layer at (and below) the base of the convection zone, which has been termed the tachocline (in analogy with the thermocline in the Earth's oceans and atmosphere).

The detailed structure of the tachocline is still uncertain; helioseismology can only determine some properties with a certain accuracy and can only provide upper bounds for such crucial properties as the thickness of the layer. For a detailed discussion of the limitations of helioseismology as applied to the tachocline see Christensen-Dalsgaard & Thompson (2007). Here we simply state that the tachocline is located at $0.69R_S$ and is prolate (with its position varying by 2% in radius). An upper bound for the thickness of the tachocline is $0.04R_S$, however estimates from sound-speed inversions place the thickness at $0.019R_S$.

In terms of physical properties, the tachocline is a high density, high temperature collisional plasma ($\rho \approx 0.2$ g/cm^3, $T \approx 2.0 \times 10^6$K). This suggests that in order to model the tachocline the equations of magnetohydrodynamics (with no further plasma effects included) are adequate. From the point of fluid dynamics, the tachocline is moderately rotating (rotationally influenced though not rotationally constrained). The top of the tachocline is believed to be in the convection zone and so superadiabatically stratified (although the convection transforms this region to a

state of adiabaticity). The convection is believed to overshoot into the upper layers of the nominally sub-adiabatic region, contributing to mixing there, though the extent of penetration is still uncertain (see e.g. Brummell *et al* 2002, Tobias *et al* 2001). Deeper in the tachocline the subadiabatic gradient becomes larger and stable stratification is believed to play a key role in the dynamics — the non-dimensional parameters will be given later. It is this region that motivates the current programme of research into the dynamics of magnetised stably stratified fluids.

2.2 Why is the tachocline there — and so thin?

The fundamental problem concerning the tachocline is that of its very existence. The angular momentum distribution in the solar convection zone is very different to that in the solar interior with the thin matching layer of the tachocline providing a boundary layer between the two regions. A natural question to ask is therefore why has the angular momentum distribution of the convection zone not been propagated into the solar interior? To answer this question it is important to identify the processes that could contribute to the transport of the azimuthal component of the angular momentum (i.e. $L = \rho r u_\phi \sin\vartheta$) from the convection zone inwards. The first is large-scale meridional flows (i.e. flows in the (r, ϑ)-plane); these simply redistribute large-scale angular momentum. The other two processes believed to be of significance are more subtle and arise owing to turbulent interactions. Reynolds stresses transport angular momentum via the net (averaged) effect of interactions via the turbulent velocity and the small-scale azimuthal flow. For these to transport angular momentum efficiently non-trivial correlations between the velocity components must exist. A similar process arises from the turbulent Maxwell stress that contributes to the Lorentz force in the momentum equation; here non-trivial correlations between the fluctuating magnetic fields and the azimuthal small-scale magnetic field can act so as to modify the momentum transport. Both of these effects are poorly understood and, as we shall see, are often parameterised in terms of poorly constrained transport coefficients. It is correctly argued that for the solar interior the contribution to angular momentum transport from molecular viscous effects is likely to be overwhelmed by those from turbulence and large-scale flows.

The seminal paper for our understanding of the tachocline is Spiegel & Zahn (1992), where the problem of the existence of the tachocline was first discussed. For the evolution of the tachocline on long time-scales it is convenient to take the angular momentum distribution of the convection zone as a given outer boundary condition for the solar radiative zone (which evolves on much longer timescales). Spiegel & Zahn argued that in the absence of turbulence and magnetic fields this latitudinal distribution would be transported via a radiation-drive meridional flow into the deeper solar interior. Although this meridional flow is slow (with a turnover time of $\sim 10^6$ years) it is still capable of significantly broadening the tachocline over the lifetime of the Sun ($\sim 10^9$ years). They therefore argued that some other

process must be acting so as to keep the tachocline thin. Given the above discussions, it is obvious that this process must either be turbulent in nature or involve magnetic fields (or both). Spiegel & Zahn opted for the presence of stably stratified *hydrodynamic* turbulence. They argued as follows: the overall stable stratification will lead to the two-dimensionalisation of turbulence (if any turbulence exists). This two-dimensional turbulence can be parameterised as an *anisotropic* turbulent viscosity acting more efficiently on latitudinal gradients of angular momentum than radial gradients. This anistropic viscosity can act so as to prevent the spread of the tachocline into the interior.

There are a number of obvious questions that arise immediately from the argument postulated by Spiegel & Zahn. The first is to question the assumption of the presence of turbulence. There are a number of linear instabilities that may lead to turbulence in the solar tachocline (which is at high Reynolds number). Some of these are magnetic in origin — for example magnetic buoyancy instabilities (see e.g. Hughes 2008) or joint instabilities (see e.g. Gilman & Cally 2008). Some however can be considered in a purely hydrodynamics framework — for example GSF instabilities, which are axisymmetric versions of baroclinic Eady modes that arise owing to the small thermal Prandtl number of the tachocline (see e.g. Rashid *et al* 2008). Another source of turbulence in the tachocline is the forcing from the convection zone. As noted above the upper surface of the tachocline is continually forced by overshooting convective downwards sinking plumes. For the purposes of modelling the tachocline these may be thought of as short duration forcing events that act in conjunction with the large-scale stresses that arise from the differential rotation in the convection zone. The second question, given the undoubted presence of turbulence, is how should such turbulence be parametrised in a rotating stably stratified environment in the presence of potential magnetic fields? Gough & McIntyre (1998) argue that within the hydrodynamic framework it is incorrect to model the transport properties of such turbulence via an anisotropic viscosity (or friction) term. They argue that stratified turbulence is long known to act so as to mix potential vorticity (PV) and so drive the system away from solid body rotation. In this respect the turbulence should be modelled as an "anti-friction" (see also McIntyre 2003). Of course this particular argument takes no account of the presence of magnetic fields, and therefore provides motivation for an investigation of the dynamics of magnetised, stratified rotating turbulence.

We conclude this section by discussing a set of alternative models for confining the tachocline. It has long been understood that even a weak large-scale magnetic field in the deep solar interior can keep the radiative interior and core rotating as a solid body. Mestel & Weiss (1987) estimate that a field as weak as $10^{-3} - 10^{-2}$G is strong enough to achieve this and that it is likely that a relic field of this size remains from the formation of the Sun. However MacGregor & Charbonneau (1999) suggested that in order to explain the presence of the tachocline the large-scale field lines need to be contained in the radiative interior (otherwise the angular momentum of the convection zone may propagate into the interior along field-lines). Various mechanisms have been proposed for confining the field to the radiative interior including the action of a two-cell meridional flow (Gough & McIntyre 1998, Garaud

2002, Garaud & Garaud 2008) and turbulent pumping of magnetic fields (Tobias *et al* 2001). However magnetic coupling between the convection zone and interior is often used to explain the spin-down of the star over its evolution, so this coupling must be large enough to spin down the star but not so large as to destroy the thin tachocline. One possibility is to place the magnetic coupling at mid-latitudes where the angular velocity of the convection zone matches that of the interior, whilst confining the magnetic field at high and low latitudes (Tobias 2005). If one adopts this magnetic mechanism for keeping the tachocline thin then it is also of interest to understand the transport properties of stratified magnetised turbulence, but now it is important to understand the magnetic as well as hydrodynamic transport properties.

3 Simplified models of stratified MHD turbulence

3.1 The parameter regime

As noted above, the tachocline is a region of strong shear that straddles the base of the solar convection zone and the top of the radiative zone below. As such, the non-dimensional parameters that control the evolution are functions of position and take on a range of values. In addition the amplitude of turbulent flows and the strength of magnetic fields are poorly constrained. For this reason, it is possible to give only an indication of the size of non-dimensional ratios that are important for modelling. The strong stratification at the base of the tachocline leads to a Froude Number $Fr \sim 0.01 - 0.1$ and a Richardson number $Ri \sim 10^3 - 10$. The turbulence is rotationally influenced as measured by a Rossby number $Ro \sim 0.1 - 1.0$ and Ekman number $Ek \sim 10^{-11}$. Any flows that are present will be turbulent owing to the large values of the fluids Reynolds and magnetic Reynolds numbers ($Re \sim 10^{10}$, $Rm \sim 10^5$). Finally although the magnetic field is strong enough to influence the dynamics of the tachocline, it must do so in a subtle manner — the ratio of the gas pressure to the magnetic pressure $\beta \sim 10^4 - 10^5$. All of these numbers are calculated assuming global lengthscales, so that a latitudinal lengthscale L is taken to be the circumference of the tachocline and a vertical lengthscale H is taken to be the thickness of the tachocline. Hence the ratios for local dynamics may vary considerably from the values quoted above.

3.2 A hierarchy of models

In theory one would like to construct a self-consistent model of the solar tachocline, including the generation of magnetic field by dynamo action the emergence of active regions via magnetic buoyancy and the turbulent transport of stably stratified rotating MHD. It is clearly impossible with current computational resources to sim-

ulate the equations of compressible MHD at the parameter values given above for the tachocline. Progress can be made by constructing simplified models that illuminates the particular physics of interest. For example, magnetic buoyancy instabilities rely on retaining some effects of compressibility and so can only be studied within a fully compressible, anelastic or magneto-Boussinesq model. Turbulent transport in the tachocline is not believed to be sensitive to the degree of compressibility and so may be studied within the framework of incompressible Boussinesq MHD. In this manner a hierarchy of models, including fully three dimensional compressible MHD, three-dimensional Boussinesq, two-dimensional shallow water MHD (see Gilman 2001) and strictly two-dimensional MHD models can be constructed. Which framework is chosen depends largely on the physics that is to be studied. In the concluding section I shall comment on the possible future directions for research. However in the next subsection I shall briefly describe the simplest possible calculation that sheds light on the role of large-scale magnetic fields in modifying the transport properties of rotating stratified turbulence — forced magnetised turbulence on a β-plane.

3.3 Formation of jets on a magnetised β-plane

The model (Tobias *et al* 2007, 2009) considers the evolution of turbulence on a magnetised β-plane. A local Cartesian axis is adopted with x representing longitude, y representing co-latitude and z representing radius. Rotation is included in the β-plane approximation by setting $\boldsymbol{\Omega} = (f+\beta y)\,\mathbf{e}_z$. In the two-dimensional model both the flows and magnetic field are considered independent of radius z, so that $\mathbf{u} = \boldsymbol{\nabla} \times (\psi(x,y)\,\mathbf{e}_z)$ and $\mathbf{B} = B_0\,\mathbf{e}_x + \boldsymbol{\nabla} \times (A(x,y)\,\mathbf{e}_z)$, so that the magnetic field is assumed to have a mean component (B_0) in the x-direction. Within this model the dynamics is controlled by evolution equations for the vertical components of the vorticity $\omega = -\nabla^2\psi$ and the flux function A i.e.

$$\omega_t = J(\psi,\omega) + \beta\psi_x + J(A,\nabla^2 A) - B_0\nabla^2 A_x + \nu\nabla^2\omega + G_0, \tag{1}$$

$$A_t = J(\psi,A) + B_0\psi_x + \eta\nabla^2 A, \tag{2}$$

where $J(a,b) = a_x b_y - a_y b_x$ and $G_0(x,y,t)$ is the z-component of the couple. Extensive numerical solutions of these equations with periodic boundary conditions have been undertaken. The forcing is small-scale and homogeneous to allow for the possibility of an inverse cascade. The other parameters are chosen so that *Re* and *Rm* are large, whilst β is moderate corresponding to the ordering found in the tachocline. In the absence of a mean magnetic field (B_0), the vector potential must decay in two dimensions and the situation reverts to the well known hydrodynamic case (see e.g. Rhines 1975, Diamond *et al* 2005). Here the two-dimensionality leads to an inverse cascade, which in the presence of the anisotropy provided by the β term leads to the formation of jets. This jet formation process can be visualised as occurring due to the merging of elongated vortices or the interaction of nonlinear dispersive Rossby

waves (Diamond *et al* 2007). The inverse cascade is halted on a scale where mean flow advection balances the $\beta\psi_x$ term (or alternatively where the decorrelation rate of the Rossby waves balances the frequency). This scale given by $k_y = (\beta/U)^{1/2}$ is often termed the Rhines scale. The inverse cascade is also often thought of as arising from the constraint of conservation of potential vorticity which is homogenised by the formation of jets.

Tobias *et al* (2007) demonstrated that the presence of a mean magnetic field can have a significant effect on the generation of zonal flows (jets). They found that if B_0 is sufficiently large (i.e. above a threshold that depends on Rm) the formation of jets is suppressed and the turbulence remains small scale. Diamond et al (2007) had argued that the presence of a magnetic field will introduce a competition between dispersive Rossby waves and non-dispersive Alfvén waves. The decorrelation of Rossby waves may now be influenced by magnetic fields and this may lead to the suppression of jets. It is also possible to view the suppression of jets as a straightforward competition between Reynolds and Maxwell stresses. The equation for the evolution of the zonal flows $\overline{u}$ in the presence of field is (Tobias *et al* 2009)

$$\frac{\partial \overline{u}}{\partial t} + \frac{\partial}{\partial y}\left(\overline{uv} - \overline{B_x B_y}\right) = \nu \frac{\partial^2 \overline{u}}{\partial y^2}. \tag{3}$$

For the strictly two-dimensional turbulence investigated, the Maxwell stresses act so as to cancel out the Reynolds stresses on average, leading to the suppression of the jets. It remains to be seen whether this cancellation is quite so exact if the assumption of two-dimensionality is relaxed. A final complementary way of understanding the result is to note that the presence of the Lorentz force term $J(A,\nabla^2 A) - B_0\nabla^2 A_x$ in the equation for ω breaks the conservation of potential vorticity constraint of the inviscid system. Since this ideal invariant is often used to explain the inverse cascade process, its absence in the presence of a magnetic field may be significant in preventing the formation of jets.

This model demonstrates that magnetic fields may have a profound effect on the transport properties of rotating turbulence. The model is the simplest possible and it remains to be seen whether the conclusions carry through to more realistic scenarios which do not include such drastic simplifications of the system.

4 Future directions

Clearly the assumption of strict two-dimensionality for the flow and field places severe restrictions on the nature of the turbulence. This limit of 'infinite stratification' has an inherent decoupling of vertical layers with the dynamics in each layer independent of nearest neighbours. Moreover the two dimensionality of the system precludes the generation of magnetic field via dynamo action and so field will decay unless the source term provided by an imposed mean field is included. Moving away

from this restriction will involve the construction of models of increasing complexity.

Effects of finite deformation radius can be included within the two-dimensional MHD system. In the solar tachocline the deformation radius is large (but finite) in the deep tachocline, but gets small at the base of the solar convection zone. The inclusion of a finite deformation radius in the hydrodynamic system may have significant effects on the jet formation and profiles and so it is of interest to examine the role of magnetic fields in this system. The next level of sophistication in modelling is to relax the assumption of strict two-dimensionality and allow deformations of the layer depth. It has been demonstrated that this shallow water MHD system *can* allow self-consistent generation of magnetic fields via dynamo action (Tobias 2009). Moreover rundown experiments in spherical shells have indicated that the presence of magnetic fields may continue to modify significantly the transport properties of the turbulence (Cho 2009). Within simplified models it is interesting also to examine the effects of the coupling of layers. Here the coupling may be via a common potential vorticity profile (as in atmospheric models), but also may include the effects of poloidal fields. The role of the Lorentz force in breaking the homogenization of potential vorticity (PV) can be investigated b examining the classic problem of jet breakdown. Here the instability of a jet profile can lead to turbulence which is mediated via the conservation of (PV). In the presence of a magnetic field, both the breakdown of the jet and the subsequent turbulence will be modified

Of course, these simplified models should be compared with simulations of three-dimensional MHD turbulence. Recent simulations of stably stratified rotating and non-rotating hydrodynamic turbulence have shown that the degree of decoupling between layers is not as great as might have been expected (Waite & Bartello 2006, Lindborg 2006). Moreover it is to be expected that even weak magnetic fields will play an important role in determining the dynamics in such systems. Finally this system is of interest from a dynamo theory perspective. It may be the case that the interaction of stably stratified turbulence and shear flows will lead to the self consistent generation of large-scale magnetic fields. Such a result would be of great importance for our understanding of the solar dynamo.

Acknowledgements I would like to acknowledge the organisers of the meeting for the invitation to speak and the Leverhulme Trust for support via a Leverhulme Prize.

References

[1] Brummell, N.H., Clune, T.L., Toomre, J.: Penetration and Overshooting in Turbulent Compressible Convection. Astrophys. J. **570**, 825–854 (2002). DOI 10.1086/339626

[2] Charbonneau, P.: Dynamo Models of the Solar Cycle. Living Reviews in Solar Physics **2**, 2–+ (2005)

[3] Christensen-Dalsgaard, J., Thompson, M.J.: Observational results and issues concerning the tachocline. In: D.W. Hughes, R. Rosner, N.O. Weiss (eds.) The Solar Tachocline, pp. 53–+ (2007)
[4] Diamond, P.H., Itoh, S.I., Itoh, K., Hahm, T.S.: TOPICAL REVIEW: Zonal flows in plasma a review. Plasma Physics and Controlled Fusion **47**, 35–+ (2005). DOI 10.1088/0741-3335/47/5/R01
[5] Diamond, P.H., Itoh, S.I., Itoh, K., Silvers, L.J.: β-Plane MHD turbulence and dissipation in the solar tachocline. In: D.W. Hughes, R. Rosner, N.O. Weiss (eds.) The Solar Tachocline, pp. 213–+ (2007)
[6] Garaud, P.: Dynamics of the solar tachocline - I. An incompressible study. Mon. Not. Roy. Ast. Soc. **329**, 1–17 (2002). DOI 10.1046/j.1365-8711.2002.04961.x
[7] Garaud, P., Garaud, J.D.: Dynamics of the solar tachocline - II. The stratified case. Mon. Not. Roy. Ast. Soc. **391**, 1239–1258 (2008). DOI 10.1111/j.1365-2966.2008.13930.x
[8] Gilman, P.A.: Magnetohydrodynamic "Shallow Water" Equations for the Solar Tachocline. Astrophysical Journal **544**, L79–L82 (2000). DOI 10.1086/317291
[9] Gilman, P.A., Cally, P.S.: Global MHD instabilities of the tachocline. In: D.W. Hughes, R. Rosner, N.O. Weiss (eds.) The Solar Tachocline, pp. 243–+ (2007)
[10] Hughes, D.W.: Magnetic buoyancy instabilities in the tachocline. In: D.W. Hughes, R. Rosner, N.O. Weiss (eds.) The Solar Tachocline, pp. 275–+ (2007)
[11] Hughes, D.W., Rosner, R., Weiss, N.O. (eds.): The Solar Tachocline (2007)
[12] Lindborg, E.: The energy cascade in a strongly stratified fluid. Journal of Fluid Mechanics **550**, 207–242 (2006). DOI 10.1017/S0022112005008128
[13] MacGregor, K.B., Charbonneau, P.: Angular Momentum Transport in Magnetized Stellar Radiative Zones. IV. Ferraro's Theorem and the Solar Tachocline. Astrophys. J. **519**, 911–917 (1999). DOI 10.1086/307389
[14] Marcus, P.S.: Jupiter's Great Red SPOT and other vortices. Ann. Rev. Astron. & Atrophys. **31**, 523–573 (1993). DOI 10.1146/annurev.aa.31.090193.002515
[15] McIntyre, M.E.: Solar tachocline dynamics: eddy viscosity, anti-friction, or something in between?, pp. 111–130 (2003)
[16] Miesch, M.S.: Large-Scale Dynamics of the Convection Zone and Tachocline. Living Reviews in Solar Physics **2**, 1–+ (2005)
[17] Ossendrijver, M.: The solar dynamo. Astron. & Astrophys. Rev. **11**, 287–367 (2003). DOI 10.1007/s00159-003-0019-3
[18] Pedlosky, J.: Geophysical fluid dynamics. New York and Berlin Springer-Verlag, 1982. 636 p. (1982)
[19] Rashid, F.Q., Jones, C.A., Tobias, S.M.: Hydrodynamic instabilities in the solar tachocline. Astronomy & Astrophysics **488**, 819–827 (2008). DOI 10.1051/0004-6361:200810039
[20] Rhines, P.B.: Waves and turbulence on a beta-plane. Journal of Fluid Mechanics **69**, 417–443 (1975). DOI 10.1017/S0022112075001504
[21] Spiegel, E.A., Zahn, J.P.: The solar tachocline. Astron. Astrophys. **265**, 106–114 (1992)

[22] Tobias, S., Weiss, N.: The solar dynamo and the tachocline. In: D.W. Hughes, R. Rosner, N.O. Weiss (eds.) The Solar Tachocline, pp. 319–+ (2007)
[23] Tobias, S.M.: The solar tachocline: Formation, stability and its role in the solar dynamo. In: A.M. Soward, C.A. Jones, D.W. Hughes, N.O. Weiss (eds.) Fluid Dynamics and Dynamos in Astrophysics and Geophysics, pp. 193–+ (2005)
[24] Tobias, S.M., Brummell, N.H., Clune, T.L., Toomre, J.: Transport and Storage of Magnetic Field by Overshooting Turbulent Compressible Convection. Astrophys. J. **549**, 1183–1203 (2001). DOI 10.1086/319448
[25] Tobias, S.M., Diamond, P.H., Hughes, D.W.: β-Plane Magnetohydrodynamic Turbulence in the Solar Tachocline. Astrophysical Journal **667**, L113–L116 (2007). DOI 10.1086/521978
[26] Waite, M.L., Bartello, P.: The transition from geostrophic to stratified turbulence. Journal of Fluid Mechanics **568**, 89–108 (2006). DOI 10.1017/S0022112006002060
[27] Weiss, N.O., Thompson, M.J.: The Solar Dynamo. Space Science Reviews **144**, 53–66 (2009). DOI 10.1007/s11214-008-9435-z

Some Unusual Properties of Turbulent Convection and Dynamos in Rotating Spherical Shells

F. H. Busse and R. D. Simitev

Abstract The dynamics of convecting fluids in rotating spherical shells is governed at Prandtl numbers of the order unity by the interaction between differential rotation and roll-like convection eddies. While the differential rotation is driven by the Reynolds stresses of the eddies, its shearing action inhibits convection and causes phenomena such as localized convection and turbulent relaxation oscillations. The response of the system is enriched in the case of dynamo action. Lorentz forces may brake either entirely or partially the geostrophic differential rotation and give rise to two rather different dynamo states. Bistability of turbulent dynamos exists for magnetic Prandtl numbers of the order unity. While the ratios between mean magnetic and kinetic energies differ by a factor of 5 or more for the two dynamo states, the mean convective heat transports are nearly the same. They are much larger than in the absence of a magnetic field.

1 Introduction

Convection of an electrically conducting fluid in a rotating system represents a basic dynamical process in planetary interiors and in stars. Astrophysicists and geophysicists have long been interested in the mechanisms that govern the convective heat transport and the generation of magnetic fields by convection in those systems. The availability in recent years of large scale computer capacities has permitted numerical simulations of detailed models for those processes. In particular, it has become possible to model the global properties of convection and dynamos in rotating spherical fluid shells to which this paper is addressed. Only the larger length scales can be

F. H. Busse
Institute of Physics, University of Bayreuth, D-95440 Bayreuth, Germany, e-mail: busse@uni-bayreuth.de

R. D. Simitev
Department of Mathematics, University of Glasgow, Glasgow G12 8QW, UK

D. Dritschel (ed.), *IUTAM Symposium on Turbulence in the Atmosphere and Oceans*, IUTAM Bookseries 28, DOI 10.1007/978-94-007-0360-5_15,

taken into account in the numerical computations, of course, and eddy diffusivities are usually introduced to model the influence of the smaller unresolved scales of the turbulent flows.

A difficulty arises from the fact that it can not generally be assumed that all eddy diffusivities are equal. First, they apply to scalar as well as to vector quantities, such as temperature and magnetic fields. Secondly, the diffusivities in the absence of turbulence differ enormously such that the turbulence may not be sufficiently strong to equalize them. In the Earth's liquid core, for instance, the magnetic diffusivity is large enough to be taken into account without the consideration of an eddy contribution while a comparable eddy viscosity would have to exceed the probable molecular viscosity value by a factor of at least 10^6. As has been demonstrated in the past [12] the dynamics of convection in rotating spherical shells and its dynamo action are very sensitive to ratios of diffusivities, especially to the Prandtl number around its usually assumed value of unity.

More complex methods for treating effects of turbulence could eventually be used, such as $k-\varepsilon$-models, and the undoubtedly important anisotropy of turbulent diffusivities in rotating systems could also be considered. Since these influences are difficult to evaluate, however, we shall restrict the attention in this paper to a minimum of physical parameters. In spite of this restriction a number of characteristic features of convection and its dynamos in rotating spherical shells can be demonstrated that are likely to exist as coherent spatio-temporal structures in natural systems.

2 Mathematical formulation of the problem and methods of solution

We consider a rotating spherical fluid shell of thickness d and assume that a static state exists with the temperature distribution $T_S = T_0 - \beta d^2 r^2/2$. Here rd is the length of the position vector with respect to the center of the sphere. The gravity field is given by $\mathbf{g} = -d\gamma\mathbf{r}$. In addition to d, the time d^2/ν, the temperature $\nu^2/\gamma\alpha d^4$ and the magnetic flux density $\nu(\mu\rho)^{1/2}/d$ are used as scales for the dimensionless description of the problem where ν denotes the kinematic viscosity of the fluid, κ its thermal diffusivity, ρ its density and μ is its magnetic permeability. Since we shall assume the Boussinesq approximation material properties are regarded as constants except for the temperature dependence of the density described by $\alpha \equiv -(\mathrm{d}\rho/\mathrm{d}T)/\rho$ which is taken into account only in the gravity term. Both, the velocity field $\mathbf{v}$ and the magnetic flux density $\mathbf{B}$, are solenoidal vector fields for which the general representation

$$\mathbf{v} = \nabla \times (\nabla u \times \mathbf{r}) + \nabla w \times \mathbf{r}, \qquad \mathbf{B} = \nabla \times (\nabla h \times \mathbf{r}) + \nabla g \times \mathbf{r}, \tag{1}$$

can be employed. By multiplying the $(\mathrm{curl})^2$ and the curl of the Navier-Stokes equations of motion by $\mathbf{r}$ we obtain two equations for u and w,

$$[(\nabla^2-\partial_t)\mathscr{L}_2+\tau\partial_\varphi]\nabla^2 u+\tau\mathscr{Q}w-\mathscr{L}_2\Theta=-\mathbf{r}\cdot\nabla\times[\nabla\times(\mathbf{v}\cdot\nabla\mathbf{v}-\mathbf{B}\cdot\nabla\mathbf{B})], \quad (2)$$

$$[(\nabla^2-\partial_t)\mathscr{L}_2+\tau\partial_\varphi]w-\tau\mathscr{Q}u=\mathbf{r}\cdot\nabla\times(\mathbf{v}\cdot\nabla\mathbf{v}-\mathbf{B}\cdot\nabla\mathbf{B}), \quad (3)$$

where ∂_t denotes the partial derivative with respect to time t and where ∂_φ is the partial derivative with respect to the angle φ of a spherical system of coordinates r,θ,φ. For further details we refer to [12]. The operators $\mathscr{L}_2$ and $\mathscr{Q}$ are defined by

$$\mathscr{L}_2\equiv-r^2\nabla^2+\partial_r(r^2\partial_r),$$
$$\mathscr{Q}\equiv r\cos\theta\nabla^2-(\mathscr{L}_2+r\partial_r)(\cos\theta\partial_r-r^{-1}\sin\theta\partial_\theta).$$

The heat equation for the dimensionless deviation Θ from the static temperature distribution can be written in the form

$$\nabla^2\Theta+R\mathscr{L}_2 u=P(\partial_t+\mathbf{v}\cdot\nabla)\Theta, \quad (4)$$

and the equations for h and g are obtained through the multiplication of the equation of induction and of its curl by $\mathbf{r}$,

$$\nabla^2\mathscr{L}_2 h=P_m[\partial_t\mathscr{L}_2 h-\mathbf{r}\cdot\nabla\times(\mathbf{v}\times\mathbf{B})], \quad (5)$$

$$\nabla^2\mathscr{L}_2 g=P_m[\partial_t\mathscr{L}_2 g-\mathbf{r}\cdot\nabla\times(\nabla\times(\mathbf{v}\times\mathbf{B}))]. \quad (6)$$

The Rayleigh number R, the Coriolis number τ, the Prandtl number P and the magnetic Prandtl number P_m are defined by

$$R=\frac{\alpha\gamma\beta d^6}{\nu\kappa}, \qquad \tau=\frac{2\Omega d^2}{\nu}, \qquad P=\frac{\nu}{\kappa}, \qquad P_m=\frac{\nu}{\lambda}, \quad (7)$$

where λ is the magnetic diffusivity. For the static temperature distribution we have chosen the case of a homogeneously heated sphere. This state is traditionally used for the analysis of convection in self-gravitating spheres and offers the numerical advantage that for Rayleigh numbers close to the critical value R_c the strength of convection does not differ much near the inner and outer boundaries. As the Rayleigh number increases beyond R_c heat enters increasingly at the inner boundary and is delivered by convection to the outer boundary. When R reaches a high multiple of R_c the heat generated internally in the fluid becomes negligible in comparison to the heat transported by convection from the inner to the outer boundary. The buoyancy distribution then becomes similar to that of a spherical shell with imposed temperature contrast and without internal heating. At low supercritical Rayleigh numbers some differences in the dynamo action of convection flows driven by different forms of heating have been noticed [8]. A stronger preference for dipolar dynamos has been found in the absence of internal heating, while with internal heating both, quadrupolar and dipolar dynamos can be found.

Fixed temperatures and stress-free boundaries,

$$u=\partial_{rr}^2 u=\partial_r(w/r)=\Theta=0 \quad \text{at } r=r_i\equiv\eta/(1-\eta) \text{ and } r=r_o\equiv 1/(1-\eta), \quad (8)$$

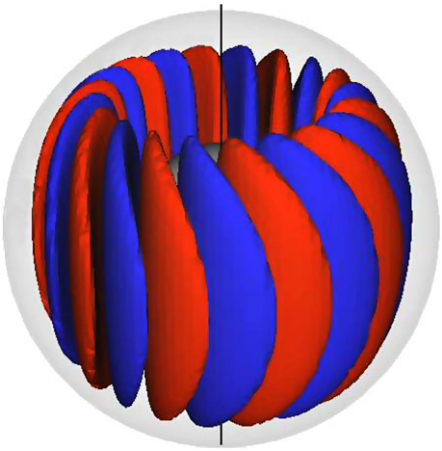

Fig. 1 Convection columns in a rotating spherical fluid shell for $\tau = 10^4$, $R = 2.8 \cdot 10^5$, $P = 1$. Blue and red surfaces correspond to a constant positive and negative value of the radial velocity.

will be assumed where η denotes radius ratio, $\eta = r_i/r_o$. In the following only $\eta = 0.4$ will be used. For the magnetic field electrically insulating boundaries are assumed such that the poloidal function h must be matched to the function $\hat{h}$ which describes the potential fields outside the fluid shell,

$$g = h - \hat{h} = \partial_r(h - \hat{h}) = 0 \quad \text{at } r = r_i \equiv \eta/(1-\eta) \text{ and } r = r_o \equiv 1/(1-\eta). \quad (9)$$

But computations for the case of an inner boundary with no-slip conditions and an electrical conductivity equal to that of the fluid have also been done [12]. The numerical integration of the equations together with the boundary conditions proceeds with the pseudo-spectral method as described in [14] and [15] which is based on an expansion of all dependent variables in spherical harmonics for the θ, φ-dependences, i.e.

$$u = \sum_{l,m} U_l^m(r,t) P_l^m(\cos\theta) \exp\{im\varphi\} \quad (10)$$

and analogous expressions for the other variables, w, Θ, h and g. P_l^m denotes the associated Legendre functions. For the r-dependence expansions in Chebychev polynomials are used. For further details see also [12]. For the non-magnetic convection calculations to be reported in the following a minimum of 33 collocation points in the radial direction and spherical harmonics up to the order 64 have been used. The resolution has been increased to 41 or 55 collocation points and spherical harmonics up to the order 96 or 128 in the case of dynamo simulations.

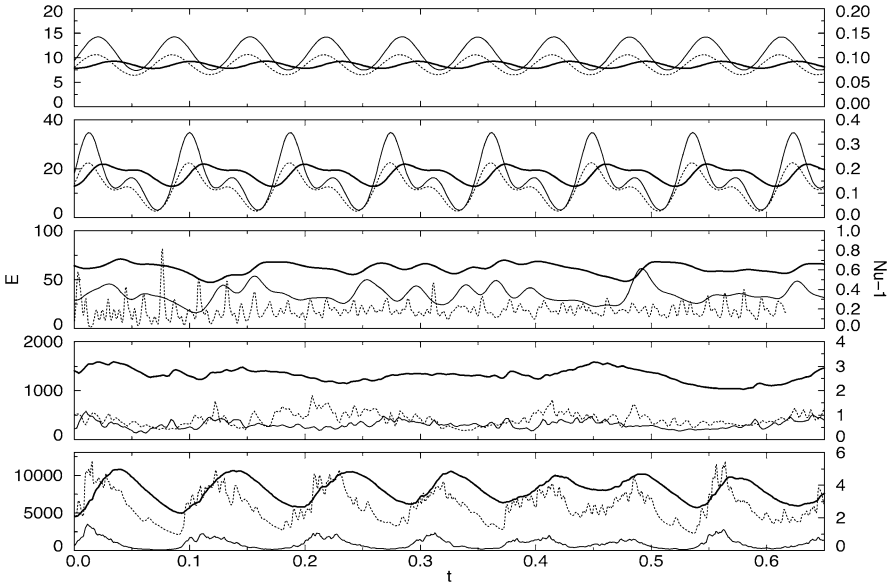

Fig. 2 Time series of energy densities of convection for $P = 1$, $\tau = 10^4$ and $R = 2.8 \times 10^5$, 3.0×10^5, 3.5×10^5, 7×10^5, 12×10^5, (from top to bottom). Solid and dashed lines indicate $\overline{E}_t$ and $\widetilde{E}_t$, respectively. The Nusselt number Nu_i is indicated by dotted lines and measured at the right ordinate.

3 Convection in rotating spherical shells

For an introduction to the problem of convection in spherical shells we refer to the review [2] and to the respective chapter in the book [5]. Additional information can be found in the papers by Grote and Busse [6], Jones et al. [7], Christensen [4] and Simitev and Busse [11]. Typically the onset of convection occurs in the form of progradely propagating thermal Rossby waves as illustrated in figure 1. Only for low Prandtl numbers P, i.e. $P < 10/\sqrt{\tau}$ according to [1], the onset occurs in the form of inertial waves attached to the outer equatorial boundary of the fluid shell as is discussed in [16], [17], [1].

Because of the symmetry of the velocity field with respect to the equatorial plane it is sufficient to plot streamlines in this plane, given by $r\partial u/\partial r = const.$, to characterize the convection flow. This has been done in figures 3 and 5. Even in the case of turbulent convection the part of the velocity field that is antisymmetric with respect to the equatorial plane is rather small as long as the parameter τ is sufficiently large.

As the Rayleigh number R grows beyond its critical value R_c, the thermal Rossby waves become modified by a sequence of bifurcations similar to those found in other problems of convection. First, oscillations of the amplitude are observed, then

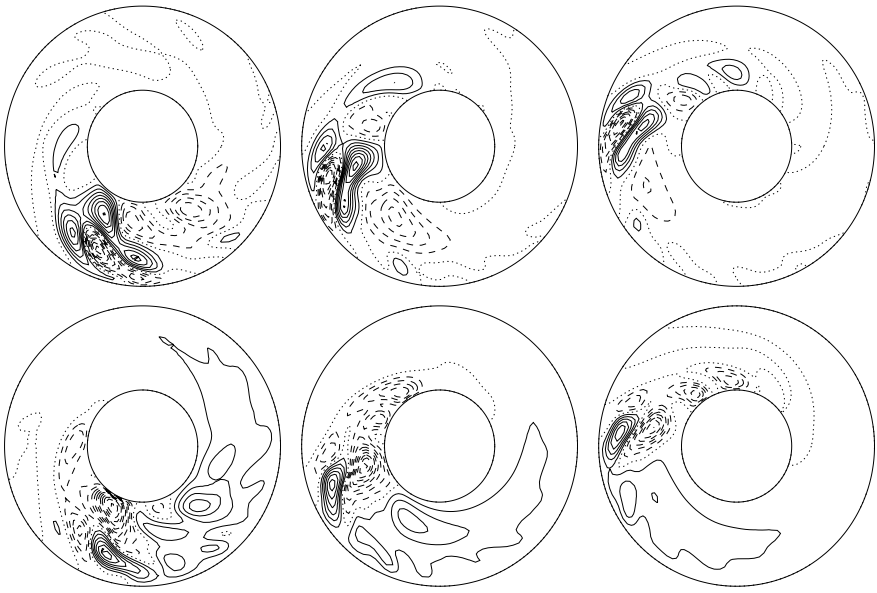

Fig. 3 Localized convection for $R = 7 \times 10^5$, $\tau = 1.5 \times 10^4$, $P = 0.5$ The streamlines, $r\partial u/\partial\varphi =$ const. (upper row) and the isotherms, $\Theta =$ const. (lower row), are shown in the equatorial plane for equidistant times (from left to right) with $\Delta t = 0.03$.

another bifurcation causes a low wavenumber modulation as function of the azimuth [11]. Finally, a chaotic state of convection is obtained.

4 Chaotic convection

The sequence of transitions can also visualized through the time dependence of average quantities such as the contributions to the kinetic energy density. These are defined by

$$\bar{E}_p = \langle | \nabla \times (\nabla \bar{u} \times \mathbf{r}) |^2 \rangle / 2, \quad \bar{E}_t = \langle | \nabla \bar{w} \times \mathbf{r} |^2 \rangle / 2 \tag{11a}$$

$$\widetilde{E}_p = \langle | \nabla \times (\nabla \widetilde{u} \times \mathbf{r}) |^2 \rangle / 2, \quad \widetilde{E}_t = \langle | \nabla \widetilde{w} \times \mathbf{r} |^2 \rangle / 2 \tag{11b}$$

where the angular brackets indicate the average over the fluid shell and where $\bar{u}$ refers to the azimuthally averaged component of u and $\widetilde{u}$ is given by $\widetilde{u} = u - \bar{u}$. At low supercritical Rayleigh numbers the energy densities corresponding to steadily drifting thermal Rossby waves are constant in time and are not included in figure 2. The onset of vacillations manifests itself in the sinusoidal oscillations of the kinetic energies as shown in the top plot of figure 2. Also plotted in figure 2 is the Nusselt number Nu_i measuring the efficiency of the convective heat transport at the inner boundary,

$$Nu_i = 1 - \frac{P}{r_i}\left.\frac{d\overline{\overline{\Theta}}}{dr}\right|_{r=r_i} \tag{12}$$

where the double bar indicates the average over the spherical surface. $\bar{E}_t$ describes the energy density of the differential rotation which increases strongly with increasing R as can be noticed in the lower plots of figure 2. This increase is caused by the strong azimuthal Reynolds stress exerted by the convection eddies resulting from their inclination with respect to radial direction as is apparent in figure 1. The increasing shear of the differential rotation tends to inhibit convection, however, in that it shears off the convection eddies. This is a consequence of the nearly two-dimensional nature of the dynamics in a rotating system: Because of the requirement that the structure of convection approaches closely the Taylor-Proudman condition, there is no possibility for a reorientation of the convection rolls as happens in non-rotating systems. In the rotating sphere convection thus generates the agent that tends to destroy it. A precarious balance in the form localized convection is the result. As shown in figure 3 convection occurs only in a restricted azimuthal section of the spherical shell where its amplitude is strong enough to overcome the inhibiting influence of the shear. For the geostrophic zonal flow it does not matter whether it is driven locally or more uniformly around the azimuth. Since in the non-convecting region thermal buoyancy accumulates, the advection of this buoyancy by the differential rotation strengthens and stabilizes the localized convection.

At even higher Rayleigh numbers this balance no longer works and instead of a localization in space the localization of convection in time is initiated as is shown in figures 4 and 5. Here convection exist only for a short period while the differential rotation is sufficiently weak. As the amplitude of convection grows, the differential rotation grows even more strongly since the Reynolds stress increases with the square of the amplitude. Soon the shearing action becomes strong enough to cut off convection. Now a viscous diffusion time must pass before the differential rotation has decayed sufficiently such that convection may start growing again. It is remarkable to see how the chaotic system exhibits its nearly periodic relaxation oscillations as shown in figure 4.

In figure 5 a sequence of plots is shown at four instances around the time of a convection peak. At first there is hardly any convection, - the dotted lines just indicate zero. At the next instance the differential rotation as shown by the upper row has decayed sufficiently such that convection columns can grow reaching nearly their maximum amplitude in the third plot. At the same time the differential rotation has grown as well and begins to exert its inhibiting effect such that convection decays at the fourth instance of the sequence, while the differential rotation reaches its maximum. It should be mentioned that localized convection and relaxation oscillations occur at moderate Prandtl numbers of the order unity or less. At higher values of P Reynolds stresses are no longer sufficiently powerful to generate a strong differential rotation. Instead variations of the temperature field caused by the dependence of the convective heat transport on latitude induce a differential rotation in the form of a thermal wind.

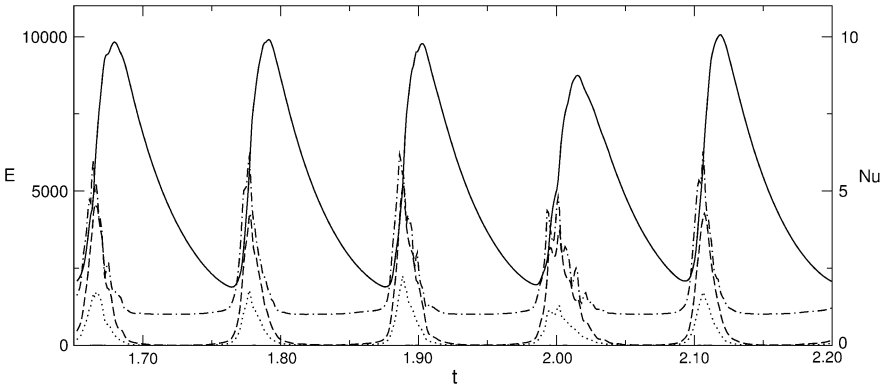

Fig. 4 Relaxation oscillations of chaotic convection in the case $\tau = 10^4$, $R = 6.5 \cdot 10^5$, $P = 0.5$. The energy densities $\overline{E_t}$ (solid line), $\widetilde{E}_t$ (dashed line), $\widetilde{E}_p$ (dotted line) and the Nusselt number (dash-dotted line, right ordinate) are shown as function of time.

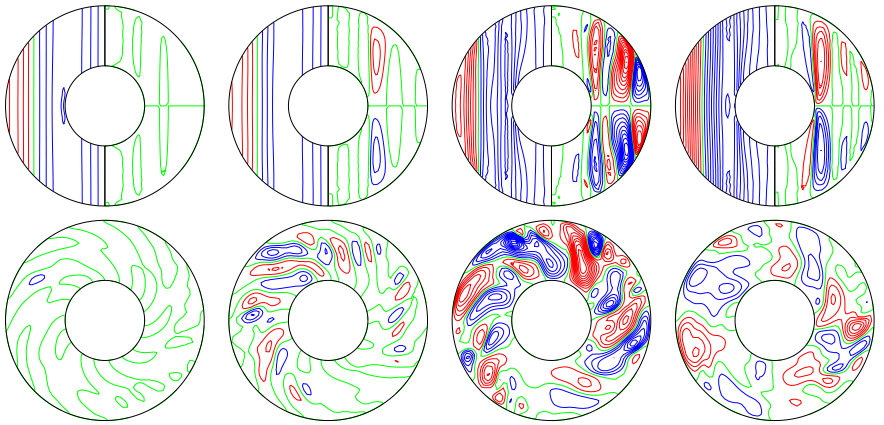

Fig. 5 Sequence of plots starting at $t = 2.31143$ and equidistant in time ($\Delta t = 0.01$) for the same case as in Fig. 8. Lines of constant $\bar{u}_\varphi$ and streamlines $r\sin\theta\partial_\theta\overline{h}$ =const. in the meridional plane, are shown in the left and right halves, respectively, of the upper row. The lower row shows corresponding streamlines, $r\partial u/\partial\varphi = $ const., in the equatorial plane.

The convective heat transport in the case of localized convection as well as in the case of relaxation oscillations is much reduced, of course, relative to a case without strong differential rotation. This causes the magnetic field to enter the problem in a crucial way provided the electrical conductivity is sufficiently high. By putting brakes on the differential rotation through its Lorentz force the magnetic field permits a much higher heat transport than would be possible in an electrically-insulating fluid. This is the basic reason that the Earth's core as well as other planets with convecting cores and rotating stars exhibit magnetic fields. A demonstration of

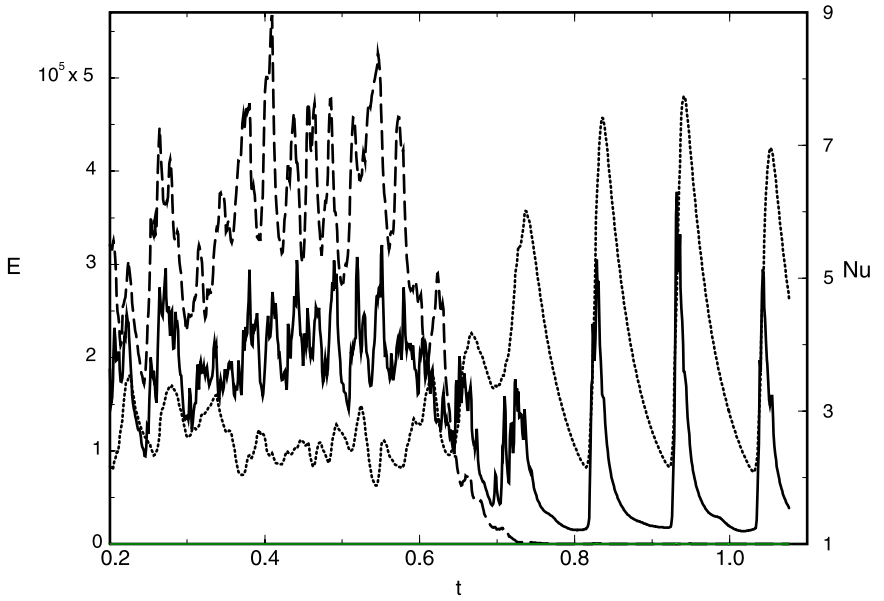

Fig. 6 Transition from a dynamo state to a state of chaotic relaxation oscillations for $\tau = 1.5 \times 10^4$, $R = 1.2 \times 10^6$, $P = P_m = 0.5$. The energy density $\overline{E}_t$ (dotted line), the total magnetic energy density (dashed line) and the Nusselt number Nu_i (solid line, right ordinate) are shown as function of time.

this effect is seen in figure 6 where by chance the convection driven dynamo was just marginal such that it could not recover after a downward fluctuation of the magnetic field. Hence the relaxation oscillations with their much reduced average heat flux take over from the dynamo state.

5 Distinct turbulent dynamos at identical parameter values

Convection driven dynamos in rotating spherical fluid shells are often subcritical as is apparent in figure 6, for instance. At somewhat higher Rayleigh numbers convection with a strong magnetic field will persist. On the other hand the dynamo will decay when the magnetic field is artificially reduced to, say, a quarter of its averaged energy. There thus exists the possibility of a convection driven dynamo state and of a non-magnetic convection state at identical values of the external parameters R, τ, P. The bistable coexistence of a non-magnetic convection state and a dynamo state is typical for subcritical bifurcations as in the analogous coexistence of laminar and turbulent states in shear flows.

More surprising is the fact that two different turbulent dynamo states can exist at identical values of the external parameters which now should include the magnetic

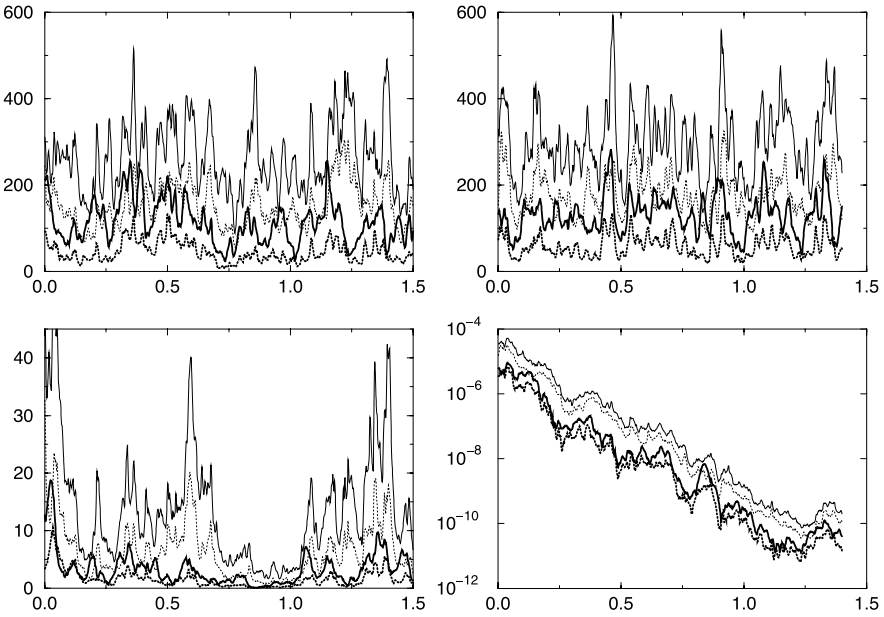

Fig. 7 Two distinct dynamos at identical parameter values, $\tau = 5 \times 10^3$, $R = 5 \times 10^5$, $P = P_m = 1$. Upper (lower) plots show time series of quadrupolar (dipolar) magnetic energy densities. Thick lines indicate mean torodial (solid lines) and poloidal (dashed lines) energy components. Thin lines indicate the same for the fluctuating components.

Prandtl number P_m. An example is shown in figure 7 where a spherical dynamo of mixed parity, i.e. with dipolar and quadrupolar components, and a purely quadrupolar dynamo evolve in time at identical external parameters. In the latter case the exponential decay of dipolar disturbances is clearly demonstrated. In figure 7 magnetic energy densities have been plotted that are defined in analogy to expressions (12),

$$\overline{M}_p = \langle \mid \nabla \times (\nabla \bar{h} \times \mathbf{r}) \mid^2 \rangle / 2, \quad \overline{M}_t = \langle \mid \nabla \bar{g}_t \times \mathbf{r} \mid^2 \rangle / 2 \tag{13a}$$

$$\widetilde{M}_p = \langle \mid \nabla \times (\nabla \widetilde{h}_p \times \mathbf{r}) \mid^2 \rangle / 2, \quad \widetilde{M}_t = \langle \mid \nabla \widetilde{g}_t \times \mathbf{r} \mid^2 \rangle / 2. \tag{13b}$$

An even more surprising case is that of two convection driven dynamos without any distinction in symmetry, just with differences in the magnitude of various energy densities as is apparent from figure 8. While a strong mean poloidal magnetic field as shown in the left half of figure 8 acts as an efficient brake on the differential rotation as measured by $\overline{E}_t$, it also inhibits convection. The alternative dynamo on the right side of the figure is characterized by a relatively weak mean magnetic field and dominant fluctuating components. Here the kinetic energy densities of convection are larger, but the differential rotation is still much weaker than it would be in the non-magnetic case.

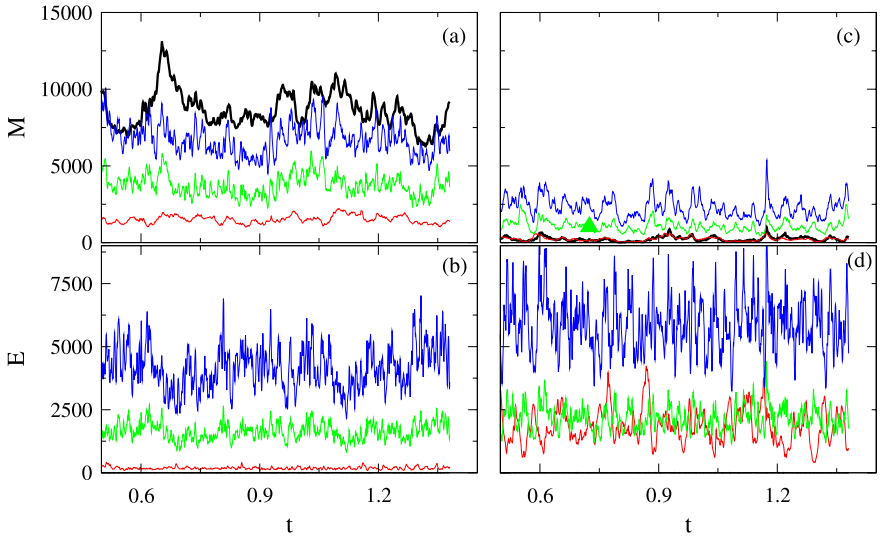

Fig. 8 Time series of two different chaotic attractors are shown - a MD (left column (a,b)) and a FD dynamo (right column (c,d)) both in the case $R = 3.5 \times 10^6$, $\tau = 4 \times 10^4$, $P = 0.5$ and $P_m = 1$. The top two panels (a,c) show magnetic energy densities. and the bottom two panels (b,d) show kinetic energy densities in the presence of the magnetic field. The components $\overline{M}_p$ are shown by thick solid black lines, while $\overline{X}_t$, $\widetilde{X}_p$, and $\widetilde{X}_t$ are shown in red green and blue respectively. X stands for either M or E.

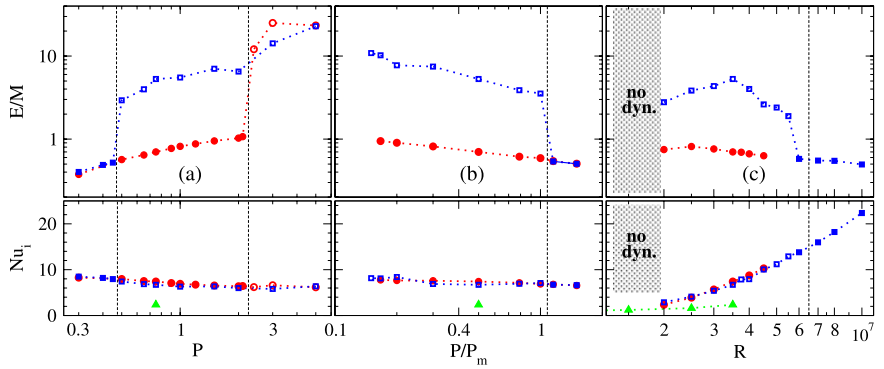

Fig. 9 The upper row shows the hysteresis effect in the ratio of magnetic to kinetic energy, E/M, at $\tau = 3 \times 10^4$ (a) as a function of the Prandtl number in the case of $R = 3.5 \times 10^6$, $P/P_m = 0.5$; (b) as a function of the ratio P/P_m in the case of $R = 3.5 \times 10^6$, $P = 0.75$ and (c) as a function of the Rayleigh number in the case $P = 0.75$, $P_m = 1.5$. Full and empty symbols indicate FD and MD dynamos, respectively and circles and squares indicate the two hysteresis branches. The critical value of R for the onset of thermal convection for the cases shown in (c) is $R_c = 659145$. A transition from FD to MD dynamos as P/P_m decreases in (b) is expected, but is not indicated owing to lack of data. The lower row shows the value Nu_i of the Nusselt number at $r = r_i$ for the same dynamo cases. Values for non-magnetic convection are indicated by triangles for comparison.

The bistability in the form of two different types of dynamos is not a singular phenomenon, but exists over an extended region of the parameter space. Since the region includes values of the Prandtl number of the order unity which has been the preferred value of P in many simulations of convection driven dynamos the phenomenon of bistable dynamos is of considerable importance. The first results of our extensive numerical simulations can be found in [13]. A typical diagram is shown in figure 9. The extended regime of coexistence of the two types of dynamo is bounded by transitions where one of the two dynamos ceases to be stable and evolves into the other one within a magnetic diffusion time. A basic reason for the competitiveness of both dynamos is that they exhibit essentially the same convective heat transport as measured by the Nusselt number Nu_i. The lower half of figure 9 not only demonstrates the surprising coincidence of the heat transports of the two dynamo types, but also indicates that these heat transports by far exceed those found in the absence of a magnetic field.

Recently the computations have been extended to higher rotation rates as shown in figure 10. At $\tau = 4 \times 10^4$ the same phenomenon of bistability has been found as at $\tau = 3 \times 10^4$. Again, the two kinds of dynamo exhibit the same heat transport as indicated in the lower part of figure 10.

6 Concluding remarks

The existence of two distinct turbulent states is a rare phenomenon, although examples exist in non-magnetic hydrodynamics, see, for instance, [10] [9]. In magnetohydrodynamics an electrically conducting fluid in the presence of a magnetic field offers new degrees of freedom which allow more than a single balance between the various forces operating in turbulent states. Initial conditions thus determine which of the competing states is actually realized.

The possibility of bistability could be of interest for the interpretation of planetary and stellar magnetism. Magnetic hysteresis effects associated with stellar oscillations may eventually be explained in this way. Anyone involved with numerical simulations of convection driven dynamos should be aware that his solutions could change drastically after different initial conditions have been introduced.

References

[1] Ardes, M., Busse, F.H., and Wicht, J.: Thermal convection in rotating spherical shells. *Phys. Earth Planet. Inter.*, **99**, 55–67 (1997)

[2] Busse, F.H.: Convective flows in rapidly rotating spheres and their dynamo action, *Phys. Fluids*, **14**, 1301–1314 (2002)

[3] Busse, F.H., and Simitev, R.: Inertial convection in rotating fluid spheres. *J. Fluid Mech.*, **498**, 23–30 (2004)

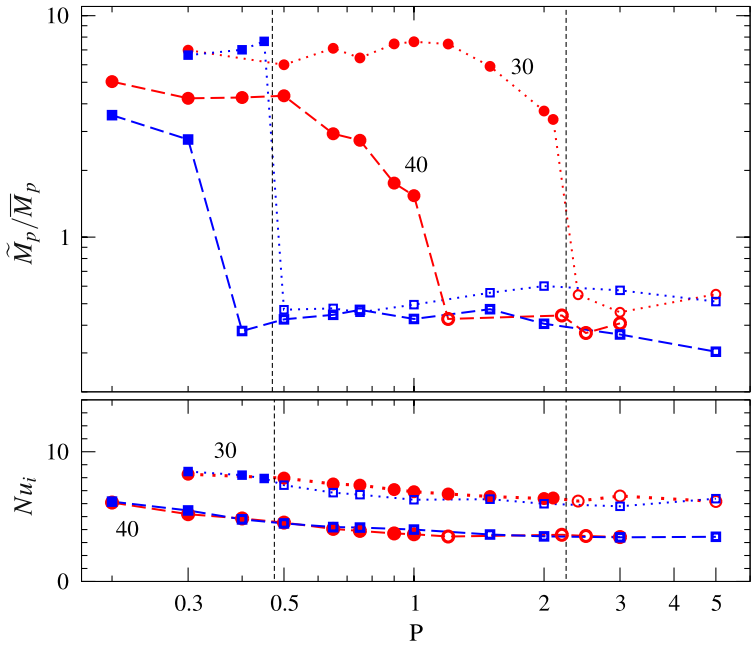

Fig. 10 The upper part shows the ratio between the energy densities of the fluctuating and the mean poloidal magnetic field, $\widetilde{M}_p/\overline{M}_p$, as a function of the Prandtl number at $\tau = 3 \times 10^4$ (denoted by 30 and dotted lines in plot)and at $\tau = 4 \times 10^4$ (denoted by 40 and dashed lines in plot) by symbols analogous to those in fig 10. In all cases $R = 3.5 \times 10^6$ and $P_m = 2P$. The lower part shows the value Nu_i of the Nusselt number for the same dynamo cases.

[4] Christensen, U.: Zonal flow driven by strongly supercritical convection in rotating spherical shells. *J. Fluid Mech.*, **470**, 115–133 (2002)
[5] Dormy, E., and Soward, A.M., eds.: Mathematical Aspects of Natural Dynamos, CRC Press, Taylor & Francis Group, 2007
[6] Grote, E., and Busse, F.H.: Dynamics of convection and dynamos in rotating spherical fluid shells. *Fluid Dyn. Res.*, **28**, 349–368 (2001)
[7] Jones, C.A., Soward, A.M., and Mussa, A.I.: The onset of thermal convection in a rapidly rotating sphere. *J. Fluid Mech.*, **405**, 157–179 (2000)
[8] Kutzner, C., and Christensen, U.: Driving mechanisms in geodynamo models. *Geophys. Res. Lett.*, **27**, 29–32 (2000)
[9] Mujica, N., and Lathrop, D.P.: Bistability and hystreresis in a highly turbulent swirling flow, *Physica A* **49**, 162–166 (2005)
[10] Ravelet, F., Marié, L., Chiffaudel, A., and Daviaud, F.: Multistability and Memory Effect in a Highly Turbulent Flow: Experimental Evidence for a Global bifurcation, *Phys. Rev. Lett.* **93**, 164501 (2004).
[11] Simitev, R.D., and Busse, F.H.: Patterns of convection in rotating spherical shells, *New J. Phys.*, **5**, 97.1–97.20 (2003)

[12] Simitev, R.D., and Busse, F. H.: Prandtl number dependence of convection-driven dynamos in rotating spherical fluid shells, *J. Fluid Mech.*, **532**, 365–388 (2003)
[13] Simitev, R.D., and Busse, F.H.: Bistability and hysteresis of dipolar dynamos generated by turbulent convection in rotating spherical shells, *Euro Phys. Lett.*, **85**, 19001 (2009)
[14] Tilgner, A., and Busse, F.H.: Finite amplitude convection in rotating spherical fluid shells, *J. Fluid Mech.*, **332**, 359–376 (1997)
[15] Tilgner, A.: Spectral Methods for the Simulation of Incompressible Flows in Spherical Shells. *Int. J. Numer. Meth. Fluids*, **30**, 713–724 (1999)
[16] Zhang, K.-K., and Busse, F.H.: On the onset of convection in a rotating spherical shells. *Geophys. Astrophys. Fluid Dyn.*, **39**, 119–147 (1987)
[17] Zhang, K.: On coupling between the Poincaré equation and the heat equation. *J. Fluid Mech.*, **268**, 211–229 (1994)

Part III
Instability and Vortex Dynamics

Zigzag instability of the Kármán vortex street in stratified and rotating fluids

Axel Deloncle, Paul Billant and Jean-Marc Chomaz

Abstract We investigate the three-dimensional stability of the Kármán vortex street in a stratified and rotating fluid by means of an asymptotic theory for long-vertical wavelength and well-separated vortices. It is found that the Kármán street with close rows is unstable to the zigzag instability when the fluid is strongly stratified independently of the background rotation. The zigzag instability bends the vortices with almost no internal deformation. The results are in excellent agreement with direct numerical stability analyses and may explain the formation of layers commonly observed in stratified flows.

1 Introduction

Kármán vortex streets can be observed in geophysical flows for instance in the wake of mountains or islands [7]. They consists in two staggered rows of vortices (Fig. 1). Much attention has been devoted to the two-dimensional stability of this flow in homogeneous fluid using point vortices (see [10]). The three-dimensional stability has been addressed by [14]. Their analysis is based on vortex filaments and is therefore limited to long axial wavelengths and well-separated vortices. They found that the Kármán vortex street is unstable to three-dimensional or two-dimensional disturbances depending on the spacing ratio of the street. The stability of such two-

Axel Deloncle
Hydrodynamics Laboratory (LadHyX), Ecole Polytechnique, 91128 Palaiseau Cedex, France, e-mail: axel.deloncle@ladhyx.polytechnique.fr

Paul Billant
Hydrodynamics Laboratory (LadHyX), Ecole Polytechnique, 91128 Palaiseau Cedex, France, e-mail: billant@ladhyx.polytechnique.fr

Jean-Marc Chomaz
Hydrodynamics Laboratory (LadHyX), Ecole Polytechnique, 91128 Palaiseau Cedex, France, e-mail: chomaz@ladhyx.polytechnique.fr

D. Dritschel (ed.), *IUTAM Symposium on Turbulence in the Atmosphere and Oceans*, IUTAM Bookseries 28, DOI 10.1007/978-94-007-0360-5_16,

dimensional vortex array has been little addressed in a stably stratified and rotating fluid. [12] have investigated numerically the stability of an infinite vortex row but only in a weakly stratified and rotating fluid. Experiments in a strongly stratified fluid have shown the formation of horizontal layers by the destabilization of the vortex streets created by towing a rake of vertical cylinders [8] or a rake of vertical flat plates [13].

The stability of a pair of columnar vertical vortices in a stratified rotating fluid has shown the existence of a three-dimensional instability called zigzag instability [2; 11] or tall-column instability [6] that vertically bends the vortices with little internal deformation. [1; 3] recently derived a general theory to treat the stability of vortices for long-axial-wavelength bending perturbations and well-separated vortices in a stratified and rotating fluid. Their analysis led to stability equations formally identical to the ones given by [4] in homogeneous fluid except that the expressions of the self-induction and mutual induction functions differ between homogeneous fluid and stratified and rotating fluid. This asymptotic theory gives results in excellent agreement with full numerical stability analysis of the zigzag instability of vortex pairs. Here, we make use of this approach to study the three-dimensional stability of the Kármán vortex street in a stratified and rotating fluid. The results are compared to direct numerical stability analyses [5].

2 Problem formulation

2.1 Pair of vortices in a stratified and rotating fluid

For clarity, we first present the stability equations for two vortices in a stratified and rotating fluid. The generalization to the Kármán street is straightforward from this case. We denote Γ_1 and Γ_2, the circulations of the two vertical vortices of radius a separated by a distance b. The Froude and Rossby numbers of each vortex are defined as follows:

$$F_{hi} = \frac{|\Gamma_i|}{2\pi a^2 N}, \quad Ro_i = \frac{\Gamma_i}{4\pi a^2 \Omega_b}, \quad \text{with} \quad i = \{1,2\}, \tag{1}$$

where N is the Brunt–Väisälä frequency and Ω_b is the rotation rate about the vertical axis.

The asymptotic theory is based on three assumptions. First, it is assumed that the vortices are well-separated: $a \ll b$. The second hypothesis is that the perturbations consist in bending deformations of the vortices with a small vertical wavenumber k_z such that $k_z F_{hi} a \ll \max(1, \sqrt{F_{hi}})\min(1, Ro_i)$. These two assumptions are similar to those assumed in vortex stability analysis using vortex filaments in a homogeneous fluid [4; 14]. The last assumption is that the strains $\Gamma_i/2\pi b^2$ are small compared to the Brunt–Väisälä frequency, or equivalently: $F_{hi} \ll b^2/a^2$. Since $b/a \gg 1$, this

condition is not only satisfied for strongly stratified fluids (i.e. $F_{hi} < 1$) but also weakly stratified fluids in the range: $1 < F_{hi} \ll b^2/a^2$.

The position of each vortex core is assumed to be perturbed by an amount $(\tilde{\Delta}x_1, \tilde{\Delta}y_1)$ and $(\tilde{\Delta}x_2, \tilde{\Delta}y_2)$. Writing these perturbations in the form:

$$(\tilde{\Delta}x_i, \tilde{\Delta}y_i) = (\Delta x_i, \Delta y_i)\mathrm{e}^{\mathrm{i}k_z z} + \text{c.c.}, \tag{2}$$

where c.c. denotes the complex conjugate, and using the three hypothesis mentioned above, the following evolution equations for the perturbations of the first vortex have been obtained by means of an asymptotic analysis

$$\begin{aligned}\frac{\mathrm{d}\Delta x_1}{\mathrm{d}t} &= -\frac{\Gamma_2}{2\pi b^2}\Delta y_1 + \frac{\Gamma_2}{2\pi b^2}\Psi(\beta)\Delta y_2 \\ &\quad + \left(f - \frac{\Gamma_1}{2\pi}\omega_{\mathrm{Re}}(k_z, F_{h1}, Ro_1)\right)\Delta y_1 + \frac{|\Gamma_1|}{2\pi}\omega_{\mathrm{Im}}(k_z, F_{h1}, Ro_1)\Delta x_1, \end{aligned} \tag{3}$$

$$\begin{aligned}\frac{\mathrm{d}\Delta y_1}{\mathrm{d}t} &= -\frac{\Gamma_2}{2\pi b^2}\Delta x_1 + \frac{\Gamma_2}{2\pi b^2}\chi(\beta)\Delta x_2 \\ &\quad - \left(f - \frac{\Gamma_1}{2\pi}\omega_{\mathrm{Re}}(k_z, F_{h1}, Ro_1)\right)\Delta x_1 + \frac{|\Gamma_1|}{2\pi}\omega_{\mathrm{Im}}(k_z, F_{h1}, Ro_1)\Delta y_1. \end{aligned} \tag{4}$$

The complementary pair of equations for the second vortex are found by interchanging the subscripts 1 and 2. These equations are written in the frame of reference rotating at angular velocity $f + \Omega_b$ where the base flow is steady. $f = (\Gamma_1 + \Gamma_2)/2\pi b^2$ is the rate at which the unperturbed vortices rotate around each other. The functions ψ and χ are the mutual-induction functions and $\omega = \omega_{\mathrm{Re}} + \mathrm{i}\omega_{\mathrm{Im}}$ is the self-induction function which can be complex in a stratified and rotating fluid. These functions will be detailed below.

These equations have the same form as the ones derived by [4] or [9] for a pair of vortices in a homogeneous fluid using the Biot–Savart law to compute the induced motion of the vortices and the cut-off approximation to determine the self-induced velocity of the individual vortices.

The physical meaning of the three terms in the righthand side of (3) is the following. The first term represents the strain effect of the basic flow field of one vortex on the perturbation sustained by the other vortex. The second term is the mutual-induction effect, i.e. the effect of the perturbation of one vortex on the basic flow of the other vortex. This effect depends on the mutual-induction functions:

$$\chi(\beta) = -\beta^2 K_1'(\beta), \qquad \psi(\beta) = \beta K_1(\beta), \tag{5}$$

where $\beta = bk_z F_{h1}/|Ro_1| = bk_z F_{h2}/|Ro_2|$ and K_1 is the modified Bessel function of the second kind of first order. These functions are the equivalent, in a stratified and rotating fluid, of the Crow's first and second mutual-induction functions [4]. χ and ψ are equal to unity for $\beta = 0$ and then goes to zero exponentially for large β.

The last term represents the effect of the rotation of the vortex pair at angular velocity f and the self-induction effect, i.e. the effect of a vortex on itself. If alone, this self-induction corresponds to a rotation of the vortex at angular velocity

$\Gamma_i/2\pi\omega_{Re}$ around its unperturbed location. When $\omega_{Im} < 0$, this rotation is damped at rate $\sigma = |\Gamma|/2\pi\omega_{Im}$. In a stratified and rotating fluid, the self-induction function[1] is given by:

$$\omega(k_z, F_{hi}, Ro_i) = \frac{k_z^2 F_{hi}^2}{2Ro_i^2}\left(-\ln\left(\frac{ak_zF_h}{2|Ro_i|}\right) + \delta(F_{hi}, Ro_i) - \gamma_e\right), \tag{6}$$

where $\gamma_e = 0.5772$ is the Euler constant and δ is a parameter depending on the Froude number F_{hi}, the Rossby number Ro_i and the non-dimensional angular velocity Ω of the individual vortices:

$$\delta(F_h, Ro) = \lim_{\eta_0\to\infty}\int_0^{\eta_0} \xi^3\Omega(\xi)^2\frac{(Ro\Omega(\xi)+1)^2}{1-F_h^2\Omega(\xi)^2}d\xi - \ln\eta_0 \tag{7}$$

In this paper, we consider the Lamb–Oseen profile: $\Omega(r) = (1/r^2)\left(1-\exp\left(-r^2\right)\right)$. In this case, the self-induction is real and positive for $F_h \leq 1$ whatever Ro in contrast to homogeneous fluids for which it is negative. For $F_h \geq 1$, the self-induction becomes complex with a negative imaginary part ω_{Im} because the bending disturbances are damped by a viscous critical layer at the radius where the angular velocity of the vortex is equal to the Brunt–Väisälä frequency.

2.2 *Kármán vortex street in a stratified and rotating fluid*

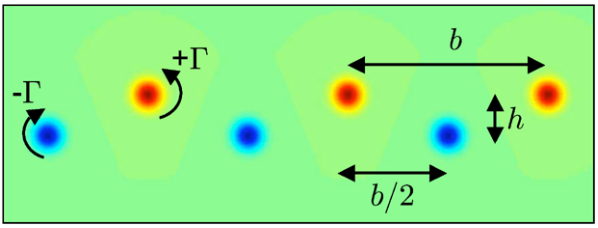

Fig. 1 Sketch of the Kármán vortex street. The vortices are initially two-dimensional with their axis in the vertical direction. The rows are infinite.

The Kármán vortex street consists in a staggered double row of two-dimensional vertical vortices (Fig. 1). The vortices of the upper row have a positive circulation Γ while those of the lower row have a negative circulation $-\Gamma$. The distance between the two rows is h. The vortices on each row are separated by a distance b and the two rows are staggered by a distance $b/2$. All the vortices have the same radius a.

[1] Note that the self-induction function is not exactly defined as in [4] or [14].

The whole unperturbed vortex array moves with a uniform velocity in the frame of reference rotating at rate Ω_b about the vertical axis. Since all vortices have the same absolute circulation, they are characterized by a single Froude number $F_h = \Gamma/2\pi a^2 N$. In contrast, the Rossby number of the vortices of the upper row is $Ro = \Gamma/4\pi a^2\Omega_b$ while the Rossby number of the vortices of the lower row is opposite: $-Ro$.

[14] have investigated the stability of the Kármán vortex street in a homogeneous fluid in the limit of well-separated vortices and long-wavelength bending perturbations following Crow's stability analysis of a counter-rotating vortex pair. Their stability equations have the same form as (3) except that they sum up all the strain and mutual-induction effects of each vortex of the array. In order to determine the three-dimensional stability of vortex arrays in a stratified and rotating fluid, we can thus follow the analysis of [14], except that the mutual-induction and self-induction functions have to be replaced by those valid in a stratified and rotating fluid.

By summing up the straining and the mutual induction effects due to each vortex, the following evolution equations for the perturbations of a vortex m in the upper row are found:

$$\begin{aligned}
\frac{\mathrm{d}\Delta x_{1,m}}{\mathrm{d}t} &= -\frac{\Gamma}{2\pi}\omega_{\mathrm{Re}}(k_z,F_h,Ro)\Delta y_{1,m} + \frac{|\Gamma|}{2\pi}\omega_{\mathrm{Im}}(k_z,F_h,Ro)\Delta x_{1,m} \\
&\quad -\frac{\Gamma}{2\pi}\sum_{p\neq m}\frac{\Delta y_{1,m}-\psi_{pm}\Delta y_{1,p}}{b_{pm}^2} \\
&\quad +\frac{\Gamma}{2\pi}\sum_{q}\frac{(\tilde{b}_{qm}^2-h^2)\Delta y_{1,m}-(\tilde{b}_{qm}^2\psi_{qm}-h^2\chi_{qm})\Delta y_{2,q}}{L_{qm}^4}, \\
&\quad +\frac{\Gamma}{2\pi}\sum_{q}\frac{\tilde{b}_{qm}h\left[2\Delta x_{1,m}-(\chi_{qm}+\psi_{qm})\Delta x_{2,q}\right]}{L_{qm}^4} \qquad (8) \\
\frac{\mathrm{d}\Delta y_{1,m}}{\mathrm{d}t} &= +\frac{\Gamma}{2\pi}\omega_{\mathrm{Re}}(k_z,F_h,Ro)\Delta x_{1,m} + \frac{|\Gamma|}{2\pi}\omega_{\mathrm{Im}}(k_z,F_h,Ro)\Delta y_{1,m} \\
&\quad -\frac{\Gamma}{2\pi}\sum_{p\neq m}\frac{\Delta x_{1,m}-\chi_{pm}\Delta x_{1,p}}{b_{pm}^2} \\
&\quad +\frac{\Gamma}{2\pi}\sum_{q}\frac{(\tilde{b}_{qm}^2-h^2)\Delta x_{1,m}-(\tilde{b}_{qm}^2\chi_{qm}-h^2\psi_{qm})\Delta x_{2,q}}{L_{qm}^4} \\
&\quad -\frac{\Gamma}{2\pi}\sum_{q}\frac{\tilde{b}_{qm}h\left[2\Delta y_{1,m}-(\chi_{qm}+\psi_{qm})\Delta y_{2,q}\right]}{L_{qm}^4}, \qquad (9)
\end{aligned}$$

where $b_{pm} = (p-m)b$, $\tilde{b}_{qm} = (q-m+1/2)b$ and $L_{qm}^2 = h^2+\tilde{b}_{qm}^2$. The subscripts on ψ and χ indicate that the function arguments are $|b_{pm}|k_zF_h/Ro$ and $|L_{qm}|k_zF_h/Ro$ for subscripts pm and qm respectively. Similar equations are found for a vortex $(2,n)$ in the lower row. We consider linear perturbations of the form:

$$(\Delta x_{1,m}, \Delta y_{1,m}) = (\Delta x_1, \Delta y_1) \mathrm{e}^{\mathrm{i}m\phi + \sigma t} \tag{10}$$

$$(\Delta x_{2,n}, \Delta y_{2,n}) = (\Delta x_2, \Delta y_2) \mathrm{e}^{\mathrm{i}(n+\frac{1}{2})\phi + \sigma t} \tag{11}$$

with σ the growth rate and $0 \leq \phi \leq \pi$. As shown by [14], ϕ/b can be considered as a wavenumber of the disturbance in the row direction. However, it is more convenient to introduce the wavelength of the disturbance $\mu b = 2\pi b/\phi$ in the row direction with $2 \leq \mu \leq \infty$. A value $\mu = 2$ implies a periodicity every two vortices, $\mu = 4$ every four vortices and so on, while $\mu = \infty$ means that all the vortices on a single row are displaced in the same direction.

Following [14], it is also convenient to introduce symmetric and antisymmetric modes:

$$(\Delta x_s, \Delta y_s) = (\Delta x_1 + \Delta x_2, \Delta y_1 - \Delta y_2),$$
$$(\Delta x_a, \Delta y_a) = (\Delta x_1 - \Delta x_2, \Delta y_1 + \Delta y_2).$$

The physical meaning of these modes can be easily understood in the case $\mu = \infty$, i.e. when all vortices of a given row are displaced in the same direction. The symmetric mode corresponds then to a displacement of each row in the same $x-$direction but in opposite $y-$direction, i.e. a modulation of the row spacing h along the vertical direction. Conversely, the antisymmetric mode corresponds to displacements of each row in opposite $x-$direction but in the same $y-$direction, i.e. a vertical modulation of the interval $b/2$ in the $x-$direction between the two rows.

However, contrary to homogeneous fluids studied by [14], the symmetric and antisymmetric modes do not always decouple because the self-induction for the vortices of the upper and lower rows are not equal: $\omega(k_z, F_h, Ro) \neq \omega(k_z, F_h, -Ro)$. A decoupling is recovered only in the limits $Ro \to \infty$ and $Ro \to 0$.

Inserting (10-11) into (8-9) and the corresponding equations for the lower row leads to an eigenvalue problem which can be easily solved [5].

3 Results

Fig. 2(a) shows the case of the Kármán vortex street with close rows $\kappa = h/b = 0.2$ for a low Froude number $F_h = 0.1$. The nondimensional theoretical growth rate $2\pi b^2 \sigma/\Gamma$ of the dominant mode is plotted (solid lines) as a function of the rescaled vertical wavenumber $bF_h k_z$ for different Rossby numbers from $Ro = \infty$ to $Ro = 0.75$. The dominant instability is three-dimensional and the rotation decreases the most amplified rescaled wavenumber. The maximum growth rate also decreases significantly ($\sim 40\%$) when Ro goes from $Ro = \infty$ to $Ro = 6$ but then remains approximately constant when Ro is further decreased. The perturbations induced by this three-dimensional instability are sketched on Fig. 3 for $Ro = \infty$. The instability is a zizag instability that bends all the vortices of a row in the same direction (i.e. $\mu = \infty$) but the two rows are bended in opposite direction, i.e. in a symmetric manner. The interval between the two rows is thus modulated along the vertical. Strikingly, this

is the opposite to the case of a homogeneous fluid where the symmetric mode is stable while the antisymmetric mode is three-dimensionally unstable [14]. For finite Ro, the eigenmode is not perfectly symmetric: the vortices in the lower row which are anticyclonic are more displaced than the cyclonic vortices in the upper row. The symbols in Fig. 2(a) show the results of a direct numerical stability analysis for a large Reynolds number close to the inviscid limit $Re = 50000$ [5]. We see that there is a perfect agreement for small values of k_z between the numerical and theoretical results (solid lines). Small departures at large wavenumbers are observed because the asymptotic theory is restricted to long-wavelength disturbances. Nevertheless, the agreement is very good and the theory predicts very well the most unstable vertical wavenumber k_{zmax} and the maximum growth rate.

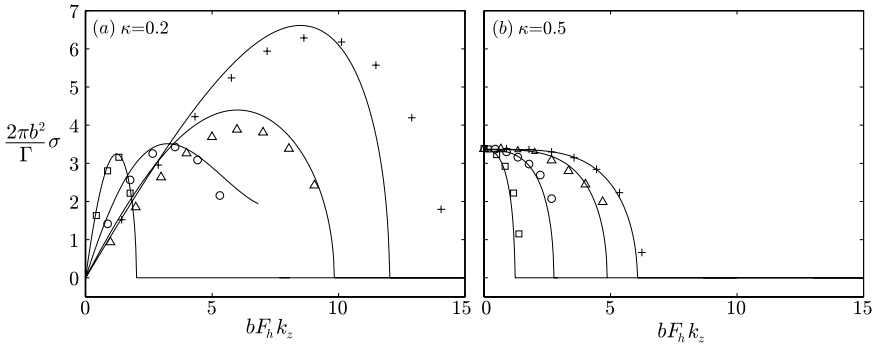

Fig. 2 Nondimensional growth rate $2\pi b^2\sigma/\Gamma$ of the dominant mode as a function of the rescaled vertical wavenumber bF_hk_z for $F_h = 0.1$ for the Kármán vortex street with (a) close rows $\kappa = 0.2$ and (b) distant rows $\kappa = 0.5$. The symbols correspond to the numerical results and the solid lines to the asymptotic theory. In each plot, the curves from right to left correspond to the Rossby numbers: $Ro = \infty$ (+), $Ro = 6$ (△), $Ro = 2$ (○), $Ro = 0.75$ (□).

Fig. 2(b) is similar to 2(a) but for a Kármán vortex street with more distant rows $\kappa = 0.5$. In this case, the most unstable mode is two-dimensional ($k_{zmax} = 0$) and thereby not affected by rotation. However, the band of unstable vertical wavenumbers narrows dramatically when the rotation increases. The agreement between numerical (symbols) and theoretical (solid lines) results is excellent over almost all the unstable band of vertical wavenumbers k_z. The dominant eigenmode has $\mu = 2$, i.e. this instability is a two-dimensional pairing instability which tends to move closer or away adjacent vortices of a given row [14].

By varying κ and μ, we have found that the zigzag instability with $\mu = \infty$ remains dominant for approximately $\kappa \lesssim 0.4$. When the two vortex rows are more distant $\kappa \gtrsim 0.4$, the dominant overall instability becomes the $\mu = 2$ two-dimensional pairing instability.

We now set the Rossby number to $Ro = \infty$ (no background rotation) and investigate the effect of the Froude number for $\kappa = 0.2$. Fig. 4 shows the growth rate of

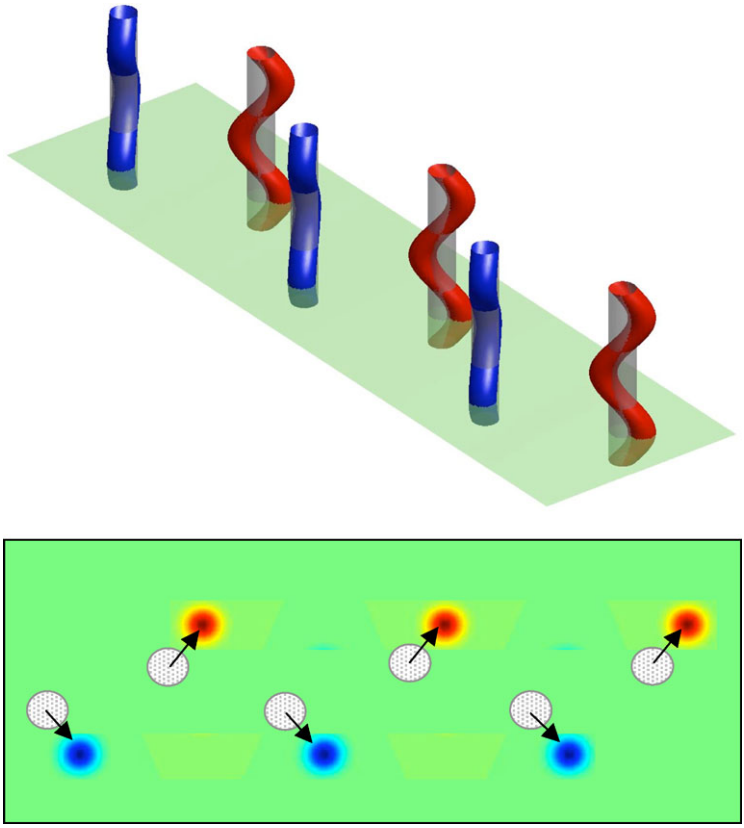

Fig. 3 Sketch of the dominant instability of the Kármán vortex street with close rows $\kappa = 0.2$ for $F_h = 0.1$ and $Ro = \infty$. The top figure is a three-dimensional view of the bending deformations induced by the isntability. The displacements of the vortices in the horizontal cross section are indicated in the bottom figure. The dominant instability is a symmetric zigzag instability.

the dominant mode for various Froude numbers from strong stratification ($F_h = 0.1$) to moderate stratification ($F_h = 1.2$). In all cases, the agreement between numerical (symbols) and theoretical (solid lines) results is very good although a slight departure is observed at large wavenumbers. We see that the growth rate curves for $F_h = 0.1$ and $F_h = 1$ are almost similar except a small decrease in the most amplified rescaled wavenumber. The stratification has thus little effect on the zigzag instability as long as $F_h < 1$. However, when the Froude number is further increased to $F_h = 1.2$, an abrupt drop of 50% of the maximum growth rate is observed. This is due to the damping of the zigzag instability by a viscous critical layer that appears for $F_h > 1$.

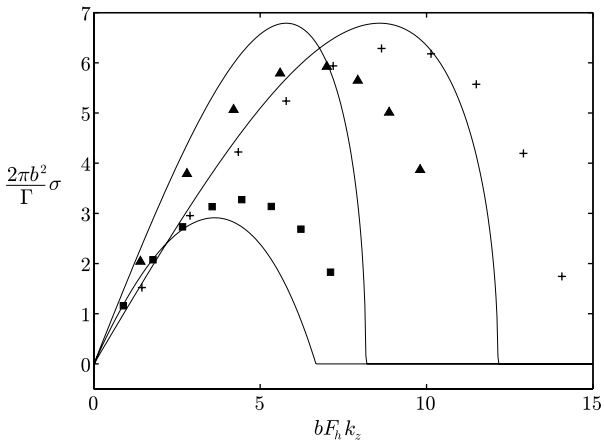

Fig. 4 Nondimensional growth rate $2\pi b^2\sigma/\Gamma$ of the dominant mode as a function of the rescaled vertical wavenumber bF_hk_z with $Ro = \infty$ for the Kármán vortex street with close rows $\kappa = 0.2$. The symbols correspond to the numerical results and the solid lines to the asymptotic theory. The curves from right to left correspond to the Froude numbers: $F_h = 0.1$ (+), $F_h = 1.$ (▲), $F_h = 1.2$ (■).

4 Conclusion

We have investigated theoretically and numerically the three-dimensional stability of a Kármán vortex street in a stratified and rotating fluid. The theoretical and numerical results are in excellent agreement for all the Rossby and Froude numbers investigated. This agreement proves that the asymptotic theory captures the physics of the instabilities due to the vortex interactions in stratified and rotating fluids. Furthermore, it works well for finite wavelengths and for close vortices despite the assumptions used in the asymptotics: long-wavelength bending perturbations and well-separated vortices.

If we summarize the stability results, we have found that when the fluid is sufficiently stratified, i.e. $F_h \leq 1.3 - 1.6$, the instability is three-dimensional whatever the Rossby number for the Kármán vortex street with close rows. It is a bending instability of the same type as the zigzag instability of vortex pairs. This instability might explain the destabilization of the Kármán vortex streets observed experimentally in stratified fluids by [8] and [13]. The Kármán vortex street for distant rows is most unstable to a two-dimensional pairing instability for any Rossby number.

References

[1] Billant, P.: Zigzag instability of vortex pairs in stratified and rotating fluid. part 1. general stability equations. (2010). *J. Fluid Mech.* (In press)

[2] Billant, P., Chomaz, J.M.: Experimental evidence for a new instability of a vertical columnar vortex pair in a strongly stratified fluid. J. Fluid Mech. **418**, 167–188 (2000)
[3] Billant, P., Deloncle, A., Chomaz, J., Otheguy, P.: Zigzag instability of vortex pairs in stratified and rotating fluid. part 2: Analytical and numerical analyses. (2010). *J. Fluid Mech.* (In press)
[4] Crow, S.C.: Stability theory for a pair of trailing vortices. A.I.A.A. J. **8**, 2172–2179 (1970)
[5] Deloncle, A., Billant, P., Chomaz, J.M.: Three-dimensional stability of vortex arrays in a stratified and rotating fluid (2010). *J. Fluid Mech.* (Submitted)
[6] Dritschel, D.G., de la Torre Juárez, M.: The instability and breakdown of tall columnar vortices in a quasi-geostrophic fluid. J. Fluid Mech. **328**, 129–160 (1996)
[7] Etling, D.: Mesoscale vortex shedding from large islands: a comparison with laboratory experiments of rotating stratified flows. Meteorol. Atmos. Phys. **43**, 145–151 (1990)
[8] Holford, M., Linden, P.F.: Turbulent mixing in a stratified fluid. Dyn. Atmos. Oceans **30**, 173–198 (1999)
[9] Jimenez, J.: Stability of a pair of co-rotating vortices. Phys. Fluids **18**, 1580–1581 (1975)
[10] Lamb, H.: Hydrodynamics. Cambridge University Press (1932)
[11] Otheguy, P., Chomaz, J.M., Billant, P.: Elliptic and zigzag instabilities on co-rotating vertical vortices in a stratified fluid. J. Fluid Mech. **553**, 253–272 (2006)
[12] Potylitsin, P.G., Peltier, W.R.: Stratification effects on the stability of columnar vortices on the f-plane. J. Fluid Mech. **355**, 45–79 (1998)
[13] Praud, O., Fincham, A.M., Sommeria, J.: Decaying grid turbulence in a strongly stratified fluid. J. Fluid Mech. **522**, 1–33 (2005)
[14] Robinson, A.C., Saffman, P.G.: Three-dimensional stability of vortex arrays. J. Fluid Mech. **125**, 411–427 (1982)

Instabilities of a columnar vortex in a stratified fluid

Patrice Meunier, Nicolas Boulanger, Xavier Riedinger and Stéphane Le Dizès

Abstract In this paper, we show that the presence of a vertical density gradient can destabilise a Gaussian vortex in two different ways. First, when the vortex axis is slightly tilted with respect to the vertical and if its Froude number is larger than one, the vortex exhibits strong axial flows inside a critical layer, which lead to a violent three-dimensional instability. Second, when the vortex axis is vertical, the vortex is weakly unstable by emission of internal gravity waves. Theoretical predictions for both instabilities are compared with experimental evidences.

1 Introduction

It is well known that rotating and stratified turbulence contains many vortices whose axes tend to align with the background rotation axis and the density gradient direction. It is thus of interest to study the stability of such vortices to gain comprehension on the mechanisms which drive rotating and stratified turbulence. As a first step, we will focus here on the effect of stratification only.

There exist many inviscid instabilities which can destabilise a vortex in a homogeneous fluid. When the velocity profile of the vortex satisfies the Rayleigh criterion, the vortex is subject to a centrifugal instability. Otherwise, all the eigenmodes of the vortex (called vortex Kelvin modes) are neutral and can only grow due to an external forcing. For example, the presence of a second vortex can induce two different instabilities: the large wavelength Crow instability [5] and the short wavelength elliptical instability [9].

The presence of a stable stratification modifies the characteristics of these three instabilities. The Rayleigh criterion is not modified by stratification but the instability is weaker as soon as viscous effects are also considered [8]. The Crow instability

Patrice Meunier
Institut de Recherche sur les Phenomenes Hors Equilibre, CNRS / Aix-Marseille Universites, 49 rue Joliot-Curie, 13384 Marseille, France, e-mail: meunier@irphe.univ-mrs.fr

D. Dritschel (ed.), *IUTAM Symposium on Turbulence in the Atmosphere and Oceans*, IUTAM Bookseries 28, DOI 10.1007/978-94-007-0360-5_17,

is transformed into a zig-zag instability [1; 6]. And the elliptical instability is weakened due to the appearance of critical points in the vortex Kelvin modes [10].

We show in this paper that the presence of stratification can also destabilise a centrifugally stable vortex. After describing the vortex and the density profile in section 2, we first focus on the effect of a tilt of the vortex in section 3. We then study the instabilities of a vertical vortex in section 4 and finally conclude in section 5.

2 A Gaussian vortex in a stratified fluid

We wish to study the stability of a Gaussian vortex, whose angular velocity profile is defined as:

$$\Omega(r) = \frac{v_\theta}{r} = \frac{\Gamma}{2\pi r^2}(1 - \mathrm{e}^{-r^2/a^2}) \tag{1}$$

for a vortex of circulation Γ and core size a. Such a vortex is stable with respect to the centrifugal instability in a non-stratified fluid. It is also interesting because it is the attractive solution for any localised patch of vorticity evolving due to viscous diffusion.

This vortex is placed in a vertical density stratification $\rho(z)$, which is assumed to be linear and characterized by a constant buoyancy frequency $N = \sqrt{-(g/\rho)(\partial\rho/\partial z)}$. We consider that the vortex axis may be tilted with respect to the vertical with an angle α, as shown on Fig. 1(a).

This system is characterised by two non-dimensional parameters: the Froude number $F = \Gamma/2\pi N a^2$ and the Reynolds number $Re = \Gamma/\nu$.

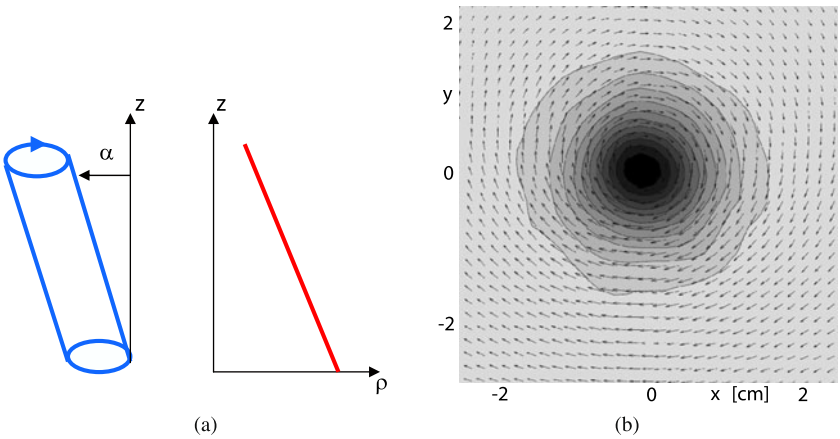

Fig. 1 (a) Sketch of a vortex inclined of an angle α with respect to a stable linear density stratfication $\rho(z)$. (b) Experimental velocity field (and vorticity contours) obtained for a vortex generated by a flat plate impulsively rotated in a stratified fluid measured by PIV.

Experimentally, it is possible to create a Gaussian vortex by rotating a flap impulsively in a fluid initially at rest. Some PIV measurements (shown on Fig. 1b) allow to check that the vortex is circular and close to Gaussian. The linear stratification of the fluid is obtained using the two-tank method with salted water.

The linear temporal stability characteristics of the vertical vortex have also been obtained by a numerical spectral method.

3 Instabilities of a tilted vortex

We show in this section that the presence of a small tilt angle α can drastically change the structure and the stability of the vortex when its Froude number is larger than one.

3.1 Spatial structure of a tilted vortex

It has been shown [2] that tilting the vortex induces an axial velocity w proportional to the tilt angle α for small angles:

$$w = \alpha \frac{r\Omega(r)^3}{\Omega(r) - N^2} \sin\theta \tag{2}$$

where θ is the angle with respect to the direction of the tilt. At low Froude number, the vertical velocity decreases as $1/N^2$ and thus vanishes, leading to the same model of vortex described by [4], where the circular streamlines are horizontal but with their centers aligned on a tilted axis. However, when the Froude number is larger than 1, this solution diverges at the critical radius r_c where the angular velocity $\Omega(r_c)$ equals the buoyancy frequency N. This creates a critical layer with strong axial velocities.

Theoretically, the addition of the viscous terms smoothes the singularity in a viscous critical layer of width $Re^{-1/3}$. In this layer, the axial velocity reaches values of order $\alpha Re^{1/3}$. In Fig. 2, the analytic solution is compared to the experimental PIV measurement of the axial velocity. A good qualitative and quantitative agreement is observed. A cut along the direction of the tilt (x-axis) indicates that the velocity profile contains a strong positive jet on one side and a strong negative jet on the other side. On the contrary, the velocity profile in the direction perpendicular to the tilt (y-axis) exhibits two shear layers on each side of the vortex center.

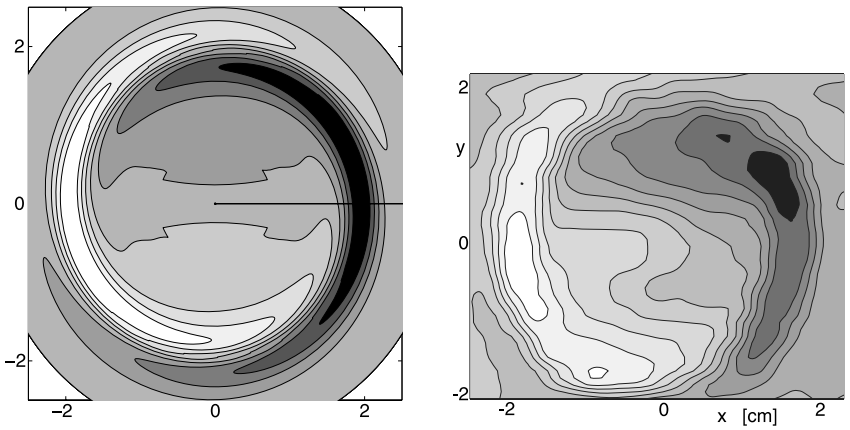

Fig. 2 (a) Theoretical and (b) experimental contours of axial velocity in a horizontal plane, for a vortex tilted with an angle $\alpha = 0.07$ rad. $Re = 450$ and $F = 3.2$.

3.2 Tilt-induced instabilities

The presence of strong axial flows inside the critical layers can destabilise the vortex. Indeed, when the Reynolds number or the tilt angle is increased, the vortex suddenly exhibits strong three-dimensional perturbations which lead to a turbulent flow inside the vortex. Such perturbations are shown on the photographs of Fig. 3 in two different sideviews.

Fig. 3(a) shows a shadowgraph visualisation in the vertical longitudinal plane (i.e. the plane of the figure in Fig. 1), where the vortex thus appears tilted. The visualisation highlights a row of clockwise vortices on each side of the vortex. These vortices correspond to Kelvin-Helmholtz billows issued from a Kelvin-Helmholtz instability of the shear present in thes critical layer. In the tilted longitudinal plane (i.e. normal to the plane of the figure in Fig. 1), on the other hand, the perturbation seems to contain a row of alternate vortices on each side (see Fig. 3b), which is due to the sinuous mode of a jet instability.

These mechanisms are further confirmed by PIV measurements in these two planes shown in Fig. 4. In the vertical longitudinal plane (Fig. 4a), the jet instability made of alternate vortices is clearly visible on each side of the vortex axis. In the tilted longitudinal plane (Fig. 4b), each mixing layer destabilizes in a row of vortices. It can be noted that the different instabilities do not correspond between visualisations and PIV measurements: they are in phase quadrature. This is due to the fact that density structures are advected by the vortex and they are thus maximal at the end of the forcing by the flow, and not in the plane where the forcing is maximal.

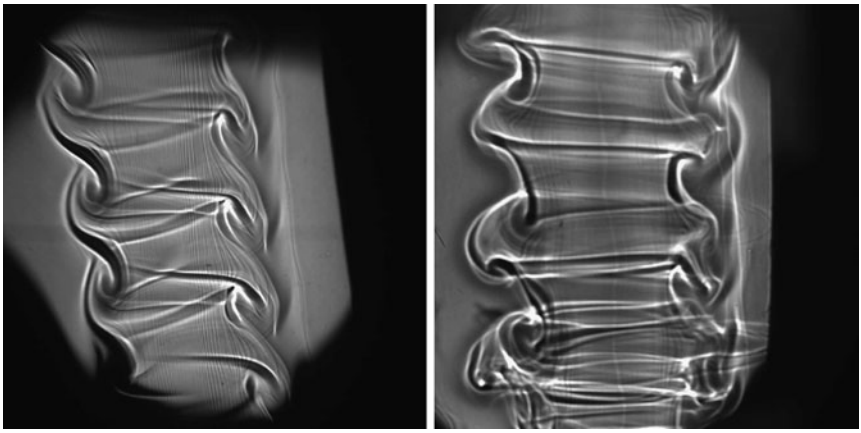

(a) (b)

Fig. 3 Shadowgraph visualisation of the tilt-induced instabilities in (a) the vertical longitudinal plane and (b) the tilted longitudinal plane. $F = 3$, $Re = 720$, $\alpha = 0.07$rad.

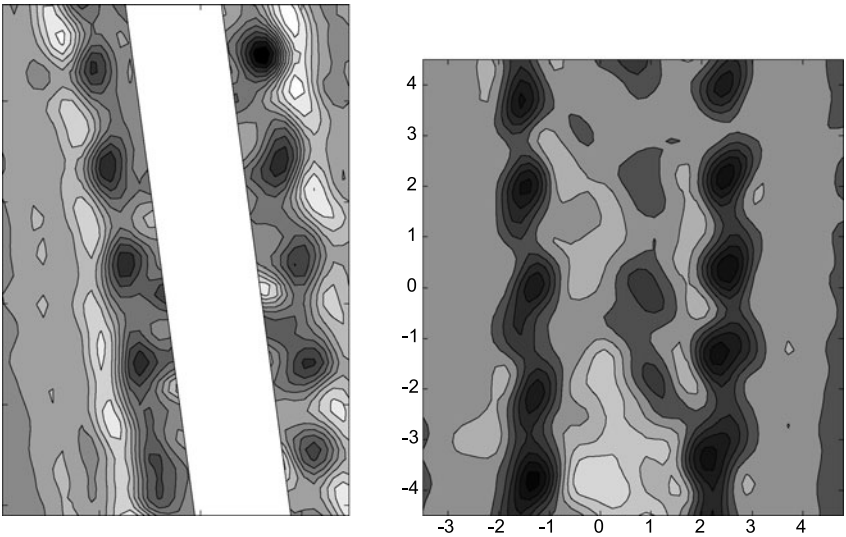

(a) (b)

Fig. 4 PIV measurements of the instantaneous azimuthal vorticity showing the tilt-induced instabilities in (a) the vertical longitudinal plane and (b) the tilted longitudinal plane.

A local stability analysis has been performed [3] and proves that the three-dimensional instability of the vortex is indeed linked to a local shear or jet instability inside the critical layer. The growth rate (of the order of $0.1\alpha Re^{2/3}N$) and the wavelength are in good quantitative agreement with the observations. Moreover, a

qualitative criterion for the stability of a tilted stratified vortex can be obtained by saying that the growth rate must be larger than the angular frequency of the vortex. The vortex is thus unstable when $\alpha Re^{2/3} \gg 1$ and for $F > 1$.

3.3 Consequences

These local instabilities create a strong turbulent flow inside the vortex. However, the vortex is not broken and its circulation remains constant even in the presence of instabilities. The only effect of the instabilities on the global properties of the vortex is to increase its core size a if the Froude number F is slightly larger than 1. This can be understood by the fact that for Froude of order 1, the critical layer is close to the vortex center and the mixing created by the instabilities can thus diffuse the vorticity more efficiently than for very large Froude number (for which the critical layer is far from the vortex center). In the presence of instabilities, the vortex core size increases, leading to a decrease of the Froude number until it becomes smaller than one at which the critical layer suddenly disappears.

Since the control parameter of the instability is $\alpha Re^{2/3}$, for the large Reynolds numbers of geophysical flow, vortices are expected to be unstable for very small tilt angle. This instability should create a deficit of vortices with a Froude number slightly above one, which could be interesting to analyse in oceanic and atmospheric data..

The strong axial velocity created in the critical layer may also be a visible effect. It could have an important impact on the diapycnal mixing in geophysical flows. It would be interesting to quantify its real contribution in oceans.

4 Radiative instability

We now focus on the stability of a Gaussian vortex whose axis is aligned with the density gradient ($\alpha = 0$).

4.1 Linear stability analysis

A linear stability analysis has been performed using a pseudo-spectral Chebyshev code. The boundary conditions, especially the condition of radiation at infinity, have been implemented by considering an integration in the complex plane. Further explanations on the numerical technique can be obtained in [12].

Figure 5(a) shows the growth rate of the most unstable eigenmode as functions of Froude and Reynolds numbers. Its spatial structure exhibits two opposite sign vortices at the center surrounded by weak edges spiralling around the vortex, associated

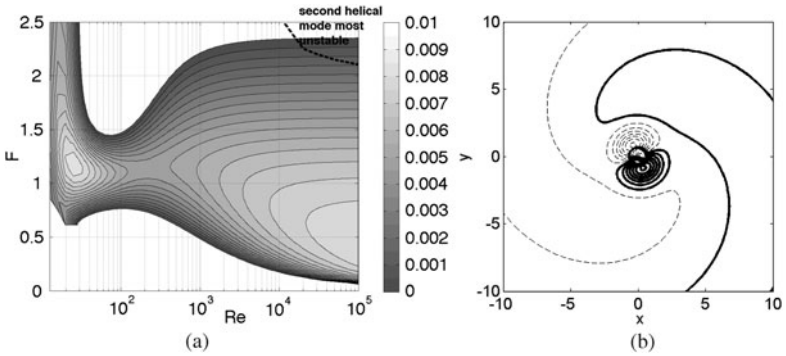

Fig. 5 (a) Growth rate of the most unstable mode for a vertical vortex in a stratified fluid. (b) Structure of the most unstable mode for $Re = 10^5$ and $F = 1.5$.

with internal gravity waves. This instablity is due to the gravity wave emission, as described in [7] and [11]. It can be understood as an interaction between the vortex Kelvin mode (creating the two central vortices) and internal gravity waves which radiate to infinity. Such a description has also been given in [13].

It can be noted that the vortex is unstable for any Reynolds number and is maximal for Froude numbers around 1. The damping of the instability at large Froude number is due to the appearance of a critical point in the eigenmode. The damping of the instability at small Froude numbers is due to viscous effects: the wavelength scales as F for small Froude numbers, and the viscous damping rate νk^2 thus increases as F^{-2} when F tends to zero. These two effects explain why the instability is only present on a band of Froude numbers around one.

4.2 Experimental evidence?

Experiments have been performed to try to observe this instability. However, the growth rate of this instability is very small (close to 0.1% of the maximal angular velocity of the vortex) and the experimental results are not clear. The vortex center, visualised by a dye, usually exhibits an undulation as shown on Fig. 6 in the unstable region of the parameter space. The wavelength of the undulation is of the order of the most unstable wavelength found theoretically although it is usually larger. For the parameters of Fig. 6, the wavelength was measured to be twice larger than the predicted wavelength.

Fig. 6 Dye visualisation of the instability of a vertical vortex in a stratified fluid (sideview). $F = 1.15$, $Re = 610$.

5 Conclusion

We have shown that the presence of stratification can drastically change the stability properties of a Gaussian vortex. Two cases have been studied. We have demonstrated that the presence of small tilt between the vortex axis and the density gradients can induce strong axial flows inside a critical layer, which lead to three-dimensional perturbations due to a Kelvin-Helmholtz or a jet instability. These instabilities are extremely violent and appear for very small tilt angles at large Reynolds numbers. Theoretical predictions are confirmed by experimental visualisations and measurements.

In a second study, we have shown theoretically that a vertical Gaussian vortex is unstable in a stably-stratified fluid whatever the Reynolds number in an interval of Froude number around one. The unstable mode creates an undulation of the vortex centerline and is associated with an emission of internal gravity waves far from the vortex center.

We believe that these results are interesting for geophysical applications because they show that the coherent structures found in stratified turbulence may not be stable, especially at high Reynolds numbers. Indeed, it is natural to think that vortices in a turbulent flow might experience a small tilt angle due to a small vertical shear or to the presence of weak internal waves. These vortices would thus be subject to the tilt-induced instability which is extremely powerful, even for small tilt angles. This would mean that stratified turbulence is not similar to a two-dimensional turbulence composed of horizontal vortices but that it is composed of intense three-dimensional motions at least for Froude numbers around 1. Another interesting consequence is

that there is a coupling between vortices and internal gravity waves since vortices can emit internal gravity waves.

Acknowledgements The support of ACI grant 'Prévention des catastrophes naturelles' and ANR grant 'Fronts, secondary cyclones and gravity waves: instability, mixing and transport' by the french ministry of research is most gratefully acknowledged.

References

[1] Billant, P., Chomaz, J.M.: Experimental evidence for a new instability of a vertical columnar vortex pair in a strongly stratified fluid. J. Fluid Mech. **418**, 167–188 (2000)
[2] Boulanger, N., Meunier, P., Le Dizès, S.: Structure of a stratified tilted vortex. J. Fluid Mech. **583**, 443–458 (2007)
[3] Boulanger, N., Meunier, P., Le Dizès, S.: Tilt-induced instability of a stratified vortex. J. Fluid Mech. **596**, 1–20 (2008)
[4] Canals, M., Pawlak, G., MacCready, P.: Tilted baroclinic tidal vortices. J. Phys. Oceanography **39**(2), 333–350 (2009)
[5] Crow, S.C.: Stability theory for a pair of trailing vortices. AIAA J. **8**(12), 2172–2179 (1970)
[6] Dritschel, D.G., Torre Juarez, M.l.: The instability and breakdown of tall columnar vortices in a quasi-geostrophic fluid. J. Fluid Mech. **328**, 129–160 (1996)
[7] Ford, R.: The response of a rotating ellipse of uniform potential vorticity to gravity wave radiation. Phys. Fluids **6**(11), 3694–3704 (1994)
[8] Hopfinger, E.J., van Heijst, G.J.F.: Vortices in rotating fluids. Annu. Rev. Fluid Mech. **25**, 241–289 (1993)
[9] Kerswell, R.R.: Elliptical instability. Annu. Rev. Fluid Mech. **34**, 83–113 (2002)
[10] Le Dizès, S.: Inviscid waves on a lamb–oseen vortex in a rotating stratified fluid: consequences for the elliptic instability. J. Fluid Mech. **597**, 283–303 (2008)
[11] Plougonven, R., Zeitlin, V.: Internal gravity wave emission from a pancake vortex: an example of wave-vortex interaction in strongly stratified flows. Phys. Fluids **14**(3), 1259–1268 (2002)
[12] Riedinger, X., Meunier, P., Le Dizès, S.: Viscous stability properties of a Lamb-Oseen vortex in a stratified fluid. J. Fluid Mech. **645**, 255–278 (2010)
[13] Schecter, D.A., Montgomery, M.T., Reasor, P.D.: A theory for the vertical alignment of a quasigeostrophic vortex. J. Atm. Sciences **59**(2), 150–168 (2002)

Geostrophic vortex alignment in external shear or strain

Xavier Perrot, Xavier Carton, and Alan Guillou

Abstract The interaction of two identical vortices at different depths is studied in a two-layer quasi-geostrophic flow with external shear or strain. The equilibria and stability of point vortices are computed, as well as their possible resonance with the forcing. The various evolutions of finite-area vortices (alignment, co-rotation, equilibria, oscillations) are presented and compared with point-vortex dynamics.

1 Introduction

Vortex alignment is the process via which two like-signed vortices at different depths join their central axes and form a taller structure. In geostrophic turbulence, vortex alignment has been related to the barotropisation of energy and enstrophy [13; 14; 5; 6]. Several studies have analysed the alignment process for two vortices isolated from any background flow. With a two-layer quasi-geostrophic model, Polvani [12] showed that two initially circular vortices with uniform potential vorticity align if they are larger (or on the order of) the deformation radius, and if they are initially separated by less than 3.3 radii (case of equal layer thicknesses). Correard and Carton [2] showed that alignment is sensitive to the initial distribution of potential vorticity, and can be weakened or prevented by hetonic effects. Sutyrin et al [16] also found a critical vertical separation between the vortex cores, beyond which alignment does not occur.

In the ocean and atmosphere, observations of vortices undergoing vertical alignment include the interaction of eddies Leo and Maria near the East Australian Current [3], and that of weak tornado-like vortices [18]. The former observation was modeled by Nof and Dewar [7], who concluded that the alignment of nonlinear lens eddies is a slow process, involving the formation of "arms" circling each eddy, and

LPO/UBO, Brest, France, xcarton@univ-brest.fr

D. Dritschel (ed.), *IUTAM Symposium on Turbulence in the Atmosphere and Oceans*, IUTAM Bookseries 28, DOI 10.1007/978-94-007-0360-5_18,

a final oscillation of the aligned vortex. The alignment (or realignment) of atmospheric vortices was modeled by several authors [17; 15] with continuously stratified quasi-geostrophic models. These studies indicated that tilted vortices realign if they are larger than the deformation radius. Otherwise, an azimuthal mode 1 perturbation propagates around the vortex, and realignment does not occur.

Both in geostrophic turbulence and in planetary observations, vortices undergoing alignment are often submitted to external influences. But alignment of vortices in shear or strain has not yet been studied. Recently, vortex merger with background flow was studied in two-dimensional flows [1; 4; 8; 9; 10; 11]. These studies showed that external strain can substantially modify the nonlinear evolution of two like-signed vortices. The present study extends these studies to stratified flows and addresses the interaction of two like-signed, pointwise or finite-area vortices, at different depths, with (steady or unsteady) background strain and rotation.

Section 2 adresses the point-vortex evolutions (equilibria and their stability, resonance and chaos). Section 3 considers the nonlinear regimes of two finite-area vortices, lying in two adjacent layers in a quasi-geostrophic model.

2 Physical configuration and model equations

Vortex alignment is studied in a two-layer quasi-geostrophic model, governed by the evolution of layerwise potential vorticity $q_j, (j = 1,2)$:

$$\frac{dq_j}{dt} = \partial_t q_j + J(\psi_j, q_j) = \nu_2 \nabla^2 q_j + \nu_4 \nabla^4 q_j$$

with

$$q_j = \nabla^2 \psi_j + F_j(\psi_k - \psi_j),\ k = 3 - j$$

and F_j is the layer coupling coefficient. The internal radius of deformation is $R_d = 1/\sqrt{F_1 F_2}$ and γ is its inverse. Here the two layers have equal thicknesses.

The flow configuration is described by figure 1. Due to center symmetry, the point vortex study can describe the motion of any of the two vortices (e.g. that located at (ρ, θ)). Its equations of motion are

$$\dot{\rho} = -s\rho \sin(2\theta) \tag{1}$$

$$\rho\dot{\theta} = \frac{1}{\rho} - 2\gamma K_1(2\gamma\rho) + \rho\omega - s\rho\cos(2\theta) \tag{2}$$

with $s = 8\pi S/\Gamma, \omega = 8\pi\Omega/\Gamma$ where S and Ω are the external strain and rotation rates, and Γ is the area integral of potential vorticity. Finally we note that s and ω can vary with time.

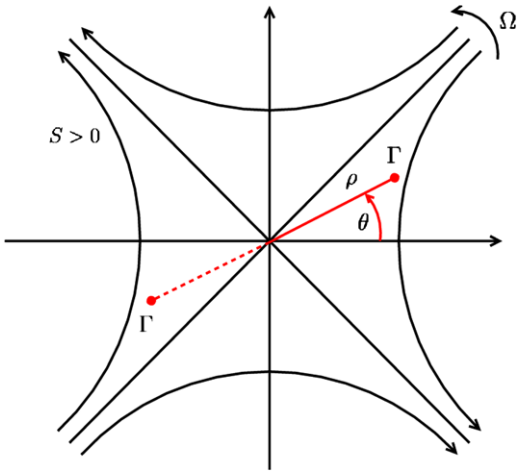

Fig. 1 Two point vortices in a two-layer model with imposed strain and solid-body rotation; the solid line indicates the upper layer vortex, the dashed line the lower layer one.

3 Evolution of two point-vortices in external strain and rotation

Perrot and Carton [8] have studied in detail the equilibria and stability for this two-vortex problem for steady external flow. We only recall the results here. The center of the plane ($\rho = 0$) is a neutral position in the absence of strain and a saddle point in its presence. The other equilibria are given by

$$\theta_{0n} = n\pi/2 \quad \text{and} \quad \frac{1}{\nu_{0n}} - K_1(\nu_{0n}) + \zeta_n \nu_{0n} = 0 \tag{3}$$

where $\nu_{0n} = 2\gamma\rho_{0n}$ and $\zeta_n = \frac{\omega_0 + (-1)^{n+1} s_0}{4\gamma^2}$. The stability of these equilibria is shown on figure 2. The oscillation frequency around the neutral equilibrium is $f_0 = \left[2s_0(-1)^{n+1}\left[\frac{2}{\rho_{0n}^2} - \frac{4\gamma}{\rho_{0n}} K_1(2\gamma\rho_{0n}) - 4\gamma^2 K_0(2\gamma\rho_{0n})\right]\right]^{1/2}$.

We restrict our study to ($\omega_0 < 0, s_0 > 0, |\omega_0| > |s_0|$), where, apart from the center, one neutral equilibrium and one unstable equilibrium exist, and we now analyse the vortex motion when the external flow is unsteady:

$$s = s_0(1 + \varepsilon^3 \delta \cos(f_0 t)),\ \omega = \omega_0(1 + \varepsilon^3 \delta \cos(f_0 t))$$

First, we study the vicinity of the neutral equilibrium. The periodic vortex motion can resonate with the external flow, and this resonance is calculated via an expansion of the vortex position in ε: $\rho(t) = \rho_0 + \varepsilon\rho_1(t) + \ldots$, $\theta(t) = \theta_0 + \varepsilon\theta_1(t) + \ldots$ and a multiple time scale expansion $\partial_t = \partial_{t_0} + \varepsilon\partial_{t_1} + \ldots$. At first order in ε, the equation describes the periodic rotation of the vortex displaced from the neutral point:

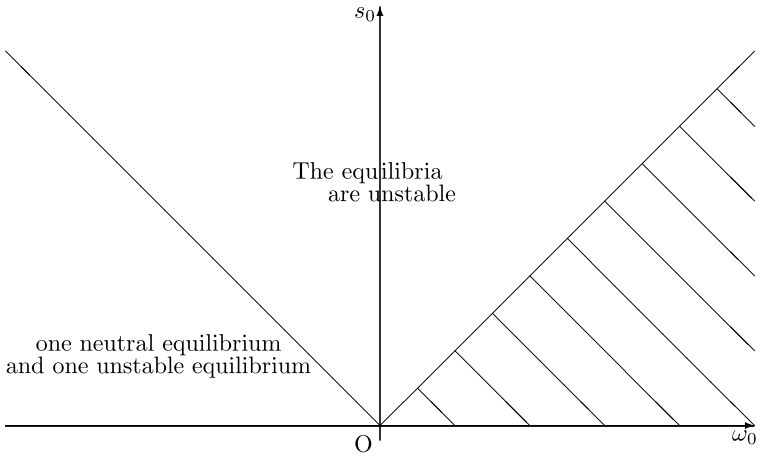

Fig. 2 Equilibria and their stability, for steady external flow, in the (ω_0, s_0) plane (the center of the physical plane which is a saddle-point in the presence of strain, and a neutral point in its absence, is not included in this description).

$$\rho_1(t_0,t_1,t_2) = A(t_1,t_2)e^{if_0t_0} + A^\star(t_1,t_2)e^{-if_0t_0}$$

$$\theta_1(t) = if_0K\left[A(t_1,t_2)e^{if_0t_0} - A^\star(t_1,t_2)e^{-if_0t_0}\right]$$

Computation of second and third-order leads to an amplitude equation which describes the slow-time modulation of vortex motion around the neutral points

$$\partial_{t_2}A(t_2) = i\left[f_0^3K^2 - \frac{3R}{2f_0} - \frac{10Q^2}{6f_0^3}\right]|A(t_2)|^2A(t_2) + i\frac{(-1)^n s_0 - \omega_0}{4f_0K}\delta e^{if_2t_2} \qquad (4)$$

with

$$R = \frac{N\rho_0^5 + M\rho_0^4 - 1}{K\rho_0^5}$$

$$N = \left[\frac{8\gamma^2}{\rho_0^3} + \frac{8\gamma^4}{3\rho_0}\right]K_0(2\gamma\rho_0) + \left[\frac{8\gamma}{\rho_0^4} + \frac{20\gamma^3}{3\rho_0^2}\right]K_1(2\gamma\rho_0)$$

$$Q = \frac{M\rho_0^4 + L\rho_0^3 + 1}{K\rho_0^4}$$

$$M = -\frac{6\gamma^2}{\rho_0^2}K_0(2\gamma\rho_0) - \left[\frac{6\gamma}{\rho_0^3} + \frac{4\gamma^3}{\rho_0}\right]K_1(2\gamma\rho_0)$$

$$L = \frac{4\gamma^2}{\rho_0}K_0(2\gamma\rho_0) + \frac{4\gamma}{\rho_0^2}K_1(2\gamma\rho_0)\,.$$

A Runge-Kutta integration of the point-vortex motion equations shows agreement with the amplitude equation within 3% for small δ (see again [8]). The main result

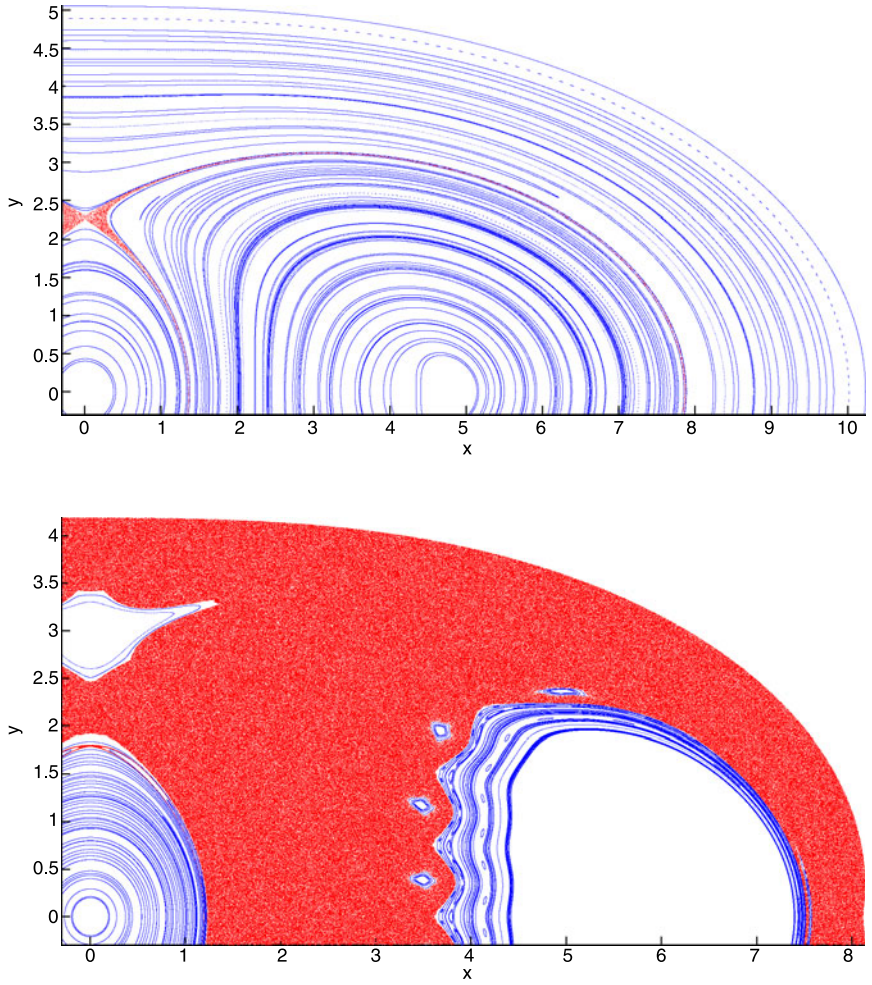

Fig. 3 Chaotic regions (in red) for $\delta = 0.001$ and $\delta = 0.1$ in the Poincaré section.

is that, for $\delta < \delta_c$, the vortex distance to the neutral point is always bounded above by its initial value. For $\delta > \delta_c$, the vortex distance to the neutral point is always larger than or equal to its initial value. For $\delta > \delta_s >> \delta_c$, the vortex distance from the neutral point is no more oscillatory, but grows to a large value and varies chaotically.

To understand how chaos appears, we now study the flow around the unstable equilibrium. There, the flow undergoes Hamiltonian chaos as soon as $\delta > 0$. The Melnikov function (see 5) shows that the heteroclinic trajectories intersect and that chaos appears in their vicinity as soon as the external flow is unsteady. Chaos spreads into the Poincaré section from the initial location of the heteroclinic tra-

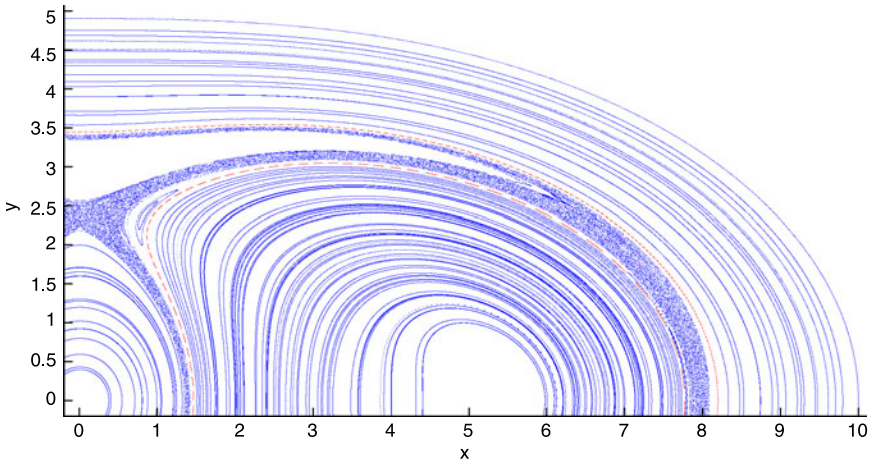

Fig. 4 Evidence for Cantor sets (in dashed red lines) in the $\delta = 0.01$ Poincaré section; the Cantor sets lie next to the chaotic region.

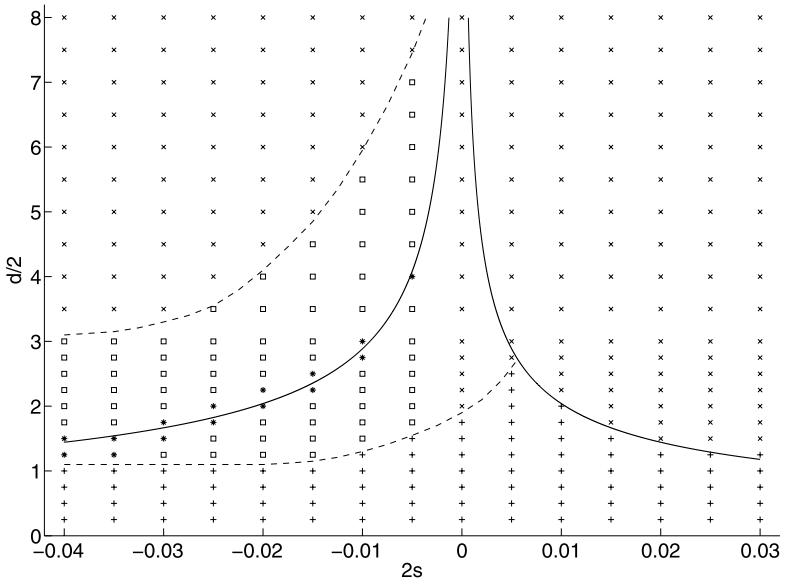

Fig. 5 Nonlinear regimes for two finite-area, piecewise-constant vortices in the $2s, d/2$ parameter plane; + indicate vortex alignment, x is co-rotation, * for equilibria, and squares for oscillations around equilibria. The dashed lines are boundaries of the vortex oscillation regime and of the alignment regime. The solid lines represent the condition for point vortex equilibria.

jectories via the destabilisation of the KAM tori (see figure 3); Cantor sets appear (see figure 4) before being replaced by chaos [19]. When vortices enter the chaotic region, they can move far away from their initial position.

4 Nonlinear regimes of finite-area vortices with background strain and rotation

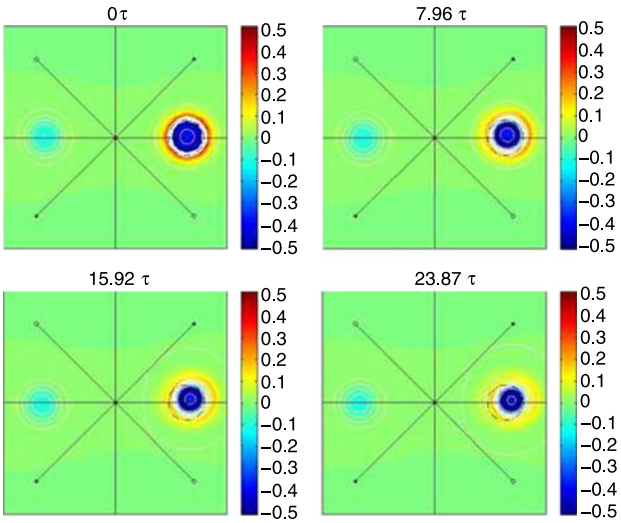

Fig. 6 Case of vortex equilibrium: Time evolution of potential vorticity (white contours) and of Okubo-Weiss criterion (squared deformation minus squared vorticity, color scale) in the upper layer of the flow, at time $t = 0, 7.96\tau, 15.92\tau, 23.87\tau$ (upper left, upper right, lower left, lower right). Solid lines are the strain axes, dashed contour is the initial vortex boundary.

In this section, we model numerically the time evolution of piecewise-constant, finite-area vortices, located in each layer of our two-layer quasi-geostrophic model, and initially separated horizontally. These vortices are submitted to the same external strain and rotation as their pointwise counterparts. This numerical integration is performed with a pseudo-spectral code, based on Fourier projection and truncation of the quasi-geostrophic equations with 256x256 colocation points. The domain is 4π-periodic in each horizontal direction. Biharmonic dissipation is added to the potential vorticity equation to remove enstrophy accumulation at small scales. The initial conditions are also slightly smoothed in potential vorticity to avoid the Gibbs phenomenon. We have checked that the outcome of the numerical model does not substantially depend on this smoothing (provided numerical instability is avoided).

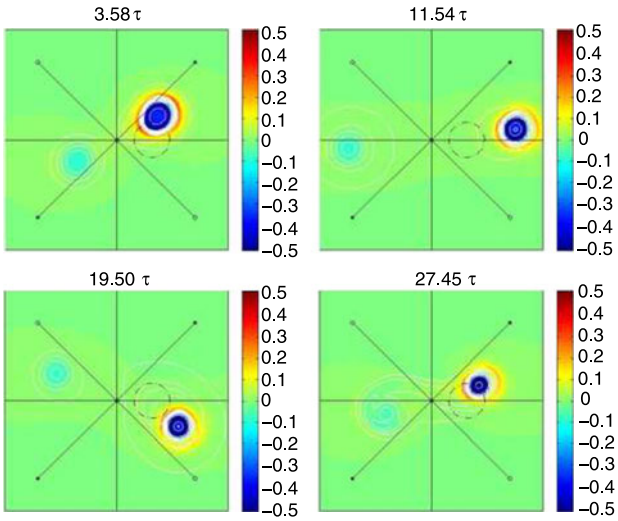

Fig. 7 Same as fig.6 for the case of oscillation near equilibrium: Time shown are $t = 3.58\tau, 11.54\tau, 19.50\tau, 27.45\tau$.

Firstly we study the evolution of two equal, like-signed vortices, under steady strain and rotation. These vortices have unit potential vorticity inside radius R, and are initially separated by an intercentroid distance d. We have set $R = 0.5, R_d = 0.25$ considering Polvani's study of vortex alignment without external flow [12]. We vary ω_0 and s_0 under the condition $\omega_0 = \pm 2 s_0 < 0$. Figure 5 shows the various nonlinear regimes of the vortex doublet in the $(2s_0, d/2)$ parameter plane.

For $s_0 < 0$, vortices align for small values of d, whereas they co-rotate for large values of d. Between the regions of alignment and of co-rotation, lies a region where the two vortices are located at or near the neutral points of the point-vortex problem. There, the vortices are either stationary, or they rotate around the equilibrium position. This similarity between pointwise and finite-area vortex behaviors holds as long as d is large enough (that is, not for large negative s_0). Indeed, under such conditions, the velocity far field of the two types of vortices is comparable.

For $s_0 > 0$, the location of neutral and saddle-points of the point-vortex problem are inverted with respect to $s_0 < 0$. If the two vortices lie initially between the saddle-points, strain brings them closer to each other, thus favoring alignment. This is observed for $2s_0 = 0.005$ for instance. When alignment does not occur, vortices co-rotate. But here, finite-area vortices cannot reach steady states, nor oscillate around them, since the point-vortex equilibria are unstable.

The time evolution of vortices in the upper layer is shown on figure 6 for equilibria, and on figure 7 for oscillations around the equilibria. Vortex deformation is concentrated near its periphery and towards the center of the plane.

For larger values of $|s_0|$ than those thown here, vortices become irreversibly elongated, along the extension axis of the external strain, so that they do not have time to interact.

Secondly, we investigate the influence of a time-varying strain and rotation on vortex alignment: we set $\delta = 0.25$. Model simulations show that this influence is weak for close vortices, except for weak strain, where co-rotating "figure-8" equilibria are found. More straining out is observed for distant vortices. Steady states disappear and are replaced by very slow oscillation regimes. For stronger unsteady strain, distant vortices move irregularly in the plane, and are eroded more rapidly than for steady strain.

5 Conclusions

The influence of external strain and rotation on geostrophic vortex alignment was studied both for point and finite-area vortices. For point vortices, steady external flow allows the existence of equilibrium positions, which can be neutral or unstable. The addition of an oscillatory component to the external flow results in a modulation of vortex rotation around neutral points: vortices follow inward or outward spiraling trajectories, depending on time and on the amplitude of unsteady external flow. For large unsteady external flow, vortices move sufficiently far away from the neutral points to reach the chaotic region of the plane. As soon as unsteady external flow is added, chaos appears in the vinicity of the heteroclinic trajectories which cross (as shown theoretically via the Melnikov function and also numerically). Chaos spreads out in the plane as the unsteady part of strain (and rotation) grows: KAM tori are replaced by Cantor sets and by chaotic region.

For finite-area cyclones with positive strain, nonlinear evolutions are comparable to those without external flow, though alignment is favored by strain for close enough vortices: close vortices align, distant vortices co-rotate. When strain is negative, the presence of neutral equilibria strongly modifies this picture by introducing an intermediate regime dominated by these equilibria, in agreement with point-vortex dynamics.

Extension of this work to continuously stratified fluid and to nongeostrophic dynamics should be performed to provide more realism with regard to oceanic and atmospheric situations.

Ackowledgements

X. Perrot was supported by a PhD grant of the Ministry of Research during the course of this work.

Appendix

The onset of Hamiltonian chaos is related to the destabilisation of the heteroclinic curves, the trajectories of point vortices along the stable and the unstable directions from/to the saddle points (the unstable equilibria). To show that the heteroclinic curves cross, we use the Melnikov theory [19]. Expanding 1-2, we obtain:

$$\begin{aligned}\dot{\rho} &= -s_0\rho\sin(2\theta) - \varepsilon\left[\delta s_0\cos(\sigma t)\rho\sin(2\theta)\right]\\ \rho\dot{\theta} &= \frac{1}{\rho} - 2\gamma \mathrm{K}_1(2\gamma\rho) + \omega_0\rho - s_0\rho\cos(2\theta) +\\ &\qquad \varepsilon\left[\delta\omega_0\cos(\sigma t)\rho - s_0\delta\cos(\sigma t)\rho\cos(2\theta)\right]\end{aligned}$$

Then the distance between two heteroclinic curves is:

$$M(t_0) = \int_{-\infty}^{+\infty} s_0\delta(1+2\gamma\rho_0(\tau)\mathrm{K}_1(2\gamma\rho_0(\tau)))\sin(2\theta_0(\tau))\cos(\sigma(\tau+t_0))\mathrm{d}\tau \quad (5)$$

where θ_0 and ρ_0 are the solution of the stationary equation of motion at the saddle-point. In fact in the stationary case the equation of motion (1-2) derive from a Hamiltonian (H):

$$\mathrm{H}(\rho,\theta) = \ln(2\rho) + \mathrm{K}_0(2\gamma\rho) + \frac{\omega_0}{2}\rho^2 - \frac{s_0}{2}\rho^2\cos(2\theta) \quad (6)$$

We compute $\mathrm{R}(\rho_r,\theta_r)$ and $\mathrm{H}(\rho_r,\theta_r)$. As the Hamiltonian is constant along a trajectory, we have

$$\mathrm{H}(\rho,\theta) = \mathrm{H}(\rho_r,\theta_r) \quad (7)$$

which implies:

$$\theta(\rho) = \pm\frac{1}{2}\arccos\left[\frac{\ln\frac{\rho^2}{\rho_r^2} + \rho_r^2\left(s_0\cos(2\theta_r)-\omega_0\right) + 2\mathrm{K}_0(2\gamma\rho) - 2\mathrm{K}_0(2\gamma\rho_r)}{s_0\rho^2} + \frac{\omega_0}{s_0}\right]$$

defined for ρ such that

$$\mathrm{f}(\rho) = \frac{\ln\frac{\rho^2}{\rho_r^2} + \rho_r^2\left(s_0\cos(2\theta_r)-\omega_0\right) + 2\mathrm{K}_0(2\gamma\rho) - 2\mathrm{K}_0(2\gamma\rho_r)}{s_0\rho^2} + \frac{\omega_0}{s_0} \in [-1;1].$$

For the particular case where neutral points and saddle points exist, and where $(\rho_r\theta_r) = (\rho_0,\theta_0)$ at the saddle-point, a study of $\mathrm{f}(\rho)$ shows that the variation of f depends on the sign of s_0.

If $s_0 > 0$:

ρ	0		ρ_0		$+\infty$
f	$+\infty$	+	0	−	0^-
f	$-\infty$	↗	1	↘	$\frac{\omega_0}{s_0}$

If $s_0 < 0$:

ρ	0		ρ_0		$+\infty$
$\dot{\mathrm{f}}$	$+$	0	$-\infty$	$+$	0^+
f	$+\infty$	$\searrow$	-1	$\nearrow$	$\frac{\omega_0}{s_0}$

where $|\omega_0/s_0| > 1$.

This implies the existence of two finite values ρ_1 and ρ_2 between which $f(\rho) \in [-1;1]$.

After some algebra, the Melnikov function is shown to be:

$$M(t_0) = A\cos(\sigma t_0) + B\sin(\sigma t_0) \tag{8}$$

where $A = \int_{-\infty}^{+\infty} s_0\delta(1+2\gamma\rho_0(\tau)\mathrm{K}_1(2\gamma\rho_0(\tau)))\sin(2\theta_0(\tau))\cos(\sigma\tau)\mathrm{d}\tau$ and $B = -\int_{-\infty}^{+\infty} s_0\delta(1+2\gamma\rho_0(\tau)\mathrm{K}_1(2\gamma\rho_0(\tau)))\sin(2\theta_0(\tau))\sin(\sigma\tau)\mathrm{d}\tau$ (these two integrals are finite).

Because of the form of (8), the Melnikov function has an infinity of zeros. This implies a topological destabilisation of the heteroclinic curves. The onset of Hamiltonian chaos depends only on the crossing of heteroclinic curves. Therefore chaos appears as soon as $\delta > 0$.

References

[1] Carton, X., Legras, B. and G. Maze (2002) Two-dimensional vortex merger in an external strain field. *Journal of Turbulence*, *3*, article 045 (IoP electronic publication)

[2] Corréard, S. and X. Carton (1998) Vertical alignment of geostrophic vortices: on the influence of the initial distribution of potential vorticity. *Simulation and identification of organised structures in flows*, Kluwer Acad. Publ., *52*, 191–200.

[3] Creswell, G.R. and R. Legeckis (1987) Eddies off southeastern Australia, 1980/91. *Deep-Sea Res.*, *34*, 1527–1562.

[4] Maze, G., Carton, X. and G. Lapeyre (2004) Dynamics of a 2D vortex doublet under external deformation. *Reg. Chaot. Dyn.*, *9*, 4, 477–497

[5] McWilliams, J.C. (1989) Statistical properties of decaying geostrophic turbulence. *J. Fluid Mech.*, *198*, 199–230.

[6] McWilliams, J.C. (1990) The vortices of geostrophic turbulence. *J. Fluid Mech.*, *219*, 387–404.

[7] Nof, D. and W.K. Dewar (1994) Alignment of lenses: laboratory and numerical experiments. *Deep-Sea Res.*, *41*, 1207–1229.

[8] Perrot, X. and X. Carton (2007) Baroclinic point vortex interaction in a time-varying flow. *Proceedings of the 18th CFM (Grenoble)*, article 1315, 6 pp (available from http://irevues.inist.fr/cfm2007).

[9] Perrot, X. and X. Carton (2008) Vortex interaction in an unsteady large-scale shear/strain flow. In *Hamiltonian Dynamics, Vortices and Turbulence*, IUTAM conference proceedings, Springer Verlag, 373–382.

[10] Perrot, X. and X. Carton (2009) Point-vortex interaction in an oscillatory deformation field: Hamiltonian dynamics, harmonic resonance and transition to chaos. *Discr. Cont. Dyn. Syst. B*, *11*, 971–995

[11] Perrot, X. and X. Carton (2010) Barotropic vortex interaction in a non uniform flow. *Theor. Comp. Fluid Dyn.*, *24*, 95–100

[12] Polvani, L.M. (1991) Two-layer geostrophic vortex dynamics. Part 2. Alignment and two-layer V-States. *J. Fluid Mech.*, *225*, 241–270.

[13] Rhines, P.B. (1979) Geostrophic turbulence. *Ann. Rev. Fluid Mech.*, *11*, 401–441.

[14] Salmon, R. (1980) Baroclinic instability and geostrophic turbulence. *Geophys. Astrophys. Fluid Dyn.*, *15*, 167–211.

[15] Schecter, D.A., Montgomery, M.T. and P.D. Reasor (2002) A theory for the vertical alignment of a quasigeostrophic vortex. *J. Atmos. Sci*. *59*, 150–168.

[16] Sutyrin, G.G., McWilliams, J.C. and R. Saravanan (1998) Co-rotating stationary states and vertical alignment of geostrophic vortices with thin cores. *J. Fluid Mech.*, *357*, 321–349.

[17] Viera, F. (1995) On the alignment and axisymmetrisation of a vertically tilted geostrophic vortex. *J. Fluid Mech.*, *289*, 29–50.

[18] Willoughby, H.E. (1990) Temporal changes of the primary circulation in tropical cyclones. *J. Atmos. Sci.*, *47*, 242–264.

[19] H. Dang-Vu and C. Delcarte, Bifurcations et Chaos, une Introduction a la Dynamique Contemporaine. *Ellipses*, Paris, 2000.

Equilibrium States of Quasi-geostrophic Point Vortices

T. Miyazaki, H. Kimura and S. Hoshi

Abstract The statistical equilibrium state of quasi-geostrophic point vortices is investigated numerically and theoretically. The numerical computations are performed using the fast special-purpose computer for molecular dynamics simulations, MDGRAPE-2/3. The equilibrium state is affected by the vertical distribution of vortices and the total energy of the vortex system. The most probable vortex distributions are determined based on the maximum entropy theory. We introduce a simplified patch model, which explains the influence of the total energy on the equilibrium state, qualitatively.

1 Introduction

Geophysical flows are under strong influence of the buoyancy and the Coriolis force. These effects suppress vertical motion, and geophysical flows are considered to be two-dimensional at the lowest order of approximation. There have been a number of theoretical and numerical studies on two-dimensional vortex systems. The statistical mechanics of two-dimensional point vortices was investigated by Onsager (1949) [1], Joyce & Montgomery (1973) [2], Kida (1975) [3] as well as Lundgren & Pointin (1977) [4]. Recently, Yatsuyanagi *et al.* (2005) [5] performed a large numerical simulation of two-dimensional point vortices ($N = 6724$), and investigated their statistical properties, renewing the interest in this classical subject.

In actual geophysical flows, the fluid motion is almost confined within a horizontal plane, but different flow patterns are allowed on different horizontal planes. The next order approximation of geophysical flows is the 'quasi-geostrophic approximation' (Pedlosky (1979) [6]), which incorporates this three-dimensionality. The numerical simulations by McWilliams *et al.* (1994) [7] of decaying quasi-geostrophic

T. Miyazaki, H. Kimura and S. Hoshi
Department of Mechanical Engineering and Intelligent Systems, University of Electro-Communications, Chofu, Tokyo, 182-8585, Japan, e-mail: miyazaki@mce.uec.ac.jp

D. Dritschel (ed.), *IUTAM Symposium on Turbulence in the Atmosphere and Oceans*, IUTAM Bookseries 28, DOI 10.1007/978-94-007-0360-5_19,

turbulence indicate that the vorticity field develops coherent vortex structures, and that their interactions dominate the dynamics of the turbulence. Meacham *et al.* (1997) [8] obtained a series of exact unsteady solutions representing an ellipsoidal vortex patch of uniform potential vorticity under the quasi-geostrophic approximation. Miyazaki *et al.* (2001) [9] developed an ellipsoidal vortex model based on Meacham's solution. Later, Dritschel *et al.* (2004) [10] proposed an improved ellipsoidal vortex model, in which a matrix is used to specify an ellipsoid and each ellipsoid is represented by several discrete point vortices in the evaluation of the interaction energy. Li *et al.* (2006) [11] proposed further refinements, by introducing a new set of nearly canonical variables with clear geometrical meaning and constructed a natural sequence of vortex models from the point model (N degrees of freedom) through the wire-(spheroidal) model ($2N$ degrees of freedom) to the ellipsoidal model ($3N$ degrees of freedom).

Recently, our group investigated the statistical properties of QG point vortices both theoretically and numerically (Hoshi & Miyazaki (2008) [12]). Numerical simulations of N-vortex system ($N = 2000$) in an infinite fluid domain are performed using a fast special-purpose computer for molecular dynamics simulations. Axisymmetric equilibrium states were formed after some evolution. The most probable distributions were determined theoretically, based on the maximum entropy theory. The theoretically predicted distribution agreed with the numerical one fairly well.

In this paper, we investigate the influence of the vertical vorticity distibution and the total energy, by performing a number of numerical simulations. We also introduce a simplified maximum entropy theory (patch model), in order to explain the parameter dependence found numerically. The angular momentum constraint plays a crucial role, as was pointed out for a two-layer quasi-geostrophic point vortex system (DiBattista & Majda (2001) [13]).

2 Quasi-geostrophic Approximation and Equations of Motion

We can introduce a stream-function $\Psi(x,y,z)$, because the fluid motion in each horizontal plane is two-dimensional:

$$u = \frac{\partial \Psi}{\partial y},\ v = -\frac{\partial \Psi}{\partial x}. \tag{1}$$

The time-evolution under the quasi-geostrophic approximation

$$\left(\frac{\partial}{\partial t} + \frac{\partial \Psi}{\partial y}\frac{\partial}{\partial x} - \frac{\partial \Psi}{\partial x}\frac{\partial}{\partial y}\right) q = 0, \tag{2}$$

means that the potential vorticity q is conserved [6]:

$$q = -\Delta\Psi = -\left(\frac{\partial^2}{\partial x^2} + \frac{\partial^2}{\partial y^2} + \frac{\partial^2}{\partial z^2}\right)\Psi. \tag{3}$$

In the point vortex system, we assume that the potential vorticity is δ-function-like concentrated at N points ($\mathbf{R}_i, i = 1,2,\ldots,N$) with strength $\hat{\Gamma}_i$:

$$q = \sum_{i=1}^{N} \hat{\Gamma}_i \delta(\mathbf{r} - \mathbf{R}_i). \tag{4}$$

Each vortex is advected by the flow field induced by other vortices.

It is known that the system of two-dimensional point vortices is a Hamiltonian dynamical system with the logarithmic interaction energy. Similarly, the Hamiltonian of a quasi-geostrophic N point vortex system is given as the summation of the interaction energy of $N(N-1)/2$ vortex-pairs:

$$H = \sum_{(i,j)}^{N} H_{mij},\ H_{mij} = \frac{\hat{\Gamma}_i \hat{\Gamma}_j}{4\pi |R_i - R_j|}. \tag{5}$$

Here, H_{mij} is the interaction energy between two point vortices located at $R_i = (X_i, Y_i, Z_i)$ and $R_j = (X_j, Y_j, Z_j)$ with strength $\hat{\Gamma}_i$ and $\hat{\Gamma}_j$. The summation is taken for $N(N-1)/2$ pairs of vortices.

We have the canonical equations of motion for the $i-$th vortex:

$$\frac{\mathrm{d}X_i}{\mathrm{d}t} = \frac{1}{\hat{\Gamma}_i} \frac{\partial H}{\partial Y_i},\ \frac{\mathrm{d}Y_i}{\mathrm{d}t} = -\frac{1}{\hat{\Gamma}_i} \frac{\partial H}{\partial X_i}. \tag{6}$$

The center of the vorticity (P, Q) and the angular momentum I are conserved besides the energy H (Hamiltonian itself):

$$P = \sum_{i=1}^{N} \hat{\Gamma}_i X_i,\ Q = \sum_{i=1}^{N} \hat{\Gamma}_i Y_i, \tag{7}$$

$$I = \sum_{i=1}^{N} \hat{\Gamma}_i (X_i^2 + Y_i^2). \tag{8}$$

We shift the coordinate origin to the vorticity center, i.e., $P = Q = 0$, below. The length scale is normalized using $(I/\hat{\Gamma}_{total})^{1/2}$. Here

$$\hat{\Gamma}_{total} = \sum_{i=1}^{N} \hat{\Gamma}_i \tag{9}$$

denotes the total strength of vortices. The time is scaled by the mean potential vorticity, and the Hamiltonian H (interaction energy) is normalized by $(\sum_{i=1}^{N} \hat{\Gamma}_i)^2$, i.e., $E = H/\hat{\Gamma}_{total}^2$.

3 Equilibrium States of Quasi-geostrophic Point Vortices

We performed numerical simulation of mono-disperse (identical $\hat{\Gamma}_i$ for $i = 1, 2, \ldots, N$) quasi-geostrophic point vortices ($N = 2000 - 8000$), starting from several initial distributions. Here, we assume a top hat vertical distribution, i.e., $P(z) = 1/2z_{max}$ for $|z| < z_{max}$. We must be careful in preparing the horizontal distributions. Hoshi & Miyazaki (2008) [12] located the vortices randomly and uniformly in a cubic box, whose size was scaled using the length $(I/\hat{\Gamma}_{total})^{1/2}$. The uniform random distribution, however, produces relatively low energy ensumbles under the constraint of fixed angular momentum. Thus, the most probable state with $E = E_c = 3.054 \times 10^{-2}$ (in Hoshi & Miyazaki (2008) [12]: we redifine $E = E_c$ as $E = E_p$ in this paper) did not correspond to the zero inverse temperature state, but it was a possitive temperature state. Here we use the normal (Gauss) distribution in the x and y directions, whereas the vertical distribution is specified by the above $P(z)$. We show the number of states as a function of energy in Fig. 1. The solid red line (right) is the result by the Gauss distribution and the broken green line (left) is by the uniform random distribution. We notice that the left side of the peak ($E = E_{zit} = 3.130 \times 10^{-2}$) of the solid red line is the positive temperature region and the right side is the negative temperature region. We consider the third case $E = E_n = 3.291 \times 10^{-2}$ as an example of negative temperature state.

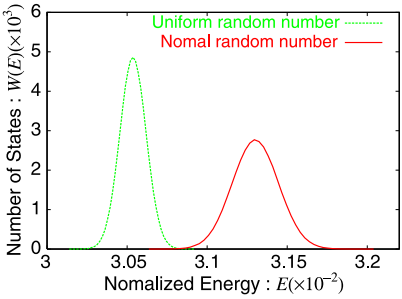

Fig. 1 Number of states as a function of energy E. The energy of the most probable state produced by the uniform random number (broken green line) is $E = E_p = 3.054 \times 10^{-2}$ and that by Gaussian (solid red line) random number is $E = E_{zit} = 3.130 \times 10^{-2}$.

We use the adaptive time integrator from the LSODE-package. Since single precision computations are performed by MDGRAPE-2/3, the energy is conserved within the numerical round-off error (6 significant digits). Similarly, the angular momentum I and the vorticity center are conserved up to 6 significant digits.

We investigate the statistics of the equilibrium state, which is obtained after $t = 10 \sim 20$ (in units of the inverse mean potential vorticity). Figs. 2(a)-(c) illustrate the equilibrium states for three different energy values $E = E_p, E_{zit}$ and E_n, respectively.

These figures are the projections onto the $xz-$plane ($y=0$). These equilibrium states are axisymmetric and we notice clear differences in the distribution of vortices. The radial distribution for $E=E_p$ expands slightly at the center ($z=0$) and that for the zero inverse temperature ($E=E_{zit}$) is almost independent of z, whereas that for the negative temperature $E=E_n$ expands near the upper and lower lids.

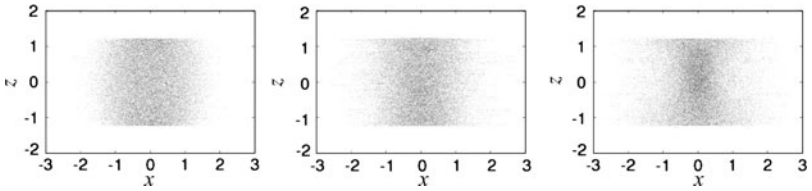

Fig. 2 Equilibrium state for (a) $E=E_p=3.054\times10^{-2}$, (b) $E=E_{zit}=3.130\times10^{-2}$, (c) $E=E_n=3.291\times10^{-2}$.

We consider the probability distribution $F(r,z)$, which is a function of the radial coordinate r and the vertical coordinate z, in order to get quantitative information. Fig. 3(a) (red line) shows the three-dimensional view of the equilibrium distribution $\hat{F}^p(r,z)=2\pi F^p(r,z)/P(z)$ starting from the state of highest multiplicity produced using uniform random distribution. We can see in Fig. 3(a), which is originally from Hoshi & Miyazaki (2008) [12], that the equilibrium distribution is almost z-independent for $|z|\leq 0.6205=z^c_{max}/2$, whereas it becomes more concentrated near the axis as $|z|$ increases. The probability density distribution of the center region seems similar to that of the two-dimensional point vortices. The three-dimensional effect appears near the upper and lower lids in the tighter concentration of vortices around the axis of symmetry. Below, we will refer to this as the 'end-effect'. In contrast, the equilibrium distribution $\hat{F}^{zit}(r,z)=2\pi F^{zit}(r,z)/P(z)$ (Fig. 3(b): red line) for the zero inverse temperature (the state of highest multiplicity produced using the Gaussian random numbers) is completely independent of z. This fact can be proved theoretically based on the maximum entropy theory, in the following section (green line). The next figure (Fig. 3(c)) shows the equilibrium distribution $\hat{F}^n(r,z)=2\pi F^n(r,z)/P(z)$ for high energy case $E=E_n$. The distribution of the center region shrinks and that of the lids spreads wider. The 'end-effect' is inverted.

Thus, in the positive temperature region with lower energy, the 'end-effect' occurs as the tighter concentaration near the upper and lower lids. On the other hand, the radial distribution near the lids expands and that of center region shrinks in the negative temperature region with higher energy.

We performed some additional numerical simulations in the positive temperature region, in which the vortices were located in two 'rectangular parallelepipeds' ($2.432\times2.432\times4.864$, $N=4000$ and $2.432\times2.432\times9.728$, $N=8000$), in order to see the characteristics of the 'end-effect' clearer. We compare the 'rectangular parallelepiped cases' and the 'cubic case'. Fig. 4 shows the equilibrium probability distributions $\hat{F}(r,z)=2\pi F(r,z)/P(z)$ for these three cases. We can see, in the 'rectangular

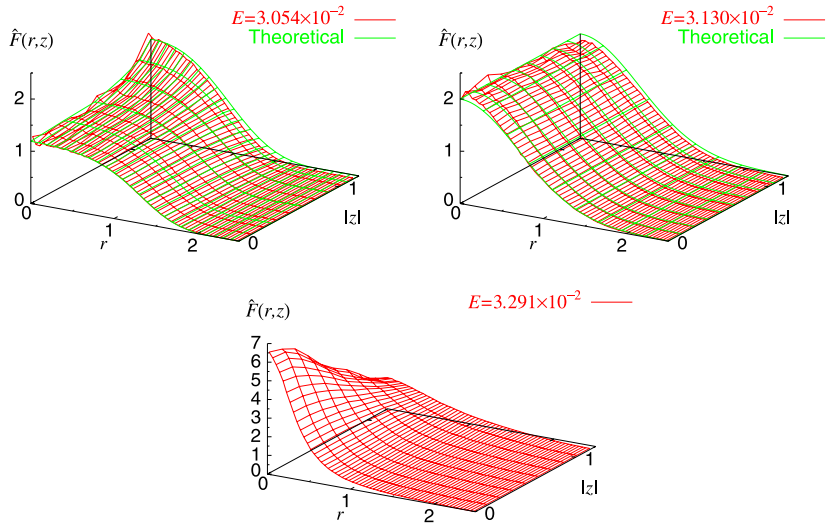

Fig. 3 Distribution function $\hat{F}^p(r,z)$ for (a) $E = E_p = 3.054 \times 10^{-2}$ [12], (b) $E = E_{zit} = 3.130 \times 10^{-2}$ and (c) $E = E_n = 3.291 \times 10^{-2}$.

parallelepiped cases', that the center region with essentially two-dimensional behavior becomes wider compared with the 'cubic case'. Thus, the lid regions, where the 'end-effect' is observed, become relatively narrower. The 'end-effect' is sharper in these cases and will become even sharper for higher boxes, where the distribution will consist of the central two-dimensional distribution and those of the thin upper and lower lid regions. In the following section, we discuss the influence of the total energy on the 'end-effect', based on the maximum entropy theory applied to a simplified model distribution (patch model).

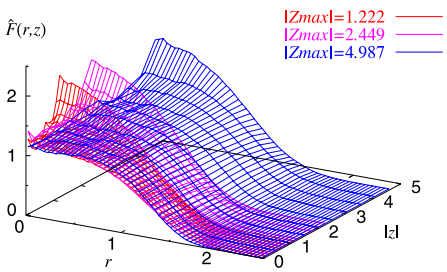

Fig. 4 Comparison of equilibrium distributions for three box-heights.

4 Maximum Entropy Theory

In this section, the equilibrium distribution is determined theoretically, based on the maximum entropy theory, which was applied to the system of two-dimensional point vortices repeatedly. We assume that N vortices are placed in the vertical range $z_1 \le z \le z_2$. The strength of each vortex is taken to be unity ($\hat{\Gamma}_{1,2,\ldots,N} = 1$). The energy E is the only parameter that determines the equilibrium distribution for a fixed angular momentum $\hat{I}(= I/N = 1)$. The number density $n(r,t)$ is related to the probability distribution function $F(r,t) = n(r,t)/N$. The vertical distribution of vortices

$$P(z) = \iint F(r)\mathrm{d}x\mathrm{d}y \left(\int_{z_1}^{z_2} P(z)\mathrm{d}z = 1 \right), \; r = (x,y,z), \tag{10}$$

does not change in time, because each vortex moves only in that horizontal plane where it had been located initially.

We introduce the Shannon entropy

$$\log \hat{Z} = -N \iiint F(r) \log F(r)\mathrm{d}r, \tag{11}$$

as the logarithm of the partition function $\hat{Z}$. The angular momentum $\hat{I}$ and the energy H (in mean field approximation) can be expressed via

$$\hat{I} = \iiint (x^2+y^2)F(r)\mathrm{d}r = 1, \tag{12}$$

$$\frac{8\pi H}{N^2} = \iiiint\!\!\iint \frac{F(r)F(r')}{|r-r'|}\mathrm{d}^3 r \mathrm{d}^3 r', \tag{13}$$

respectively.

The maximum entropy theory assumes that the equilibrium distribution should maximize $\hat{Z}$, under the constraints of fixed $P(z)$, I and E. Then, the equilibrium distribution satisfies the following nonlinear integral equation, which is derived by requiring that the first variation of $\hat{Z}$ should vanish:

$$\log F(r) + 1 + \alpha(z) + \beta(x^2+y^2) + \frac{\gamma}{4\pi} \iiint \frac{F(r')}{|r-r'|}\mathrm{d}^3 r' = 0. \tag{14}$$

with the Lagrange multipliers $\alpha(z)$, β and γ (inverse temperature) associated with $P(z)$, I and E, respectively.

4.1 Zero Inverse Temperature State

We have an exact solution of the above equation for the zero inverse temperature state, where the Lagrange multiplier γ is zero. Here, the Gaussian radial distribution

gives the maximum entropy state:

$$F(r,z) = \frac{P(z)}{\pi} \exp(-r^2). \tag{15}$$

The Lagrange multiplier β is determined to be unity, using the constraint on the total angular momentum. We can see that the numerically obtained equilibrium for this case ($E = 3.130 \times 10^{-2}$) in the previous section is actually a z-independent Gaussian distribution (See Fig.3(b): green line). This observation confirms that the numerically obtained equilibrium state is actually the state of maximum entropy.

4.2 Positive and Negative Temperature States

For general cases, we must solve the integral equation numerically, using an appropriate iteration method. Because the equilibrium distribution for the positive and negative temperature states is a function of r and z, it requires long computational time and a good initial guess to obtain convergence. The main concern is whether the 'end-effect' found for the equilibrium states of general temperature can be captured theoretically.

We solve the integral equation by a numerical iteration (Eq. (14)). The Gaussian integration method with six points ($z_i = 0$, 0.331, 0.639, 0.899, 1.09, 1.20) in the interval $[-z_{max}, z_{max}]$ is used in evaluating the vertical integration, which is enough to capture the 'end-effect'. The obtained equilibrium distribution $\hat{F}^p(r,z_i)$ agrees fairly well with that of the direct numerical simulation (Fig. 3(a): green line ([12])). This confirms that the numerically obtained equilibriums are actually the maximum entropy states under the constraints of the total energy and the angular momentum, even for general cases.

4.3 Patch Model

In the previous subsection, we have seen that the maximum entropy approach works well even for a continuous three-dimensional distribution. It is, however, difficult to investigate a large parameter regime because the numerical iteration is quite time-consuming. Therefore, we introduce as further simplification, 'a patch model', in which the probability density is assumed to be a constant within a certain radius $a(z)$ around the axis and else vanishes:

$$F(r,z) = \begin{cases} \dfrac{P(z)}{\pi a^2(z)}, & \text{for } 0 \le r \le a(z) \\ 0, & \text{for } r \ge a(z). \end{cases} \tag{16}$$

Here $P(z)$ is the vertical distribution given in Eq. (10). We approximate a continuous radial distribution by a top hat with the same zeroth and second order moments. The problem is reduced to find $a(z)$ that maximizes the entropy under the constraints of the fixed angular momentum and the fixed energy.

It is of interest to investigate the influence of the energy E on the equilibrium distribution. Fig. 5(a) illustrates the vertical profile of the normalized angular momentum $J^*(z^* = z/z_{max})$, which is related to the patch radius $a(z)$ by $J^*(z^*) = a^2(z)/2$, for various values of the energy. The five energy levels, i.e., $E = 3.0350 \times 10^{-2}$, 3.0400×10^{-2}, 3.0454×10^{-2}, 3.0540×10^{-2}, 3.0600×10^{-2} are studied via a Gaussian integration with thirty points. At the zero inverse temperature under the patch approximation ($E = E_{zitp} = 3.0454 \times 10^{-2}$), $J^*(z^*)$ is independent of the vertical height. This energy value is smaller than $E = E_{zit} = 3.130 \times 10^{-2}$ for the Gaussian distribution, which is similar to the fact that the uniform random numbers produce ralatively low energy ensembles than the Gaussian random numbers. The vertical distribution of the angular momentum $J^*(z^*)$ changes with the energy, although the integrated value of the angular momentum remains constant ($\hat{I} = 1$). As the energy is decreased (in the positive temperature region), the patch-radius increases for $|z| \lesssim 0.66|z_{max}|$ and decreases for $|z| \gtrsim 0.66|z_{max}|$. In contrast, as the energy is increased (in the negative temperature region), the inverse 'end-effect' appears, i.e., the distribution of center region becomes tighter and those of the lids become wider. We illustrate the vertical distribution of the normalized angular momentum in Fig. 5(b) corresponding to the numerical equilibrium distributions obtained in the previous section. We can see that the patch model captures the influence of the total energy, qualitatively.

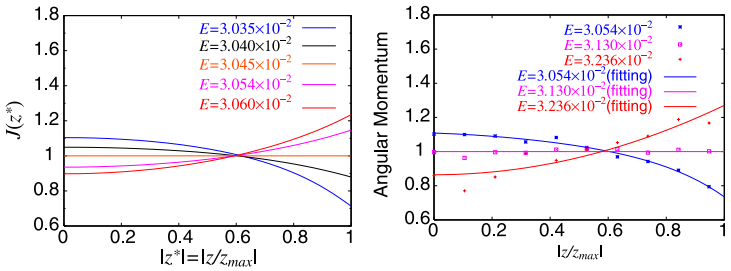

Fig. 5 Angular momentum profile $J^*(z^*)$: (a) Patch model, (b) Numerical data (lines are data fits).

The interpretation of this behavior is complicated. The entropy becomes larger if the distribution spreads wider in the radial direction, which is, in turn, constrained by the angular momentum invariance. The energy increases if the distribution is concentrated more closely around the axis of symmetry. The angular momentum is determined by a simple summation of the value on each horizontal plane, whereas the energy is determined by the whole three-dimensional distribution. The 'end-effect' appears as a delicate balance between these competing effects. The distribution in the center region has stronger influence on the energy, which expands radially for

lower energy and shrinks for higher energy. In order to keep the angular momentum unchanged, the distribution near the lids should shrink for lower energy and should expand for higher energy. Thus, the 'end-effect' for lower energy (positive temperature) appears as tighter concentration near the axis of symmetry, and the inverse is observed for higher energy (negative temperature).

5 Summary

We have investigated the statistics of quasi-geostrophic point vortices both numerically and theoretically. The axisymmetric equilibrium distribution is obtained after $t = 10 \sim 20$. The equilibrium distribution at zero inverse temperature is uniform vertically and Gaussian in the radial direction. In the positive temperature region, the equilibrium distribution near to the center of the vertical axis is similar to that of two-dimensional point vortices, whereas the distribution near the upper and lower lids under the influence of the 'end-effect' concentrates more tightly around the axis of symmetry. In contrast, the equilibrium distribution in the negative temperature region shrinks in the center and expands near the lids. The results based on the maximum entropy theory are in good agreement with the numerical equilibrium distributions. As the energy increases, the vortices are concentrated closer to the axis of symmetry in the center region, whereas the vortex cloud expands near the upper and lower lids, in order to keep the total angular momentum unchanged. A simple patch model captures the essential mechanism of the 'end-effect', predicting the vertical distribution of angular momentum, qualitatively.

Acknowledgements We are grateful for the support of Dr. Matsubara (RIKEN) throughout this work, and thank for computational resources of the RIKEN Super Combined Cluster (RSCC).

References

[1] L. Onsager, Nuovo Cimento Suppl. **6**, 279 (1949)
[2] G. Joyce, D. Montgomery, Journal of Plasma Physics **10**, 107 (1973)
[3] S. Kida, Journal of the Physical Society of Japan **39**, 1395 (1975)
[4] T.S. Lundgren, Y.B. Pointin, Journal of Statistical Physics **17(5)**, 323 (1977)
[5] Y. Yatsuyanagi, Y. Kiwamoto, H. Tomita, M.M. Sano, T. Yoshida, T. Ebisuzaki, Physical Review Letters **94**, 054502 (2005)
[6] J. Pedlosky, in *Geophysical fluid dynamics* (Springer, New York, 1979), pp. 362–365
[7] J.C. McWilliams, J.B. Weiss, I. Yavneh, Science **264**, 410 (1994)
[8] S.P. Meacham, P.J. Morrison, G.R. Flierl, Physics of Fluids **9**, 2310 (1997)
[9] T. Miyazaki, Y. Furuichi, N. Takahashi, Journal of the Physical Society of Japan **70(7)**, 1942 (2001)

[10] D.G. Dritschel, J.N. Reinaud, W.J. McKiver, J. Fluid Mech. **505**, 201 (2004)
[11] Y. Li, H. Taita, N. Takahashi, T. Miyazaki, Physics of Fluids **18(7)**, 076604 (2006)
[12] S. Hoshi, T. Miyazaki, Fluid Dynamics Research **40**, 662 (2008)
[13] M.T. DiBattista, A.J. Majda, Theoret. Comput. Fluid Dynamics **14**, 293 (2001)

Part IV
Jets: Formation and Structure

The structure of zonal jets in shallow water turbulence on the sphere

R. K. Scott

Abstract This paper reviews some recent results concerning the formation and structure of zonal jets in forced shallow water turbulence on the surface of a rotating sphere. Attention is given to the role of the Rossby deformation radius in determining the degree to which jets align zonally; to the limiting case of the axisymmetric "potential vorticity staircase"; and to the issue of equatorial superrotation, which is shown to arise robustly when energy is dissipated through a representation of radiative relaxation.

1 Introduction

The large-scale motions of planetary atmospheres and oceans, constrained by strong stable stratification and rapid rotation, are characterized in part by quasi-two dimensional turbulent motion and in part by coherent structures, such as vortices, zonal jets, and low-frequency waves. These motions are intimately linked and understanding their complex and multiscale interactions presents a complex and formidable challenge. Broadly speaking, turbulent motions can be thought of as occurring primarily at small scales and zonal jets and wave motions at large scales. However, turbulence is organized into latitudinal bands by these zonal jets, while the jets themselves are maintained against dissipation by turbulent and wave motions, via eddy momentum fluxes [e.g., 15; 2, and references therein]. Examples of zonal jets include the winter polar night jet in the Earth's stratosphere and the sub-tropical jet stream (both driven diabatically but intensified by wave/turbulent processes), and, perhaps most famously, the jets responsible for the characteristic banded structure observed on the giant planets. These zonal jets are instrumental in determining the transport of heat, chemical tracers, kinetic energy and angular momentum. Trans-

R. K. Scott
School of Mathematics, University of St Andrews, Scotland, e-mail: rks@mcs.st-and.ac.uk

D. Dritschel (ed.), *IUTAM Symposium on Turbulence in the Atmosphere and Oceans*, IUTAM Bookseries 28, DOI 10.1007/978-94-007-0360-5_20,

port is rapid along the jet axis, but is strongly inhibited across the jet axis due to enhanced "Rossby wave elasticity", the dynamic resiliance of jets to latitudinal displacements, and strong latitudinal shear on the jet flanks. Transport of water vapor within the troposphere, for example, a major influence on climate, is sensitive to the latitudinal position of the atmospheric jet stream. In the stratosphere, details of wave breaking in the vicinity of the polar night jet determine the meridional transport of chemical species involved in ozone chemistry and ultimately determines the rate of ozone recovery [30]. On the giant planets, jets separate regions of different trace chemical composition, giving rise to the coloured bands.

The emergence of zonal jets in geostrophic turbulence can be associated with the action of Rossby waves in arresting the upscale cascade of energy in a two-dimensional turbulent flow [20; 29]. As energy accumulates at larger scales and lower frequencies, a point is reached where wave motions become significant and their capacity for long-range momentum transport leads to zonal accelerations and the emergence of well-defined zonal jets. In the simple geometry of the β-plane, where planetary rotation varies linearly about a typical midlatitude value, zonal jets possess a well-defined latitudinal structure [e.g., 14; 10; 6] with a direct relationship between jet strength and spacing that is now reasonably well understood. At scales for which advection of relative vorticity ζ dominates advection of planetary vorticity, the gradient of planetary rotation β can be neglected and a timescale for the motion at scale $L \sim k^{-1}$ can be taken as $\tau \sim (kU)^{-1}$, where k is a wavenumber, or inverse length scale and U is a typical velocity [see, e.g., 27, for an overview]. In such a flow, classical phenomenology predicts that energy cascades to ever larger scales, coherent vortices merge and grow. However, the advection of planetary vorticity also supports the propagation of Rossby waves with frequency ω satisfing the dispersion relation $\omega = k\beta/(k^2 + l^2)$ (although this must be modified when significant zonal motions are present), where now k and l are zonal and latitudinal wavenumbers, respectively. These waves will be excited if there is an overlap between the frequency of the turbulent motion with the frequency of the waves, i.e. when $\tau \sim \omega^{-1}$, and this occurs at the Rhines scale, $L_{\mathrm{Rh}} \sim \sqrt{U/\beta}$. Low frequency wave motions and accompanying radiation stresses make possible long range transport of zonal momentum and thereby give rise to coherent zonal jets, providing an effective halt to the inverse energy cascade at a Rhines scale L_{Rh} [20; 29].

These predictions have been generally well supported by many numerical, experimental and observational studies. In particular, numerical calculations have verified the direct relation between jet spacing and either the initial energy in the freely decaying case [e.g. 31; 3; 4; 12], or the forcing amplitude in the continuously forced case [e.g. 28; 18; 10]. Typically zonal jets are found that are very steady in time. Other studies have demonstrated a similarity between power spectra of simulations and observations from the giant planets [9; 11; 24] or considered the effect of dissipation on jet spacing [23; 25].

The remainder of this paper reviews and updates some recent results of shallow water turbulence on the surface of a rotating sphere, examining, separately, the effects of compressibility or free surface deformations together with the associated means of energy dissipation [21; 22] and the consequences of global angular mo-

mentum and barotropic stability constraints [8], of which the latter provides a simple relation between jet spacing and jet strength that is independent of the phenomenology reviewed above. In particular, and as discussed further below, we venture the suggestion that the deformation radius appropriate to jets on the giant planets may be larger than usually considered, based on an examination of the degree of zonal alignment of high latitude jets in numerical simulations. We also summarize the recent result of Scott & Polvani [22] that a representation of large-scale energy dissipation through radiative process, or thermal damping, leads robustly to superrotating equatorial jets, even in the case of small deformation radius.

2 Jet undulations

Including the effects of compressiblility introduces another length scale, the deformation radius, L_D, representing the scale on which gravitational and rotational forces are comparable. In the Earth's troposphere $L_D \approx a$, the planetary radius, in the oceans $L_D \approx 0.1a$, while in the atmospheres of Jupiter and Saturn $L_D \approx 0.025a$ [e.g. 5; 13]. Purely 2D flow is recovered in the limit $L_D \to \infty$. Accounting for finite L_D alters the Rossby wave dispersion relation and suggests a modified Rhines scale $L_{\mathrm{Rh}} \sim \sqrt{U/\beta(1-\alpha)}$ where $\alpha = U/\beta L_D^2$. This means that when $L_D^2 < U/\beta$ (i.e. $\alpha > 1$), there will be no overlap between the turbulent and wave motions and that the flow will remain isotropic [19; 23; 26]. On the sphere L_D varies with latitude, increasing toward the equator; therefore, for certain parameters a dual regime may exist comprising isotropic 2D turbulent motion at high latitudes and coherent jets at low latitudes.

Fig. 1 shows snapshots of relative vorticity from simulations with random isotropic vorticity forcing at small scales, similar to those described in [21] but repeated here at higher resolution, and illustrates the influence of the latitudinal variation of L_D on the emerging structure of goestrophic turbulence. Sharp jumps in values correspond to eastward jets. In (a), where $L_D/a = 1$ at the pole, jets are visible at all latitudes across the sphere and are strongly zonal. By contrast, in (b), where $L_D/a = 0.025$ at the pole, jets only appear at low and mid-latitudes. At higher latitudes the jets become increasingly undular until, in polar regions there are no jets at all, and instead the flow is dominated by circular vortices. This behaviour is consistent with the scaling arguments just presented [see 21, for further discussion].

At values of deformation radius typical of the giant planets planets, numerical experiments consistently produce high latitude jets that are significantly more undular than their planetary counterparts. Only at values of deformation radius double or more the planetary values do we begin to see stongly zonal jets at mid and high latitudes. Estimates of deformation radius for the giant planets are, however, typically inferred from observations or numerical modelling of the structure of coherent vortices such as the Great Red Spot [e.g. 5; 13]. The aforementioned numerical experiments suggest, therefore, that jets may have a deeper structure, and a correspondingly larger effective deformation radius, than smaller scale vortices. Such a

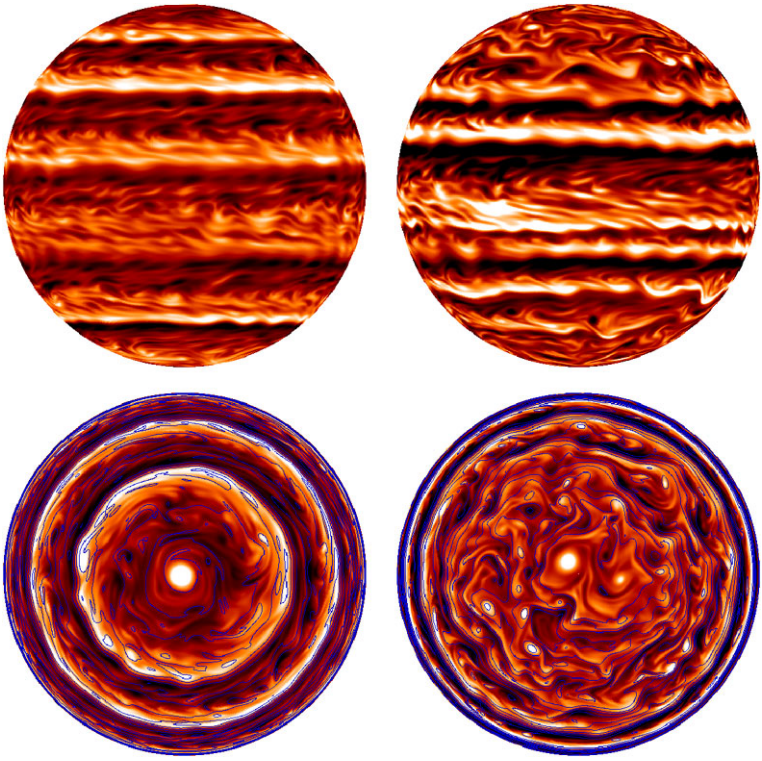

Fig. 1 Illustration of the latitudinal confinement of zonal jets: $L_D/a = 1$ (left), $L_D = 0.025$ (right); shaded quantity is the relative vorticity, the contours in the lower panels show the potential vorticity. Top: equatorial view; bottom: polar view.

structure may arise naturally through the process of barotropization and is observed to occur in many flows in the terrestrial atmosphere and oceans. In the above experiments, high latitudes cease to be strongly zonal when L_D/a is below around 0.1.

Although the polar views of relative vorticity field shown in Fig. 1 appear increasingly isotropic at small L_D/a, an examination of the potential vorticity field (blue contours) indicates the flow is not isotropic. Contours of potential vorticity are highly undular but nevertheless circumscribe the pole. Interestingly, the strong coherent cyclonic vortices seen near the pole are a persistent feature of these and many other numerical experiments and bear some resemblence to the polar cyclones observed on Jupiter and Saturn.

3 The potential vorticity staircase

Several recent studies [2; 7; 8; 16] have emphasized the dual role of turbulent mixing and long-range interactions, the latter arising from the property of potential vorticity inversion and including long-range momentum transport by waves. In fact, the idea of inhomogeneous mixing of potential vorticity in the context of Rossby wave–mean flow interaction appeared over 25 years ago in the McIntyre [15] review of stratospheric sudden warmings and the related discussion by McIntyre & Palmer [17] of a midlatitude "surf zone" bounded on both sides by sharp gradients of potential vorticity and tracer. Material conservation and invertibility of potential vorticity give rise to a "Rossby-wave elasticity" or resiliance to latitudinal displacements of regions of strong potential vorticity gradients. Mixing of potential vorticity is therefore highly inhomogeneous: stronger gradients have greater elasticity and so resist mixing by eddy or wave motions; where gradients are weaker, mixing is stronger and contours of constant potential vorticity can be more easily deformed irreversibly. Mixing here means latitudinal mixing across the planetary vorticity gradient and thus acts to further weaken local potential vorticity gradients in mixing regions, and strengthen them in between. Zonal jets are a direct consequence of the resulting potential vorticity staircase structure through the relation

$$\bar{q} = -\frac{1}{a^2}\frac{d\bar{m}}{d\mu} \tag{1}$$

where $\mu = \sin\phi$, ϕ is latitude, $\bar{m} = a\cos\phi(\Omega a\cos\phi + \bar{u})$ is the angular momentum, $\bar{u}$ is the zonal velocity, Ω is the planetary rotation, and the overbar denotes a zonal mean. The potential vorticity staircase solution corresponds to latitudinal bands of constant $\bar{q}$ separated by jumps, as shown in Fig. 2. According to (1), uniform $\bar{q}$ implies that $\bar{m}$ is linear in μ. The associated $\bar{u}$ is then obtained from the departure of $\bar{m}$ from the parabolic profile of the resting atmosphere. The construction shown here follows that of Dunkerton & Scott [8]. Note that the staircase construction gives an immediate explanation, which is hidden in the phenomenological arguments reviewed in §1, of the asymmetry between sharp, narrow prograde jets and broad, weak retrograde flow generically observed in geostrophic turbulence.

If further we assume a rearrangement of potential vorticity from a resting atmosphere that conserves total angular momentum and assume that the resulting flow be barotropically stable, then the staircase construction also provides an explicit constraint on the jet spacing for a given jet strength: geometrically, it is easy to see that we may either have a few strong jets or many weak ones, as illustrated by the two rows in Fig. 2. We may term the scale arising from this constraint a "geometric Rhines scale" [8], since it arises independently of any details of the turbulent phenomenology or potential vorticity mixing. It complements the notion of dynamical Rhines scale discussed in §1 (Rhines, 1975) or similar estimates based on the spectral flux of energy (Maltrud and Vallis, 1991), but is conceptually simpler, requiring only that potential vorticity be homogenized within mixing zones located between prograde jets, in a barotropically stable configuration. Further analysis shows that

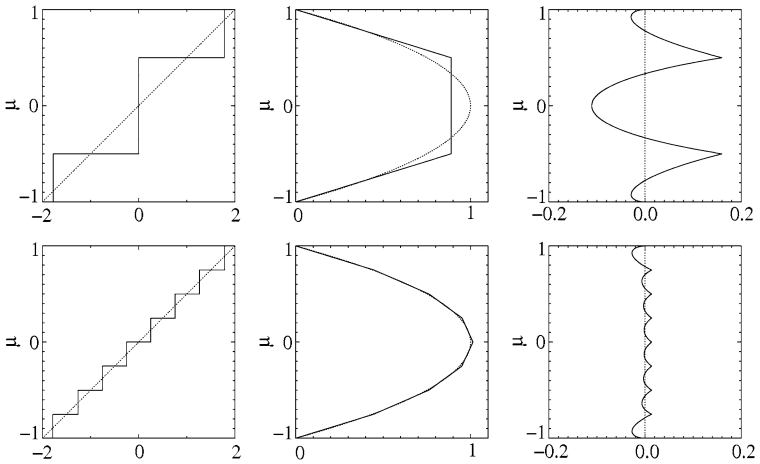

Fig. 2 Illustration of the potential vorticity staircase and the geometric Rhines constraint; top, few large steps; bottom, many small ones; $\bar{q}$ (left), $\bar{m}$ (centre) $\bar{u}$ (right), against $\mu = \sin\phi$, where ϕ is latitude. Dotted lines correspond to an atmosphere at rest.

jets are spaced slightly further apart than predicted by the arguments of §1. Since the staircase solution assumes perfect homogenization of potential vorticity between jets it should also be considered as a limiting situation.

The β-plane case with finite L_D/a was discussed in Dritschel & McIntyre [7]. There, exact solutions were found for the staircase solution, which led to the estimate $L_{\rm jet} \sim \max(L_{\rm Rh}, L_{\rm Rh}^2/L_D)$ for the jet spacing. In other words the jet spacing scales as $L_{\rm Rh}$ at large L_D, but is modified for $L_D \ll L_{\rm Rh}$. Note, however, that in the latter case, zonal jets are typically undular, similar to the high latitudes of Fig. 1, and their identification becomes increasingly difficult, since, for example, zonal averaging will smooth out the along jet velocity.

The scaling for the barotropic case on the sphere was confirmed to hold over a wide range of energy injection rates [8]. A further example is shown in Fig. 3, for a case of finite deformation radius with small-scale forcing and large-scale energy dissipation by thermal relaxation. In this case, the potential vorticity profile is close to the limiting case of the perfect staircase, and the corresponding jet asymmetries are apparent. The full potential vorticity field is also shown and illustrates the turbulent mixing between the locations of strong gradients.

4 Equatorial superrotation

With physically appropriate parameters, Cho & Polvani [4] showed that the scale of zonal jets in freely decaying shallow water turbulence was consistent with the observed zonal mean winds of the four giant planets. However that study, and many others since have found that equatorial jets tend to be subrotating, or retrograde,

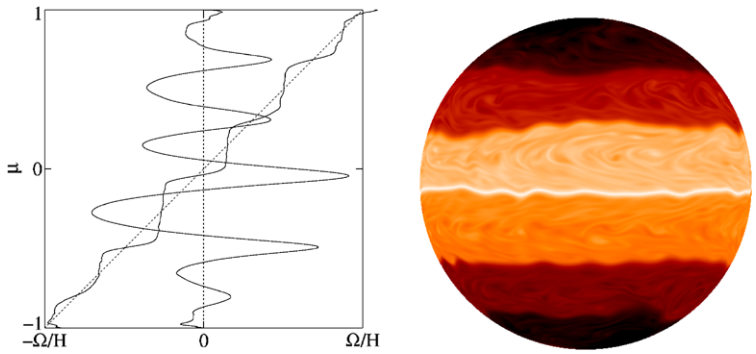

Fig. 3 Forced numerical staircase for a case with $L_D = 0.05$ and radiative relaxation: left, $\bar{q}$ and $\bar{u}$; right, the potential vorticity.

when L_D/a is small, in contrast to the equatorial jets observed on Jupiter and Saturn. Although this result has sometimes been used in arguments for the role of deep convection as the driving mechanism for the observed jets, it is important to remember that subrotating jets are only predominant at small L_D/a: when L_D/a is large subrotating and superrotating equatorial jets appear to emerge with approximately equal probability when forced randomly, as was demonstrated in an ensemble of calculations performed by [8].

The staircase construction discussed above is again useful in understanding the nature of the equatorial jets. Whether an equatorial jet is superrotating or subrotating is determined simply by whether the equator coincides with a potential vorticity jump or mixing zone. The emergence of equatorial superrotation in a nonaxisymmetric, turbulent flow can be understood in terms of the Taylor identity [16], relating eddy potential vorticity fluxes and eddy momentum flux convergence, which, in the simplest case of barotropic motion, takes the form

$$\overline{v'q'} = -\frac{1}{a}\frac{d}{d\mu}\left(\overline{u'v'}\sqrt{1-\mu^2}\right). \tag{2}$$

Advective mixing of potential vorticity is always associated with a downgradient potential vorticity flux or divergence of eddy momentum flux, and a consequent reduction of angular momentum and deceleration of the zonal velocity. To establish a potential vorticity jump at the equator, a nonadvective upgradient flux is necessary, giving rise to a local acceleration of the zonal velocity: positive jets must necessarily be associated with positive $\overline{v'q'}$. Such upgradient fluxes are associated with wave transience or dissipation.

While subrotating and superrotating jets appear equally likely at large L_D/a, recent calculations [22] have shown that even at small L_D it is possible to ensure the emergence of superrotation, simply by including the physical mechanism of thermal relaxation. That the nature of the equatorial jets depends on details of energy dissipation is perhaps not surprising, in view of the above and the work of [1] that

demonstrated a sensitivity of mean flow changes at the equator to dissipation of Rossby-gravity waves. The example in Fig. 3 illustrates a typical example of equatorial superrotation obtained in the presence of thermal dissipation, despite a small value of L_D/a.

5 Open questions: the nature of forcing and dissipation

The degree to which potential vorticity homogenisation occurs between jets will depend both on the way in which the mixing is forced and on the form of energy dissipation at large scales. What forms are used should be dictated by the physical situation of interest. On the gas giants, for example, the absence of a solid ground beneath the weather layers of these atmospheres together with measurements of radiative fluxes suggest that thermal relaxation is a more appropriate choice of dissipation than frictional damping.

The issue of forcing poses a major challenge. Potential vorticity mixing results from the motion of both coherent vortices and Rossby wave breaking. Random, isotropic forcing in spectral space, as was used in the experiments reported above, is convenient, but its effect on potential vorticity mixing may differ significantly from physical space forcing because of the loss of phase information.

Moreover, in a physical system, the zonal flows that arise from potential vorticity mixing will themselves affect the efficiency of a given forcing mechanism, for example by fixing the regions where waves may propagate and break. In a perfect potential vorticity staircase, waves are excluded from the regions between jets and may exist only on the discontinuities themselves, as edge waves (some instances can be discerned in Fig. 3). Forcing with a fixed rate of energy input, as is typically used in numerical studies of two-dimensional or geostrophic turbulence, and in the calculations presented here, ignores the natural adjustment of energy uptake by the flow as zonal jets intensify. In the terrestrial atmosphere the forcing of large-scale wave motions by topographic effects and land-sea temperature contrasts is relatively well-understood. On the gas giants, on the other hand, very little is known about the motion of the atmospheres at depth and the correct choice of forcing remains difficult to determine.

Acknowledgements The author would like to thank James Cho, David Dritschel, Tim Dunkerton, Michael McIntyre, Lorenzo Polvani, and Jurgen Theiss for many interesting discussions. He also wishes to express his gratitude to the organizers of the IUTAM symposium on rotating stratified flows where this work was presented. Financial support for much of the original work was provided by the National Science Foundation.

References

[1] Andrews, D. G., & McIntyre, M. E. 1976. Planetary waves in horizontal and vertical shear: asymptotic theory for equatorial waves in weak shear. *J. Atmos. Sci.*, **33**, 2049–2053.

[2] Baldwin, M. P., Rhines, P. B., Huang, H.-P., & McIntyre, M. E. 2007. The Jet-Stream Conundrum. *Science*, **315**, 467–468.

[3] Cho, J. Y-K., & Polvani, L. M. 1996a. The emergence of jets and vortices in freely-evolving shallow-water turbulence on a sphere. *Phys. Fluids*, **8**, 1531–1552.

[4] Cho, J. Y-K., & Polvani, L. M. 1996b. The morphogenesis of bands and zonal winds in the atmospheres on the giant outer planets. *Science*, **273**, 335–337.

[5] Cho, J. Y-K., de la Torre Juárez, M., Ingersoll, A. P., & Dritschel, D. G. 2001. A high-resolution, three-dimensional model of Jupiter's Great Red Spot. *J. Geophys. Res.*, **106**, 5099–5105.

[6] Danilov, S., & Gurarie, D. 2004. Scaling, spectra and zonal jets in beta-plane turbulence. *Phys. Fluids*, **16**, 2592–2603.

[7] Dritschel, D. G., & McIntyre, M. E. 2008. Multiple jets as PV staircases: the Phillips effect and the resilience of eddy-transport barriers. *J. Atmos. Sci.*, **65**, 855–874.

[8] Dunkerton, T. J., & Scott, R. K. 2008. A barotropic model of the angular momentum conserving potential vorticity staircase in spherical geometry. *J. Atmos. Sci.*, **65**, 1105–1136.

[9] Galperin, B., Sukoriansky, S., & Huang, H.-P. 2001. Universal n^{-5} spectrum of zonal flows on giant planets. *Phys. Fluids*, **13**, 1545–1548.

[10] Huang, H.-P., & Robinson, W. A. 1998. Two-dimensional turbulence and persistent zonal jets in a global barotropic model. *J. Atmos. Sci.*, **55**, 611–632.

[11] Huang, H.-P., Galperin, B., & Sukoriansky, S. 2001. Anisotropic spectra in two-dimensional turbulence on the surface of a rotating sphere. *Phys. Fluids*, **13**, 225–240.

[12] Iacono, R., Struglia, M. V., Ronchi, C., & Nicastro, S. 1999. High-resolution simulations of freely decaying shallow-water turbulence on a rotating sphere. *Il Nuovo Cimento*, **22C**, 813–821.

[13] Ingersoll, A. P., Dowling, T. E., Gierasch, P. J., Orton, G. S., Read, P. L., Sanchez-Lavega, A., Showman, A. P., Simon-Miller, A. A., & Vasavada, A. R. 2004. *Dynamics of Jupiter's atmosphere*. Cambridge Univ. Press. Pages 105–128.

[14] Maltrud, M. E., & Vallis, G. K. 1991. Energy spectra and coherent structures in forced two-dimensional and beta-plane turbulence. *J. Fluid Mech.*, **228**, 321–342.

[15] McIntyre, M. E. 1982. How well do we understand the dynamics of stratospheric warmings? *J. Meteorol. Soc. Japan*, **60**, 37–65. Special issue in commemoration of the centennial of the Meteorological Society of Japan, ed. K. Ninomiya.

[16] McIntyre, M. E. 2008. Potential-vorticity inversion and the wave–turbulence jigsaw: some recent clarifications. *Adv. Geosci.*, **15**, 47–56.
[17] McIntyre, M. E., & Palmer, T. N. 1983. Breaking planetary waves in the stratosphere. *Nature*, **305**, 593–600.
[18] Nozawa, T., & Yoden, S. 1997. Formation of zonal band structure in forced two-dimensional turbulence on a rotating sphere. *Phys. Fluids*, **9**, 2081–2093.
[19] Okuno, A., & Masuda, A. 2003. Effect of horizontal divergence on the geostrophic turbulence on a beta-plane: suppression of the Rhines effect. *Phys. Fluids*, **15**, 56–65.
[20] Rhines, P. B. 1975. Waves and turbulence on a beta-plane. *J. Fluid Mech.*, **69**, 417–443.
[21] Scott, R. K., & Polvani, L. M. 2007. Forced-dissipative shallow water turbulence on the sphere and the atmospheric circulation of the gas planets. *J. Atmos. Sci.*, **64**, 3158–3176.
[22] Scott, R. K., & Polvani, L. M. 2008. Equatorial superrotation in shallow atmospheres. *Geophys. Res. Lett.*, **35**, L24202.
[23] Smith, K. S. 2004. A local model for planetary atmospheres forced by small-scale convection. *J. Atmos. Sci.*, **61**, 1420–1433.
[24] Sukoriansky, S., Galperin, B., & Dikovskaya, N. 2002. Universal spectrum of two-dimensional turbulence on rotating sphere and some basic features of atmospheric circulations on giant planets. *Phys. Rev. Lett.*, **89**, 124501.
[25] Sukoriansky, S., Dikovskaya, N., & Galperin, B. 2007. On the arrest of inverse energy cascade and the Rhines scale. *J. Atmos. Sci.*, **64**, 3312–3327.
[26] Theiss, J. 2004. Equatorward energy cascade, critical latitude, and the predominance of cyclonic vortices in geostrophic turbulence. *J. Phys. Oceanogr.*, **34**, 1663–1678.
[27] Vallis, G. K. 2006. *Atmospheric and Oceanic Fluid Dynamics*. Cambridge University Press.
[28] Vallis, G. K., & Maltrud, M. E. 1993. Generation of mean flows on a beta plane and over topography. *J. Phys. Oceanogr.*, **23**, 1346–1362.
[29] Williams, G. P. 1978. Planetary circulations: 1. Barotropic representation of Jovian and terrestrial turbulence. *J. Atmos. Sci.*, **35**, 1399–1424.
[30] World Meteorological Organization. 2007. *Scientific Assessment of Ozone Depletion 2006 (Global Ozone Research and Monitoring Project - Report No. 50)*. Geneva: World Meteorological Organization.
[31] Yoden, S., & Yamada, M. 1993. A numerical experiment on two-dimensional decaying turbulence on a rotating sphere. *J. Atmos. Sci.*, **50**, 631–643.

Jet formation in decaying two-dimensional turbulence on a rotating sphere

Shigeo Yoden, Yoshi-Yuki Hayashi, Keiichi Ishioka,
Yuji Kitamura, Seiya Nishizawa, Sin-ichi Takehiro, and Michio Yamada

Abstract Jet formation in decaying two-dimensional turbulence on a rotating sphere is reviewed from the view point of wave mean-flow interaction for both shallow-water case and non-divergent case as the limit of Fr (Froude number) going to zero. A series of computations have been performed by ourselves to confirm the behavior of zonal mean zonal flow generation on the parameter space of the non-dimensional rotation rate Ω and Fr. When the flow is non-divergent and Ω is large, intense retrograde circumpolar jets tend to emerge in addition to a banded structure of mean zonal flows with alternating flow directions in middle and low latitudes. As Fr increases, the circumpolar jets disappear and a retrograde jet emerges in the

Shigeo Yoden
Division of Earth and Planetary Sciences, Graduate School of Science, Kyoto University, Kyoto, 606-8502, Japan, e-mail: yoden@kugi.kyoto-u.ac.jp

Yoshi-Yuki Hayashi
Graduate School of Science, Kobe University, Kobe, 657-8501, Japan, e-mail: shosuke@gfd-dennou.org

Keiichi Ishioka
Division of Earth and Planetary Sciences, Graduate School of Science, Kyoto University, Kyoto, 606-8502, Japan, e-mail: ishioka@gfd-dennou.org

Yuji Kitamura
Meteorological Research Institute, Japan Meteorological Agency, Tsukuba, 305-0052, Japan, e-mail: kitamura@mri-jma.go.jp

Seiya Nishizawa
Graduate School of Science, Kobe University, Kobe, 657-8501, Japan, e-mail: seiya@gfd-dennou.org

Sin-ichi Takehiro
Research Institute for Mathematical Sciences, Kyoto University, Kyoto, 606-8502, Japan, e-mail: takepiro@gfd-dennou.org

Michio Yamada
Research Institute for Mathematical Sciences, Kyoto University, Kyoto, 606-8502, Japan, e-mail: yamada@kurims.kyoto-u.ac.jp

D. Dritschel (ed.), *IUTAM Symposium on Turbulence in the Atmosphere and Oceans*,
IUTAM Bookseries 28, DOI 10.1007/978-94-007-0360-5_21,

equatorial region. The appearance of the intense retrograde jets can be understood by the angular momentum transport associated with the propagation and absorption of Rossby waves. When the flow is non-divergent, long Rossby waves tend to be absorbed around the poles. In contrast, when Fr is large, Rossby waves can hardly propagate poleward and tend to be absorbed near the equator. The direction of the equatorial jet, however, is not always retrograde. Our ensemble experiments showed the emergence of a prograde jet, though less likely. This result is contrasted with the previous studies that reported retrograde equatorial jets in most cases for shallow-water turbulence. Furthermore, a mean zonal flow induced by wave-wave interactions was examined using a weakly nonlinear model to clarify the acceleration mechanisms of the equatorial jet. The second-order acceleration is induced by the Rossby waves and mixed Rossby-gravity waves and the acceleration mechanism can be categorized into two types.

1 Introduction

In late 1970s, the first research on two-dimensional turbulence on a rotating sphere was done numerically by Williams [17], where he showed that a zonally banded structure of stream function field which resembles telescope images of Jupiter was formed. While that study treated a forced-dissipative turbulence, numerical experiments on decaying turbulence on a rotating sphere were firstly conducted by Yoden and Yamada [18]. They showed that spontaneous formation of retrograde circumpolar jets from turbulent initial fields is a robust feature of two-dimensional decaying turbulence on a rotating sphere. While these studies considered 2D non-divergent fluid, the effect of horizontal divergence was firstly incorporated by Cho and Polvani [1]. They studied decaying shallow water turbulence on a rotating sphere to show spontaneous appearance of a retrograde equatorial jet as a robust result. After these several studies on turbulence on a rotating sphere have been done both for forced-dissipative and decaying cases. For forced-dissipative turbulence, a non-divergent case are studied by Nozawa and Yoden [8; 9] and a shallow water case by Scott and Polvani [12]. For decaying turbulence, the mechanism of flow pattern formation has been studied thoroughly with high-resolution numerical models [3; 6; 14; 15; 19]. Those studies, however, treated a non-divergent case only. Therefore, the mechanism how the horizontal divergence effect causes a retrograde equatorial jet in decaying turbulence had not been explored in detail.

Recently, our research group published two papers on this subject as a fruit of Chapman Conference on Jets and Annular Structures in Geophysics held in 2006.[1] Hayashi et al. [4] clarified the horizontal divergence effect on producing retrograde jets whether at the poles or at the equator with parameter sweep experiments, while Kitamura and Ishioka [7] conducted a large number of ensemble experiments to study the formation mechanism of the equatorial jet and the robustness of the ap-

[1] http://www-mete.kugi.kyoto-u.ac.jp/yoden/research/Chapman_Web/ChapmanConference2006Jets.htm

pearance of the retrograde equatorial jet, in other words, whether a prograde equatorial can be formed or not [2]. In this article, we review the spontaneous polar/equatorial jet formation process in decaying 2D non-divergent/shallow water turbulence on a rotating sphere referring to the results of these two papers. Furthermore, very recent developments on shallow water turbulence by other research groups are also mentioned.

2 Parameter sweep experiments (Hayashi et al., 2007)

The system under consideration is a 2D flow on a rotating sphere which is described by the following shallow water equations.

$$\frac{Du}{Dt} - uv\tan\phi - 2\Omega v\sin\phi = -\frac{1}{\mathrm{Fr}^2}\frac{\partial\eta}{\cos\phi\partial\lambda} + (\text{hyper-viscosity}),$$
$$\frac{Dv}{Dt} - u^2\tan\phi + 2\Omega u\sin\phi = -\frac{1}{\mathrm{Fr}^2}\frac{\partial\eta}{\partial\phi} + (\text{hyper-viscosity}),$$
$$\frac{D\eta}{Dt} + (1+\eta)\left(\frac{\partial u}{\cos\phi\partial\lambda} + \frac{\partial(v\cos\phi)}{\cos\phi\partial\phi}\right) = (\text{hyper-diffusivity}).$$

Here, t is the time normalized by a/U, a is the radius of the sphere, U is the velocity scale, λ is the longitude, ϕ is the latitude, η is the surface elevation normalized by H, which is the mean depth of the fluid, (u,v) is the (eastward, northward) velocity normalized by U, Ω is the rotation rate of the sphere normalized by U/a, $\mathrm{Fr} = U/\sqrt{gH}$ is the Froude number, and g is the gravity acceleration.

The basic equations are spatially discretized using the Galerkin spectral method with spherical harmonics of truncation wavenumber 170 and time-integrated with the classical 4th order Runge-Kutta method from a random vorticity field which has an energy peak at the total wavenumber 50.

To study the effect of the horizontal divergence and the rotation rate, parameter sweep experiments are conducted changing Fr and Ω. Used parameter settings are summarized in Table 1 with four important numbers for dynamical understanding, k_β, L_{Dp}, L_{De}, and $\tilde{\phi}$, deduced from Ω and Fr [3] [4]. Here, the setting of $\mathrm{Fr} = 0$ corresponds to the non-divergent case.

Flow patterns appearing from the decaying turbulence depend on the horizontal divergence effect. Figure 1 shows snapshots of vorticity fields at $t = 5$ inte-

[2] Iacono *et al.* [5] showed a possibility of a prograde equatorial jet when Ro and Fr are relatively large. However, they did not conduct ensemble experiments so that the possibility in which a prograde equatorial jet is formed was not explored.

[3] In some cases, the numerical resolution is not enough to resolve the radius of deformation. However, since the initially given field has the larger resolvable scales, these results are robust qualitatively to increasing resolution if the initial field is kept unchanged.

[4] Although the value of $\mathrm{Fr}^2\Omega$ is very large in some cases, no "dry-up" occurred in the course of time-evolutions because gravity modes are dominant in the initial field in those cases.

Table 1 Summary of the experimental parameters: $k_\beta = \sqrt{2\Omega\cos\phi/\langle u\rangle}$: the Rhines wavenumber where $\langle u\rangle = \sqrt{2}$, L_{Dp}: the radius of deformation at the poles, L_{De}: the equatorial radius of deformation, $\tilde{\phi}$: the latitude where $L_D = 1/k_\beta$, $L_D = L_{Dp}/\sin\phi$: the radius of deformation.

Ω	Fr	$k_\beta(\phi=0)$	L_{Dp}	L_{De}	$\tilde{\phi}$
0	$1/\sqrt{10}$	0	0	0	–
25	$1/\sqrt{10}$	5.9	0.063	0.25	0.37 (21°)
50	$1/\sqrt{10}$	8.4	0.032	0.18	0.26 (15°)
100	$1/\sqrt{10}$	12	0.016	0.13	0.19 (11°)
400	$1/\sqrt{10}$	24	0.004	0.063	0.09 (5°)
400	$1/\sqrt{100}$	24	0.013	0.11	0.30 (17°)
400	$1/\sqrt{1000}$	24	0.04	0.2	0.86 (49°)
400	$1/\sqrt{10000}$	24	0.13	0.35	1.47 (84°)
400	0	24	∞	∞	–
4000	$1/\sqrt{10}$	75	0.0004	0.02	0.03 (1.7°)

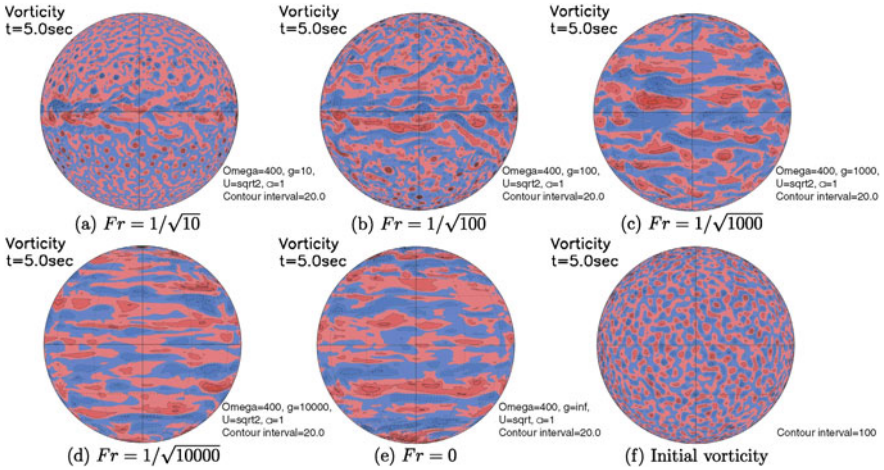

Fig. 1 Vorticity at $t = 5$ for various values of Fr with $\Omega = 400$ (a–e), and the initial vorticity field (f). Contour intervals are 20 for (a) to (e) and 100 for (f). 0 contour is suppressed. Gray to bluish colors indicate negative values. (adopted from [4]).

grated from the same initial random vorticity field (f) for five values of Fr with a fixed $\Omega = 400$ [5]. When $\mathrm{Fr} = 1/\sqrt{100}$ (b), coherent vortices appear in high latitudes and zonally elongated structures appear in low latitudes. The boundary latitude between the coherent vortices and the zonally elongated structures shifts equatorward for $\mathrm{Fr} = 1/\sqrt{10}$ case (a) while it shifts poleward for $\mathrm{Fr} = 1/\sqrt{1000}$ case (c). For $\mathrm{Fr} = 1/\sqrt{10000}$ case (d) and non-divergent case (e), the zonally elongated struc-

[5] The coherent vortices in high latitudes in Figs 1(a,b) are not mere remnants of the initial field because they have strong cyclonic/anticyclonic asymmetry.

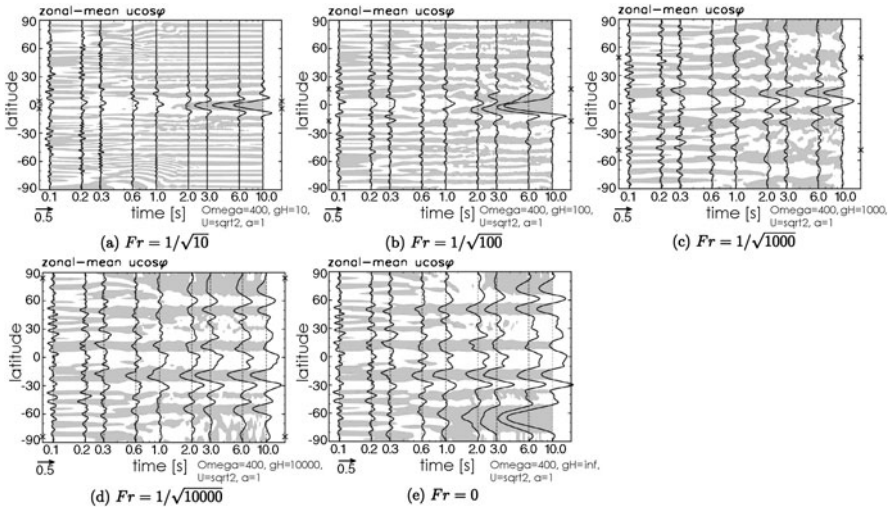

Fig. 2 Time evolutions of zonal mean angular momentum $\overline{u}\cos\phi$ with $\Omega = 400$ for various values of Fr. Lines are the profiles at selected times $t =$ 0.1 0.2, 0.3, 0.6, 1.0, 3.0, 6.0, and 10.0. The magnitude corresponding to the value of 0.5 is indicated by the arrow at the bottom left of each panel. Shaded areas in the background indicate that $\overline{u}\cos\phi$ is negative at the respective latitude and time. Crossmarks on the right edge for each panel indicate the latitudes $\pm\tilde{\phi}$ listed in Table 1. (adopted from [4]).

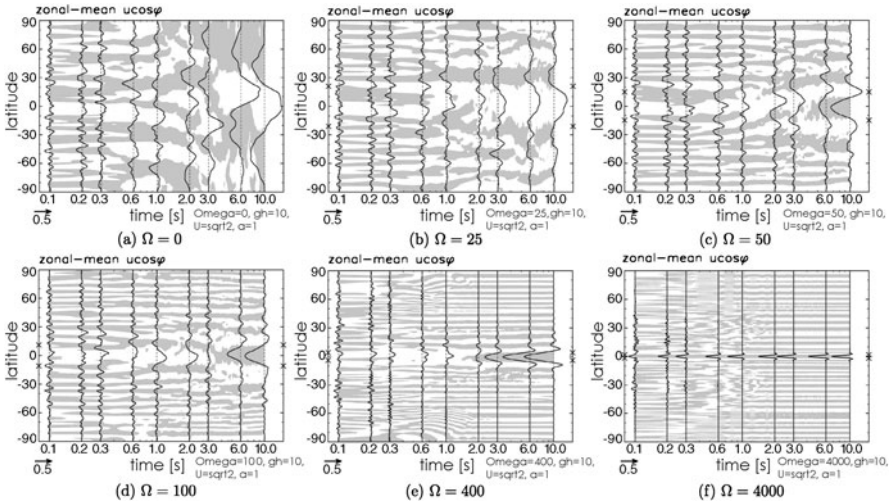

Fig. 3 Same as Fig. 2 but for various values of Ω with $Fr = 1/\sqrt{10}$. (adopted from [4]).

tures fill all over the sphere. The latitude $\tilde{\phi}$ where the radius of deformation L_D equals the Rhines scale defined as $1/k_\beta = \sqrt{\langle u\rangle/(2\Omega\cos\phi)}$ gives a good estimate of the boundary latitudes (Table 1). The result that the latitude $\tilde{\phi}$ roughly divides the structure of vorticity field is consistent with the finding of Theiss [16], where

the quasi-geostrophic equation on a plane with variable β is used. The reason why a banded structure cannot develop where $\phi > \tilde{\phi}$, that is, $L_D < 1/k_\beta$, can be understood as follows. For a zonal banded structure to appear, the linear effect (the β effect) must overwhelm the nonlinear advection effect, which leads to anisotropy. When $L_D < 1/k_\beta$, however, Rossby waves become almost non-dispersive in advection time scale so that the linear effect cannot overwhelm the nonlinear effect. This interpretation is firstly introduced by Okuno and Masuda [10] in 2003. For further discussion, see our paper [4].

The importance of $\tilde{\phi}$ can be also seen in the corresponding time evolutions of zonal mean angular momentum (Fig. 2). For $\mathrm{Fr} = 1/\sqrt{1000}$ case, a banded structure of zonal mean angular momentum with alternating flow directions develops in middle and low latitudes. The latitudinal extent of a banded structure is roughly estimated by $\tilde{\phi}$ (indicated by "$\times$" in the figure) as seen in Fig. 1(c). This is also the case in the other figures of Fig. 2. It can be seen in the time evolutions that a banded structure is established by the time $t \sim 1.0$. On the other hand, retrograde polar jets in (e) and retrograde equatorial jets in (a) and (b) grow continuously and relatively slowly, which is suggestive that these retrograde jets are intensified through accumulation of eddy angular momentum by Rossby waves.

While the direction of the equatorial jets seen in Figs. 2(a) and (b) are retrograde, it is not always the case. Figure 3 shows the dependence of the time evolution of zonal mean angular momentum on the rotation rate Ω. When the rotation is rapid as (c), (d), (e), and (f), the direction is retrograde. For slow rotation case (b), however, a prograde equatorial jet develops. Whether this prograde jet formation is a very rare case depending on the initial condition or not must be checked with ensemble experiments. This is the main subject of the next section.

3 Ensemble experiments (Kitamura and Ishioka, 2007)

To examine the possibility of the appearance of a prograde equatorial jet from decaying shallow water turbulence on a rotating sphere as seen in the previous section, Kitamura and Ishioka [7] conducted a large number of ensemble experiments changing initial random vorticity field (up to 1000 members). The experimental settings and the numerical method is almost the same as in the previous section [4] except for the value of initial root mean square velocity $\langle u \rangle$: The initial $\langle u \rangle$ is set to $\sqrt{2}$ in [4], while it is set to 1 here in [7]. Therefore, for example, $\mathrm{Fr} = 0.3$ in this section corresponds to $\mathrm{Fr} = 0.3/\sqrt{2} \approx 0.21$ in the previous section. Furthermore, in this section, the effect of rotation is indicated by the Rossby number $\mathrm{Ro} = \langle u \rangle / (2\Omega)$ so that $\mathrm{Ro} = 0.03$ in this section corresponds to $\Omega = \sqrt{2}/(2\mathrm{Ro}) \approx 23.6$ in the previous section.

The direction of an equatorial jet emerging from decaying shallow water turbulence is not always retrograde depending on experimental parameters as seen in the end of the previous section. Figure 4 shows histograms of the zonal mean zonal flow at the equator ($\langle u \rangle_{\mathrm{eq}}$) at $t = 5$ and $t = 15$ for three values of Ro. While the distributions of the histograms are almost symmetric at $t = 5$, the distributions shift to the retrograde side as time goes on. A retrograde equatorial jet is formed in all the

ensemble members at $t = 15$ for $\mathrm{Ro} = 0.01$. For $\mathrm{Ro} = 0.02$ and $\mathrm{Ro} = 0.03$ cases, on the other hand, a retrograde jet survives in some ensemble members till $t = 15$. In particular, the number of the members of $\langle u \rangle_{\mathrm{eq}} \geq 0.5$ increases in the period from $t = 5$ to $t = 15$ for $\mathrm{Ro} = 0.03$, which indicates that there are some mechanisms accelerating an equatorial jet not only westward to the retrograde direction but also eastward to the prograde direction.

As pointed out in the previous section, the slowness of the acceleration of an equatorial jet seems to indicate that the acceleration caused by momentum transfer due to waves. To examine this effect, linearized equations with a time-constant zonally symmetric basic flow, $[u]$, are integrated from the eddy fields at $t = 5$ up to 125-member ensembles which are obtained by the full nonlinear time integrations. In the time integrations, second order acceleration of mean zonal flow by the linear disturbances is evaluated. Furthermore, the initial eddy field is decomposed into normal-mode waves so that contributions by each mode-coupling to the acceleration can be evaluated. Figure 5 shows ensemble mean of the second order acceleration between $t = 5$ and $t = 15$ for the basic flow with $[u] = 0$ in $\mathrm{Ro} = 0.03$ and $\mathrm{Fr} = 0.3$ cases. The second order acceleration is almost completely due to couplings of Rossby waves (here, westward Rossby-Gravity waves are categorized into Rossby waves for convenience) and it is westward at the equator not only in retrograde members but also prograde members. Retrograde acceleration mechanism by Rossby waves can be explained as follows. While the zonal wavenumber k and the zonal phase velocity c are conserved along a ray in the WKB approximation, the meridional wavenumber l varies so that the dispersion relation,

$$l^2 = -(k^2 + 1/L_D^2) + \bar{q}_y/(\bar{u} - c),$$

is satisfied. Here, $\bar{u}$ and $\bar{q}$ are the zonal velocity and potential vorticity of the basic flow, respectively. Here, in this relation, l becomes larger when the deformation radius L_D increases as the wave packet approaches the equator, or when the phase velocity is closer to the zonal velocity of the basic flow. Large l leads to quick dissipation of the Rossby wave packet so that it leaves its pseudomomentum.

The second order acceleration of Rossby waves cannot cause a prograde equatorial jet with the zero basic flow as seen above. With a non-zero basic flow, however, the situation changes because the basic flow changes the propagation properties of linear waves. Figure 6 shows the second order acceleration evaluated in time-integrations of linearized equations with a weak prograde basic flow. In this case, the acceleration at the equator is prograde. Decomposing the acceleration, a half of the prograde accelerations can be attributed to westward Rossby-gravity waves as shown in Fig. 6(right). The mechanism of this acceleration can be understood by wave tilting as follows. When there is an equatorial jet as a basic state, equatorial waves may be modified by the jet shear. For the modified waves, there can be correlation between u' and v', which induces meridional transfer of zonal momentum as shown in Fig. 7. Therefore, if a weak prograde zonal flow is formed by chance in an early stage of nonlinear time evolutions, a prograde acceleration by the waves can breed a prograde equatorial jet.

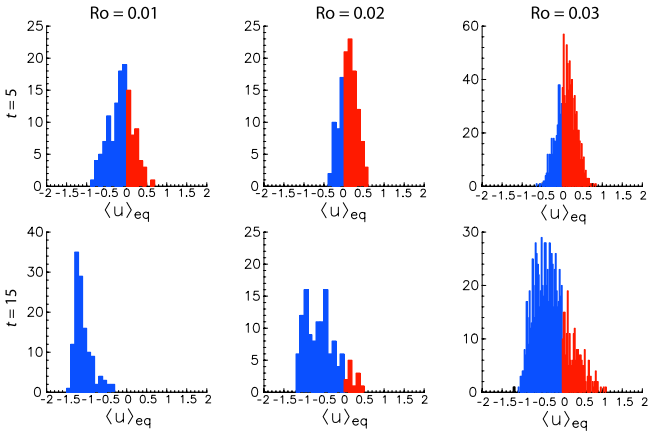

Fig. 4 Histograms of the zonal mean zonal flow at the equator for Fr= 0.3 cases: (left) Ro= 0.01, (middle) Ro= 0.02, (right) Ro= 0.03. Snapshots at $t = 5$ (top) and $t = 15$ (bottom) are shown. (adopted from [7]).

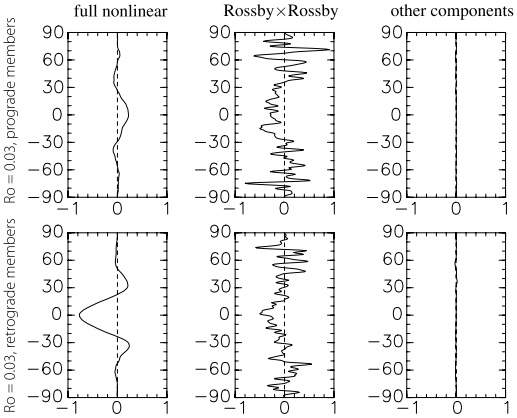

Fig. 5 Acceleration of zonal mean zonal angular momentum between $t = 5$ and $t = 15$. The vertical axis indicates latitudes ϕ(deg.), and the horizontal axis indicates $\Delta\bar{u}\cos(\phi)$. (top) for 50 prograde ensemble members in Ro= 0.03, and (bottom) for 50 retrograde ensemble members in Ro= 0.03 are used. (left) The acceleration obtained in the full nonlinear model. (middle) The second order acceleration induced by the Rossby modes (including westward Rossby-gravity modes) only. (right) The second order acceleration induced by the other components. (adopted from [7]).

4 Summary and Discussion

In this short article, we briefly reviewed two of our recent papers conducting parameter-sweep and large-ensemble experiments for decaying shallow water turbulence on a rotating sphere. One of main results in the parameter sweep experiments is that whether the radius of deformation L_D is larger than the Rhines scale $1/k_\beta$

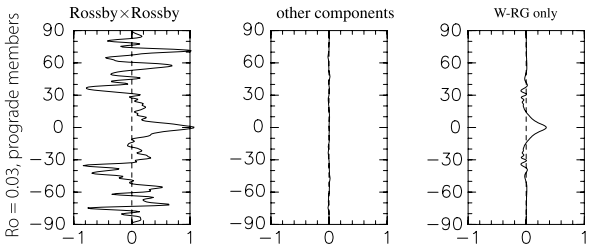

Fig. 6 Second order acceleration of zonal mean zonal angular momentum between $t = 5$ and $t = 15$ with a weak prograde jet as a basic state. 50 prograde ensemble members are used for the ensemble mean. (left) The acceleration induced by the Rossby modes (including westward Rossby-gravity modes) only. (middle) The acceleration induced by the other components. (right) The acceleration induced by westward propagating Rossby-gravity modes. (adopted from [7]).

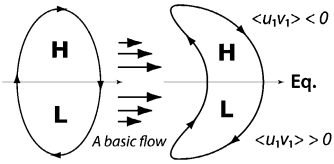

Fig. 7 Schematic illustration of the jet intensification mechanism by a Rossby-gravity wave. (adopted from [7]).

is important for the jet formation. Recently, Sayanagi et al. [11] showed that this is also true in 3D β-plane turbulence. For the equatorial jet formation, the large-ensemble nonlinear and linear experiments showed that it can be understood by the acceleration mainly due to weakly-nonlinear wave dynamics. One significant result in the ensemble experiments is that a prograde equatorial jet is obtained with a fixed possibility when Ro is not very small.

The formation of a prograde equatorial jet from a turbulent flow is a hot topic relating to the outer giant planets, Jupiter and Saturn. Recently, Scott and Polvani [13] showed that a robust prograde equatorial jet emerges from a forced-dissipative shallow water turbulence on a rotating sphere with an imitated Newtonian cooling effect. The obtained prograde jet is so robust independent of experimental parameters that there must exist some other formation mechanisms than the weak nonlinear acceleration mechanism proposed by Kitamura and Ishioka [7]. Farrel and Ioannou [2] applied Stochastic Structural Stability Theory (SSST) to shallow water forced-dissipative turbulence on a β-plane to obtain both prograde and retrograde equatorial jets when the forcing is weak though the system is a little different from that concerned in this article. For strong forcing, however, a retrograde equatorial jet loses stability, which leads to the dominance of a prograde equatorial jet. Although the latter case seems due to the barotropic instability of the retrograde zonal jet, the former case where an equatorial jet of both direction is possible seems related to the positive-feedback acceleration mechanism proposed by [7]. However, as described in Hayashi et al. [4], further investigations seem to be still needed to understand forced-dissipative and decaying shallow water turbulence on a rotating sphere comprehensively.

References

[1] Cho, J. Y-K., Polvani, L. M.: The emergence of jets and vortices in freely evolving, shallow-water turbulence on a sphere. Phys. Fluids, **8**, 1531–1552 (1996)

[2] Farrell, B. F., Ioannou, P. J.: Emergence of jets from turbulence in the shallow water equations on an equatorial beta-plane. J. Atmos. Sci. *to appear* (2009)

[3] Hayashi, Y.-Y., Ishioka, K., Yamada M., Yoden, S.: Emergence of circumpolar vortex in 2-D turbulence on a rotating sphere. *in IUTAM Symposium on Developments in Geophysical Turbulence (Proceedings of the IUTAM Symposium held at the National Center for Atmospheric Research, Boulder, CO, 16-19 June 1998) (Fluid Mechanics and Its Applications Vol.58), Ed R.M. Kerr and Y. Kimura*, Kluwer Academic Publishers, 179–192 (2000)

[4] Hayashi, Y.-Y., Nishizawa, S., Takehiro, S., Yamada, M., Ishioka, K., Yoden, S.: Rossby waves and jets in two-dimensional decaying turbulence on a rotating sphere. J. Atmos. Sci., **64**, 4246–4269 (2007)

[5] Iacono, R., Struglia, M. V., Ronchi, C., Nicastro, S.: High-resolution simulations of freely decaying shallow-water turbulence on a rotating sphere. Il Nuovo Cimento, **22 C**, 813–821 (1999)

[6] Ishioka, K., Yamada, M., Hayashi, Y.-Y., Yoden, S.: Technical approach for the design of a high-resolution spectral model on a sphere: application to decaying turbulence. Nonlinear Processes in Geophysics, **7**, 105–110 (2000)

[7] Kitamura, Y., Ishioka, K.: Equatorial jets in decaying shallow-water turbulence on a rotating sphere. J. Atmos. Sci., **64**, 3340–3353 (2007)

[8] Nozawa, T., Yoden, S.: Formation of zonal band structure in forced two-dimensional turbulence on a rotating sphere. Phys. Fluids, **9**, 2081–2093 (1997)

[9] Nozawa, T., Yoden, S.: Spectral anisotropy in forced two-dimensional turbulence on a rotating sphere. Phys. Fluids, **9**, 3834–3842 (1997)

[10] Okuno, A., Masuda, A.: Effect of horizontal divergence on the geostrophic turbulence on a beta-plane: suppression of the Rhines effect. Phys. Fluids, **15**, 56–65 (2003)

[11] Sayanagi, K. M., Showman, A. P., Dowling, T. E.: The emergence of multiple robust zonal jets from freely evolving, three-dimensional stratified geostrophic turbulence with applications to Jupiter. J. Atmos. Sci., **65**, 3947–3962 (2008)

[12] Scott, R. K., Polvani, L. M.: Forced-dissipative shallow water turbulence on the sphere: equatorial confinement of zonal jets. J. Atmos. Sci., **64**, 3158–3176 (2007)

[13] Scott, R. K., Polvani, L. M.: Equatorial superrotation in shallow water atmospheres. Geophys. Res. Lett., **35**, L24202 (2008)

[14] Takehiro, S., Yamada, M., Hayashi, Y.-Y.: Circumpolar jets emerging in two-dimensional non-divergent decaying turbulence on a rapidly rotating sphere. Fluid Dyn. Res., **39**, 209–220 (2007)

[15] Takehiro, S., Yamada, M., Hayashi, Y.-Y.: Energy accumulation into easterly circumpolar jets generated by two-dimensional barotropic decaying turbulence on a rapidly rotating sphere. J. Atmos. Sci., **64**, 4088–4101 (2007)
[16] Theiss, J.: Equatorward energy cascade, critical latitude, and the predominance of cyclonic vortices in geostrophic turbulence. J. Phys. Oceanogr., **34**, 1663–1678 (2004)
[17] Williams, G. P.: Planetary circulations: 1. Barotropic representation of Jovian and terrestrial turbulence. J. Atmos. Sci., **35**, 1399–1426 (1978)
[18] Yoden, S., Yamada, M.: A numerical experiment on two-dimensional decaying turbulence on a rotating sphere. J. Atmos. Sci., **50**, 631–643 (1993)
[19] Yoden, S., Ishioka, K., Hayashi, Y.-Y., Yamada M.: A further experiment on two-dimensional decaying turbulence on a rotating sphere. Il Nuovo Cimento, **22 C**, 803–812 (1999)

Triple cascade behaviour in QG and drift turbulence and generation of zonal jets

Sergey Nazarenko, Brenda Quinn

Abstract We study quasi-geostrophic turbulence and plasma drift turbulence within the Charney-Hasegawa-Mima (CHM) model extending the work reported in [24]. We focus, theoretically and using numerical simulations, on conservation of *zonostrophy* and on its role in the formation of the zonal jets. The zonostrophy invariant was first predicted in [6; 5] in two special cases – large-scale turbulence and anisotropic turbulence. Papers [6; 5] also predicted that the three invariants, energy, enstrophy and zonostrophy, will cascade anisotropically into non-intersecting sectors in the k-space, so that the energy cascade is "pushed" into the large-scale zonal scales. In the present paper, we consider the scales much less than the Rossby deformation radius and generalise the Fjørtoft argument of [6; 5] to find the directions of the three cascades in this case. For the first time, we demonstrate numerically that zonostrophy is well conserved by the CHM model, and that the energy, enstrophy and zonostrophy cascade as prescribed by the Fjørtoft argument if the nonlinearity is sufficiently weak. Moreover, numerically we observe that zonostrophy is conserved surprisingly well at late times and the triple-cascade picture is rather accurate even if the initial nonlinearity is strong.

1 Introduction and the model

Zonal jets are prominent features in geophysical fluids, e.g. atmospheres of Jupiter and Saturn [29; 28; 11] and the earths' atmosphere [20; 13] and oceans [13; 11; 23]. Zonal jets have also been observed in fusion plasmas [9]. Zonal jets are important

Sergey Nazarenko
Mathematics Institute, University of Warwick, Gibbet Hill Road, Coventry CV4 7AL, UK, e-mail: S.V.Nazarenko@warwick.ac.uk

Brenda Quinn
Mathematics Institute, University of Warwick, Gibbet Hill Road, Coventry CV4 7AL, UK, e-mail: B.E.Quinn@warwick.ac.uk

D. Dritschel (ed.), *IUTAM Symposium on Turbulence in the Atmosphere and Oceans*, IUTAM Bookseries 28, DOI 10.1007/978-94-007-0360-5_22,

because they can suppress the small-scale turbulence and block the transport in both geophysical settings [17] and in plasmas [4; 33; 9].

Two main zonal jet generation mechanisms considered in the literature are the modulational instability [21; 12; 18; 22; 30; 25; 31; 8] and the anisotropic inverse cascade [34; 26; 27; 4]. The inverse cascade mechanism brings the energy from initial small-scale turbulence to the large-scale zonal flows in a step-by-step (local in the scale space) transfer mechanism similar to the inverse cascade in 2D Navier-Stokes turbulence [10; 19]. On the other hand, the modulational instability brings energy to the large zonal scales directly, skipping the intermediate scales. It appears to be more relevant if the small-scale turbulence has a narrow initial spectrum, whereas the cascade picture is more accurate when the initial spectrum is broad. We will report on our recent analytical and numerical studies of the modulational instability elsewhere [8], whereas the present paper will focus on the turbulent cascades.

The mechanism for an inverse cascade in geophysical quasi-geostrophic (QG) turbulence and in plasma drift turbulence is quite similar to the one of the 2D Navier-Stokes turbulence [10; 19], but the presence of the beta-effect (non-uniform rotation of geophysical fluids or plasma inhomogeneity) makes this cascade anisotropic leading to condensation into large-scale zonal flows rather than round vortices [34; 26; 27].

In this paper we will follow the approach put forward in papers [6; 5] which is most relevant (and asymptotically rigorous) when the QG/drift turbulence is weak. In this case the turbulence is dominated by waves which are involved in triad interactions. These three-wave interactions are shown to conserve an additional positive quadratic invariant. This invariant and the other two quadratic invariants, the energy and the potential enstrophy, are involved in a triple cascade process, which can be described via an argument similar to the standard Fjørtoft argument originally developed for the 2D Navier-Stokes turbulence [10]. It was found that each of the invariants is forced by the other two to cascade into its own anisotropic sector of scales and, in particular, the energy is forced to cascade to long zonal scales. Considering its important role in the zonation process, hereafter we will label the extra invariant as *zonostrophy*.

On the other hand, work [6; 5] was limited to considering either very large scales (longer than the Rossby deformation radius or the Larmor radius) or to the scales which are already anisotropic and are close to zonal. Besides, the conservation of the extra invariant is based on the weakness of nonlinearity and on the randomness of phases (conditions of validity of the wave kinetic equation), which, even when present initially, can break down later on during the zonation process. Thus, numerical checks of robustness of the zonostrophy conservation were needed, and they have not been done until the work reported in the present paper.

Soon after papers [6; 5], the zonostrophy invariant was generalized to the whole of the k-space in [1]. This was a significant achievement because the extra invariant of such a kind appeared to be unique for Rossby/drift systems and is not observed in any other known nonlinear wave model [2]. Besides, its conservation has revealed interesting geometrical properties of the wave dispersion relation [2]. Unfortunately, the general expression for zonostrophy appeared to have a form for

which the Fjørtoft argument cannot be used (not scale invariant, not sign-definite). However, an alternative zonation argument was put forward in [3].

In the present paper we will focus on the special case when the scales are much smaller than the deformation (Larmor) radius, which is the most important and frequently considered limit (at least in the GFD context). Taking the respective limit in the general zonostrophy expression obtained in [1], we obtain the zonostrophy expression for such small-scale turbulence and show that it is positive and scale invariant. The latter observation is extremely important because it means that we can once again apply the generalized Fjørtoft argument developed in [6; 5], which is done in the present paper. Note that the Fjørtoft argument of [6; 5] is somewhat preferential over the argument presented in [3] because it predicts not only zonation but also the anisotropic k-space flow paths of the three invariants during the zonation process.

Having obtained these analytical predictions, we then proceed to direct numerical simulations (DNS) of the QG/drift turbulence to (i) test the conservation of the zonostrophy for different levels of initial nonlinearity, and (ii) test predictions of the generalized Fjørtoft argument by tracking in time the transfer path of the three invariants in the k-space. As a result, we confirm conservation of zonostrophy and its important role in directing the energy to the zonal jet scales.

2 Charney-Hasegawa-Mima model

The reason why geophysical quasi-geostrophic (QG) flows and plasma drift turbulence are often mentioned together (in particular when discussing the zonal jet formation) is that some basic linear and nonlinear properties in these two systems can be described by the same PDE, the Charney-Hasegawa-Mima (CHM) equation [7; 15]:

$$\partial_t \Delta \psi + \beta \partial_x \psi + (\partial_x \psi)\partial_y \Delta \psi - (\partial_y \psi)\partial_x \Delta \psi = 0, \tag{1}$$

where ψ is the streamfunction, β is a constant proportional to the gradient of the horizontal rotation frequency or of the plasma density in the GFD and plasma contexts respectively. In the GFD context, the x-axis is in the west-east and the y-axis is along the south-north directions respectively. In plasmas, the y-axis is along the plasma density gradient and the x-axis, of course, is transverse to this direction. Here, we consider only small-scale turbulence with scales much smaller than the Rossby deformation radius in GFD and the ion Larmor radius in plasma contexts (this has already been taken into account in the CHM model, (1)).

Let us put our system in a periodic square box with side length L and introduce the Fourier transform of the streamfunction,

$$\psi_{\mathbf{k}} = \frac{1}{L^2} \int \psi(\mathbf{x}) e^{-i\mathbf{k}\cdot\mathbf{x}} d\mathbf{x},$$

where $\mathbf{k} = (k_x, k_y)$ is a wavevector in the 2D plane. In k-space the CHM equation (1) becomes:

$$\partial_t \hat{\psi}_{\mathbf{k}} = i\,\omega_{\mathbf{k}}\,\hat{\psi}_{\mathbf{k}} + \frac{1}{2}\sum_{\mathbf{k}_1+\mathbf{k}_2=\mathbf{k}} T(\mathbf{k},\mathbf{k}_1,\mathbf{k}_2)\,\hat{\psi}_{\mathbf{k}_1}\,\hat{\psi}_{\mathbf{k}_2}\,, \tag{2}$$

where

$$\omega_{\mathbf{k}} = -\frac{\beta k_x}{k^2} \tag{3}$$

is the dispersion relation for the frequency of linear waves (Rossby or drift waves in the GFD and plasma contexts respectively), $k = |\mathbf{k}|$, and

$$T(\mathbf{k},\mathbf{k}_1,\mathbf{k}_2) = -\frac{(\mathbf{k}_1\times\mathbf{k}_2)_z\,(k_1^2-k_2^2)}{k^2} \tag{4}$$

is a nonlinear interaction coefficient.

3 Conservation of energy and enstrophy

It is well known that the CHM equation, (1) conserves the energy and the enstrophy which in physical space are defined respectively as

$$E = \frac{1}{2}\int (\nabla\psi)^2\,d\mathbf{x} \tag{5}$$

and

$$\Omega = \frac{1}{2}\int (\triangle\psi)^2\,d\mathbf{x}. \tag{6}$$

In Fourier space these conserved quantities can be expressed in terms of the wave action

$$n(\mathbf{k}) = \frac{k^4|\hat{\psi}_k|^2}{2\beta k_x}.$$

We have

$$E = \int |\omega_{\mathbf{k}}| n_{\mathbf{k}}\,d\mathbf{k} \tag{7}$$

and

$$\Omega = \int k_x n_{\mathbf{k}}\,d\mathbf{k}. \tag{8}$$

4 Conservation of zonostrophy

The energy and the enstrophy are *exact* invariants of the small-scale CHM model (1). *Zonostrophy* is an exact invariant of the *kinetic equation*:

$$\dot{n}_{\mathbf{k}} = \int |V_{12k}|^2 \, \delta(\mathbf{k}_1 + \mathbf{k}_2 - \mathbf{k}) \delta(\omega(\mathbf{k}_1) + \omega(\mathbf{k}_2) - \omega(\mathbf{k})) \times \\ [n(\mathbf{k}_1) n(\mathbf{k}_2) - 2n(\mathbf{k}) n(\mathbf{k}_1) \, \mathrm{sign} - n(\mathbf{k}) n(\mathbf{k}_2) \, \mathrm{sign}\,(k_x k_{2x})] \; d\mathbf{k}_1 d\mathbf{k}_2, \tag{9}$$

where

$$V_{12k} = |k_x k_{1x} k_{2x}|^{1/2} \left(\frac{k_{1y}}{k_1^2} + \frac{k_{2y}}{k_2^2} - \frac{k_y}{k^2} \right).$$

Thus, it should be clear that the zonostrophy is only proven to be a conserved quantity under the same conditions for which the kinetic equation (9) is valid, namely *weak nonlinearity* and *random phases*. It is presently unknown if the zonostrophy conservation extends to a broader range of situations or not. Thus, the numerical tests of zonostrophy conservation are crucial, and this is one of the aims of the present work.

In terms of the wave action spectrum, zonostrophy Z can be written as

$$Z = \int \zeta_{\mathbf{k}} n_{\mathbf{k}} \, d\mathbf{k}, \tag{10}$$

where function $\zeta_{\mathbf{k}}$ is the density of zonostrophy in the k-space which satisfies the triad resonance condition

$$\zeta(\mathbf{k}) = \zeta(\mathbf{k}_1) + \zeta(\mathbf{k}_2) \tag{11}$$

for all wavevectors $\mathbf{k}, \mathbf{k}_1$ and $\mathbf{k}_2$ which lie on the resonant surface given by the solutions of the wavevector and frequency resonance conditions,

$$\mathbf{k} = \mathbf{k}_1 + \mathbf{k}_2 \tag{12}$$

and

$$\omega(\mathbf{k}) = \omega(\mathbf{k}_1) + \omega(\mathbf{k}_2). \tag{13}$$

Expressions for $\zeta_{\mathbf{k}}$ were first found in [6; 5] in the special cases of large-scale turbulence ($\rho k \ll 1$ where ρ is the Rossby deformation radius in GFD or ion Larmor radius in plasmas) and for anisotropic turbulence ($k_x \ll k_y$), after which a general expression was found for all $\mathbf{k}$'s in [1]. This expression is

$$\zeta(\mathbf{k}) = \arctan \frac{k_y + k_x \sqrt{3}}{\rho k^2} - \arctan \frac{k_y - k_x \sqrt{3}}{\rho k^2}. \tag{14}$$

This expression can change sign and it is not a scale-invariant function of the wavevector components, which means that one cannot use the generalized Fjørtoft argument of [6; 5] to find the cascade directions in such a general case.

To find zonostrophy in the special case of small-scale turbulence (which is considered in the present paper) we have to take the limit $\rho k \to \infty$ in the general expression (14). It turns out that naively taking limit leads to an already known integral, the energy and one has to go to further orders in the Taylor expansion of (14) until we reach an expression which is independent of E and Ω. Interestingly, such an independent invariant appears only in the fifth order, and the derivation details are

given in Appendix A. The result is

$$\tilde{\zeta} = -\lim_{\rho\to\infty} \frac{5\rho^5}{8\sqrt{3}}(\zeta - 2\sqrt{3}\omega/\beta\rho) = \frac{{k_x}^3}{k^{10}}({k_x}^2 + 5{k_y}^2). \tag{15}$$

The integral (10) with the density (15) is an exact invariant of the kinetic equation (9) and thus it is an *approximate* invariant of the small-scale CHM equation (1). Later on we will examine numerically the precision with which this invariant is conserved.

Expression (15) for the new invariant in the small-scale limit, $\rho k \gg 1$, allows us to explicitly see that the invariant's density is strictly positive and scale-invariant, which is good news because once again one can use the generalized Fjørtoft argument of [6; 5] to find the cascade directions of the three invariants: the energy, the enstrophy and the zonostrophy.

5 Triple cascade behaviour

5.1 Dual cascades in 2D Navier-Stokes turbulence

Before we present the generalized Fjørtoft argument, we will remind the reader of the classical Fjørtoft argument leading to the prediction of the dual cascade behaviour in 2D Navier-Stokes turbulence [10]. This will be instructive because by now there exists several versions of such an argument and the one we use here is not necessarily the most familiar.

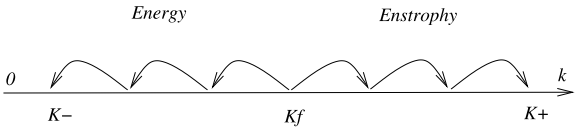

Fig. 1 Dual cascade behaviour in 2D Navier-Stokes turbulence.

Let us consider 2D turbulence described by the Navier-Stokes equations excited at some forcing scale $\sim k_0$ and dissipated at very large ($\sim k_- \ll k_0$) and at very small scales ($\sim k_+ \gg k_0$), see Fig. 1. The conservative ranges between the forcing scale and the dissipation scales, $k_- \ll k \ll k_0$ and $k_0 \ll k \ll k_+$ are called the inertial ranges. The two conserved quantities in this case, in the absence of forcing and dissipation, are the energy and the enstrophy which are given by the same expressions as for the small-scale CHM model, namely by (5) and (6) in the x-space and by (7) and (8) in the k-space. In the presence of forcing and dissipation in steady-state turbulence, the rate of production of the energy and the enstrophy by forcing must

be exactly the same as the dissipation rates, ε and η respectively. Our task now is to determined where exactly E and Ω are dissipated, at $\sim k_-$ or at $\sim k_+$.

First, we note that the k-space densities of E and Ω differ by a factor of k^2, and therefore the energy dissipation rate ε is related to the enstrophy dissipation rate η as $\eta \sim {k_0}^2\varepsilon$. Now, let us suppose *ad absurdum* that at $\sim k_+$ the energy is dissipated at a rate comparable to the rate of production at the forcing scales, i.e. $\sim \varepsilon$. But this would mean that the enstrophy would be dissipated at the rate $\sim k_+^2\varepsilon$ which is impossible in steady state since this amount greatly exceeds the rate of the enstrophy production $\eta \sim\sim {k_0}^2\varepsilon$. Thus we conclude that most of the energy must be dissipated at the scales $\sim k_-$, i.e. that the energy cascade is *inverse* (with respect to its direction in 3D turbulence).

Similarly, assuming *ad absurdum* that most of the enstrophy is dissipated at $\sim k_-$ would also lead to a conclusion that the amount of energy dissipated is much greater than the energy produced, which is impossible. Therefore, the enstrophy cascade is direct, i.e. it is dissipated at wavenumbers $\sim k_+$ which are greater than the forcing scale k_0.

5.2 Triple cascades in CHM turbulence

From the Fjørtoft argument presented above, the reader should notice that the quantities that determine the cascade directions are the k-space densities of the invariants or, more precisely, the scaling of the ratios of these densities with k. It is also important that these k-space densities are positive (as is the case for E, Ω and Z in our situation, see (7), (8) and (15)) because otherwise a large positive and a large negative amount of the same invariant could be produced in different corners of the k-space, with the net result zero and the Fjørtoft argument would not work. Further, it is important that all of the invariants have the same scaling with respect to the turbulence intensity so that their ratios are functions of $\mathbf{k}$ and not of the turbulent intensity. This condition is satisfied, for both Navier-Stokes and in the CHM model since E, Ω and Z are linear in n_k, see (7), (8) and (15).

The ratio of the k-space densities of Ω and E is k^2 which allows us to conclude that Ω must go to $k \gg k_0$ and E must cascade to $k \ll k_0$. In other words, each of the invariants cascades to the scales where its density is dominant over the density of the other invariant. This argument is easily generalizable to the CHM model and the respective three invariants, E, Ω and Z. Now we have three invariants, and the cascade picture would necessarily be anisotropic (it is impossible to divide the 2D $\mathbf{k}$-space into three non-intersecting cascade regions in an isotropic way).

Let us suppose that turbulence is produced near $\mathbf{k}_0 = (k_{0x}, k_{0y})$ and it can be dissipated only in regions which are separated in scales from the forcing scale, i.e. either at $k \gg k_0$ (short scales), or at $k_x \ll k_{0x}$ (nearly zonal scales), or at $k_y \ll k_{0y}$ (nearly meridional scales), see Fig. (2). Then each of the invariants (e.g. E), must cascade to the scales where its density is dominant over the densities of the other two invariants (e.g. Ω and Z). The boundaries between the cascading ranges lie on

the curves in the k-space where the ratios of the different invariant densities (taken pairwise) remain constant (equal to the respective initial values).

We note that because $k^2 \le {k_x}^2 + 5{k_y}^2 \le 5k^2$, and because because the Fjørtoft argument operates only with the strong inequalities ($\gg$ and $\ll$ rather than $>$ and $>$), we can replace the zonostrophy density (15) with a simpler expression,

$$\tilde{\zeta}_{\mathbf{k}} \sim \frac{{k_x}^3}{k^8}. \tag{16}$$

Thus we have for the boundaries between the different cascade sectors, see Fig. (2):

- E/Ω *boundary:* As for the 2D Navier-Stokes turbulence considered before, we have for this boundary separating the energy and the enstrophy cascades,

$$k^2 \sim k_0^2, \tag{17}$$

  (i.e. a circle in the 2D k-space, $k_x^2 + k_y^2 = k_0^2$.)
- E/Z *boundary:* Equating the ratio of the energy density $|\omega_k|$ to the zonostrophy density ${k_x}^3/k^8$ to the initial value of this ratio, we get for the boundary separating the energy and the zonostrophy cascades,

$$k^3/k_x \sim k_0^3/k_{0x}. \tag{18}$$

- Ω/Z *boundary:* Equating the ratio of the enstrophy density k_x to the zonostrophy density ${k_x}^3/k^8$ to the initial value of this ratio, we get for the boundary separating the enstrophy and the zonostrophy cascades,

$$k^4/k_x \sim k_0^4/k_{0x}. \tag{19}$$

The first of these expressions, (17), says that (like in 2D turbulence before) the energy must go to larger scales and the enstrophy must go to smaller scales.

The second expression, (18), says that the energy must go to the zonal scales, $k_y \gg k_x$. Moreover, this expression also poses a particular restriction on the path of the energy to the zonal scales, e.g. for $k_y \gg k_x$ it should zonate at least as fast as $k_y = \text{const}\, k_x^{1/3}$, see Fig. (2).

The last relation, (19), is also interesting. Because $k \ge k_x$, the curve (18) intersects the k_x-axis at a finite distance,

$$k_x^* \sim k_0^{4/3}/k_{0x}^{1/3}. \tag{20}$$

We see that the zonostrophy cannot cascade too far to large k's, unless one starts with nearly zonal scales, $k_{0y} \gg k_{0x}$. In particular, if $k_{0y} = k_{0x}$ we have $k_x^* = 2^{1/6} k_0$, i.e. the maximal allowed wavenumber for the zonostrohy cascade is practically the same as the initial scale. In other words, in this case the zonostrophy can only cascade to the larger scales.

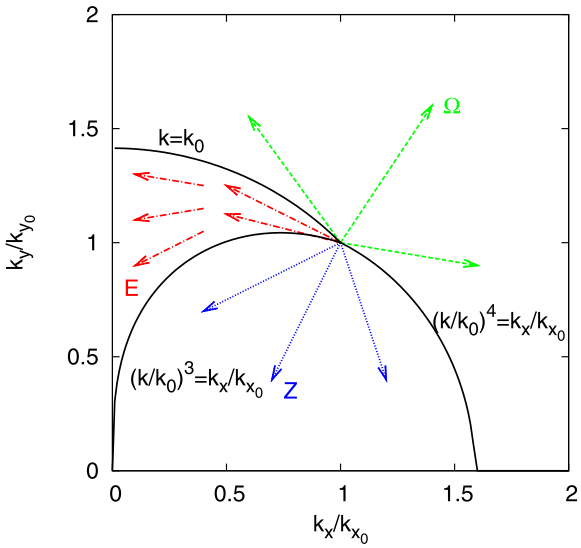

Fig. 2 Non-intersecting sectors for triple cascade as predicted by the generalized Fjørtoft argument.

5.3 Alternative argument for zonation

The generalized Fjørtoft argument presented above was based on the zonostrophy conservation which was proven for the wave kinetic equation and therefore, it is expected to work well for the weakly nonlinear case. However, later we are going to present numerics in which we "push" the formal boundaries of validity and test the performance of the triple cascade picture in the case when the initial nonlinearity is strong.

Because we are going to consider cases with strong nonlinearity, we would like to mention an alternative argument for zonation which makes sense when the initial turbulence is strong. Suppose that turbulence is forced strongly at large k's, so strongly that the linear term is negligible compared to the nonlinear one in the CHM equation (1). Since the linear term is the only source of anisotropy in the CHM model, the system is expected to build an isotropic inverse energy cascade identical to one of the 2D Navier-Stokes turbulence. As the inverse cascade progresses toward the larger scales, the linear dynamics (β-effect) become more and more important. A well-known boundary exists which defines the crossover from strong to weak turbulence, dominated by weakly nonlinear waves. This boundary is defined by the transitional wavenumber where the characteristic times of the linear and the nonlinear dynamics become equal. As it follows from the above speculation about the inverse cascade, the scaling for the nonlinear time has to be taken from a Kolmogorov-type estimate, $\tau_{NL} \sim (\varepsilon k^2)^{-1/3}$ and the linear time is just the inverse

wave frequency, $\tau_L = k^2/(\beta k_x)$. Equating τ_{NL} and τ_L we get

$$k^8 = k_\beta^5 k_x^3, \tag{21}$$

where $k_\beta = (\beta^3/\varepsilon)^{1/5}$. This curve is plotted in Fig. (3) and it is the well-known 'dumb-bell' or 'lazy 8' curve [16; 32]. For the modes which lie outside the curve, isotropic turbulence is the dominant process, whereas for those modes inside the dumb-bell, anisotropic Rossby wave turbulence is the dominant process.

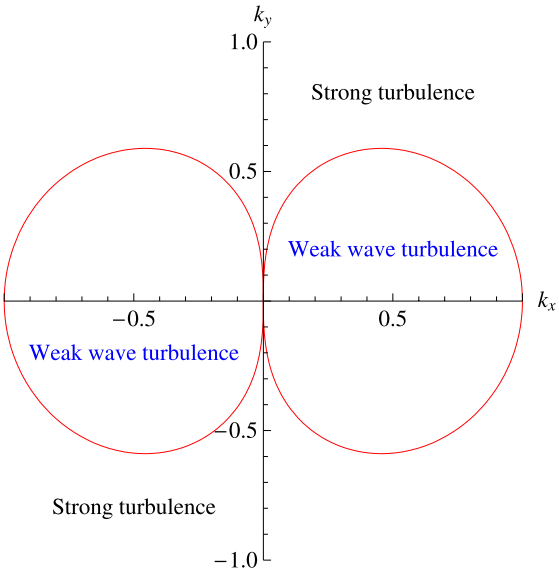

Fig. 3 Dumb-bell curve in the Fourier space defining crossover from strong to weak turbulence.

The alternative zonation argument is based on the observation that weak wave turbulence is much less efficient in supporting the energy cascade than the strongly nonlinear interactions. Thus one can suppose that the energy cascade does not penetrate inside of the dumb-bell curve, but rather, it turns and continues along this curve to the larger scales. This condition that the linear and the nonlinear times are balanced *scale-by-scale* could be called a "critical balance", in analogy with similar arguments about the critical balance state discussed in MHD turbulence [14].

The critical balance picture would mean that the energy cascade path of zonation would be given by expression (21), which incidentally is very close to the path predicted by the Fjørtoft argument (18), if $k_0 \sim k_\beta$ (the power $3/8$ indeed very close to $1/3$).

A closer look reveals that the alternative zonation argument is actually not so "alternative" as it does not contradict our generalized Fjørtoft argument based on the zonostrophy concentration. Indeed, if the energy followed a path through the scales at which the linear and the nonlinear timescales balance then the zonostrophy

would flow below this path, i.e. to the weakly nonlinear scales. Thus, the zonostrophy would be supported at the weakly nonlinear scales and therefore would be conserved (even though both the energy and the enstrophy would be supported in the intermediately and strongly nonlinear scales in this case). But then all the three invariants are conserved (no need for weak nonlinearity for conservation of E and Ω) and the generalized Fjørtoft argument is once again valid.

One should also keep in mind that for the dumb-bell curve the estimation of the shape is only approximate because it is based on the expression for τ_{NL} which is valid, strictly speaking, only at k's which are much greater than the dumb-bell (i.e. in the region of the isotropic inverse cascade). With this observation, we can put together the "kinematic" view of the Fjørtoft argument and the "dynamic" critical balance condition, and suggest that:

- Invariants E, Ω and Z cascade in the sectors prescribed by the generalized Fjørtoft argument, i.e. (17), (18) and (19).
- The energy cascade follows a path along the scales at which $\tau_{NL} \sim \tau_L$ which lies somewhere in the sector (18) and which does not strictly follow the dumb-bell prescription (21) (because of the unprecise definition of the dumb-bell discussed above).
- This picture is of course preceded by the usual isotropic inverse cascade of E in the case when the initial turbulence is very strong.

We emphasize that in this section we only considered the case when the initial turbulence is strong. If the initial turbulence is weak, i.e. well within the dumb-bell, then the energy cascade path remains in the weakly nonlinear scales (at least for a while) rather than lie on the dumb-bell curve.

Now we will proceed to testing our theoretical predictions about the conservation of the zonostrophy and the triple cascade behavior via numerical simulations of the CHM equation in the Fourier space, Eqn (2).

6 Numerical study

A pseudospectral code has been written to solve equation (2). No dissipation is used and the initial condition is given by

$$\hat{\psi}_{\mathbf{k}}|_{t=0} = Ae^{\left(\frac{|\mathbf{k}-\mathbf{k}_0|^2}{k_*^2} + i\phi_{\mathbf{k}}\right)} + \text{image}, \tag{22}$$

where k_0 and k_* are constants and $\phi_{\mathbf{k}}$ are random independent phases, and by "image" we mean the mirror-reflected spectrum with respect to the k_x axis. Note that only the semi-plane $k_x \geq 0$ was used in our computations because of the symmetry $\hat{\psi}_{-\mathbf{k}} = \hat{\psi}^*_{\mathbf{k}}$ arising from the fact that the streamfunction ψ in the CHM equation (1) is a real function.

We opted to simulate such an evolving non-dissipative system rather than a forced/dissipated steady-state turbulence considered by the Fjørtoft argument be-

cause it appears to be more physically relevant (since there appears to be no physically meaningful dissipation acting selectively on nearly zonal and nearly meridional scales only). Yet, we hope that the cascade picture obtained via the Fjørtoft argument is meaningful for such decaying turbulence too, similar to what appears to be the case e.g. in the 2D Navier-Stokes turbulence.

Of course, when calculating a non-dissipative system one has to be aware of the possible bottleneck accumulation of turbulence near the maximum wavenumber after the turbulent front reaches these scales. Thus we make sure to stop our simulations before this happens.

6.1 Centroids

To quantify the cascades of the energy, enstrophy and zonostrophy in the time-evolving non-dissipative turbulence we introduce the *centroids* ("centres of mass") of the total of each invariant defined respectively as follows,

$$\mathbf{k}_E(t) = \frac{1}{E}\int \mathbf{k}\, k^2 |\hat{\psi}_k|^2 \, d\mathbf{k}, \tag{23}$$

$$\mathbf{k}_\Omega(t) = \frac{1}{\Omega}\int \mathbf{k}\, k^4 |\hat{\psi}_k|^2 \, d\mathbf{k}, \tag{24}$$

$$\mathbf{k}_Z(t) = \frac{1}{Z}\int \mathbf{k}\, \frac{k_x^4}{k^6}(k_x^2 + 5k_y^2) |\hat{\psi}_k|^2 \, d\mathbf{k}. \tag{25}$$

Of course, it is not *apriori* clear if the Fjørtoft argument formulated for the steady-state forced/dissipated turbulence has a predictive power for the trajectories of the centroids in the k-space. In the present paper we "experimentally" verify that this is indeed the case.

For the 2D Navier-Stokes (Euler), it is actually possible to recast the Fjørtoft argument for the non-dissipative evolving turbulence directly in terms of the centroids in a rigorous way, see Appendix B. However, the structure of the CHM is more involved and it is not clear if one can produce a generalized Fjørtoft's argument for the triple cascades in terms of the centroids in a rigorous way. This is certainly an interesting question to be addressed in future.[1]

[1] We have been able to find some of the relevant inequalities in terms of the centroids, but most of the conditions restricting the triple cascade sectors are still missing.

6.2 Settings for the weakly nonlinear and the strongly nonlinear runs

We have chosen two sets of parameters to be used in two runs corresponding to weak and strong initial nonlinearities respectively.

The weakly nonlinear and the strongly nonlinear runs were performed at resolutions 512^2 and 1024^2 respectively. This is because the weakly nonlinear systems evolve much slower that the strongly nonlinear ones and one has to compute them for much longer. Correspondingly, the centre of the initial spectrum and its width were chosen to be $\mathbf{k_0} = (20, 20)$ and $k_* = 8$ in the weakly nonlinear run and $\mathbf{k_0} = (40, 40)$ and $k_* = 16$ in the strongly nonlinear run.

The initial amplitudes in the weakly nonlinear and the strongly nonlinear runs are $A = 10^{-6}$ and $A = 5 \times 10^{-7}$ respectively. Determining the relevant degree of nonlinearity σ that corresponds to these initial conditions is tricky. One can directly estimate the linear and the nonlinear terms in the Eqn (2) and take into account the fact that there will be statistical cancellations in the sum of the nonlinear term due to the random phases, i.e. schematically

$$\left| \sum_{j=1}^{N} \text{individual-term}_j \right| \sim \sqrt{N} \ |\text{individual-term}| \, .$$

This way we get an estimate

$$\sigma \sim \frac{2\sqrt{2\pi} k_0^3 k_* A}{\beta}, \tag{26}$$

which gives $\sigma \sim 0.09$ for the weakly nonlinear run and $\sigma \sim 0.7$ for the strongly nonlinear run. However, it is likely that in the strongly nonlinear case the phases will quickly become correlated to a certain degree. Evaluating the nonlinear term in the extreme case when the phases are totally coherent would give an extra factor of $\sqrt{N} \sim 2\sqrt{\pi k_*^2} \sim 100$, so we would have for the strongly nonlinear run $\sigma \sim 70$, which obviously is an overestimate. From common sense, in a non-rigorous way, we believe that the true relevant value for σ in this case is closer to the random-phase estimate, but perhaps slightly higher, e.g. $\sigma \sim 1 - 2$, which is approximately "on the dumb-bell".

6.3 Weakly nonlinear case

For this case, the degree of nonlinearity is weak, $\sigma \sim 0.09$, so that the initial turbulence is well within the dumb-bell. Fig. (4) shows the conservation of each invariant. Because of the slow weakly nonlinear evolution, any quantity proportional to the turbulent intensity could look "conserved", so to demonstrate the true conservation of the zonostrophy we plot its time evolution along with a non-conserved

quantity, $\int \psi^2 \, d\mathbf{x}$. It is clear that all three invariants, E, Ω and Z are well conserved. Namely, the energy is conserved within 0.01%, the enstrophy - within 0.15% and the zonostrophy is conserved within 1 %. Note that this is a first numerical demonstration of the conservation of the zonostrophy invariant. We remind the reader that Z is precisely conserved by the wave kinetic equation (9) and therefore its conservation by the dynamical CHM equation (2) is subject to the applicability conditions of this kinetic equation, namely the weak nonlinearity and the random phases. It is not *apriori* clear how well these conditions are satisfied throughout the k-space (particularly near the zonal scales).

The cascade directions for E, Ω and Z are plotted in Fig. (5) in terms of the paths followed by the respective centroids, (23), (24) and (25). Note that for convenience we normalize the centroids to their initial values, $k^c_{E0}, k^c_{\Omega 0}$ and k^c_{Z0} (which are different from k_0) so that the centroid paths start from the same point in Fig. (5).

In Fig. (5) we see that each invariant cascades well into its predicted sector. Interestingly, the enstrophy and the zonostrophy paths are well inside their respective cascade sectors, whereas the energy follows the boundary of its sector with the zonostrophy sector. One should remember, however, that the boundaries between the sectors are not sharp because the Fjørtoft argument operates with strong inequalities ($\ll$ and $\gg$ rather than $<$ and $>$).

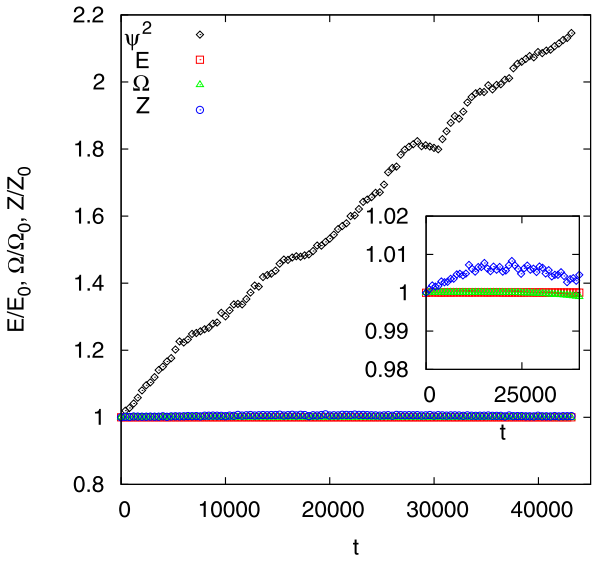

Fig. 4 Conservation of energy, enstrophy and zonostrophy for the weakly nonlinear case. Non-conserved quantity Ψ^2 also shown.

Three successive frames of the energy spectrum in the 2D k-space along with the x-space frames of vorticity distributions at the same moments of time for the weak nonlinearity case are shown in Fig. (8). The initial spectrum, which represents a

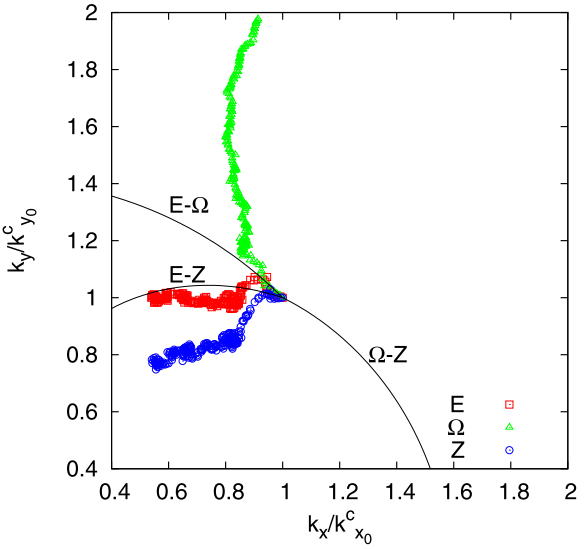

Fig. 5 The cascades of energy, enstrophy and zonostrophy for the weakly nonlinear case, tracked by their centroids.

gaussian spot centered at $\mathbf{k_0}$ and its mirror image, is seen to grow "arms" toward the coordinate origin, so that a closed "ring" forms and then starts shrinking in size. The ring is suggestive of the dumb-bell shape (when complemented with the other half of the distribution at $k_x < 0$), although the similarity is only visual rather than quantitative, because the nonlinearity is quite small. Presumably, the growing of arms and the ring shrinking are indicative of the structure of the anisotropic inverse energy cascade process. On the respective vorticity x-plots, we see initial dominant short-wave components propagating at $\pm 45^o$ (corresponding to the position of the initial maxima in the spectrum) which in time evolve into a more disordered turbulent state with a predominant zonal orientation.

6.4 Strongly nonlinear case

For this case, $\sigma \sim 1-2$ so that the initial turbulence is near the boundary of the dumb-bell. Fig. (6) shows the conservation of each invariant. While the energy and enstrophy are still well conserved (the energy within 0.2% and the enstrophy - within 1.2%), the zonostrophy is not conserved initially. This is not surprising considering that the zonostrophy is only expected to be conserved if the nonlinearity is weak. What is more interesting, however, is that the zonostrophy growth saturates as time proceeds, so that the zonostrophy is rather well conserved in this case for large times. This suggests, as we argued before, that for large times the scales that support the

zonostrophy invariant are weakly nonlinear, even though the energy scales probably remain moderately nonlinear, and the enstrophy scales are definitely strongly nonlinear.

The cascade paths for E, Ω and Z in terms of the respective centroids are plotted in Fig. (7). Once again we see a picture which is similar to the one already observed for the weakly nonlinear case: the enstrophy and the zonostrophy cascades lie well inside their respective theoretically predicted sectors, and the energy cascade follows the boundary of its sector. It is quite possible that the energy path lies in the "critically balanced" scales where the nonlinear and the linear time scales are of the same order. However the measurement of the nonlinear time scale is quite ambiguous and it is still unclear if the critical balance approach can be formulated in a more precise way in this case. In any case, one can clearly see that even in this strongly nonlinear case the zonostrophy invariant is conserved for large times, and that the triple cascade picture predicted using this invariant provides a reasonable description of the turbulence evolution and explanation of the zonal jet formation.

We have also looked at the energy spectra in the 2D wavenumber space and at the 2D vorticity distributions on the x-plane evolving in time, see Fig. (9). The essential features of the evolution of these distributions appeared to be remarkably similar to the ones of the weakly nonlinear case, with somewhat more evident zonal jets at later times. This can be explained by the fact that the strongly nonlinear systems evolve faster than the weakly nonlinear ones, so that what we see here is a more advanced stage of zonation.

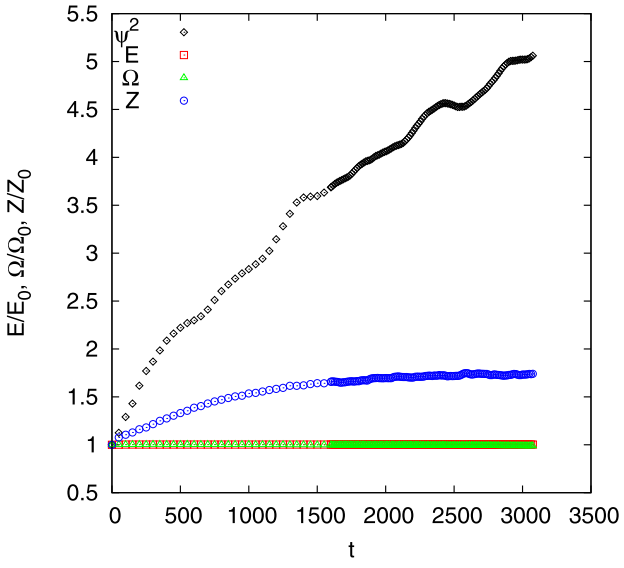

Fig. 6 Conservation of energy, enstrophy and zonostrophy for the strongly nonlinear case. Non-conserved quantity Ψ^2 also shown.

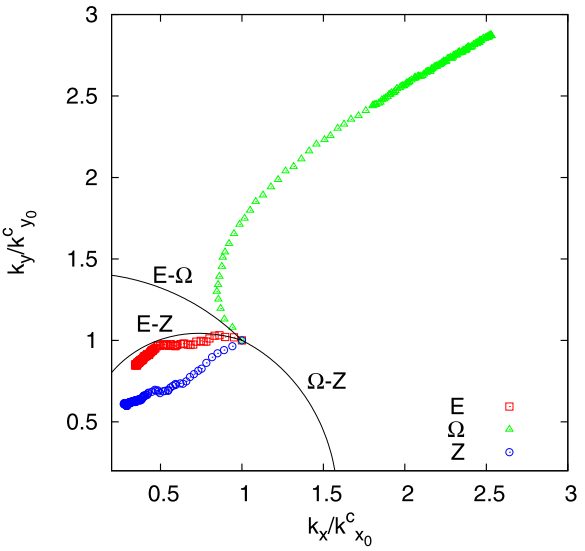

Fig. 7 The cascades of energy, enstrophy and zonostrophy for the strongly nonlinear case, tracked by their centroids.

7 Summary

In the present paper the generalized Fjørtoft argument was used to predict a triple cascade behaviour of the CHM turbulence, in which the energy, the enstrophy and the zonostrophy are cascading into their respective non-intersecting sectors in the scale space. These cascades are anisotropic and the energy cascade is predicted to be directed to the zonal scales, which provides a physical explanation and the character of the formation of the zonal jets in such systems.

The zonostrophy conservation, as well as the triple cascade picture, were tested numerically for the cases of both weak and strong initial nonlinearities. The zonostrophy invariant was shown to be well conserved in the weakly nonlinear case. Moreover, the zonostrophy conservation was also observed for the case with strong initial nonlinearity after a transient non-conservative time interval. Presumably, this is because the zonostrophy moves in time to the scales that are weakly nonlinear (even though the energy and the enstrophy remain in the strongly nonlinear parts of the Fourier space). Using the energy, the enstrophy and the zonostrophy centroids for tracking the transfers of these invariants in the Fourier space, we demonstrated that all the three invariants cascade as prescribed by the triple cascade Fjørtoft argument in both the weakly nonlinear and in the strongly nonlinear cases. The energy appears to be somewhat special among the three invariants in that it tends to cas-

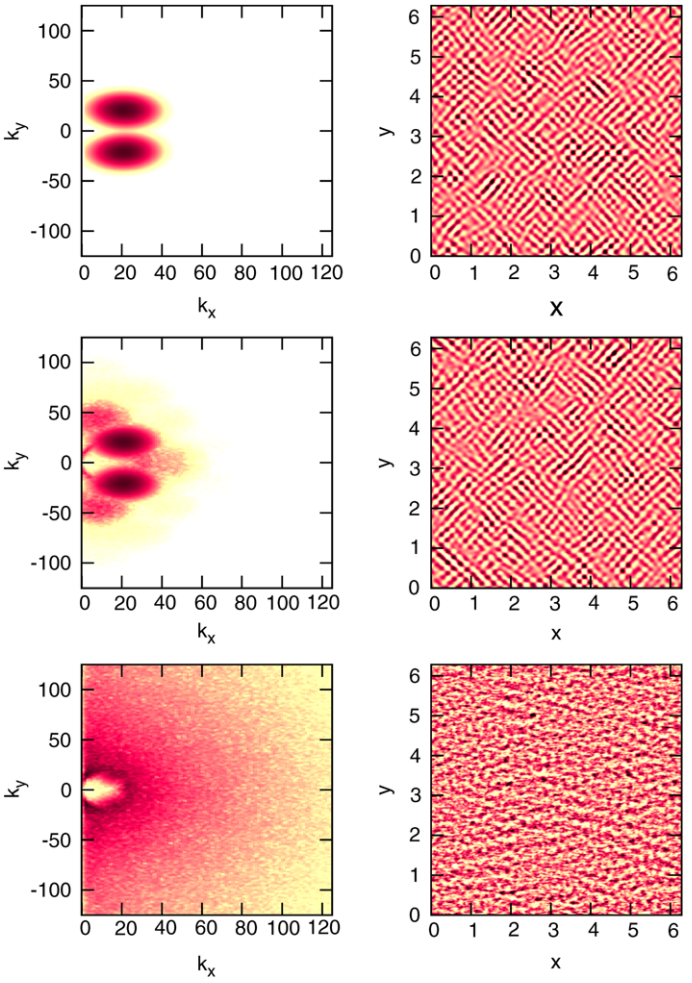

Fig. 8 Contour plots of the $2D$ energy spectrum in k-space (left) and corresponding contours of vorticity in x-space (right) for the weakly nonlinear case.

cade along the edge of the sector allowed by the Fjørtoft argument, namely along the curve $k \propto k_x^{1/3}$.

We believe that further studies would be helpful, both theoretical and numerical, for establishing the conditions under which the zonostrophy is conserved, in particular finding out the extent to which the statistical properties of the system (e.g. random phases) are important in addition to weak nonlinearity of the zonostrophy supporting scales. It would be also interesting to study the behaviour of zonostro-

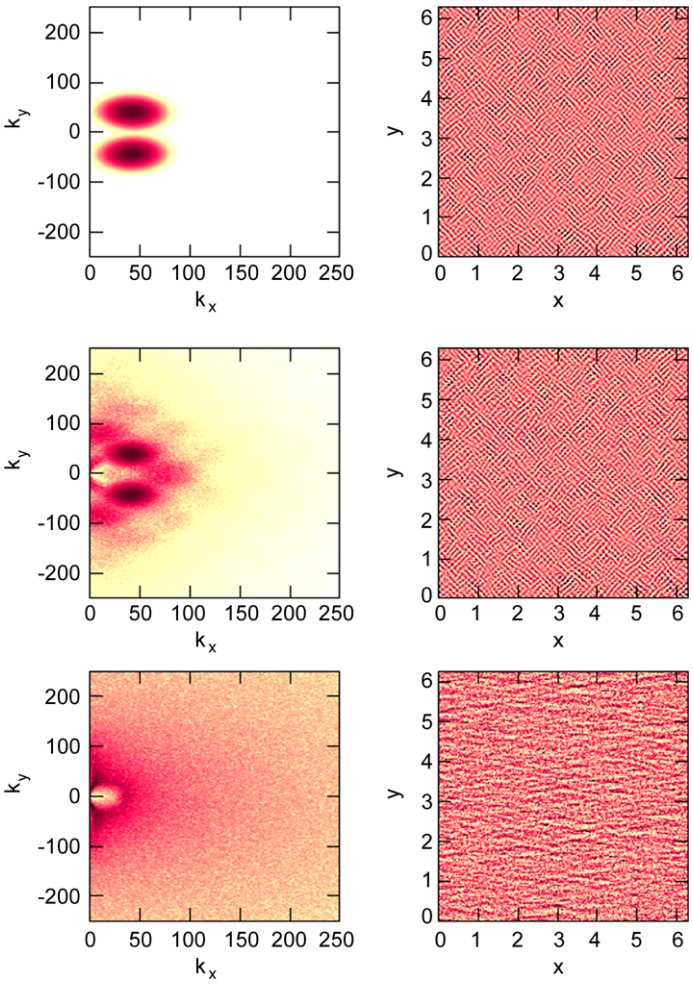

Fig. 9 Contour plots of the 2*D* energy spectrum in *k*-space (left) and corresponding contours of vorticity in *x*-space (right) for the strongly nonlinear case.

phy in the other setups within the CHM model, e.g. the modulational instability and truncated systems of coupled resonant triads.

Acknowledgements We acknowledge stimulating discussions with Alexander Balk, Peter Bartello, David Dritschel, Volker Naulin and Peter Rhines, whose comments and suggestions we greatly appreciate. Our special thanks to Colm Connaughton, who helped developing the numerical code, and to Gregory Eyink, who proposed using Cauchy-Schwartz inequality for proving the inequalities involving the centroids.

Appendix A - Small-scale limit of Zonostrophy

The general expression for the zonostrophy density is given by [1]:

$$\zeta = \arctan\frac{k_y - k_x\sqrt{3}}{\rho k^2} - \arctan\frac{k_y + k_x\sqrt{3}}{\rho k^2} \tag{27}$$

Expanding this expression in the powers of $1/\rho$ up to ninth order, we get

$$\begin{aligned}\zeta = \; & -2\sqrt{3}\frac{k_x}{\rho k^2} + 2\sqrt{3}\frac{k_x}{\rho^3 k^4} \\ & -2\sqrt{3}\frac{k_x}{\rho^5 k^{10}}[k_y^4 + 6k_x^2k_y^2 + \frac{9}{5}k_x^4] \\ & +2\sqrt{3}\frac{k_x}{\rho^7 k^{14}}[\frac{27}{7}k_x^6 + 27k_x^4k_y^2 + 15k_x^2k_y^4 + k_y^6] \\ & -2\sqrt{3}\frac{k_x}{\rho^9 k^{18}}[9k_x^8 + 108k_x^6k_y^2 + 126k_x^4k_y^4 \\ & +28k_x^2k_y^6 + k_y^8] + O(\rho^{-10}).\end{aligned}$$

We note that the Taylor expansion of the frequency $\omega_k = -\beta/(k^2 + \rho^{-2})$ in the powers of $1/\rho$ is

$$\omega_k = \sum_{n=1}^{\infty}\omega^{(n)} = \sum_{n=1}^{\infty}\frac{(-1)^n\beta\rho^2 k_x}{(\rho k)^{2n}}. \tag{28}$$

We see that in the leading order $\zeta = \frac{2\sqrt{3}}{\beta\rho}\omega_k$, i.e. in the small-scale limit ζ is proportional to the energy and not an independent invariant.

Thus, to find the truly independent invariant in the small-scale limit we must subtract this "energy" part. To have a simpler expression which is ρ-independent in the leading order, we will also multiply the result by $-\frac{5\rho^5}{8\sqrt{3}}$. Re-defined this way, the zonostrophy invariant is

$$\begin{aligned}\tilde{\zeta} = & -\frac{5\rho^5}{8\sqrt{3}}(\zeta - 2\sqrt{3}\omega/\beta\rho) = \\ & k_x^3(\frac{5k_y^2 + k_x^2}{k^{10}} - 5\frac{\frac{5}{7}k_x^4 + 6k_x^2k_y^2 + 3k_y^4}{\rho^2 k^{14}} + 5\frac{2k_x^8 + 26k_x^6k_y^2 + 30k_x^4k_y^4 + 6k_x^2k_y^2}{\rho^4 k^{18}}),\end{aligned}$$

which in the limit $\rho \to \infty$ becomes the expression we were looking for,

$$\tilde{\zeta} = k_x^3\frac{k_x^2 + 5k_y^2}{k^{10}}. \tag{29}$$

Appendix B - Fjørtoft argument in terms of the centroids

Let us consider an evolving hydrodynamic 2D turbulence in the absence of forcing and dissipation. Here we will re-formulate the Fjørtoft argument in terms of the energy and enstrophy centroids in the k and l (i.e. scale) spaces. This formulation will be rigorous and quite useful for visualizing the directions of transfer of of the energy and the enstrophy. In contrast with the version of the Fjørtoft argument give in the main text, this formulation is for a non-dissipative turbulence rather than a forced/dissipated system.

The energy and the enstrophy k-centroids are defined respectively as

$$k_E = \int_0^\infty k E_k \, dk / E, \tag{30}$$

$$k_\Omega = \int_0^\infty k^3 E_k \, dk / \Omega, \tag{31}$$

and the energy and the enstrophy l-centroids as defined respectively as

$$l_E = \int_0^\infty k^{-1} E_k \, dk / E, \tag{32}$$

$$l_\Omega = \int_0^\infty k E_k \, dk / \Omega \equiv k_E E / \Omega, \tag{33}$$

where E_k is the 1D energy spectrum (i.e. the energy density in $|k|$).

Theorem 1 *Assuming that the integrals defining $E, \Omega, k_E, k_\Omega, l_E$ and l_Ω converge, the following inequalities hold,*

$$k_E \le \sqrt{\Omega / E}, \tag{34}$$

$$k_\Omega \ge \sqrt{\Omega / E}, \tag{35}$$

$$k_E k_\Omega \ge \Omega / E, \tag{36}$$

$$l_E \ge \sqrt{E / \Omega}, \tag{37}$$

$$l_\Omega \le \sqrt{E / \Omega}, \tag{38}$$

$$l_E l_\Omega \ge E / \Omega. \tag{39}$$

We are going to prove this theorem using Cauchy-Schwartz inequality[2], which states that

$$\left| \int_0^\infty f(k) g(k) \, dk \right| \le \left| \int_0^\infty f^2(k) \, dk \right|^{1/2} \left| \int_0^\infty g^2(k) \, dk \right|^{1/2}$$

[2] The suggestion to use the Cauchy-Schwartz inequality for reformulating the Fjørtoft argument in terms of the centroids was made to us by Gregory Eyink during the INI workshop the proceedings of which are published in this book.

for any functions $f(k), g(k) \in L^2$. We will only deal with positive functions, so the absolute value brackets may be omitted. Being in L^2 in our case means that all the relevant integrals converge, as suggested in the statement of the problem.

First, let us consider integral $\int kE\,dk$ and apply Cauchy-Schwartz inequality as follows,

$$\int_0^\infty kE\,dk = \int_0^\infty (kE^{1/2})(E^{1/2})\,dk \le \left(\int_0^\infty k^2E\,dk\right)^{1/2}\left(\int_0^\infty E\,dk\right)^{1/2},$$

which immediately yields (34) and (38).

Second, let us consider $\Omega = \int k^2E\,dk$ and split it as,

$$\int_0^\infty k^2E\,dk = \int_0^\infty (k^{3/2}E^{1/2})(k^{1/2}E^{1/2})\,dk \le \left(\int_0^\infty k^3E\,dk\right)^{1/2}\left(\int_0^\infty kE\,dk\right)^{1/2},$$

which immediately yields (36). Combining (36) with (34) gives (35).

Now, let us split $\int kE\,dk$ in a different way,

$$\int_0^\infty kE\,dk = \int_0^\infty (k^{3/2}E^{1/2})(k^{-1/2}E^{1/2})\,dk \le \left(\int_0^\infty k^3E\,dk\right)^{1/2}\left(\int_0^\infty k^{-1}E\,dk\right)^{1/2},$$

which immediately yields (39). Combining (39) with (38) gives (37).

We see that according to inequalities (34) and (35), during the system's evolution the energy centroid $k_E(t)$ is bounded from above and the enstrophy centroid $k_\Omega(t)$ is bounded from below (both by the same wavenumber $k = \sqrt{\Omega/E}$), as one would expect from Fjørtoft argument. Further, inequality (36) means that if $k_E(t)$ happened to move to small k's then $k_\Omega(t)$ *must* move to large k's, that is roughly, there cannot be inverse cascade of energy without a forward cascade of enstrophy. Note that there is no complimentary restriction which would oblige $k_E(t)$ to become small when $k_\Omega(t)$ goes large, so the k-centriod part of the Fjørtoft argument is asymmetric, and one has to consider the l-centroids to make it symmetric. Indeed, in additions to conditions (37) and (38) which are similar to (34) and (35), we have inequality (39) meaning that if $l_\Omega(t)$ happened to move to small l's then $l_E(t)$ *must* move to large l's, i.e. any forward cascade of enstrophy must be accompanied by an inverse cascade of energy.

Importantly, we do not always have $k_E \sim 1/l_E$ and $k_\Omega \sim 1/l_\Omega$. Indeed, consider a state with spectrum $E_k \sim k^{-5/3}$ for $k_a < k < k_b$ (with $k_b \gg k_a$) and $E_k \equiv 0$ outside of this range. It is easy to see that for this state $k_E \sim k_b^{1/3}k_a^{2/3}$ and $l_E \sim 1/k_b$ (i.e. $k_E \nsim 1/l_E$) and $k_\Omega \sim 1/l_\Omega \sim k_b$.

References

[1] Balk, A. M. 1991 A new invariant for rossby wave systems. *Phys. Lett. A* **155**, 20–24.

[2] Balk, A. M. 1997 New conservation laws for the interaction of nonlinear waves. *SIAM Review* **39** (1), 68–94.
[3] Balk, A. M. 2005 Angular distribution of rossby wave energy. *Physics Letters A* **345**, 154–160.
[4] Balk, A. M., Nazarenko, S. V. & Zakharov, V. E. 1990 On the nonlocal turbulence of drift type waves. *Phys. Lett. A* **146**, 217–221.
[5] Balk, A. M., Nazarenko, S. V. & Zakharov, V. E. 1991 A new invariant for drift turbulence. *Phys. Lett. A* **152**, 276–280.
[6] Balk, A. M., Zakharov, V. E. & Nazarenko, S. V. 1990 On the structure of the rossby/drift turbulence and zonal flows. Proceedings of the international symposium "generation of large-scale structures in continuous media". *Perm-Moscow, USSR* pp. 34–35.
[7] Charney, J. G. 1949 On a physical basis for numerical prediction of large-scale motions in the atmosphere. *J. Meteor* **6**, 371–385.
[8] Connaughton, C. P., Nadiga, B. T., Nazarenko, S. V. & Quinn, B. E. 2010 Modulational instability of rossby and drift waves and generation of zonal jets. *Journal of Fluid Mechanics* **654**, 207–231.
[9] Diamond, P. H., Itoh, S.-I., Itoh, K. & Hahm, T. S. 2005 Zonal flows in plasma - a review. *Plasma Phys. Control. Fusion* **47** (5), R35–R161.
[10] Fjørtoft, R. 1953 On the changes in the spectral distribution of kinetic energy for two-dimensional non-divergent flow. *Tellus* **5**, 225–230.
[11] Galperin, B., Nakano, H., Huang, H.-P. & Sukoriansky, S. 2004 The ubiquitous zonal jets in the atmospheres of giant planets and earth's oceans. *Geophys. Res. Lett.* **31**, L13303.
[12] Gill, A. E. 1974 The stability of planetary waves on an infinite beta-plane. *Geophys. Fluid Dyn.* **6**, 29–47.
[13] Gill, A. E. 1982 *Atmosphere - Ocean Dynamics*. Academic Press, New York.
[14] Goldreich, P. & Sridhar, S. 1995 Toward a theory of interstellar turbulence. 2: Strong alfvénic turbulence. *Astrophysical Journal* **438**, 763–775.
[15] Hasegawa, A. & Mima, K. 1978 Pseudo-three-dimensional turbulence in magnetized nonuniform plasma. *Phys. Fluids* **21**, 87–92.
[16] Holloway, G. 1984 Contrary roles of planetary wave propagation in atmospheric predictability. *AIP Conf. Proc.* **106**, 593–599.
[17] James, I. N. 1987 Suppression of baroclinic instability in horizontally sheared flows. *J. Atmo. Sci.* **44** (24), 3710.
[18] Mima, K. & Lee, Y. C. 1980 Modulational instability of strongly dispersive drift waves and formation of convective cells. *Phys. Fluids* **23**, 105.
[19] Kraichnan, R. H. 1967 Inertial ranges in two-dimensional turbulence. *Phys. Fluids* **10**, 1417–1423.
[20] Lewis, J. M. 1988 Clarifying the dynamics of the general circulation: Phillips's 1956 experiment. *Bull. Amer. Met. Soc.* **79** (1).
[21] Lorentz, E. N. 1972 Barotropic instability of rossby wave motion. *J. Atmo. Sci.* **29**, 258–269.

[22] Manin, D. Yu. & Nazarenko, S. V. 1994 Nonlinear interaction of small–scale Rossby waves with an intense large–scale zonal flow. *Phys. Fluids* **6** (3), 1158–1167.

[23] Maximenko, N. A., Melnichenko, O. V., Niiler, P. P. & Sasaki, H. 2008 Stationary mesoscale jet-like features in the ocean. *Geophys. Res. Lett.* **35**, L08603.

[24] Nazarenko, S. & Quinn, B. 2009 Triple Cascade Behavior in Quasigeostrophic and Drift Turbulence and Generation of Zonal Jets. *Phys. Rev. Lett.* **103**, 118501.

[25] Onishchenko, O.G., Pokhotelov, O.A., Sagdeev, R.Z., Shukla, P.K. & Stenflo, L. 2004 Generation of zonal flows by Rossby waves in the atmosphere. *Nonlin. Proc. Geophys.* **11**, 241–244.

[26] Rhines, P. 1975 Waves and turbulence on a betaplane. *J. Fluid Mech.* **69**, 417–443.

[27] Rhines, P. B. 1979 Geostrophic turbulence. *Ann. Rev. Fluid Mech.* **11**, 401–441.

[28] Sanchez-Lavega, A., Rojas, J. F. & Sada, P. V. 2000 Saturn's zonal winds at cloud level. *Icarus* **147**, 405.

[29] Simon, A. A. 1999 The structure and temporal stability of jupiter's zonal winds: A study of the north tropical region. *Icarus* **141**, 29.

[30] Smolyakov, A. I., Diamond, P. H. & Shevchenko, V. I. 2000 Zonal flow generation by parametric instability in magnetized plasmas and geostrophic fluids. *Phys. Plasmas* **7**, 1349.

[31] Smolyakov, A. I. & Krasheninnikov, S. I. 2008 Generation of electromagnetic structures via modulational instability of drift waves. *Phys. Plasmas* **15**, 072302.

[32] Vallis, G. & Maltrud, M. 1993 Generation of mean flows and jets on a β-plane and over topography. *J. Phys. Oceanography* **23**, 1346–1362.

[33] Wagner, F., Becker, G., Behringer, K., Campbell, D., Eberhagen, A., Engelhardt, W., Fussmann, G., Gehre, O., Gernhardt, J., Gierke, G. v., Haas, G., Huang, M., Karger, F., Keilhacker, M., Klüber, O., Kornherr, M., Lackner, K., Lisitano, G., Lister, G. G., Mayer, H. M., Meisel, D., Müller, E. R., Murmann, H., Niedermeyer, H., Poschenrieder, W., Rapp, H. & Röhr, H. 1982 Regime of improved confinement and high beta in neutral-beam-heated divertor discharges of the asdex tokamak. *Phys. Rev. Lett.* **49** (19), 1408–1412.

[34] Williams, G. P. 1978 Planetary circulations: Barotropic representation of jovian and terrestrial turbulence. *J. Atmos. Sci.* **35**, 1399–1426.

The HyperCASL algorithm

David G. Dritschel and Jérôme Fontane

Abstract This paper outlines a major new extension to the diabatic Contour-Advective Semi-Lagrangian (CASL) algorithm [5; 8]. The extension, called the 'HyperCASL' (HCASL) algorithm, advects material potential vorticity contours like in CASL, but treats diabatic forcing or damping with a Vortex-In-Cell (VIC) algorithm. As a result, HCASL is fully Lagrangian regarding advection. A conventional underlying grid is used as in CASL for 'inversion', namely for obtaining the advecting velocity from the potential vorticity.

1 Introduction

Herein we outline a powerful new approach to the simulation of layerwise-2D geophysical flows. Our approach combines the CASL algorithm [5; 6; 7; 8; 11], a hybrid contour-dynamics [21] method exploiting the efficiency gained by the use of an underlying grid, with a vortex-in-cell method [2]. The latter is here used to compensate for errors arising from contour regularisation or 'surgery' [3; 4] appearing at the level of the grid. In this way, (essential) dissipation occurs only at sub-grid scales, and there is no direct impact of surgery on the computed velocity field, which is obtained on the grid by standard spectral methods. This is particularly important for long-term simulations, where error accumulation needs to be minimised [10].

This new approach, here coined the '*HyperCASL algorithm*', also allows for general non-conservative effects, by design. For instance, one may take account of radiative (thermal) effects which drive a given flow to some thermal equilibrium distri-

David G. Dritschel
University of St Andrews, Mathematical Institute, St Andrews KY16 9SS, Scotland, e-mail: dgd@mcs.st-and.ac.uk

Jérôme Fontane
ISAE – DAEP, 1 place Emile Blouin, BP 75064, 31033 Toulouse, France, e-mail: j.fontane@isae.fr

D. Dritschel (ed.), *IUTAM Symposium on Turbulence in the Atmosphere and Oceans*,
IUTAM Bookseries 28, DOI 10.1007/978-94-007-0360-5_23,

bution (which is unstable in the case of the Earth's atmosphere, see [1; 16; 18; 9] & refs. therein). Or, one can account for 'Ekman pumping' which converts wind stress at the ocean's surface into a vorticity source or sink there [14]. In fact, in the algorithm outlined below, very general forms of forcing or damping can be accounted for (e.g. stochastic, small-scale convection, etc.).

2 Brief Description of the Numerical Algorithm

In previous works, various means to include such forcing and damping in the CASL algorithm have been described and tested. In [8], the dynamical evolution equation for the scalar potential vorticity (PV) q was split into two equations

$$\frac{\mathrm{D}q_a}{\mathrm{D}t} = 0 \qquad ; \qquad \frac{\mathrm{D}q_d}{\mathrm{D}t} = S \tag{1}$$

where $\mathrm{D}/\mathrm{D}t \equiv \partial/\partial t + \mathbf{u}\cdot\nabla$ is the material derivative, $S(\mathbf{x},t)$ is any source term, and we require $q = q_a + q_d$. Here, q_a is called the 'adiabatic PV' and q_d is called the 'diabatic PV'. The adiabatic PV is materially conserved, whereas the diabatic PV changes on fluid 'particles' in response to the 'forcing' S. Note, the velocity $\mathbf{u}$ is obtained from the combined PV q (and in general other fields e.g. representing non-advective processes like gravity wave propagation), so the equations are in fact coupled. Nevertheless, adding them together gives $\mathrm{D}q/\mathrm{D}t = S$, which is the exact equation satisfied by PV.

The reason for splitting the PV equation is to exploit the numerical advantages of CASL in modelling conservative, adiabatic PV evolution. The CASL algorithm is capable of following extraordinary detail at a tiny fraction of the cost of conventional (e.g. pseudo-spectral) methods [6; 11]. The CASL algorithm evolves q_a by contour advection — merely moving a set of 'nodes' $\{\mathbf{x}_i\}$ $(i = 1, \ldots, n)$ on contours representing the field q_a:

$$\frac{\mathrm{d}\mathbf{x}_i}{\mathrm{d}t} = \mathbf{u}(\mathbf{x}_i, t)\,. \tag{2}$$

The contours separate regions of uniform q_a, and since they are normally generated by contouring a prescribed gridded field, the jump in q_a across each contour is a fixed constant Δq. It is noteworthy that a modest number of contours can represent a continuous PV distribution astonishingly well [11].

Contours, however, are poorly suited for representing diabatic effects, i.e. forcing and damping. The diabatic PV q_d is better handled by other numerical methods, and in [8], a standard 'semi-Lagrangian' method [20; 12] was employed. The semi-Lagrangian method approximates the trajectories of fluid particles which arrive at grid points at the end of a time step. The method therefore obtains the positions of particles at the beginning of a time step, and from these positions, the initial value of q_d, using a bi-cubic interpolation formula. If the source $S = 0$, then this value of q_d is simply copied into the value for the grid point lying at the end of each particle

trajectory. This appears to solve $\mathrm{D}q_d/\mathrm{D}t = 0$ exactly, except that interpolation errors induce significant numerical diffusion [6]. The method is used in [8] with $S \neq 0$ simply because it is convenient to obtain the integral of S along trajectories, and because there is no CFL or numerical stability restriction on the time step.

More recently, long-time integrations of 2D turbulence were carried out using a similar approach, except that a standard pseudo-spectral method was used to handle q_d [10]. In these integrations, q_d was *not* used to represent some prescribed diabatic source S, but rather errors coming from the regularisation of contours or 'surgery' that is necessary for efficiency and for maintaining adequate point resolution along contours. For short to moderate integrations, this error is not significant, as demonstrated in a recent comparison between the CASL and pseudo-spectral methods [11]. But for long integrations, this error leads to spurious growth in the large-scale energy spectrum, and often a small growth in the total energy. Essentially, the removal of thin PV filaments by surgery projects on a broad range of wavenumbers in spectral space. This problem was solved in [10] by taking the error from surgery (and from periodic re-contouring, see below) and transferring it to q_d as a source, thereby removing all error explicitly at the level of the grid (in fact, a similar procedure was also carried out in [8]).

The evolution of q_d within a standard pseudo-spectral method cannot however be accomplished without numerical diffusion. Whereas in the semi-Lagrangian method this diffusion is implicit in the interpolation of the trajectory starting positions, in the pseudo-spectral method this diffusion must be added explicitly to the evolution equation. In [10], ordinary molecular-like diffusion was used, at the smallest possible level, to minimise diffusion.

An alternative approach, using sets of contours having different PV jumps (Δq, $\alpha\Delta q$, $\alpha^2\Delta q$, …, $\alpha < 1$) is described in [15]. In this approach, it is possible to dispense entirely with the semi-Lagrangian and pseudo-spectral methods, and instead treat the source S by judicious and frequent contouring, thereby using contours only. However, contouring is not an efficient procedure, and the algorithm is complicated by the need to specify many control parameters.

2.1 Fully Lagrangian Advection

We demonstrate next that the diabatic evolution of q_d can be accomplished simply and efficiently in a fully *Lagrangian* manner, and *without* numerical diffusion all the way down to the grid scale. In this new approach, all dissipation takes place at sub-grid scales (principally by contour surgery).[1] Instead of conventional grid-based

[1] Arguably, such dissipation is an *essential* feature of any discrete approximation to a fluid dynamical system, *even when the system is perfectly conservative*. Even the 'perfect' discrete model which obtains the exact average value of fields over grid cells would exhibit apparent dissipation, simply because averaging appears diffusive. Squared integrals of quantities like q^2 would appear to diminish even though they are constant in the original system. A simple thought experiment is a tracer θ being stirred by the 2D potential flow $(-cy/r^2, cx/r^2)$ where c is a constant and $r^2 = x^2 + y^2$. In

methods, we employ an array of point vortices to model diabatic PV evolution, i.e. solve $\mathrm{D}q_d/\mathrm{D}t = S$. In our approach, this equation is solved *exactly* at the level of the grid. This is accomplished by letting the circulations Γ_k of individual vortices vary with time. By choosing $\mathrm{d}\Gamma_k/\mathrm{d}t$ appropriately, we can ensure that $\mathrm{D}q_d/\mathrm{D}t = S$ is satisfied *at every grid point*.

2.2 Transfer of Diabatic Forcing to Point Vortices

The essential details of the method are given next. Here, we consider the simplest 2D rectangular domain, which may be periodic. We suppose we have divided this domain into some convenient regular grid, with grid lengths Δx and Δy. At any given time t, we arrange to have $m \times m$ point vortices per grid box, on average (typically, we use $m = 2$, the minimum value that works). Every so often, the vortices are re-arranged on a regular grid and their circulations Γ_k are modified to ensure that the re-arrangement has no effect on the PV they induce at each grid point.[2] As in the CASL algorithm [5], we use bi-linear interpolation to transfer information from the grid to the vortices, and, here, *vice versa*. For example, the PV at a grid point (i, j) due to point vortices is obtained by the sum

$$q_d = \sum_{k \in G_{ij}} w_{ijk} \tilde{q}_k \tag{3}$$

where G_{ij} is the domain consisting of the (typically 4) grid boxes surrounding (i, j), w_{ijk} are the bi-linear interpolation weights, and $\tilde{q}_k = \Gamma_k \Delta x \Delta y$ are normalised circulations (having units of PV). The weights are explicitly given by

$$w_{ijk} = (1 - |x_k - \bar{x}_i|/\Delta x)(1 - |y_k - \bar{y}_j|/\Delta y) \tag{4}$$

where (x_k, y_k) is the position of vortex k, and $(\bar{x}_i, \bar{y}_j)$ are the coordinates of grid point (i, j). The vortices lying within G_{ij} are found simply by integer arithmetic.

All of this is standard. The difficulty we face with diabatic forcing is that we are given $\mathrm{D}q_d/\mathrm{D}t$ (as some function $S(\mathbf{x}, t)$), and we must therefore invert

$$S_{ij} = \sum_{k \in G_{ij}} w_{ijk} \frac{\mathrm{d}\tilde{q}_k}{\mathrm{d}t} \tag{5}$$

time, without diffusion the tracer will spiral ever more tightly, eventually reaching arbitrary small scales. While the integral of θ^2 remains conserved in time, any averaging of θ before computing this integral will result in a smaller value — apparent dissipation.

[2] We typically re-arrange the vortices when the integral $\int_{t_0}^{t} |\zeta|_{\max} \mathrm{d}t \approx 0.5$, where ζ is the relative vertical vorticity and t_0 is the previous time the vortices were re-arranged. This ensures that the vortex array does not get too deformed, and that minimal computational effort is put into the re-arrangement.

to find $\mathrm{d}\tilde{q}_k/\mathrm{d}t$. (Note that we do not need to include $\mathrm{d}w_{ijk}/\mathrm{d}t$; this term makes no contribution as can be seen in the adiabatic case when $S = 0$ and $\mathrm{d}\tilde{q}_k/\mathrm{d}t = 0$.) There are potentially many solutions to this problem. Here, we seek the solution for which the local vortex density ρ_k multiplied by $\mathrm{d}\tilde{q}_k/\mathrm{d}t$ can be expressed as a bi-linear interpolation of an unknown gridded field F over the grid box B_{ij} containing vortex k:

$$\rho_k \frac{\mathrm{d}\tilde{q}_k}{\mathrm{d}t} = w_k^{00} F_{i,j} + w_k^{10} F_{i+1,j} + w_k^{01} F_{i,j+1} + w_k^{11} F_{i+1,j+1}. \tag{6}$$

Here, $w_k^{\alpha\beta} = w_{i+\alpha,j+\beta,k}$ above (commas between indices added). The vortex density ρ_k is found itself by bi-linear interpolation; first we compute the density at each grid point $\bar{\rho}_{ij}$ from

$$\bar{\rho}_{ij} = \sum_{k \in G_{ij}} w_{ijk} \tag{7}$$

then we set

$$\rho_k = w_k^{00} \bar{\rho}_{i,j} + w_k^{10} \bar{\rho}_{i+1,j} + w_k^{01} \bar{\rho}_{i,j+1} + w_k^{11} \bar{\rho}_{i+1,j+1}. \tag{8}$$

We solve for $\mathrm{d}\tilde{q}_k/\mathrm{d}t$ iteratively, normally starting from the known value at the previous time step (or fractional time step). Occasionally, after re-arranging the vortices, we do not have a known value, so we make a guess using 6 with $F = S$. On a regular array, the method described below converges most rapidly [13], so a poor starting guess is not problematic.

The following describes one iteration of the procedure. We first initialise a residual matrix $R_{ij} = S_{ij}$ outside the iteration loop. Then, the first step is to subtract the right-hand-side of 5 from R_{ij}, thereby redefining the residual. If this residual is zero, we have clearly solved the problem. In general it is not, and so we add the right-hand-side of 6, with $F_{ij} = R_{ij}$, to $\mathrm{d}\tilde{q}_k/\mathrm{d}t$. We then check if $\max |R_{ij}| < \varepsilon$, some preset tolerance. If it is, we are finished, otherwise we carry out another iteration.

This procedure is simple and efficient. Typically at most a few tens of iterations are ever required for an accurate representation of the gridded source S_{ij}. And, while we may use 4 times as many vortices as grid points, the operations over vortices are all simple and add only a small extra cost to the complete numerical algorithm. Full details of these costs, together with inter-algorithm comparisons, are presented in a longer article [13].

3 An Example: A Diabatically-Forced Jet

Here, we illustrate the new HyperCASL algorithm in the simulation of a jet over weak topography. The jet, a parallel flow $u(y)$, is in thermal equilibrium, but the equilibrium is arranged to be unstable. As in a previous study [8], we use the standard quasi-geostrophic equations governing the motion of a mid-latitude 2D shallow-water flow in near hydrostatic and geostrophic equilibrium:

$$\frac{\mathrm{D}q}{\mathrm{D}t} = \frac{\psi - \psi_e}{\tau_{\rm th} L_D^2} - \frac{\zeta}{\tau_{\rm ek}} \tag{9}$$

$$(\nabla^2 - L_D^{-2})\psi = q + q_{\rm bot} - \beta y \qquad ; \qquad \mathbf{u} = (u,v) = \left(-\frac{\partial\psi}{\partial y}, \frac{\partial\psi}{\partial x}\right).$$

Here ψ is the streamfunction, ψ_e is a prescribed thermal equilibrium streamfunction, $\tau_{\rm th}$ is the thermal damping time, L_D is the Rossby deformation length ($= \sqrt{gH}/f_0$ where g is gravity, H is the mean fluid depth, and f_0 is the mean Coriolis frequency), $\zeta = \nabla^2\psi$ is the relative vertical vorticity, $\tau_{\rm ek}$ is the Ekman damping time, $q_{\rm bot}$ is the PV associated with bottom topography at $z = b(\mathbf{x})$ ($q_{\rm bot} = -fb/H$), and β is the variation of the Coriolis frequency across the domain. Here, we consider a doubly-periodic domain of (scaled) dimensions $2\pi \times 2\pi$. This dynamical system is rich in parameters and not well understood; yet, it is a major simplification of the equations used e.g. in weather forecasting and ocean modelling.

The specific simulation illustrated starts from a state of rest with $\psi_e(y) = -wU_{\max}\mathrm{sech}(y/w)\tanh(y/w)$, with $w = 0.2$ and $U_{\max} = 1$, the maximum equilibrium jet velocity occurring at $y = 0$. We take a random bottom topography with spectrum (or shell integral of squared Fourier coefficients) proportional to $Bk/(k^2+k_0^2)^2$, where $k = |\mathbf{k}|$ is the wavenumber, with $k_0 = 10$ and B chosen to give a maximum $q_{\rm bot}$ of 0.04π. This is a small amplitude topography, as the PV associated with the $\psi_e(y)$ is nearly 100 times larger. The purpose of the topography is simply to destabilise the jet. We also take $\tau_{\rm th} = 20$ and $\tau_{\rm ek} = \infty$ (no Ekman damping), $L_D = 0.1$ and $\beta = 0$.

Numerically, we simulate the flow on a basic grid of dimensions 256×256 (called the 'inversion grid' since this is the grid used to find ψ and $\mathbf{u}$ given q in 9). For efficiency, we take the minimum number of 2×2 point vortices per grid box to uptake forcing and surgical errors (see below). We choose a PV jump $\Delta q = 0.4\pi$ across all contours, and a PV 'conversion grid' 4 times finer (in each direction) than the inversion grid (for converting the contours to gridded values). The latter is standard. What is new here are proposed fixed settings for the contour resolution parameters. Based on exhaustive tests reported in [13], we fix the maximum node separation μL on the contours at $1.25\Delta x$, where $\Delta x = 2\pi/256$ is the inversion grid length, and we fix the surgical scale δ at $\Delta x/16$. Coupling this with the required relationship $\delta = \mu^2 L/4$, this implies a dimensionless node separation parameter $\mu = 0.2$ and a characteristic length $L = 6.25\Delta x$. Fixing μL in this way ensures contours can bend in response to the flow field. This is important.

Contours are regularised by surgery whenever $\int_{t_0}^{t} |\zeta|_{\max}\mathrm{d}t$ exceeds 2.5, where t_0 is the previous surgery time. The value of 2.5 was obtained by carefully analysing contour stretching characteristics [13]. Every 20th regularisation, surgery is replaced by recontouring [8], to transfer the PV in the vortices to contours, and to avoid potential errors of overlapping contours [19]. New contours are built on an ultra-fine 'contouring grid' 16 times finer (in each direction) than the inversion grid, after merging the contour and point vortex PV on this grid. Note: the contouring grid length matches the surgical scale; this new setting has been found to markedly improve conservation properties [13]. The gridded PV associated with the new con-

tours will generally not match the original PV on the inversion grid, and so the difference is given to the point vortices at the beginning of the next simulation cycle. In this way, *neither surgery nor recontouring changes the gridded PV*.

The time step Δt is adapted to accurately resolve the vortical motion by setting $\Delta t = \min(0.0625, \pi/10|\zeta|_{\max})$. A 4th-order Runge-Kutta method is used for integrating 2 for the contour nodes and for the point vortices.

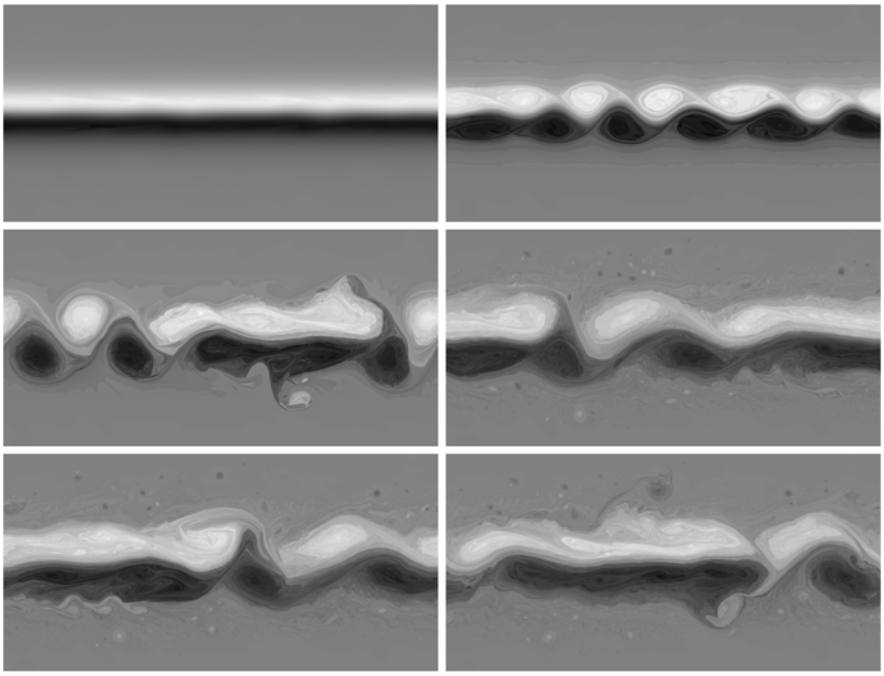

Fig. 1 The PV q within the inner half of the domain $|y| < \pi/2$ at times $t = 25$ and 50 (top row), at $t = 75$ and $t = 425$ (middle row), and at $t = 450$ and 475 (bottom row). A linear grey scale is used with white being the highest PV value and black being the lowest. The maximum value of $|q|$ at these times is 9.55, 12.96, 13.94, 14.98, 14.51 and 15.64, respectively.

Figure 1 exhibits the evolution of the PV field q at early times (top row) and at late times (bottom row). See also figure 2 for an enlarged view of the final time, $t = 500$. The flow becomes statistically stationary with nearly constant levels of energy and enstrophy (mean-square PV) from $t = 100$ to 500, the end of the simulation (a unit of time here roughly corresponds to a day — the time mean value of $|\zeta|_{\max}$ is 5.55 while that of $\zeta_{\rm rms}$ is 2.94). A jet spanning part of the domain forms and moves eastward by gobbling up vortices left in the wake of the jet and shedding new vortices. The late time images shown in the bottom row reveal the wealth of detail that can be captured by the HyperCASL algorithm at modest resolution. The images were created by merging the contour and point vortex PV on the ultra-fine

contouring grid (here 4096×4096). The entire simulation took 8 hours on a single 2.4GHz Intel processor.

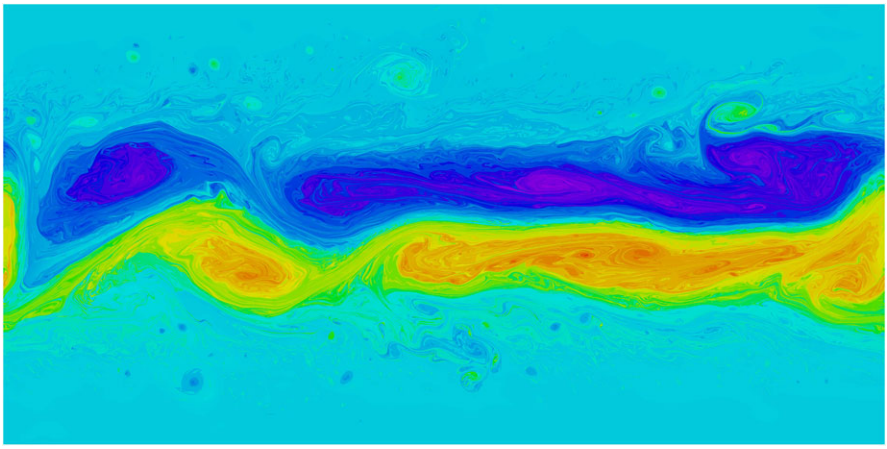

Fig. 2 An enlarged view of the PV q at the final time $t = 500$, rendered as in figure 1. The maximum value of $|q|$ is 15.20.

4 Conclusions and Future Extensions

The HyperCASL algorithm represents a radically new opportunity for modelling complex geophysical flows efficiently. Preliminary results indicate that potentially enormous gains in accuracy may result by applying and generalising this new approach. Extensions to more complete equation sets are straightforward (cf. [7]), and for these an accurate treatment of PV is *also* vital for an accurate representation of the complete dynamics. There are also some challenges, such as treating spherical geometry (the atmosphere) or complex domains (the oceans). HyperCASL is not limited to PV, but can be applied to other tracers (like chemical species in the atmosphere), including moisture. In particular, modelling water vapour by contours and subgrid-scale convection by Lagrangian particles may be a timely opportunity to improve the forecasting of precipitation [17].

Acknowledgements DGD would like to thank the staff at the Isaac Newton Institute in Cambridge for their help in creating an ideal atmosphere for the IUTAM/INI symposium.

References

[1] Andrews, D.G., Holton, J.R., Leovy, C.B.: Middle Atmosphere Dynamics. Academic Press (1987)

[2] Christiansen, J.P., Zabusky, N.J.: Instability, coalescence and fission of finite-area vortex structures. J. Fluid Mech. **61**, 219–243 (1973)

[3] Dritschel, D.G.: Contour surgery: a topological reconnection scheme for extended integrations using contour dynamics. J. Comput. Phys. **77**, 240–266 (1988)

[4] Dritschel, D.G.: Contour dynamics and contour surgery: numerical algorithms for extended, high-resolution modelling of vortex dynamics in two-dimensional, inviscid, incompressible flows. Computer Phys. Rep. **10**, 77–146 (1989)

[5] Dritschel, D.G., Ambaum, M.H.P.: A contour-advective semi-Lagrangian numerical algorithm for simulating fine-scale conservative dynamical fields. Quart. J. Roy. Meteorol. Soc. **123**, 1097–1130 (1997)

[6] Dritschel, D.G., Polvani, L.M., Mohebalhojeh, A.R.: The contour-advective semi-Lagrangian algorithm for the shallow water equations. Mon. Wea. Rev. **127**, 1551–1565 (1999)

[7] Dritschel, D.G., Viúdez, Á.: A balanced approach to modelling rotating stably-stratified geophysical flows. J. Fluid Mech. **488**, 123–150 (2003)

[8] Dritschel, D.G., Ambaum, M.H.P.: The diabatic contour advective semi-Lagrangian algorithm. Mon. Weather Rev. **134**, 2503–2514 (2006)

[9] Dritschel, D.G., McIntyre, M.E.: Multiple jets as PV staircases: the Phillips effect and the resilience of eddy-transport barriers. J. Atmos. Sci. **65**, 855–874 (2008)

[10] Dritschel, D.G., Scott, R.K., Macaskill, C., Gottwald, G.A., Tran, C.V.: Unifying scaling theory for vortex dynamics in two-dimensional turbulence. Phys. Rev. Lett. **101**, 094501 (2008)

[11] Dritschel, D.G., Scott, R.K.: On the simulation of nearly inviscid two-dimensional turbulence. J. Comput. Phys. **228**, 2707–2711 (2009)

[12] Durran, R.R.: Numerical Methods for Wave Equations in Geophysical Fluid Dynamics. Springer (1999)

[13] Fontane, J., Dritschel, D.G.: The HyperCASL Algorithm: a new approach to the numerical simulation of geophysical flows. J. Comput. Phys. **228**, 6411–6425 (2009)

[14] Gill, A.E.: Atmosphere-Ocean Dynamics. Academic Press (1982)

[15] Mohebalhojeh, A.R., Dritschel, D.G.: The diabatic contour-advective semi-Lagrangian algorithms for the spherical shallow water equations. Mon. Wea. Rev. **137**, 2979–2994 (2009)

[16] Panetta, R.L.: Zonal jets in wide baroclinically unstable regions: persistence and scale selection. J. Atmos. Sci. **50**, 2073–2106 (1993)

[17] Pierrehumbert, R.T.: The hydrologic cycle in deep time climate problems. Nature **419**, 191–198 (2002)

[18] Rhines, P.B.: Jets. Chaos **4**, 313–339 (1994)

[19] Schaerf, T.M.: On contour crossings in contour-advective simulations of geophysical fluid flows, Ph.D. Thesis, University of Sydney (2006)
[20] Smolarkiewicz, P.K., Pudykiewicz, P.: A class of semi-Lagrangian approximations for fluids. J. Atmos. Sci. **49**, 2082–2096 (1992)
[21] Zabusky, N.J., Hughes, M.H., Roberts, K.V.: Contour dynamics for the Euler equations in 2 dimensions. J. Comput. Phys. **30**, 96–106 (1979)